UNIVERSITY COLLEGE LONDON

Faculty of Mathematics & Physical Sciences

Department of Physics & Astronomy

A Multi-Wavelength Study Of Fast Winds From Central Stars Of Planetary Nebulae

Thesis submitted for the
Degree of Doctor of Philosophy
University College London

by

Simon Elsdon Hodges

Supervisors:
Prof. Raman Prinja
Prof. Ian Howarth

Examiners:
Prof. Allan Willis
Dr. Ian Stevens

June 15, 2011

This thesis is dedicated to...

Mum & Dad

Abstract

Structure has been observed in the stellar outflows of hot, luminous OB stars through the temporal spectral analysis of UV data: the absorption troughs of wind-accelerated P-Cygni profiles of certain UV 'super-ions', particularly the P v $\lambda\lambda\,1118, 1128$ doublet, have revealed the presence of additional absorption components which have been observed to migrate through the wind. Similar P-Cygni profiles have also been observed in the the UV spectra of Central Stars of Planetary Nebulae (CSPNs), but detailed temporal analysis of CSPN outflows has been frustrated due to a lack of substantial time-series data. However, the Far Ultraviolet Spectroscopic Explorer (FUSE) satellite has provided high-resolution time-series data for CSPNs, and therefore the nature of the time-variance of UV P-Cygni profiles can be investigated. To this end FUSE spectroscopic data has been obtained, and certain key UV resonance lines, as found in the stellar wind, have been subjected to various time-series analysis tools including Time Variance Spectra (TVS) and Fourier-based periodicity analysis.

Also, optical time-series data of young CSPNs has been obtained via the ESO High-Accuracy Radial velocity Planetary Searcher (HARPS) spectrograph, and therefore similar temporal analysis has been carried out into the possible appearance of time-varying structure of Helium lines found in the deep photospheric regions of the atmosphere with the aim of detecting the presence of modulated structure at the base of the stellar wind – with the aim of discovering a causal mechanism for the higher wind-related phenomena.

The presence of such structure in the stellar outflows of CSPNs (and likewise, OB stars) suggests that non-LTE stellar atmosphere analysis techniques – such as the Sobolev with Exact Integration (SEI) method used within this thesis – which assume a spherically smooth wind may provide inaccurate levels of mass loss from the stellar atmosphere; also,

the possible non-smooth nature of the wind is considered from the viewpoint of possessing a more porous 'clumped' material which would also have an affect upon mass loss determinations, a key factor in the understanding of the latter stages of stellar evolution.

Acknowledgements

I would like to take this opportunity to thank my PhD supervisor, Professor Raman Prinja, for guidance – and above all, patience – as I've endeavoured to complete this thesis.

I am indebted to a small and select group of people whose help and advice through the many computer-related trials and tribulations has been invaluable: Dr Adam Burnley, for acting as my chaperone in La Silla on my first observing trip; Dr Dugan Witherick, who first set me up in my temporal analyses; Dr Fabrizio Sidoli, for help far beyond the call of duty in dealing with innumerable computing crises; Dr Matt North, for his patience in getting this technophobe to stick with given tasks by taking things one step at a time; Dr Samantha Searle, for her encouragement; and finally Dr-in-waiting Joanna Fabbri, for all her help in getting this work onto the pages of latex in some kind of order, and above all, for simply being around and listening to my woes, even when she has had her own terrific tome to complete...

I, Simon Elsdon Hodges, confirm that the work presented in this thesis is my own. Where information has been derived from other sources, I confirm that this has been indicated in the thesis.

"O, there's so much I don't know about astrophysics – I wish I'd read that book by that wheelchair guy."

Homer J. Simpson – Explorer in the Third Dimension

Contents

List of Figures

List of Tables

Chapter 1

Introduction

1.1 Introduction to Planetary Nebulae

For a low-mass Dwarf Star – luminosity class V – for which $M_\star \sim 3M_\odot$, during its main sequence core hydrogen-burning phase, the mass-loss incurred is of little significance to its evolution, being only of the order of only $10^{-12}\ M_\odot\,\mathrm{yr}^{-1}$; and with a main sequence lifetime of approximately 400 million years (4×10^8 years), the amount of mass lost is negligible.

When core H-burning ceases but continues in a H-burning shell surrounding the inert core, the outer envelope, heated by the burning H-shell, expands and cools and the subsequent appearance of a temperature gradient within the envelope sets up a convective zone which extends as far down as the region where the products of the core burning are present, and so starts to 'dredge' the H-burning products from the core to the surface; and when the envelope is fully convective, the star enters the so-called Red Giant Branch (RGB) – luminosity class III – upon the Hertzsprung-Russell Diagram (HRD).

When the inert core, now shrunken and degenerate (where the pressure inside is independent of temperature), has reached a high enough temperature to remove the degeneracy through the helium core flash, core He-burning commences, the core expands and the swollen envelope shrinks – the star then enters upon the horizontal branch of the HR diagram.

When core helium-burning is exhausted, the star continues to burn helium in a shell

around the now carbon core (in a similar manner as the hydrogen burning shell around the formerly helium core, following the main sequence). The H-burning shell continues; and so the star now enters upon a double shell-burning phase, where 10% of the star's luminosity is generated from the inner He-burning shell surrounding the inert carbon core, and 90% if generated by the outer H-burning shell surrounding the inert helium zone between the two burning shells. Again the inert core starts to shrink and once again become degenerate; again the burning shells expand the star's outer envelope, but to radius approximately 10 times that of the former red giant stage; it now moves onto the Asymptotic Giant Branch (AGB) – also luminosity class III. Another temperature gradient establishes itself and so, once again, the envelope becomes deeply – almost completely – convective, dredging up the material created by the H-burning shell. While in the AGB phase, the star's further evolution is now completely dominated by mass-loss.

The He-burning shell continues to dump fresh (carbon) material upon the inert core, thereby increasing its mass, and with increasing mass so the star's luminosity increases and moves up the AGB; the mass-loss rate increases tremendously from about 10^{-9} to about 10^{-5} $M_{\odot}\,\mathrm{yr}^{-1}$ at the 'tip' of the AGB.

The increased mass-loss rate coincides with the onset of thermal pulses: after it has burned outward for some time, the H-burning shell cools and 'switches off'; the He-shell continues to burn and so likewise moves outward in mass until it reaches the H-rich layers; and as this material meets the 10^8 K He-burning shell, it is re-ignited – producing a thermal pulse in the star, and as a result of which, the star once again experiences a double shell-burning.

Once again the H-burning shell moves outwards, cools, and is subsequently extinguished; and the whole process, culminating in a thermal pulse, repeats, and continues to do so with a period of approximately 10^4 years, during the AGB phase. The instability results in a third and final convection-based 'dredge-up', enabling the products of the He-burning shell, namely carbon and possibly oxygen, to reach the surface.

The mass of the convective envelope decreases due to two co-existing processes: inwardly, the shell-burning process continue to add mass to the inert core; and also outwardly, the stellar wind mass-loss continually removes material from the outer envelope.

During the AGB phase the effective temperature of the star is of the order of $T_{\mathrm{eff}} \simeq$ 3000 K, so the radius scales as $R_{\star} \sim {L_{\star}}^{0.5}$. As the luminosity increases exponentially, the mass-loss rate increases almost exponentially. With $L_{\star} = 10^4\ L_{\odot}$, $R_{\star} = 400\ R_{\odot}$ and $M_{\star} \simeq$

$M_\odot$, this gives a mass-loss rate of around 4 $\times 10^{-6}$ $M_\odot\,\mathrm{yr}^{-1}$.

When the mass of the envelope has reached a minimum value of around 10^{-3} $M_\odot$, there is now not enough (envelope) material to be able to sustain the convection within; and so the envelope starts to contract into radiative equilibrium. The star then moves to the left on the HRD as the AGB phase comes to an end. It can be shown that for a star of initial mass 3 $M_\odot$ the core mass at the end of the AGB is 0.64 $M_\odot$ – almost equal to the star's entire mass by this stage – this of course depends upon the amount of mass lost thus far.

Once the star has left the AGB, it contracts and moves to the left in around 10^4 years, with little (vertical) change of luminosity; and as the core mass hardly changes during this time, the luminosity remains constant, and so the leftward move is horizontal upon the H-R diagram. The location of the star along this line is therefore determined by the mass of the envelope. The very small envelope mass decreases steadily because the fusion taking place within shells (H & He) removes material from the envelop and dumps it upon the core; and also because of a stellar wind – now of the order of $10^{-9} M_\odot\,\mathrm{yr}^{-1}$ during this phase. When the envelope mass has reduced to about $10^{-4} M_\odot$ the star has an effective temperature of about 30,000 K . In actual fact the time it takes for the star to move across this post-AGB line on the HRD – the 'crossing time' – is determined by how long it take for the star's effective temperature to rise from about $T_{\mathrm{eff}} \simeq 3000$ K to about $T_{\mathrm{eff}} \simeq 30{,}000$ K. Once at this high temperature the star, now with a radius $R_\star \simeq 4R_\odot$ will develop a line-driven wind with a mass-loss rate of 10^{-9} to $10^{-7} M_\odot\,\mathrm{yr}^{-1}$ and a velocity of around 1000 $\mathrm{km\,s}^{-1}$. This fast line-driven wind will overtake the slow dust-driven wind of $v_\infty \simeq 10$ $\mathrm{km\,s}^{-1}$ from the AGB phase, and the two will interact to produce a *planetary nebula*. The remaining star – now really just the inert core – is now the *central star* of the planetary nebula.

The central star producing the significantly radiatively-driven wind mass-loss of around 10^{-9} to $10^{-7} M_\odot\,\mathrm{yr}^{-1}$ will reduce the envelope mass to a even lower value; and when the envelope mass becomes too low, $M_{env} < 10^{-5} M_\odot$, shell-burning will stop, and the central star will cool down and transform into a degenerate White Dwarf – luminosity class VII.

The white dwarf's mass is almost equal to that of the mass of the star's core as it left the AGB, with only a slight increase in mass as it crossed the HRD. The mass of the white dwarf is $0.64 M_\odot$, whereas the initial mass of the star was $3 M_\odot$ – so the star has lost $2.36 M_\odot$.

White dwarf masses are typically between 0.5 and $0.7M_{\odot}$, and stars with an initial ZAMS (zero age main sequence) mass of up to $8M_{\odot}$ can eventually form white dwarfs; so these stars must have lost a significant proportion of their mass over their evolutionary lifetime in the form of a stellar wind.

1.1.1 Hydrogen-rich CSPNs

In this thesis the focus will be on spectral Of-type hydrogen rich CSPNs: those which exhibit strong hydrogen lines (in absorption and emission) in their spectra; and are therefore often called O-type, as this higher level of spectral hydrogen in analogous to that of hot OB-type stars. The Of-type CSPN is therefore categorically separate from the hydrogen-deficient Wolf-Rayet (WR-type) CSPNs, whose central stars exhibit a hydrogen-depleted core, thereby revealing the helium-rich layers, the spectra of which therefore show strong absorption and emission lines in helium particularly.

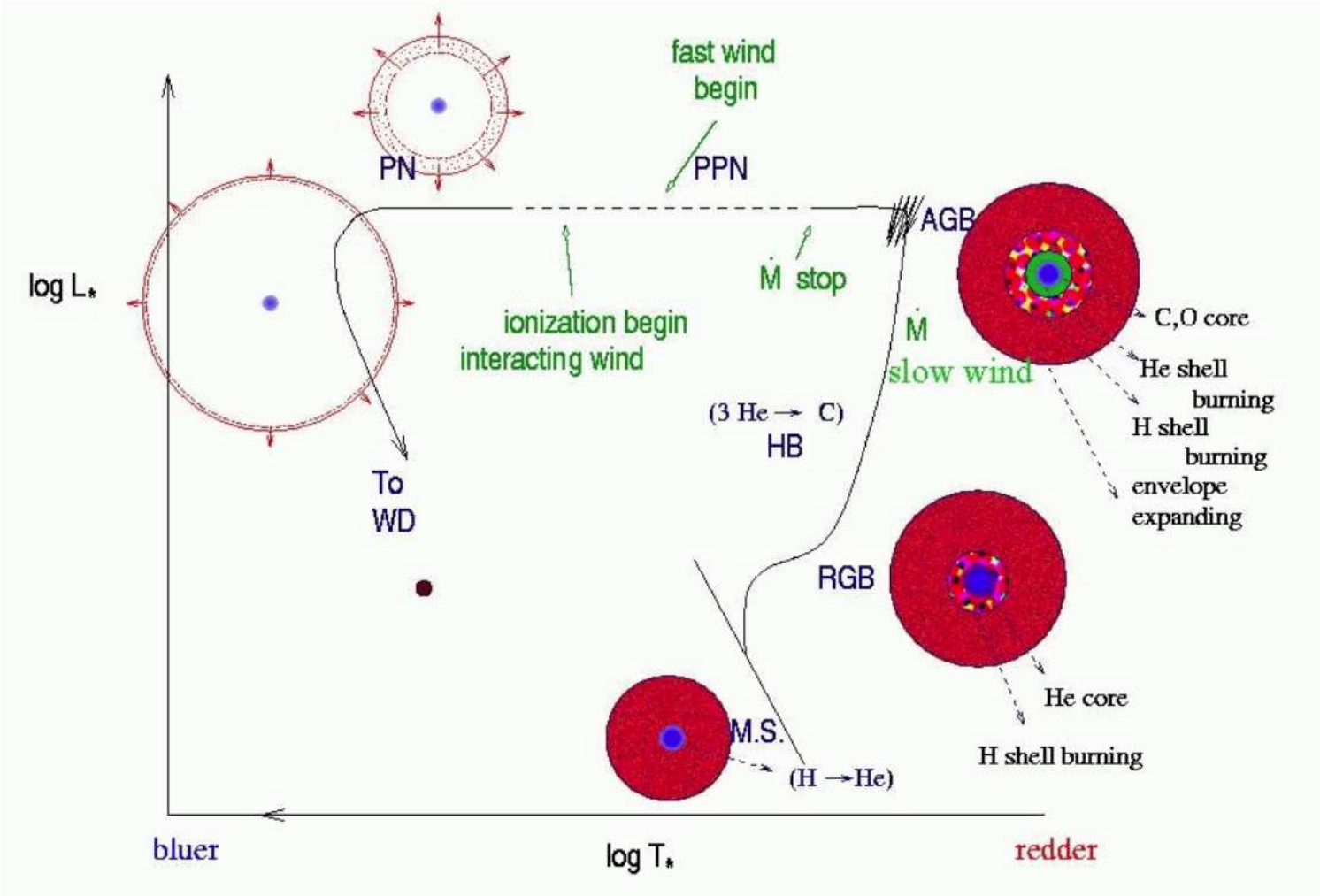

Fig. 1.1. Diagram of stellar evolution of a solar mass star from the main sequence to a white dwarf, courtesy of R.K. Prinja (via private communication).

1.2 The Introduction of Stellar Winds

A stellar wind is the term which was first ascribed by Eugene Parker in 1960 to the outflow of material from the surface of a star, for as well as radiation, a star emits particles. It is the both the rate at which the material flows out, and the structural form of this material which is of tremendous importance in the way in which the star evolves through the latter stages of its life; and indeed, its ultimate end is determined by the rate at which this 'wind-blown' material is lost.

In 1600, the astronomer Blaeu discovered a 'new star', or 'nova'; but unlike those stars so named today, which catastrophically end their lives in supernovae explosions, Blaeu's 'nova' is merely a star with a very strong but steady stellar wind. This star became known as *P Cygni*, and in the nineteenth century optical prism-based observations of other stars also showed stellar line profiles similar to those noted within the spectra of P Cygni: these profiles possess a blue-shifted absorption component and a red-shifted emission component, and such line profiles have proven to be key diagnostic tools when investigating the physical properties of stellar winds.

1.2.1 The Observation of Stellar Winds

It is the emission of particles from a star that is given the semi-misnomic appellation of a stellar wind. This emanation of material from the surface of the star can be described using the parameters of *mass-loss rate* – the amount of mass lost by a star per unit time – and the wind's *terminal velocity* – the speed the wind approaches at a relatively infinite distance from the star.

Mass-loss is conventionally described in units of solar masses (lost) per year i.e $M_{\odot}\,\mathrm{yr}^{-1} = 6.303 \times 10^{22}\ \mathrm{kg\ s}^{-1}$ with typical values in the order of $\dot{M} = 10^{-6} M_{\odot}\,\mathrm{yr}^{-1}$ or the equivalent loss of mass equal to the mass of the Earth every three years; a star's terminal velocity can range from a little as 10 $\mathrm{km\,s}^{-1}$ for a cool supergiant to around 3000 $\mathrm{km\,s}^{-1}$ for a luminous hot star.

In it simplest model form, a star with a stationary spherically symmetric wind experiences a mass-loss rate which is related to its density and velocity at any radial point in the wind via the *equation of mass continuity*:

$$\dot{M} = 4\pi r^2 \rho(r) v(r) \tag{1.1}$$

where r is the (radial) distance from the star's centre, ρ is its density, and v its velocity. The equation states that the same amount of gas flows per second through a sphere of radius r from the centre of the star – and therefore no material is created or destroyed in the wind.

Gas escaping for the photospheric surface of the star is accelerated outward – initially by radiation pressure – from a small radial velocity $v \leq 1\mathrm{km\,s^{-1}}$ at the photosphere to a much higher velocity at a great distance from the star – it eventually asymptotically approaches a terminal velocity $v_\infty = v(r \to \infty)$.

The wind's velocity distribution at a distance r from the star is given by a velocity law *v(r)* which is itself governed by a *β-law* which shows the rate of variation of the distribution:

$$v(r) \simeq v_0 + (v_\infty - v_0)\left(1 - \frac{R_\star}{r}\right)^\beta \tag{1.2}$$

This shows the increase of v with distance r from the star, from v_0 at the surface to v_∞ at great distance, with $v_0 > v_\infty$. The β-factor describes the steepness of the increasing velocity curve.

By introducing relative variables, $w = v/v_\infty$ and $x = r/R_\star$, the above velocity law becomes parametrised thus:

$$w \simeq w_0 + (1 - w_0)\left(1 - \frac{1}{x}\right)^\beta \tag{1.3}$$

It is this standard form which will be used within the Sobolev with Exact Integration (SEI) stellar wind modelling process in later chapters.

1.3 The Formation of Spectral Lines

Spectral lines found within stellar winds are easily distinguishable from photospheric lines due to their larger width and wavelength shift; they can be formed via photon absorption, emission, or a combination of the two processes: a P Cygni profile.

1.3.1 Line scattering

A photon emitted by the photosphere can be absorbed by an by an atom and an electron excited to a higher energy level. After a short time the electron can subsequently return through de-excitation to its original level, re-emitting a photon with almost a similar energy to that of the initial, the only difference in energy due to the Doppler shift owing to the thermal motions of the atom. As the photon is only altered upon emission in terms of its direction of travel this process is referred to as *line scattering*. If the electron is excited from its ground state then the line transition is referred to as a *resonance transition* and the scattering is specifically called *resonance scattering* – this is the process that results in the formation of a P-Cygni line profile.

1.3.2 Line emission by recombination

An ion within the stellar wind can encounter an electron and recombine with it, with the most likely recombination being back down to the ground state of the atom. It is also possible however for the atom and electron to recombine to a higher, excited state. The electron may then drop down from higher to lower energy states emitting line photons into the stellar wind at each stage of its *cascade* through photo-de-excitation. Lines formed through specific transitions that have a high probability of being produced via photo-de-excitation will then be seen in emission, such as the Hα and infra-red lines in hot star winds.

1.3.3 Line emission for collisional- or photo-excitation

Atomic excitations from the ground state to an excited state can also occur via collisions where kinetic energy is converted, via the initial excitation and subsequent photo-de-excitation to a lower level, into photon energy.

1.3.4 Pure absorption

Photo-excitation of an electron from a lower energy level to a higher one can be followed by spontaneous de-excitation to another lower level, whereby the initial transition photon is destroyed and new photons created by the second transition. However this is not a major occurrence in stellar winds as the majority of atoms in the stellar wind are in their ground state.

1.3.5 Masering by stimulated emission

If a photon travelling through a stellar wind can hit an excited atom or molecule that can emit a similar photon through photon-de-excitation then the process of stimulated emission becomes an important factor. The atom (electron) de-excites to a lower level by emitting a photon with the same frequency and in exactly the same direction as the original photon. So now there will be two similar photons travelling in the same direction, and if this process is repeated the result will be large numbers of line photons travelling in the same direction a process called *masering*. In order to be a significant source of photon emission a large number of atoms/molecules have to be in an excited 'upper level of transition' and there should not be a velocity gradient present in the direction of the travelling photons - if there was, then the Doppler shift will curtail this process.

This process is responsible for the very strong and very narrow maser emission lines of abundant molecules in the winds of cool stars.

1.4 P Cygni Profiles

Spectral lines caused by atomic transitions/excitation of electrons from the ground state to higher states – called resonance lines – offer the most sensitive indicators of mass-loss. In the ultraviolet (UV) the most common are the resonance lines of C IV , N V , and Si IV .

There is a large abundance of these ions, and with the the large oscillator strength of their atomic resonance transitions they can show an observable line absorption that exhibits Doppler shift due to the outflow – even if the rate of mass-loss is small.

For a column density of between 10^{13} to 10^{14} ions cm^{-2}, the resonance lines produce a small but significant (i.e. weak but observable) absorption component which is subsequently Doppler shifted to a shorter wavelength because it is formed in a region that is moving outward from the star i.e. towards the observer.

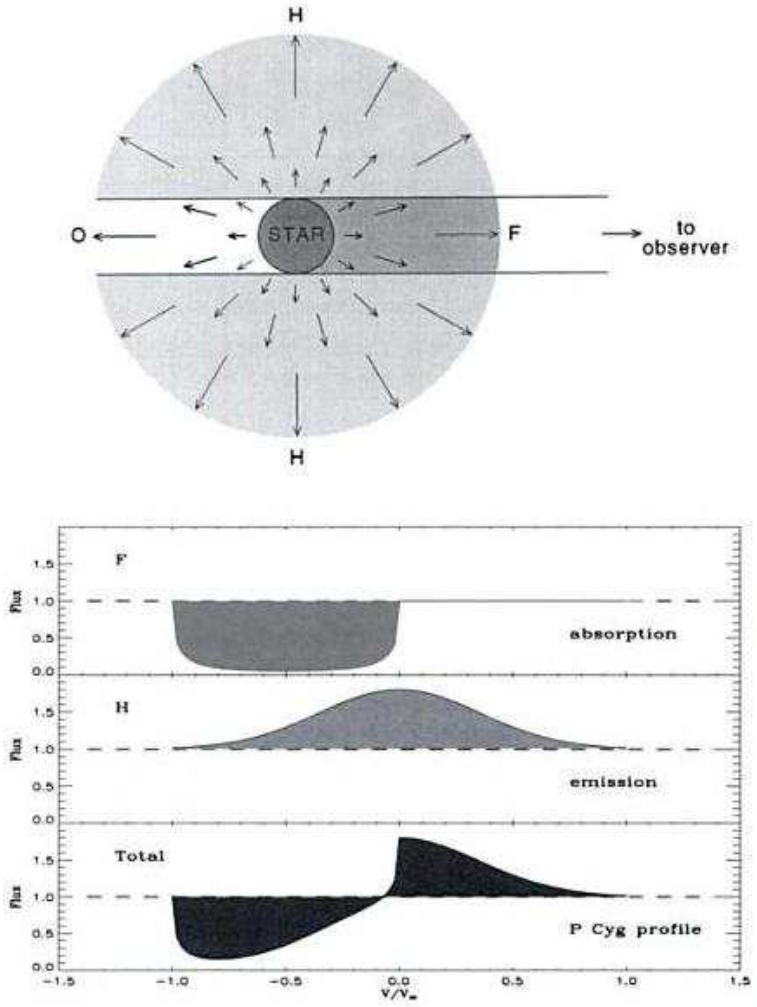

Fig. 1.2. Diagram of components of a UV P Cygni resonance line profile: Lamers & Cassinelli (1999)

But if the column density is in the region of 10^{15} ions cm^{-2} then a P Cygni profile is formed, with a blue-shifted absorption component and a red-shifted emission component.

1.4.1 The Formation of P Cygni Profiles

The manner in which a P Cygni profile is formed is best explained using a model of a spherically symmetric star with a similarly-spherical outflowing wind in which the velocity increases as the wind travels outwards.

Four regions contribute to the observed profile:

• S: the star emitting a continuum - with a photospheric absorption component at the rest wavelength, λ_0, of the line.

• F: the 'tube', the region of outflow in front of the stellar disk. The gas in F is moving towards the observer with velocities ranging between v_0 and v_∞.

• O: the 'tube', the region of outflow occulted by the stellar disk. Gas is moving away from the observer; radiation from this region does not reach the observer.

• H: the regions to the sides of the star that would be observed as a halo – if the wind could be resolved spatially by the observer. The gas in the region has both positive and negative velocity components along the line of sight of the observer.

Figure 1.2 shows how the spectral contributions from all the different regions go toward producing a P Cygni profile.

1.5 Mass-Loss Studies from P Cygni Profiles

Spectroscopic studies have been carried out using P Cygni resonance line profiles, particularly UV resonance lines found within the spectra of early-type stars, whence information about the mass-loss involved and wind profile information has been obtained (Lamers & Cassinelli 1999). The profiles of strongly saturated resonance lines are strongly sensitive to the velocity law, and subsequently an accurate estimation of the wind terminal velocity can be obtained from the position of the very steep blueward edge of the absorption line which reaches the continuum at a Doppler velocity of $v_{edge} \simeq -(v_\infty + 2v_{\rm turb})$, where $v_{\rm turb}$ is the turbulent velocity in the wind at a distance of $r \gtrsim 10R_\star$ where the wind reaches its terminal velocity, v_∞. Whereas the terminal velocity can be directly measured from a saturated resonance line, *unsaturated* lines are used to derive the mass-loss rate.

Observed profiles are compared to predicted profiles of different radial positions $n_i(r)$ of the observed ions in the wind, and when the observed and predicted profiles match, then the distribution of $n_i(r)$ is known. Using the ion density $n_i(r)$ can be converted into a density distribution $\rho(r)$ using the abundance and the ionisation fraction of the observed ion is known in the wind:

$$n_i = \frac{n_i(r)}{n_E(r)}\frac{n_E(r)}{n_H(r)}\frac{n_E(r)}{\rho(r)}\rho(r) = q_i(r)A_E\frac{n_H}{\rho}\frac{\dot{M}}{4\pi r^2 v(r)} \tag{1.4}$$

where $A_E = n_E/n_H$ is the abundance of element E with respect to H and $q_i = n_i/n_E$ is the fraction of ions in the right stage of ionisation and excitation to produce the line. The ratio n_h/ρ depends on the composition of the wind and is $(1.36m_H)^{-1} = 4.43 \times 10^{23}$

atoms g^{-1} for solar composition. The mass continuity equation here gives ρ in terms of $\dot{M}$, so that if *v(r)* and $\rho(r)$ are known then the mass-loss rate and the wind's terminal velocity – as well as the wind's velocity law in – can be derived from P-Cygni resonance profiles.

1.6 Spectroscopic Investigations into Central Stars of Planetary Nebulae

Studies of stellar winds & mass-loss have been extended from OB stars to hydrogen-rich O-type CSPNs and observational data has been analysed with a view to compare the mechanisms and subsequently derived parameters from both, and to see if the two types of stars have a common relation between their luminosity and their mass-loss through their stellar winds.

UV spectra of CSPNs show P Cygni profiles in ions C IV , N V , and Si IV , and sometimes lines from excited levels of N IV , O IV , and O V . The high effective temperatures of these stars is between 30,000 K and 120,000 K and their luminosities range between $3.5 < \log L_\star/L_\odot < 4.3$. This implies a radii of about 0.3 to 3 $R_\odot$ – from $L_\star/L_\odot = 4\pi(R_\star/R_\odot)^2\sigma(T_\star/T_\odot)^4$. Masses are small and of the order 0.5 to 0.6 $M_\odot$ because they are the progenitors of white dwarfs. The combination of low mass, small radii and high luminosities implies that the effective escape velocity at the stellar surface is between 200 and 800 $\mathrm{km\,s^{-1}}$.

Mass-loss rates for CSPNs have been derived from the P Cygni profiles of UV lines, and from optical emission lines (see Méndez et al. 1992; Perinotto 1993; Kudritzki et al. 1997). Mass-loss rates are small and of the order of 10^{-9} to 10^{-7} $M_\odot\,\mathrm{yr^{-1}}$, however these low mass-loss rates provide strong P Cygni profiles because the stars' radii are so small. The optical depth of the P Cygni profiles scale roughly with the column density in the wind and inversely with the terminal velocity, so $\tau \sim \dot{M}/(R_\star v_\infty^2)$. A typical CSPN with $\dot{M} = 10^{-8} M_\odot\,\mathrm{yr^{-1}}$, $v_\infty = 3000\ \mathrm{km\,s^{-1}}$ and $R_\star = R_\odot$, will have approximately the same optical depth of the P Cygni profiles as a typical O supergiant of $R_\star = 50\ R_\odot$ with $v_\infty = 2000\ \mathrm{km\,s^{-1}}$ and $\dot{M} = 2 \times 10^{-5} M_\odot\,\mathrm{yr^{-1}}$.

Much of the diagnostic work carried out upon stellar wind spectra has centred upon the creation of plane-parallel nLTE model atmospheres and their comparison with the observational equivalent, which has led to the determination of parameters such as effective

temperature, surface gravity, and chemical/helium abundance. The establishment of such parameters, and the consequential attribution of a key position upon the $\log T_{\rm eff}$ – $\log g$ plane and the spectroscopic determination of temperature and gravity, has subsequently aided in the estimation of stellar luminosities, masses, radii and distances when compared with post-AGB predictions and the core mass - luminosity relationship.

According to stellar theory, stars close to the Eddington limit in the $\log g$ – $\log T_{\rm eff}$ diagram should show signs of an active radiatively-driven wind, and successful theory should be able to quantitatively reproduce wind conditions to those observed in CSPNs – in a similar fashion to the hitherto successful reproduction of winds observed from O, B, and A stars (Kudritzki et al. 1997); also the radiatively-driven wind theory predicts – assuming solar abundances – that a relationship exists between the mass-loss - terminal velocity product, $\dot{M}v_{\infty}$, having dimensions of momentum-loss rate, and the stellar luminosity:

$$\dot{M}v_{\infty} \sim R_{\star}^{-0.5} L_{\star}^{(1/\alpha)} \tag{1.5}$$

where α is the power law exponent of the line strength distribution function and has a value $\simeq 2/3$ (Kudritzki et al. 1995; Puls et al. 1996). Hence the stellar momentum-loss rate and luminosity are proportionally-related thus:

$$\dot{M}v_{\infty}R_{\star}^{0.5} \sim L_{\star}^{(1/\alpha)} \tag{1.6}$$

A plot of $\log \dot{M}v_{\infty}{R_{\star}}^{0.5}$ against $\log L_{\star}$ shows – in the first approximation – a linear relationship which is followed by massive hot stars of solar abundances, see Figure 1.3.

It was found that the CSPNs studied and analysed with the fitting of the H_{α} lines fitted the straight line plot, although there was a split between the two groups – with the implication that some of the CSPNs possessed a strong stellar wind, whereas others were weaker – as shown in Figure 1.3. A similar diversity of wind strengths had been found in massive hot stars but this was attributed to a difference in relative metallicities between the two sub-groups: the hot stars of the SMC had a lower average metallicity and a weaker wind than those found in the LMC or the galaxy. However, at the time little was known about the metallicities of CSPNs and so no metallicity-dependent comparisons could be drawn, but there existed a motivation to investigate the UV spectral lines e.g

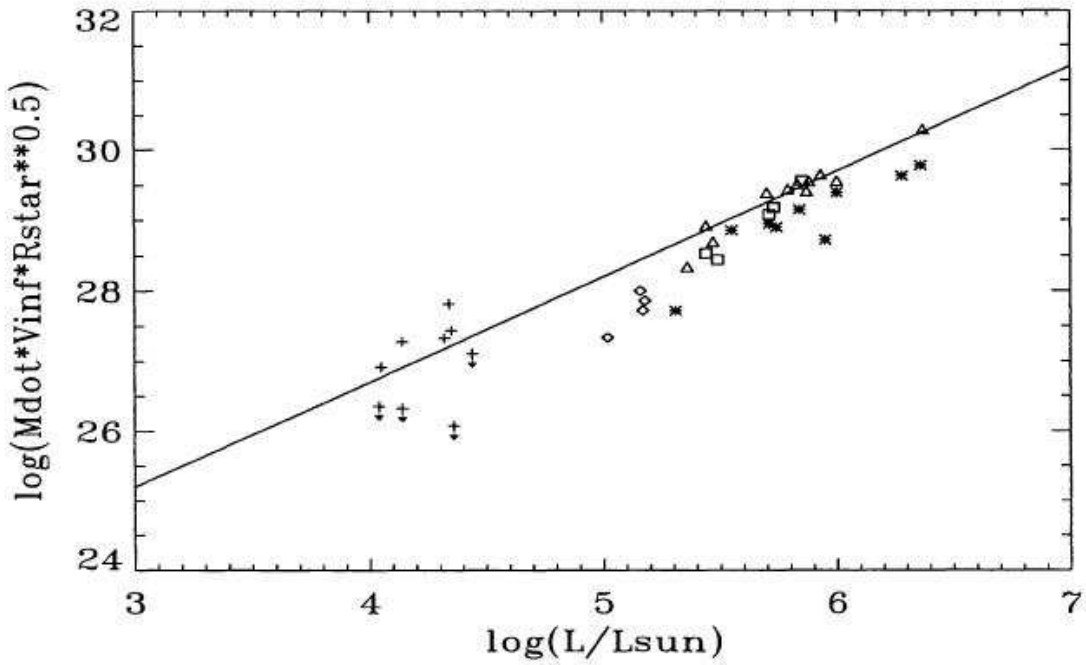

Fig. 1.3. The log of the quantity $\dot{M}v_{\infty}{R_{\star}}^{0.5}$ as a function of the log of stellar luminosity for a selection of hot stars: open triangles, squares, and diamonds indicate O, B and A supergiants; asterisks indicate lower luminosity class O stars (giants to main sequence stars). Plus signs are for CSPNs. The straight line is the indicator of the relation following the 3/2 power of stellar luminosity: Kudritzki et al. (1997).

the abundant Ni and Fe lines. Another consideration as a possible cause of the diversity was the luminosity class of the progenitor of the CSPN, as the lower-classed hot stars.

The modelling methods used also predicted high masses and luminosities which were not expected: some are comparable to some of the masses derived in earlier hydrostatic models by Méndez et al. (1988), where it was expected that they would be closer to masses as predicted by the later models of Méndez et al. (1992); the highest luminosities of Kudritzki et al. (1997) contradict the theoretical post-AGB evolution where such high mass objects should possess far lower luminosities akin to the tracks marked out by cooling white dwarfs.

Unfortunately high luminosities were needed in order to position the CSPNs into such an agreeable place upon the momentum loss rate – luminosity diagram, and reducing the luminosities, as well as the mass-loss rates and radii, the CSPN winds would be strong enough to move the objects above the line-fit – the winds' strengths seemingly proven

higher than the radiatively-driven wind theory could account for. Perhaps there was some as yet unaccounted for aspect within the wind which would allow for this?

Early plane-parallel-based model fitting of H and He lines of CSPNs was only useful in predicting values for surface temperature, He abundance and $\log g$, and not useful in deriving stellar luminosities or masses, but only L/M ratios; and the lack of distance data of CSPNs could not solve this problem (Pauldrach et al. 2003). Therefore the positions of CSPNs were plotted upon the $\log g$ – $\log T_{\rm eff}$ diagram and compared with plots of post-AGB tracks derived from the $\log$ Ł – $\log T_{\rm eff}$ diagram. It was then possible to return to the former diagram and read off the CSPN stellar mass, from which the luminosity could be derived; and with a knowledge of the de-reddened stellar magnitude, one could calculate a so-called 'spectroscopic distance' – all assuming that the stellar evolution models provide an accurate relation between stellar mass and luminosity.

Hydrodynamic Modelling: A Different Approach

An alternative method (Pauldrach et al. 2003) is based upon a homogeneous, stationery, extended, outflowing, spherically symmetric atmosphere for which the hydrodynamic and the radiative transfer and rate equations for a nLTE have to be solved: the calculations for which are performed iteratively, as described briefly below (and in greater detail by Pauldrach et al. 2001).

An initial estimate for $T_{\rm eff}$ is assumed from a preliminary study of a given star's visual or UV spectrum; the latter will also provide a measure of the wind's terminal velocity, v_∞. An initial value for the stellar radius R, for the Rosseland optical depth, of 2/3 is submitted. From the theory of radiatively driven winds, where v_∞ scales with $\sqrt{M/R}$, the current values of R and v_∞ will lead to an estimate of the stellar mass. With (an assumed set of abundances and) these values of R, $T_{\rm eff}$, M, the model stellar atmosphere is solved, with the velocity field, the mass-loss rate. The synthetic spectrum which is subsequently produced is compared with an observed one and the accuracy of the resulting fit is considered. If the fit is less than satisfactory then the mass-loss rate, $\dot{M}$, is re-calculated with a new value for R (as the radiatively-driven wind theory states that $\log \dot{M} \sim \log L$). However, in order to keep a consistent value of v_∞ – one that will still match the observed/derived value – the stellar mass has also to be adjusted along with the change in radius. The modelling process is then repeated and the match of the model wind profile to the observed one is again considered; and so on, with each iteration moving the model

closer to the observed wind.

This iterative procedure was successful in modelling the wind of massive Population I stars such as the supergiant α Cam (HD 30614), and so the aim was to apply a similar procedure to UV spectra of CSPNs as a means by which to verify whether CSPNs followed the wind-momentum-luminosity relationship as forwarded by Kudritzki et al. (1997).

The problem lay in the apparent establishment of two sub-groups of CSPNs, lying above and below the $\dot{M} v_\infty {R_\star}^{0.5} - L_\star$ relationship line, with the two groups having either stronger or weaker winds for their given luminosities. Furthermore, some of the predicted stellar CSPN masses were high ($M > 0.8 M_\odot$), a contradiction of theoretical post-AGB evolutionary speeds.

Using the hydrostatic models, the terminal velocities and mass-loss rates for the similar selection of CSPNs were calculated following the current theoretical post-AGB tracks, and the resulting wind momenta plotted upon the wind-momenta-luminosity diagram. As with the earlier prediction, the CSPNs do follow the expected wind-momentum-luminosity relation, but these models (Pauldrach et al. 2003) form a smaller tighter group that those CSPNs produced by Kudritzki et al. (1997); also the resulting stellar masses have a lesser spread, between 0.6 and 0.95 $M_\odot$.

Conflicting Results from Terminal Velocities & Mass-Loss Rates

To try and understand the problem, the relations of v_∞ and $\dot{M}$ were studied separately.

An odd discrepancy is immediately apparent: the measures of v_∞ cluster about the evolutionary tracks for masses between 0.5 and 0.6 $M_\odot$, but on the other hand, the mass-loss rate measurements are so placed for stellar masses above 0.7 $M_\odot$. When considering individual CSPNs these discrepancies between implied stellar masses are even wider. For Hen 2-131, v_∞ predicts a mass of 0.6 $M_\odot$, but its $\dot{M}$ is not compatible with its v_∞, and instead indicates a mass of 0.94 $M_\odot$; for NGC 2392, v_∞ predicts a mass of 0.9 $M_\odot$, but its $\dot{M}$ is too small for this mass, and would rather indicate a mass of nearer 0.6 $M_\odot$.

In order to try to resolve these difficulties, Pauldrach et al. (2003) turned to the modelling of UV spectra. An initial UV spectrum modelled for Hen 2-131 for a stellar mass of 0.6 $M_\odot$ clearly demonstrates that this is too low a mass-loss rate as the spectrum contains almost only photospheric lines and shows little impact of a wind, which indicates that the luminosity is too low and needs to be much higher, as it is this which will affect the mass-loss rate. To correct this, a series of spectra, each calculated with a different

luminosity, were produced, each time also adjusting the mass so that the wind terminal velocity remained the same; and the best overall fit was a spectrum giving the required mass-loss rate as that previously predicted.

For NGC 2392, the problem appeared in reverse: the UV spectrum was dominated by many wind-contaminated lines which were not evident in the observed spectrum, which is mainly dominated by photospheric lines. Here, the luminosity is too high, leading to a mass-loss rate far higher than is the case. A lower luminosity and lower mass-loss rate produces a spectrum which shows a much better fit to the observed UV spectrum.

NGC 2392: $T_{\rm eff}$ is determined from the ionisation equilibrium of Fe ions in the stellar UV spectrum – not too different from that derived from the ionisation equilibrium of He I and He II absorption lines in the optical spectrum. The low terminal velocity from direct measurement and the luminosity, decreased from earlier assumption to provide a model that fits the observed spectrum, have both led to a smaller radius, $1.5 R_{\odot}$, and v_{∞} of 400 $\mathrm{km\,s^{-1}}$; these lead to a stellar mass of $0.41 M_{\odot}$, which is a much smaller value than that arrived at via the assumption of post-AGB mass-luminosity relation as used by Kudritzki et al. (1997), who thus calculated a stellar mass of $0.9 M_{\odot}$.

Hen 2-131: $T_{\rm eff}$ of 33 kK and the measured v_{∞} of 500 $\mathrm{km\,s^{-1}}$ and the higher luminosity than that suggested by the post-AGB mass-luminosity relation (with which Kudritzki et al. 1997 derived a stellar mass of 0.9 $M_{\odot}$) has, with a increased stellar radius in order to increase $\dot{M}$ to thereby achieve a satisfactory fit, resulted in a stellar mass of 1.39 $M_{\odot}$, which is extremely closer to the Chandrasekhar level above which a type Ia supernova can result.

These results – particularly the wide range of derived stellar masses, between 0.4 and 1.4 $M_{\odot}$ – evidently do not agree with predictions set by the post-AGB mass-luminosity relationship. However, when the UV spectra-based results are added to the wind-momentum-luminosity diagram for hot stars and CSPNs, they possess a tighter dispersion along the extrapolation of the wind-momentum-luminosity relation as defined for massive hot stars – see Figure 1.4. This has been due to fitting stellar parameters to UV spectra via modern hydrodynamically consistent models.

Pauldrach et al. (2004) used the theory of radiative driven winds in an alternative way by looking at the dependence of mass-loss rates and terminal velocities on stellar luminosities and stellar mass, and developed a method devised by Kudritzki & Puls (2000) to determine stellar masses and luminosities from observed/measured wind terminal ve-

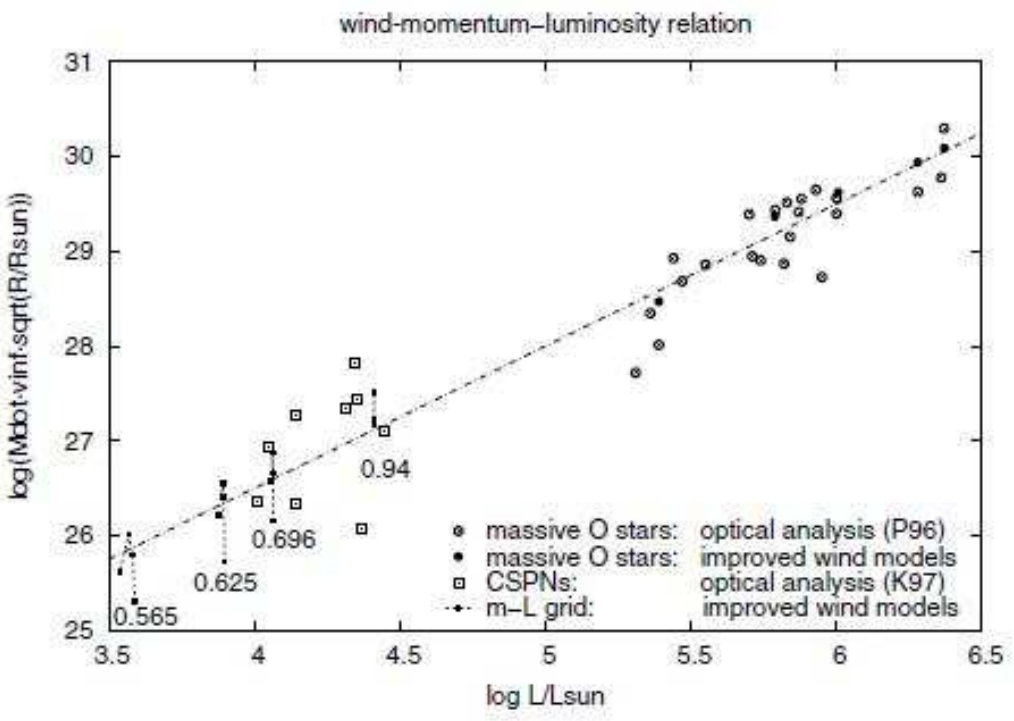

Fig. 1.4. The wind-momentum-luminosity relation for massive O stars and CSPNs. Data is derived from Hα analysis (Puls et al. 1996) – P96; similar for CSPNs (Kudritzki et al. 1997) – K97. Additionally plotted are the wind momenta for O stars and CSPNs based upon the hydrodynamic models following post-AGB evolutionary tracks: Pauldrach et al. (2003).

locities and UV mass-loss rates. Applying these techniques to the same select CSPNs as had been analysed by Kudritzki et al. (1997), they obtained very similar values for $T_{\rm eff}$, but very different values for mass and/or luminosity. Which of the two approaches: the post-AGB core mass-luminosity relationship used by Kudritzki et al. (1997), or the stellar wind-based hydrodynamics of Pauldrach et al. (2003), could be proven the more accurate method? If the latter study was the more physically-sound method to use, then that would have further repercussions for theory of post-AGB evolution. However, the hydrodynamic study was based upon a stationary, smooth homogeneous wind, which more recent study has cast as a false assumption.

1.6.1 Further Considerations of Wind-born Metal Lines & the Contribution of 'Clumping'.

The primary indication was that winds are radiatively-driven – it is difficult to explain the stronger wind-momentum-luminosity relation with any other dominant wind mechanism;

and despite the same model atmospheres working well enough for the massive hot stars, the spread in the CSPN masses was still a mystery that needed explaining.

The previous models, although based upon nLTE, did not take into account metal line opacities nor the presence/action of a stellar wind upon the circumstellar nebula, and so UV spectra of CSPNs, available from IUE, HST and FUSE, and containing many P Cygni absorption profiles, were now used to determine terminal velocities for the wind as well as the stellar mass-loss rate.

The appearance of thousand of photospheric metal lines offered a source for determining the metallicity of the CSPN, and provide a alternative source from which to determine $T_{\rm eff}$ and through the ionisation equilibrium, for example, of Fe IV /Fe V : e.g. Pauldrach et al. (2004) and Herald & Bianchi (2004), whose work on this confirmed the earlier optically-derived temperatures of Méndez et al. (1988) and Kudritzki et al. (1997).

The inclusion of the opacities of millions of metal lines in nLTE with optical spectra would have two effects: firstly, absorption by strong metal lines in the outer atmosphere causes a change in the spectra energy distribution in the UV; secondly, around 50% of the photons are scattered backwards into the inner atmosphere where they supply an additional energy input to heat the deeper photosphere. This second warming effect increases the photospheric emission of the continuum and so affects the ionisation equilibrium such as He I /He II which are used to determine $T_{\rm eff}$. Such ionisation equilibria are shifted towards lower $T_{\rm eff}$. Also, pressure broadened wind of Balmer lines – used as a diagnostic for log g – become weaker as the millions of metal lines increase the radiative acceleration $g_{\rm rad}$ and as such the effective gravity, $g_{\rm eff} = g - g_{\rm rad}$, is decreased, and so higher gravities are needed to fit the Balmer lines. This effect, in combination with the lowered $T_{\rm eff}$, leads to an overall shift in the $\log g$ – $\log T_{\rm eff}$ plane, which when compared with the post-AGB evolutionary tracks, leads to a reduction of CSPN masses, radii, luminosities, and distances.

The effects of nLTE metal line-blanketing were considered by Kudritzki et al. (2006), while reassessing the former optical study of CSPNs (Kudritzki et al. 1997), with the aim of making a new comparison with the UV study carried out by Pauldrach et al. (2004).

For this, a more up-to-date nLTE wind-analysis code, FASTWIND (Puls et al. 2005), was used, modelling the wind by including the effects of nLTE metal line opacities, stellar winds and stellar extension; but ostensibly using a similar method to that used back in 1997: $T_{\rm eff}$ and He abundance are obtained form a fit to the He I and He II lines' ionisation

equilibrium; gravity ($\log g$) is obtained from a fit of the Balmer lines, and as Hα is the strongest hydrogen line formed in the stellar wind then this is used to gauge the stellar mass-loss rate. As usual, P Cygni lines are used as a measure for the wind's terminal velocity, v_∞.

Hα , used as a diagnostic tool for mass-loss rates can be affected by stellar wind clumping.

It had been well documented that line driven winds are unstable (see Owocki et al. 1988), which might lead to inhomogeneity within the wind, commonly known as *clumping* (as described by Runacres & Owocki (2002)), where there are regions within the wind, the *clumps*, which possess a higher density, ρ_{cl}, and also appositely, regions which are much less dense. The clumping density is related to the mean density of the wind by a simply *clumping factor*, f_{cl}, such that $\rho_{cl} = \rho_{av} f_{cl}$ – there is a similar relationship with the clumping factor and the occupation numbers n_i of ions.

Line opacities κ depend upon density as $\kappa \propto n_i \propto \rho^x$. For optically thin clumps the average optical line depth is given $\tau_{av} \propto n_i^{av} \propto n_i^{cl} f^{-1} \propto \rho_{av}^x f^{x-1}$. For a dominant ionisation stage $x = 1$, and so the clumping along the line of sight cancels ($f^0 = 1$) and does not affect the diagnostics.

There are challenges in deriving the clumping diagnostics for CSPNs, as the density dependence exponent x will be different for different ions. WR-type CSPNs have very dense winds and strong wind emission lines and incoherent line scattering produces wide emission wings, the strength of which goes with $x \sim 1$. O-type CSPNs have much less dense winds and so this technique is unworkable. The UV P Cygni profiles of dominant ions tend to be saturated and so the ionisation equilibria become uncertain. However recent work with massive O-stars using FUSE spectra have used the P V resonance lines 1118 and 1128 Å, as having a low cosmic abundance: these lines are *un*-saturated even when in the dominant ion stage, and significant clumping has been found (Hillier et al. 2003; Bouret et al. 2005; Fullerton et al. 2006*b*).

1.6.2 FUSE & the Contribution of UV Resonance Line Modelling

In attempting to gain an understanding of the mass-loss rate of a given star, there are certain key diagnostics to look for: 1. free-free continuum emission in the radio wavelength range, located in the rarefied outer edge of the stellar atmosphere; 2. Hα line emission, detected in the dense and rapidly accelerating region close to the star; and then 3. UV

resonance-line absorption, found between the two other extremes. The physical mechanics behind these diagnostics also differ in their dependency on local conditions: emission $\propto \rho^2$; absorption $\propto \rho$.

The main problem in attempting to gain reliable information about mass-loss rates from resonance line profiles is that their strength depends upon the radial optical depth detected at a particular point, i.e:

$$\tau_{\rm rad} \propto \dot{M} q_{\rm i} A_E \tag{1.7}$$

where A_E is the abundance of element E and $q_{\rm i}$ is the ionisation fraction of stage i.

Consequently, this implies that for a dominant ion ($q_{\rm i} \sim 1$) the mass-loss rate can be measured directly. However many dominant UV resonance lines are saturated, particularly those abundant elements, e.g. C, N, O, and so cannot provide reliable values. This usually leaves elements with only trace ionisation species, where $q_{\rm i} \lesssim 10^{-3}$, used to calculate $\dot{M} q_i$ and with little information regarding estimates of $q_{\rm i}$, there can be little reliability in prediction of $\dot{M}$ from such sources. As a result, mass-loss rate estimates have been taken from measures of free-free radio emission, $\dot{M}$(radio), and Hα , $\dot{M}$(Hα) (see Lamers & Cassinelli 1999; Puls et al. 1996). However, these sources are not without their problems: radio emission sources are regarded as the most reliable, it is relatively weak, and due to the ρ^2 dependence of the mass-loss rate, the star in question has to be fairly close by. Alternatively, Hα emission (also ρ^2 dependent) can be viewed in distant objects, but its use depends upon a knowledge of, and the ability to model, the wind-photosphere interface, which is more difficult.

In recent years, access to data obtained via the *Far Ultraviolet Spectroscopic Explorer* satellite (*FUSE*) has offered a range of resonance lines in the far-ultraviolet (FUV) – and as a result, analysis of UV resonance lines has been reviewed and compared with the more 'traditional' Hα $\dot{M}(\rho^2)$ measurements of mass-loss. This reassessment of UV resonance line-based mass-loss estimations is based upon work carried out upon the P V $\lambda\lambda$ 1118, 1128 doublet: important because the lines, despite the high ionic abundance, are *unsaturated* as the cosmic abundance of P is low. Also, unlike C, N, and O, P is not a product of hydrogen-burning and so its abundance is little changed over the lifetime of a star, so differences in abundance from star to star matter little to the general range of mass-loss

calculations.

A P V -based O star mass-loss survey, conducted by Fullerton et al. (2006*a*), established a strong set of UV resonance line-based density-dependent mass-loss calculations for comparison with results from both former radio-based and Hα -based ρ^2-dependent mass-loss measurements. The survey is biased toward more luminous O stars as all three mass-loss diagnostics, the two ρ^2-dependent and the P V lines, are detected in the denser outflows of this type of object.

The ratios of $\dot{M}$(Hα) to $\dot{M}$(P V) and $\dot{M}$(radio) to $\dot{M}$(P V) were calculated for each of the stars studied were all much greater than unity, and these deviations can also be categorised in terms of the spectra classes of the stars:

1. mid O-type stars (O4 - O7.5) with strong wind features (those with log $\dot{M}$q(P V) $\geq$ -8) show the smallest deviations from the values of $\dot{M}$(Hα) or $\dot{M}$(radio).

2. earlier (O2 - O3.5) and latest (O8 - O9.7) O-type stars show larger deviations from the 1:1 correlation line.

3. The largest deviations belong to a group of five mid O dwarfs and giants that have $\dot{M}$(Hα) measurements and only upper limits for $\dot{M}$q(P V).

If $q(\mathrm{P}^{4+})$ approaches unity for a range of O stars then $\dot{M}(\mathrm{P}^{4+})$ should agree with both $\dot{M}$(radio) and $\dot{M}$(Hα) for a similar range of stars.

There was found to be an overall trend that the resulting measured values for $\dot{M}q(\mathrm{P}^{4+})$ were significantly smaller than $\dot{M}(\rho^2)$ and the deviations do not depend upon whether the $\dot{M}(\rho^2)$ values are either $\dot{M}$(radio) or $\dot{M}$(Hα) . It was noted however that stars of classes O4 - O7.5 deviated the least and those of classes O2 - O3.5 and O8 - O9.7 deviated the most.

$$\dot{M}q(P^{+4};w) = \frac{m_e c}{\pi e^2}\frac{4\pi\mu m_H}{f_{ij}\lambda_0 A_P} R_\star v_\infty^2 x^2 w \frac{dw}{dx}\tau_{rad}(w), \tag{1.8}$$

The $\dot{M}q(\mathrm{P}^{4+})$ equation (1.8) shows that $\dot{M}q(\mathrm{P}^{4+})$ could be underestimated if either the oscillator strength, f_{ij}, or the abundance of P, A_P, is overestimated. As P^{4+} is lithium-like, according to Morton (2003), there is no reason to suppose there is any significant uncertainty with the oscillator strength.

The abundance of P is a little more uncertain: Pauldrach et al. (1994, 2001) have adopted sub-solar values to achieve good wind profile fits for select stars, but otherwise

there is little evidence to assume sub-solar P abundances systematically; other studies – e.g Lebouteiller et al. (2005) – have also argued that P abundance is solar.

The most likely reason for $\dot{M}q(\mathrm{P}^{4+})$ being generally underestimated is that its q value never reaches a dominant level of ~ 1, however this is not predicted by standard wind models, but a suggestion of Pauldrach et al. (1994) is that as the ionisation of He II (54.416 eV; 228 Å) seemingly coincides with that of P V (65.023 eV; 191 Å), then it is suspected that the behaviour of $q(\mathrm{P}^{4+})$ might be influenced by that of He II .

Maybe the production of soft X-rays, which are themselves beyond the standard wind model, may also have an effect upon the ionisation balance of the wind, but ions with ionisation states above (e.g. S^{5+}) and below (e.g P^{3+}) P^{4+} shows no signs of overpopulation.

Therefore, in terms of the standard wind model, there is no definitive reason why measurements of $\dot{M}q(\mathrm{P}^{4+})$ should be underestimated by a factor ≤ 10.

1.6.3 Introducing the Concepts of 'Clumping'

The lack of definite cause for the discrepancies between mass-loss calculations between differing methods of measurement begs one to question the assumptions inherent within the standard wind model, particularly the assumption of the apparent smoothness of the density distribution (Fullerton et al. 2006*b*). Selected idiosyncrasies noted in the modelling of winds include: striking variability in UV and Hα profiles (e.g. see Prinja & Howarth 1986; Kaper et al. 1996; de Jong et al. 2001; Markova et al. 2005); variable blue wings in saturated absorption profiles of UV resonance lines (Puls et al. 1993); variable underlying structures seen in emission-lines (Eversberg et al. 1998); and X-rays detected in stellar winds (Cassinelli et al. 2001) – all factors indicating an apparent instability inherent in stellar winds, possibly resulting in a redistribution of material into a far more *in*-homogeneous wind, subsequently peppered by denser 'clumps'.

With Hα and radio emission mass-loss calculations dependent upon ρ^2 diagnostics as they are produced from the interaction of two particles, the effect of clumping should significantly affect such mass-loss measurements; and with subsequently interpretation after a standard model smooth wind, the ρ^2 diagnostic will consequently *over-estimate* the true mass flux, as the denser inhomogeneity of the medium (in producing a heightened level of emission) will be incorrectly supposed to have arisen from a smooth and homogeneously denser medium.

Clumping is described in a two component model: dense clumps of density ρ_H sep-

arated by rarefied inter-clump gas, density ρ_L – this depicts a redistribution of the gas material while preserving the overall mean density, ρ_s

$$\rho_s = f\rho_H + (1-f)\rho_L = \rho_H[f + (1-f)x] \tag{1.9}$$

where f is the volume filling factor of the denser component, $0 < f \leq 1$, x is the density contrast, $x = \rho_L/\rho_H$

With a lack of understanding of the precise mechanism which redistributes the material in the wind into clumps, the above formulae is often simplified by an assumption of the dense clumps being separated by a vacuum, so that $x = 0$ and $\rho_s = f\rho_H$

In considering the mis-interpretation of ρ^2 diagnostics, Abbott et al. (1981) have shown that the mass-loss, $\dot{M}(\rho^2)$ will be overestimated by a factor:

$$\left\{\frac{[f + x(1-f)]^2}{f + (1-f)x^2}\right\}^{1/2} \tag{1.10}$$

So that in the extreme case that $x = 0$, that is if the clumps were separated by a vacuum, $\dot{M}$ is overestimated in the smooth wind model by a factor of $1/\sqrt{f}$, leading to $\dot{M}(\rho^2)_{\,c} = \sqrt{f}\dot{M}(\rho^2)_{\,s}$ – "c" and "s" for clumped and smooth.

Alternatively, $\dot{M}q$ measurements, based upon UV resonance line profiles, are not similarly affected by clumping: being based upon the determination of the radial optical depth of the material associated by a specific ion along the line of sight, resulting in the formation of the observed P-Cygni absorption trough. Optical depth is an *integral* quality, and so $\dot{M}q$ measurements are not sensitive to the distribution of material along the line of sight (Fullerton et al. 2006*b*). Actually, if the clumps are optically thin on the spatial scales relevant to the line transfer, then they will not hide any 'inter-clump' material and measurements taken will be reasonably accurate; however, if clumps are optically thick, then their distribution will essentially create a porous structure in the wind which must be taken into account.

1.6.4 The Additional Effects of Porosity

Massa et al. (2003) have shown how the porosity in the wind can, in extreme cases,

produce unsaturated profiles which would otherwise be saturated if the wind were treated as smooth.

On larger spatial scales, inhomogeneities will be directly observable in the way they affect the expected shape of P-Cygni profiles – in the wind profiles of O-type star these have been assigned as discrete absorption components (DACs) – (see Prinja & Howarth 1986; Kaper et al. 1996) – readily modelled by SEI code.

An excellent SEI fit to the P V profiles of HD 190429A (O4 If+) provides a very well determined $\dot{M}q(\mathrm{P}^{4+})$ – Bouret et al. (2005) achieved a similar fit but only for a clumped model with a P V abundance reduced to $\mathrm{P}/\mathrm{P}_{\odot} = 0.5$, and with this P abundance, their $\dot{M}$, their mean $q(\mathrm{P}^{4+}) = 0.5$ over the velocity range 100 – 1000 km s^{-1}, the clumped CMFGEN model predicts $\log \dot{M}q(\mathrm{P}^{4+}) = -6.08$. In comparison SEI model results scales to their P abundance (half-solar) gives $\log \dot{M}q(\mathrm{P}^{4+}) = -6.06$ – this agreement confirms that both techniques determine the same optical depth in the line when clumping is incorporated in the models and all other factors are equal i.e. clumping does not bias the determination of $\dot{M}q$ from wind profile fits to UV resonance lines.

In recent years the *Chandra* X-ray satellite has detected the emission of X-rays emanating from the atmospheres of hot supergiant stars, in the form of resolved X-ray emission-line profiles with half-widths of ~ 1000 km s^{-1}, leading to the idea that these are produced within the expanding & accelerating stellar wind by the shock/interaction of instabilities embedded within the stellar outflow (Owocki & Cohen 2006). Also the apparent symmetry of the line which is in opposition to the more asymmetric shape as predicted by the standard wind theory, with 'traditionally'-derived mass-loss rates – i.e. taken from measurements of either Hα or free-free radio emission – where bound-free optical depths are expected to be of the order of 10 (Hillier et al. 1993), and subsequent attenuated redshifted emission. However, in trying to fit the observed symmetrical emission lines, the mass-loss rates have had to be reduced by at least a factor of 5: this may be yet another aspect of the now long held view that 'standard' mass-loss rate calculations, based upon the hitherto standard stellar *smooth* wind model (ρ^2) have led to an overall overestimation of mass-loss rates, if, as is now strongly suspected, the winds are actually clumped.

An alternative suggestion to clumping as a possible cause of the strange symmetry of the X-ray emission profiles is the potential effect of porosity of the wind, namely that if the wind material is compacted into clumps then redshifted X-ray emission might more readily be transmitted through the relatively low density of the apparent porous spaces

between the said clumps (Owocki & Cohen 2006).

An important concept when considering the level of porosity of the wind material is that it can depend on both the scale size of the individual clumps as well as the overall proportion or filling factor of the clumpiness – large porous gaps will arise from a combination of large clumps combined a relatively low number of such in a given volume.

Emission and absorption that arise from atomic states arise from recombination collisional excitation or free-free processes all depend upon the proximate interaction of two constituents e.g. ions and electrons, and thus scale with their individual particle (number) densities i.e. $n_e n_i$ which for a fixed ionisation and abundance is simply proportional to the square of the mass density, ρ^2; and so the effect upon spatial structure on such diagnostics is traditionally accounted for in terms of a simple density-squared clumping correction, C_c:

$$C_c \equiv < \rho^2 > / < \rho >^2 \tag{1.11}$$

In a model medium which is comprised of clumps of mass, m_c of scale l separated by a distance $L \gg l$, the mean density is $< \rho >= m_c/L^3$ and the individual clump has a density $\rho_c = m_c/l^3 =< \rho > /(L/l)^3$

The clumping correction is simply given by the inverse of the filling factor – the filling factor given as the ratio between the volume of the individual clump to the volume associated with the clump separation i.e. $f = l^3/L^3$ – this is different from the filling fraction, f', which is given as $f' \equiv l^3/(l^3 + L^3) = f/(1 + f)$, normalised to vary between 0 and 1.

$$C_c = 1/f' \tag{1.12}$$

For traditional mass-loss rate diagnostics – Balmer or radio emission, proportional to ρ^2 – the associated overestimate is inferred mass-loss rate scales as $\dot{M} \sim C_c^{1/2} \sim 1/\sqrt{f'}$

So the density-squared correction factor depends only on the filling factor and not on the scale of the individual clumps. As long as the emission can escape from the individual clumps – if they are optically thin – then the correction factor can be applied to a wide range of structure.

Attenuation of X-rays occurs through bound-free absorption, often from the ground

state; and as this is the dominant stage of the absorbing ions, there is no interaction with other particles, so the absorptions scales *linearly* with density.

The attenuation per unit length – the volume opacity – is given by $\chi = \kappa\rho$, where κ is the mass opacity – the mass absorption coefficient. This linear-density absorption is considered to be unaffected by clumping.

However, for individual clumps which are optically thick, the effective opacity can be written in terms of the ratio of the physical cross-section of the clumps to their mass:

$$\kappa_{eff} \equiv \frac{l^2}{m_c} = \frac{\kappa}{\tau_c}; \tau_c > 1 \tag{1.13}$$

showing that, relative to atomic opacity, κ, the effective opacity is reduced by a factor that scales with the inverse of the clump optical thickness, $\tau_c = \kappa\rho_c l = \kappa < \rho > l/f$

The clump optical thickness that determines the effective opacity depends upon the ratio of the clump scale to the volume filling factor – the ratio is called the porosity length, $h \equiv l/f$.

The difference therefore between porosity and the aforementioned density-squared clumping correction, which depends solely upon the filling factor, is that the porosity also depends upon the scale length of the individual clumps.

The effective absorption of clumps is generally set by the geometric cross section multiplied by a correction for the net absorption fraction, $\sigma_{eff} = l^2[1 - exp^{-\tau_c}]$ and applying this to the scaling equation above, provides a general porosity reduction in opacity in the form:

$$\frac{\kappa_{eff}}{\kappa} = \frac{1 - e_c^{-\tau_c}}{\tau_c} \tag{1.14}$$

In the optically thick clump limit, $\tau_c \gg 1$, this leads to a reduced opacity of $\kappa_{eff}/\kappa \simeq 1/\tau_c$; while in optically thin material, $\tau_c \ll 1$, it recovers the same opacity, $\kappa_{eff} \simeq \kappa$.

1.7 Investigations into Variability in Stellar Winds from OB Stars

Although knowledge existed of the variable nature of OB stars, a more detailed exploration of this potentially interesting aspect of hot massive stars was brought about with the advent of the *International Ultraviolet Explorer* (IUE) satellite. From the extensive UV data available it soon became clear that hot star wind variability was ubiquitous and therefore not so much a phenomenon isolated to perhaps a handful of such stars, but in fact an intrinsic property of all hot stars. Because of this ever-fluctuating facet of the stellar wind 'behaviour', single exposure UV spectroscopy can only provide perhaps a glimpse of merely an average moment; but how would it be possible to tell – knowing that the wind's physical characteristics are ever-changing – that what one observes within the UV spectra is a manifestation of a maximum or minimum flux, or some level in between. As soon as evidence of varying wind signatures came to light, then the logical step was to establish time-series studies, and from such multi-exposure spectra one could explore the variable UV P Cygni profiles via more mathematical analyses of their flip-book nature.

The most immediate implication of the variable nature of the outflow was that all measures of stellar mass-loss had to be revised as they were calculated based upon the erroneous assumption of the steady-state of a given star's continual loss of mass. In order to more accurately predict stellar evolutionary stages and the timescales therein, it is absolutely crucial to possess an accurate understanding of the mass-loss driving this evolution (Massa et al. 1995).

From time-series UV spectra now available from IUE, new aspects of observation could be exploited and subsequent theories derived. Through two-dimensional greyscale representations of temporally-stacked one-dimensional spectra, it became apparent that certain recurrent features could be observed (Prinja 1988; Prinja et al. 1992). The blueward migration of Discrete Absorption Components (DACs) – small but significant additional absorption features found within the absorption troughs of P Cygni profiles – was seen to be recurrent, and estimates of the modulation of this were found to be strongly correlated with the proposed rotation velocity, $v \sin i$, of the star.

The physical origins of these additional optical depth components started another branch of speculation: as the temporal greyscale images showed that the DACs are initially broad, then as they migrate through the absorption trough in which they appear, they

narrow while accelerating to higher velocities, it was speculated that the causes of these additional structures was some form of disturbance upon the stellar surface.

Whatever the initial cause of the DACs, the mechanisms by which they travel outward from the stellar surface and through the wind has been attributed to Co-rotating Interaction Regions (CIRs) (Owocki 1994; Cranmer & Owocki 1996). Perturbations in the radiative driving force at the stellar surface, causing alternating bright and dark spots of localised increases and decreases in the radiative driving force, are carried outward, co-rotating through the wind, as alternative regions of slow travelling, high density material, and regions of faster, lower density. When the faster material catches up with the slower material ahead, the two regions interact, and this is considered the direct cause of plateau-ing in the velocity gradient of the accelerating wind: a key component in the creation and subsequent appearance of the blueward-migrating DACs.

Therefore establishing the direct cause of the photospheric perturbations has proven to be yet another challenge. One suggestion has been that the disturbances are caused by structures in the magnetic field, but magnetic field measurements carried out by de Jong et al. (2001) only produced a null-detection. An alternative potential source of the surface disturbances are so-called Non-Radial Pulsations (NRPs), which have been developed as a source following on from variability studies of photospheric absorption and emission lines which have been shown to possess modulation periods: Reid & Howarth (1996) discovered a modulation period of 19.6 hrs in the absorption profile of the photospheric Hα line of the O supergiant ζ Puppis – a modulation akin to those discovered in the time-series UV resonance lines spectra of B Supergiant HD 64760.

1.8 From O Stars...to Central Stars: Research Objectives

The main focus of this thesis is to extend the time-series-based analysis, hitherto performed in the study of O and B star stellar winds, to those emanating from the Central Stars of Planetary Nebulae. The investigations into this are will be set out and described as follows:

In Chapter 2, descriptions are given of mathematical techniques behind time variance and optical depth modelling of absorption line profiles.

The initial investigation is detailed in Chapter 3: an in-depth study of the stellar outflow from the central star of the Cat's Eye Nebula, NGC 6543, undertaken using time-

series FUV data taken from the Far Ultraviolet Spectroscopic Explorer (FUSE) satellite. The variable nature of the wind is uncovered as expressed via the temporal behaviour of UV resonance absorption features, containing what appear to be Discrete Absorption Components (DACs) akin to those discovered in the stellar winds of OB stars. Key features are modelled also, providing further insights into their nature.

In Chapter 4, the search for wind variability is extended to other CSPNs, using (as far as possible) similar analysis techniques where, although the ability to do this is somewhat restricted because of the limited data available, further evidence of a structured nature to CSPN outflows is presented.

And then in Chapter 5, the investigation into temporal variability is carried to the very base of the wind where, using optical time-series data obtained via the ESO 3.6 m telescope and the High-Accuracy Radial Velocity Planet Searcher (HARPS) spectrograph, the potentially-variable behaviour of photospheric absorption lines is tested in order to provide clues to possible causes of the variability found further out in the stellar wind.

Finally in Chapter 6, the conclusions of the thesis are set out, and future investigations proposed.

Chapter 2

Mathematical techniques

In this chapter a brief description will be given of the mathematical techniques used to analyse time-series data in order to uncover the temporal behaviour and underlying physics of stellar winds.

2.1 Equivalent Width (EW) Measurements

As a primary demonstration of the extent of the variability of the spectral absorption lines, for each time-series exposure, the equivalent width (EW) of a given line will be measured: the mean EW can thus be derived and more importantly the maximum and minimum EW for each time-series can be noted and hence the maximum percentage variation from the mean can be calculated.

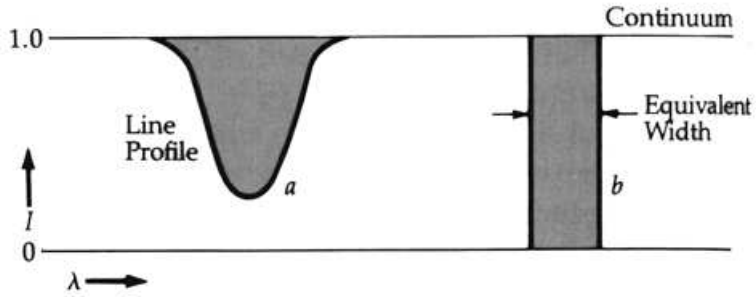

Fig. 2.1. Diagram comparing the strength of a typical spectra absorption line, *a*, with its 'equivalent width', *b*.

As a measure of the strength of an absorption line profile, the equivalent width of a given line is essentially a rectangular area between a normalised continuum and zero; the width (W) of the rectangle is such that the rectangular area is equivalent to the integral area of the line profile beneath the level of the continuum, as shown in Figure 2.1. Mathematically, the equivalent width, EW, is given by:

$$EW = \int_{\lambda_1}^{\lambda_2} \frac{F_c - F_\lambda}{F_c} d\lambda \tag{2.1}$$

where F_c is the intensity of the normalised continuum, F_λ is the intensity profile of the absorption line, and $d\lambda$ is the integral sampling in wavelength space; the strength of the profile is defined as the integral of the profile between λ_1 and λ_2, two points at the extreme ends of the wings of the broadened absorption line where they merge back into the continuum.

2.2 Spectral Time Variance Analysis

Each fits file-based spectra will be processed in four stages, each stage revealing a different aspect of any variability which might be occurring: each of the following processes is performed via an *Interactive Data Language* (IDL) package.

2.2.1 Temporal Variance Spectra (TVS)

As the aim of this project is to seek variability in the stellar outflows of central stars from the observation and analysis of central star spectra, an initial aim must be to qualitatively test these spectra for evidence of variability. This is achieved by passing a set of time-series spectra through a temporal variance programme. This measures the inherent flux variability of each bin in either wavelength or velocity space for each spectra in the selected series and produces a temporal variance spectrum for the given wavelength/velocity range for the series.

The IDL commands executed during this procedure are as follows:

• `load_fits_ts`: The time series to be analysed is loaded.

• `define_continuum`: With this command, coupled with the given name of the input dataset, a simple integer-based command structure appears whereby the normalised con-

tinuum of the time-averaged spectrum – appearing in a separate window – can be defined in space by short wavelength sections about the targeted line profile.

• `dug_tvs`: Using the continuum sections as defined in the previous step, the TVS algorithm then statistically analyses the continuum, including the behaviour of the noise levels therein, to assess the basic level of variation. From this initial analysis the TVS predicts a 95% confidence level (roughly 2 standard deviations from the mean variability of the continuum) which it uses as a guide by which any variabilty along the line profile which is greater than this indicates a significant level of activity in the line profile and which requires further investigation.

To calculate the TVS for a given spectra series the following equation is applied:

$$TVS_j = \frac{1}{N-1}\sum_{i=1}^{N} d_{ij}^2 \tag{2.2}$$

(Fullerton et al. 1996)

Here the jth wavelength pixel of the ith spectrum of N spectra in a given dataset. d_{ij} is called the residual spectrum and is defined by:

$$d_{ij} = S_{ij} - \bar{s_j} \tag{2.3}$$

where S_{ij} represents a specific matrix element and $\bar{s}_j$ is the column average given by:

$$s_j = \frac{1}{N}\sum_{i=1}^{N} S_{ij} \tag{2.4}$$

The TVS spectrum produced is a plot of the calculated TVS against either wavelength or velocity of the line profile. Any variability within the spectra is recorded and displayed upon the TVS spectrum: an example of TVS applied to the P v $\lambda\lambda$ 1117.98, 1128.01 doublet is shown in Figure 2.2.

In practice, the output images display the wavelength-dependent variations of $(TVS)^{\frac{1}{2}}$, instead of TVS: this is because the rooted TVS scales with the spectral deviations, giving a more accurate impression of the relative amplitudes of line profile variations from star to star (Fullerton et al. 1996).

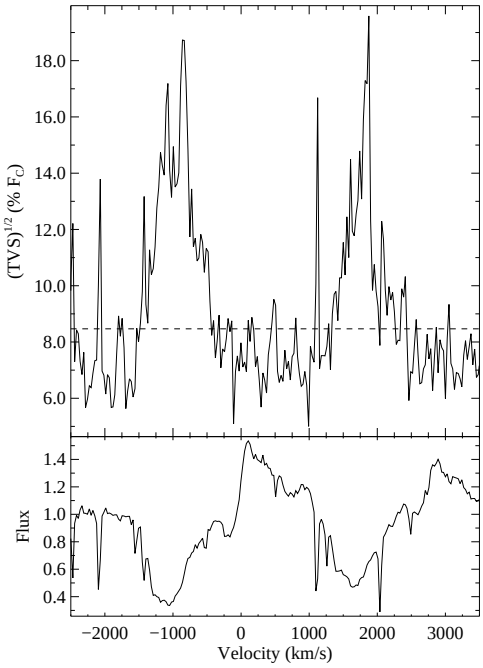

Fig. 2.2. Time Variance Spectra (TVS) of the most developed P Cygni absorption doublets from the F034 time-series spectra of PN NGC 6543: the well-developed but unsaturated P v $\lambda\lambda\,1117.98, 1128.01$ doublet is clearly strongly variable across both the blue and red absorption troughs of the doublet, showing broad peaks above the dotted 95% confidence line

2.2.2 Greyscale I

Using the information obtained in the TVS stage i.e. where along a given spectra noticeable variance is occurring and particularly at which spectral lines variability is most pronounced, one is able to produced a visually descriptive means by which one can display flux variability of spectral lines along the timescale given for a particular observing run.

The IDL commands are as follows:

• `load_fits_ts`: The time series is loaded as above.

• `greyscale`: The time series is fed into the greyscale algorithm and a GUI window is displayed in which are displayed various parameters of the input data, the values of which can be altered for preferential displays. For instance the first two boxes, `xlow` and `xhigh` contain the values of the wavelength extremities of the loaded time series; a third box, `Rest Wavl` – rest wavelength, is, by default, set to zero. With these default settings the spectrum displayed beneath the corresponding greyscale is simply labelled by wavelength; however, if a value is entered for the rest wavelength e.g. for the rest wavelength value

of a particular absorption or emission line, then the algorithm will convert the spectrum readout from wavelength space to velocity space, and hence the rest wavelength will be converted to the zero-value of velocity. In this case the values entered into the `xlow` and `xhigh` boxes must be in terms of velocity, and therefore represent the extent of *blueshift* (the `xlow` box) and *redshift* (the `xhigh` box) which is required for the spectrum displayed in the greyscale output – the velocity space Doppler shift can therefore set to as close to or as far from the zero shift velocity (taken from the given rest wavelength).

Another of the GUI input settings which yields a significant output is the option to `subtract`, or alternatively `divide` by, the mean flux levels from the varying intensity values produced by the algorithm and so the resultant greyscale is now a more accurate depiction of the variable nature of the time series flux with the extreme of black and white representing levels of $\pm$ 2 standard deviations in from the mean flux, therefore any excessive flux from the average is represented by the lighter grey to white end of the scale; any flux reduced below the average is thus represented by the darker grey to black end.

• `greyscaleplot`: The greyscale calculated by the algorithm is displayed with a mean spectrum of the time series across the bottom as a reference to the greyscale plotted directly above. Using this plot it is possible to see whether any evidence for variability exists.

The greyscale of these dynamic spectra is, in its relation to the average flux, a "difference flux".

2.2.3 Two-dimensional Fourier analysis: power spectra

The discovery of variability with the outflow is only the first step. What is required is to uncover a form of periodic variability, and to do this the technique of Fourier analysis is utilised.

Fourier analysis uses the theory that any periodic function *f(x)* can be broken down to (and subsequently re-synthesised as) a series of sinusoidal functions:

$$f(x) = a_0 + \sum_{k=1}^{\infty}(a_k cos kx + b_k sin kx) \tag{2.5}$$

where the coefficients a_0, a_k and b_k are given by:

$$a_0 = \frac{1}{2\pi}\int_0^{2\pi} f(x)dx, a_k = \frac{1}{\pi}\int_0^{2\pi} f(x)cos(kx)dx, b_k = \frac{1}{\pi}\int_0^{2\pi} f(x)sin(kx)dx \quad (2.6)$$

Therefore in applying Fourier techniques to a given set of time series spectra one can attempt to discover whether any such periodic variability exists or not. In order to uncover time-based periodic functions the spectra are passed through a Fourier transform algorithm. Time-dependent functions can be represented by a superposition of +/− components throughout the entire frequency range:

$$f(t) = \int_{-\infty}^{+\infty} d\nu F(\nu)e^{+2\pi i\nu t}, -\infty \leq t \leq +\infty \quad (2.7)$$

(Roberts et al. 1987).

The function f is therefore given by the superposition of the Fourier transform and the contribution of each ν to f is thus defined.

The Fourier transform itself is given by:

$$F(\nu) \equiv FT[f] \equiv \int_{-\infty}^{+\infty} dt f(t)e^{-2\pi i\nu t} \quad (2.8)$$

for $-\infty \leq \nu \leq +\infty$.

The plotted Fourier transforms – the power spectra – depict the contribution of ν to the variance of f thus:

$$P(\nu) = |F(\nu)|^2 \quad (2.9)$$

for $-\infty \leq \nu \leq +\infty$.

It should be pointed out, however, that Fourier transforms only work in an effective manner when the function under analysis is continuous; whereas the spectral sections being fed into the Fourier transform algorithm are, by their very nature of being of a restricted wavelength range, finite. This causes problems with the outputted frequency power spectrum: noise is created by the transform trying to cope with a finite function,

resulting in numerous ghost frequencies being displayed within the output spectrum.

To solve this the output power spectrum is then passed through a cleaning algorithm which works by identifying the strongest peaks in the power spectrum and then removing a fraction – the 'gain' – of them. This process is repeated over and over until what remains in the output is the noise only i.e. what has been removed is the required noise-less power spectrum.

Again, the requisite IDL commands are as follows:

• `load_fits_ts`: The time series data files are loaded as before.

• `fourier2d`: As with the greyscaling process, the input time series is fed into the algorithm but before set in motion a GUI window appears in which various processing and display parameters can be adjusted. Among these are two which affect the way in which various possible frequencies are tested against the inputted time series in the Fourier analysis: `df` adjusts the spacing between consecutive test frequencies, and `fmax` sets the upper limit of the test frequencies, in cycles per day.

For the purposes of the initial experiments with this system, each of the line profiles was tested with upper limits of test frequency of 12, 14, 16, 18 and 20 cycles per day, each with a frequency spacing of 0.2 cycles per day.

As with the `greyscale` GUI there are also boxes contained within the `fourier2d` GUI where the rest wavelength of the given line profile, and the limits for both the blue and redshifted velocities either side of the zero velocity of the rest wavelength, are entered.

• `fourier2dplot`: The two-dimensional Fourier transform power spectra is displayed with a mean spectrum about the selected line plotted at the bottom of the display and above which appears the result of the two-dimensional Fourier analysis. The pattern of dots displayed is interpreted at the top and to the right hand side: effectively the dots and broader markings are added up in two different directions:

• 1: Added vertically (and working form left to right) the markings reveal the variance along the line profile and indeed the graph at the top of the display is similar to that of the TVS plot for the similar line profile.

• 2: Added horizontally (and working from bottom to top) the markings reveal the strength of response to each test frequency – the power of each test frequency (labelled from up the left hand side from zero to the `fmax` value) over the extent of the test range: figure 3.

It is the right hand side power spectrum which shows the frequencies most likely to

be occurring with the variability of the time series spectra. Often a large peak occurs at the top near the `fmax` value but this is simply a normal product of the algorithm. The main frequencies contained within the time series should be revealed by the larger peaks between zero and the maximum, however as mentioned above, unless the cleaning process has been undertaken there may be many false peaks appearing within the power spectrum due to noise caused by the discontinuous nature of the line profile. Once cleaned, a more reliable power spectrum should reveal the period(s) inherent in the time series. Examples of Fourier analyses output are shown in Figure 2.3.

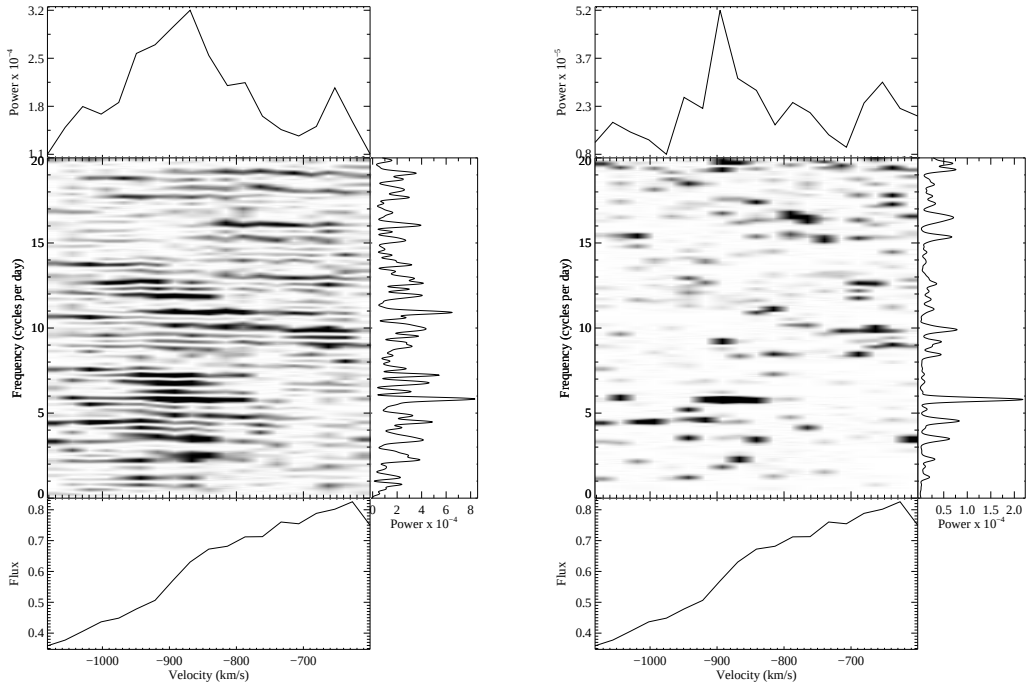

Fig. 2.3. Full-panel displays of Fourier-based frequency analysis of the blue trough of the P v doublet, as seen in the F034 spectra of PN NGC 6543, analysed between $-600 - -1100$ km s^{-1}, with the 'dirty' analysis on the left, and the 'clean' analysis (gain = 0.500) on the right.

2.2.4 Greyscale II

Once potential periods of cycle have been identified from the cleaned power spectrum then the greyscale technique can be reapplied and now, using the GUI window appears it contains a box in which one is able to enter the test period (i.e. the frequency as displayed by the Fourier power spectrum but inverted) and can also indicate that the output is

'folded' so as to display this periodic variability. The folding technique essentially takes the period value as entered in the greyscale GUI and then compares the input time series data comparing its time axis with the different phases of the period as applied. It then fills in any phase gaps across the timescale of the data with greyscale sections of comparable phase from elsewhere along the same timescale. When all gaps have been filled – the data effectively folded in on itself – then the output displays another greyscaled image but with the vertical axis scaled to one (or more) period(s): see Figure 2.4.

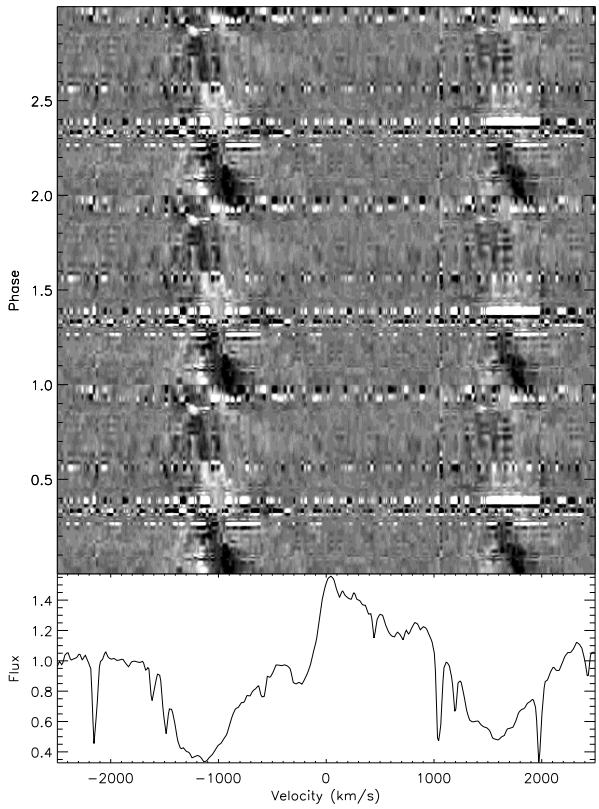

Fig. 2.4. Greyscale representation of the F034 P V doublet of PN NGC 6543, folded over a period of 0.172 days – here displayed over three cycles.

2.3 Analysing Line Profiles within the Wind: SEI Code

The study of line profiles in stellar spectra can reveal fundamental information about the wind: they can reveal physical details about the structure of the wind, as well as more

intrinsic qualities by conveying information about mass-loss. Spectral line profiles can be in emission, absorption or in combination, such as within the P Cygni profiles found in UV spectra of OB stars; or as investigated in this thesis, the FUV spectra of CSPNs. The way to extract this information is to computer model of the given wind profile on top of that observed in the spectra, and from a comparison of the two, one is able to obtain information of the velocity law governing the wind, and also to derive the column density and understand the distribution of the ions under observation, as a function of velocity.

To this end, the *Sobolev with Exact Integration* (SEI) method is employed for the purpose of generating model fits to the P Cygni profiles found in both the UV (IUE) and far-UV (FUSE) wave-bands. The model P Cygni fits yield measurements of wind optical depths as a function of velocity for each ion analysed; the results are given as a product of the mass-loss rate and the ionisation fraction, $\dot{M}q_i(v)$

The method works by first evaluating the source function using the Sobolev approximation, where for a fast accelerating stellar wind the source function is calculated using the escape probability method. The approximation treats the line absorption coefficient as a delta function in frequency: this is allowed if the velocity gradient, dv/dr is much larger than the v_t/l fraction, where v_t represents the combined thermal and turbulent velocity for ions in the wind, and l is the characteristic length over which either the density or ionisation changes Lamers et al. (1987). Then the radiative transfer equation can be solved accurately, and thence calculating line profiles occurring within the expanding stellar atmosphere via a monotonically accelerating velocity law in which random chaotic motions can be treated as a one-dimensional radial turbulence (and for which a radially dependent macro-turbulent parameter was introduced to the method by Haser et al. (1998)), thereby modelling small-scale perturbations in the velocity law.

The Source Function

The source function of a two-level atom is given as:

$$S_\nu(x) = [\beta_c(x) I^*_\nu + \epsilon' B_\nu(x)]/(\beta + \epsilon') \tag{2.10}$$

where I^*_ν is the stellar intensity at frequency ν of the radiation leaving the photosphere, β_ν is the Planck function of the wind, and $\epsilon = C_{ul}/A_{ul}$ is the ratio of collisional to radiative

de-excitations. Here β is the escape probability for line photons:

$$\beta(\tau_0, \sigma) = \int_0^1 \left(\frac{1+\sigma\mu^2}{\tau_0}\right)\left[1 - \exp\left(-\frac{\tau_0}{1+\sigma\mu^2}\right)\right] d\mu \tag{2.11}$$

and β_c is the penetration probability for continuum photons:

$$\beta_c(\tau_0, \sigma, z) = \frac{1}{2}\int_{\mu_c}^1 \left(\frac{1+\sigma\mu^2}{\tau_0}\right)\left[1 - \exp\left(-\frac{\tau_0}{1+\sigma\mu^2}\right)\right] d\mu \tag{2.12}$$

where

$$\sigma = \frac{x}{w}\frac{dw}{dx} - 1 \tag{2.13}$$

and $\mu_c = (1 - z^2)^{1/2}$

The optical depth above is defined as:

$$\tau_0(x) = \frac{\pi e^2}{mc}(gf)_{lu}\left(\frac{n_l}{g_l} - \frac{n_u}{g_u}\right)\frac{R_\star}{v_\infty}\frac{c}{\nu_0}\frac{x}{w} \tag{2.14}$$

However, for resonance lines $n_u/g_u \gg n_l/g_l$ and so the optical depth can be approximated by:

$$\tau_0(x) \approx \frac{\pi e^2}{mc} f\lambda_0 n_i \frac{x}{w}\frac{R_\star}{v_\infty} \tag{2.15}$$

where n_i is the number of ions per unit volume.

In a case where the photospheric spectrum contains a continuum I_c with an absorption line, then

$$I_\nu^\star = I_c[1 - A(\nu - \nu_0)] \tag{2.16}$$

where A is the absorption.

The intensity at a distance x, frequency ν_0, and angle μ is given by:

$$I_{\nu_0}(x,\mu) = I_c[1 - A(\Delta\nu')] \tag{2.17}$$

where $\Delta\nu' = \nu_0 v_\infty w(x)\mu/c$. The penetration probability β_c of the contribution of the continuum photons to the mean intensity $\bar{J}_\nu$ becomes:

$$\beta_c(\tau_0,\sigma,z) = \frac{1}{2}\int_{\mu_c}^{1}[1 - A(\Delta\nu')] \times \left(\frac{1+\sigma\mu^2}{\tau_0}\right)\left[1 - \exp\left(-\frac{\tau_0}{1+\sigma\mu^2}\right)\right] d\mu \tag{2.18}$$

where β remains as before.

Solving the Transfer Equation

The solution to the transfer equation gives the intensity as seen by the observer for a line of sight p as:

$$I_\nu(p) = \int_{z=-\infty}^{z=\infty} S_\nu(z')e^{-\tau_\nu(z')}d\tau_\nu(z'), \tag{2.19}$$

for $p \geq 1$

$$I_\nu(p) = \int_{z=-\infty}^{-z_\star} S_\nu(z')e^{-\tau_\nu(z')}d\tau_\nu(z') + I_\nu^\star e^{-\tau_\nu(-z^*)}, \tag{2.20}$$

for $p < 1$

The second part of the equation describes the intensity coming from the line of sight intersecting the star at $z = -z_* = -(1-p^2)^{1/2}$ and containing a contribution from the photospheric radiation I_ν^*.

The optical depth in the expression for $I_\nu(p)$ is:

$$\tau_\nu(z') = \int_\infty^{z'} \tau_0(x)\Phi_\nu(z)/(1+\sigma\mu^2)dz \tag{2.21}$$

where the integration is made along a line of sight of constant p.

In this expression the profile function $\Phi_n u(z)$ is determined by the local turbulence in the wind. If ϕ is expressed in terms of the dimensionless velocity w:

$$\phi(\Delta\omega) = \pi^{-1/2} w_D^{-1} \exp[-(\Delta w/w_D)^2] \tag{2.22}$$

with $w_D^2 = w_T^2 + w_t^2$, where $w_T = v_{turb}/v_\infty$ and $w_t = v_{thermal}/v_\infty$, then $\Phi_\nu(z)$ is defined by:

$$\Phi_\nu(z) = \phi \left[\Delta w = \mu w(x) - \frac{\nu - \nu_0}{\nu_0} \frac{c}{v_\infty} \right] \frac{dw_z}{dz} \tag{2.23}$$

where z and x are coupled by the condition that p is constant.

The flux, normalised to the continuum, is given by:

$$F_\nu = \int_0^\infty [I_\nu(p)/I_c] 2p dp \tag{2.24}$$

The parametrised velocity law is given as:

$$w(x) = w_0 + (1 - w_0)(1 - 1/x)^\beta \tag{2.25}$$

often with $\beta = 1$ and $w_0 = 0.01$. The parametrised optical depth is given as:

$$\tau_1(w) = T(\gamma + 1)(1 - w_0)^{-1-\gamma}(1 - w)^\gamma \tag{2.26}$$

where $\tau_1(x)$ is defined:

$$\tau_1(x) = \frac{\pi e^2}{mc} f \lambda_0 n_i \frac{dr}{dv} = \tau_0(x) \frac{d \ln x}{d \ln w} \tag{2.27}$$

However, with a modified code (see Massa et al. 2003), the optical depth is set by adjusting that as set by 21 velocity bins, each approximately $0.05 v_\infty$ wide.

The following section describes in detail the component parts of the SEI code calculations.

2.3.1 The SEI Method

The SEI method assumes a homogeneous, spherically symmetrical wind, progressing with smoothly accelerating velocity laws. It can be used to model either single absorption lines but has the ability to accommodate the blending of closely-spaced doublets also.

The various input parameters are as follows:

1. Terminal velocity: a measure of v_∞ is required in order to calculate the normalised velocity parameter, $w \equiv v(r)/v_\infty$.

2. Velocity law: a standard parametrised β-law is assumed to represent the expansion and acceleration of the wind. This has the form:

$$w = w_0 + (1 - w_0)\left(1 - \frac{1}{x}\right)^\beta \tag{2.28}$$

where $x = r/R_*$ and R_* is the stellar radius (Lamers et al. 1987). w_0 is set as 0.01 in all calculations. The value of β determines the shape of the overall profile – it governs the density distribution, $\rho(x)$, as described via the equation of mass continuity:

The shape of the entire distribution of the wind is set by the value of β: it controls the density distribution as given my the Mass Continuity equation:

$$\dot{M} = 4\pi {R_\star}^2 v_\infty x^2 w(x)\rho(x) \tag{2.29}$$

3. Turbulent velocity: is depicted by a Gaussian distribution, with a 1 σ dispersion parameter w_D. It is an additional effect added to account for an include such effects as shocks in the wind upon the line profile. It smooths the distribution of optical depth as a function of w – its extends saturated portions of strong P Cygni profiles by 'a few times w' – it notably decreases the sharpness of the absorption trough near v_∞, and spreads out the profile in that it shifts the maximum velocity in absorption blueward and the strength of the emission peak redward.

4. Photospheric spectrum: this is given by a Gaussian distribution of optical depth.

$$r_w = exp\left\{-\tau_0^B exp\left(\frac{-w^2}{\sigma_w^2}\right) - \tau_0^R exp\left[\frac{-(w-\delta_w)^2}{\sigma_w^2}\right]\right\} \tag{2.30}$$

where $\tau_0^R/\tau_0^B = f_R/f_B$ the ratio of the oscillator strengths for the doublet (or zero for a singlet); δ_w is the spacing of the doublet in normalised velocity; and σ_w is related to the full width of the line expressed as a velocity, v_G, by $v_G = 2(ln2)^{1/2}\sigma_w v_\infty$.

5. Optical depth of the wind: this is given from the radial Sobolev optical depth, $\tau_{rad}(w)$, which is derived/modelled from 21 independent velocity bins which are individually adjusted to provide the best model fit for the spectrum of the wind line – the optical depth is the only remaining free parameter to be tested once the terminal velocity and the photospheric spectrum are fixed.

In fitting the model wind profile in this manner, the adjustment of the standardised-velocity-dependent optical depths is reliant upon the premise that in a monotonically expanding spherically symmetric outflow, only material with $w \leq w + w_D$ contributes to the formation of the line, (as given in Lamers & Cassinelli 1999).

The fitting itself is achieved by first adjusting the level of the optical depth velocity bin at $w = 1$ i.e. at the blue-ward terminal velocity edge of the P Cygni profile of the given stellar wind absorption line under scrutiny. Thence fits are obtained for each velocity bin, in steps inward of the wind, with adjustments made for optical depth for each w_i until a satisfactory fit of the profile is made at each of the 21 points.

If all assumptions concerning spherical symmetry and the monotonic simplicity of the β-law are correct, then the fits to $\tau_{rad}(w_i)$ can be regarded as reliable.

6. In manipulating the optical depth levels for each of the 21 velocity bins, what in fact is actually being derived is the ionisation level for each of the bins along the velocity profile. This is because the ionisation profile of each bin, $q_i(w)$, is related to the corresponding optical depth optical depth, $\tau_{rad_i}(w)$ (see Olson 1982) by

$$q_i(w) = \frac{m_e c}{\pi e^2}\frac{4\pi\mu m_H}{f\lambda_0 A_E}\frac{R_\star v_\infty^2}{\dot{M}}x^2 w\frac{dw}{dx}\tau_{rad}(w), \tag{2.31}$$

where $q_i(w)$ is the fraction of element E in ionisation state q_i at (standardised) velocity w. $\dot{M}$ is the mass-loss rate of the star, v_∞ is the wind's terminal velocity i.e. the factor by

which the profile's velocity bins are standardised, μ is the mean molecular weight of the plasma – set to 1.35 for all stars, A_E is the abundance of element E relative to Hydrogen.

The Key Steps of the Fitting Procedure

• Estimation of interstellar H1 and H2 column densities – solar abundances assumed for all objects in this thesis.

• A saturated wind line is used to provide parameter values for the wind law, namely the acceleration profile factor β, the terminal velocity of the wind v_∞, and w_D, the wind turbulent velocity factor. The line used is usually the C IV $\lambda\lambda$1548,1550 doublet - this is strongly saturated and therefore sensitive to the wind's terminal velocity – the farthest blueward edge of the 1548 Å line is where the blue-shifted terminal velocity is measured.

• An estimate of the size and shape of the input photospheric spectral line being modelled is obtained using the spectral line rotational broadening program TLUSTY (see below).

• As stated above, once the velocity law parameters of β, v_∞, and w_D have been set, resonance lines are finally fitted through the adjustment of 21 velocity bins in the form of a histogram of τ_{rad}.

2.4 A Brief Introduction & Description of TLUSTY

Following advances in observational data and computational abilities Lanz & Hubeny (2003) were encouraged to adopt the physically sound and powerful Accelerated Lambda Iteration (ALI) which, combined with a wealth of atomic data available via such projects as the Opacity Project (Seaton 1987), the IRON project (Hummer et al. 1993), and the OPAL project (Iglesias & Rogers 1991), provided the raw materials from which to derive physically accurate stellar atmosphere models.

Various driving factors which warranted the application of advanced techniques to produce such stellar atmosphere models included the ongoing investigations into stellar outflows of O-type stars, necessitating theoretical departures from local thermodynamic equilibrium (LTE) assumptions while at the same time combining the effects of atmospheric line blanketing, particularly via the thousands of iron group lines found in such outflowing atmospheres.

Also, the development of so-called 'unified' stellar model atmosphere codes – such as CMFGEN (introduced in the next chapter) – which aim to construct models from the

stellar surface right out into the wind, also require, for the desire of accuracy, to be able to include metal line blanketing in such an nLTE atmosphere. However, whereas CMFGEN employs spherical symmetry in its construction of a 'unified' atmosphere, thereby extending the model into the wind; TLUSTY assumes the simpler plane-parallel geometry to develop an accurate description of the stellar photosphere, thereby providing an accurate lower boundary for stellar wind models.

The *Complete Linearisation* (CL) method, introduced by Auer & Mihalas (1969) provided a computational platform from which it was possible to simultaneously solve the equations of radiative transfer, hydrostatic equilibrium, radiative equilibrium, and also those of statistical equilibrium: physically it was the appreciation of the effect of *coupling* parameters such as energy level populations with the radiation field and its temperature, that provided the initial conceptual breakthrough; unfortunately at the time the limitations of computer power meant that only a very few energy levels of only a handful of lines could be dealt with, out of the potential millions.

It then became apparent that the monumental task of mathematically solving radiative transfer, etc., for all these lines, could in fact be simplified through by a combination of mathematical breakthroughs: firstly, the introduction of Anderson's *superlevels* (1985,1989) – collating all individual frequencies into select frequency blocks, whereupon radiative transfer is solved explicitly for a given block, and solutions for individual constituents of the block are converged iteratively.

The application of powerful iteration techniques provided another breakthrough, particularly the development of ordinary lambda iteration into the *accelerated* version. Here, the introduction of the *approximate lambda operator* acts upon the source function, plus a correction term from the previous iteration, rapidly, and accurately, reduces the computation time for complex line-blanketed atmospheres. A description of the accelerated lambda iteration technique is given below, followed by a brief introduction to Anderson's superlevels.

2.4.1 Accelerated Lambda Iteration (ALI)

Accelerated Lambda Iteration (ALI) is the key powerful computational technique employed in the TLUSTY method in its production of a modelled stellar atmosphere. In simple terms – for example for a 1-D homogenous static medium – the main task is to solve the both the radiative transfer equation (which is both angle and frequenct dependent)

and the equation of statistical equilibrium: in combination, these equations can be solved iteratively, but because of the angle-frequency coupling of radiative transfer which leads to a matrix repersentation of the atmosphere, the iteration involved is unfortunately too time consuming (Hubeny 2003).

Stellar atmosphere solving iteration begins with the angle-and-frequency-dependent radiative transfer equation can be written:

$$\mu \frac{dI_{\mu\nu}}{d\tau_{\mu\nu}} = I_{\mu\nu} - S_\nu \tag{2.32}$$

where $\mu = \cos\theta$

The formal solution to this may be written:

$$I_{\mu\nu} = \Lambda_{\mu\nu}[S] \tag{2.33}$$

where Λ operates on the source function. Through integration the frequency-averaged intensity can be given as:

$$\bar{J} = \Lambda[S] \tag{2.34}$$

where:

$$\bar{J} = \int J_n u \phi_\nu d\nu \tag{2.35}$$

and:

$$\Lambda = \int \Lambda_\nu \phi_\nu d\nu \tag{2.36}$$

with ϕ_ν is the normalised absorption profile.

$$J_d = \sum_{d'}^{D} \Lambda_{dd'} S_{d'} \tag{2.37}$$

The equation of statistical equilibrium which in a simple two-level atom can be written:

$$S = (1 - \epsilon)\bar{J} + \epsilon B \tag{2.38}$$

where ϵ is the collisional probability and B is the Planck function.

In substituting Equation 2.34 into Equation 2.38, the source function can be written:

$$S = (1 - \epsilon)\Lambda[S] + \epsilon B \tag{2.39}$$

and if Λ were linear, then the solution can be arrived at in one step:

$$S = [1 - (1 - \epsilon)\Lambda]^{-1}\epsilon B \tag{2.40}$$

Unfortunately Λ is in reality a matrix and its implied inversion is by no means a simple matter and particularly time-consuming.

It can be solved however through iterating between the intensity and the source function, where successive solutions can be found thus:

$$S^{n+1} = (1 - \epsilon)\Lambda[S^n] + \epsilon B \tag{2.41}$$

This is the essence of *Lambda Iteration*. Unfortunately, this method can be tremendously time-consuming, taking a very long time before convergence is achieved; there is also a tendency for the solution to stabilise, with differences in successive solutions becoming negligible thereby reaching a conclusion before the correct solution has been obtained.

A much faster iteration method can be afforded by so-called operator splitting, where the Λ operator is written as:

$$\Lambda = \Lambda^* + (\Lambda - \Lambda^*) \tag{2.42}$$

where Λ^* is an approximate lambda operator. Now the iterative-solving equation can be written:

$$S^{n+1} = (1-\epsilon)\Lambda^*[S^{n+1}] + (1-\epsilon)(\Lambda - \Lambda^*)[S^n] + \epsilon B \tag{2.43}$$

The exact operator is now split into two contributions: the approximate Λ^* operator acts upon the new iterate of the source function, and the difference between the exact and approximate operators acts upon the the previousm known source function.

The source function is now iterated to convergence – despite using an approximate operator – and so radiative transfer is solved exactly.

An alternative from of the above equation can be formed using a so-called immediate source function taken from the old source function by the formal solution (FS):

$$S^{FS} = (1-\epsilon)\Lambda[S^n] + \epsilon B \tag{2.44}$$

and so the diffrence bewteen successive iterations can be expressed thus:

$$\delta S \equiv S^{n+1} - S^n = \left[1 - (1-\epsilon)\Lambda^*\right]^{-1} \left[S^{FS} - S^n\right] \tag{2.45}$$

2.4.2 Simplification through Super-levels

When attempting to deal with iron species line blanketing one soon discovers that any iteration code has to somehow deal with 10^4 – 10^5 energy levels and consequently 10^6 – 10^7 energy transitions: such incredible complex calculations would tax even the most rapid computational machinery, and so clearly some method need to be found to somehow reduce the complexity of these calculations without unduly robbing the user of all important data which might otherwise be lost through over-simplification (Hubeny & Lanz 1995).

In order to be able to deal with the thousands upon thousands of lines encountered in a

line blanketed stellar atmosphere, Anderson (1989) introduced the concept of 'superlevels': here a great many energy levels can be grouped together so that a large number of energy levels, j, can be formed into a superlevel, J, their common factor being that they possess the same nLTE departure coefficient – that is to say they all the j components are in Boltzmann equilibrium with respect to one another.

Anderson (1989) and later Dreizler & Werner (1993) partitioned the true levels into superlevels based upon their energies only, and so the number of superlevels was small, 7 to 8 per degree of ionisation. However Hubeny & Lanz (1995) considered this too much of a simplification because the subsequent wide energy widths of the superlevels would not reflect the true nature of indvidual transitions, and also transitions between components of an given superlevel have to be considered.

In choosing the number and nature of the superlevels, one must decide how to sort out the innumerable levels into these. Clearly the individual energies of the level components must be close and possess similar properties i.e. they should belong to the same spectroscopic multiplet, have the same parity, etc.; but there should not be too many superlevels chosen as this would defeat the object of this attempt at simplification.

So accordingly, all levels within a superlevel must possess similar parity, and differences between energy levels must be small. This has the result that there are 10 – 15 superlevels per system and so 20 – 30 superlevels per ion (Hubeny & Lanz 1995). In putting together these superlevels only the those with measured energy levels, and not predicted ones, are considered: high-energy levels are considered separately via appropriate partition functions (see Hubeny 1988).

2.4.3 The Incorporation of the TLUSTY Models into the SEI Code

One of the main initial parameters to be fed into the SEI code – perhaps the most fundamental – is that of the photospheric profile of the resonance line under investigation, and particularly is shape: its depth and width: the depth giving an indication of the level of absorption/absorbers present and the particular frequency; the width giving an indication of the scale of the stellar rotation which broadens the spectral line.

An estimate of the depth and FWHM width of the photospheric absorption line to be used as an input for the SEI code can be provided by the TLUSTY grid of models which essentially provide one with an estimate of the shapes of absorption lines as they are affected by the rotation of a star of a given temperature and surface gravitational

acceleration.

When downloaded, the TLUSTY grid of models presents the user with a range of model stellar spectra of different values of surface temperature and (logarithmic) surface gravity, each combination of $T_{\rm eff}$ and $\log g$ having two files: one containing the spectral line information, the other containing that of the model continuum. The spectra and continuum corresponding to the $T_{\rm eff}$ and $\log g$ of the star under investigation (or as close to it as possible) are chosen.

For a given stellar wind UV resonance line or lines e.g. the P V $\lambda\lambda$ 1117.98,1128.01 doublet, an small section of the overall TLUSTY model spectral range – say approximately 100 Å i.e. $\sim$ 50 Å either side of the singlet/doublet under investigation – is fed into a simple rotationally-broadening algorithm, ROTIN, for which an approximate 'typical' rotational velocity ($v \sin i$) of 100 km s^{-1} is selected.

The resultant (broadened) spectra output can then be viewed through a standard analysis tool such as DIPSO, and a measurement taken of the FWHM of the rotationally broadened spectral line, which can then be used for the FWHM value for the input photospheric absorption line for the SEI model. The TLUSTY output spectrum is also normalised – as will be the input spectrum for the SEI code – and so a simple visual check will give an estimate of the initial optical depth required by the photospheric absorption line before it is affected by the motions of the stellar wind in the SEI model.

2.4.4 Example of an SEI Model Fit – Description of Panels

To illustrate a typical result of an absorption line fit using the SEI method, Figure 2.4 is given as an example:

• Top panel:

This depicts the SEI-generated stellar wind model overlaid on top of the observed spectrum. The rest position of the red component of the doublet is indicated by a thick tick mark along the normalised velocity axis. As well as the resultant model profile, the panel also shows the component parts of the model, namely the direct (transmitted) and diffuse (scattered) components, shown as respective dotted and dashed lines. These aspects of the model fit can help to assess the validity of the parameters used to construct the model. The addition of optical depth to decrease the transmitted flux at a high velocity will subsequently increase the forward-scattered component at low velocities within the absorption trough of the P Cygni profile. Once the increase of high-velocity optical depth/absorption

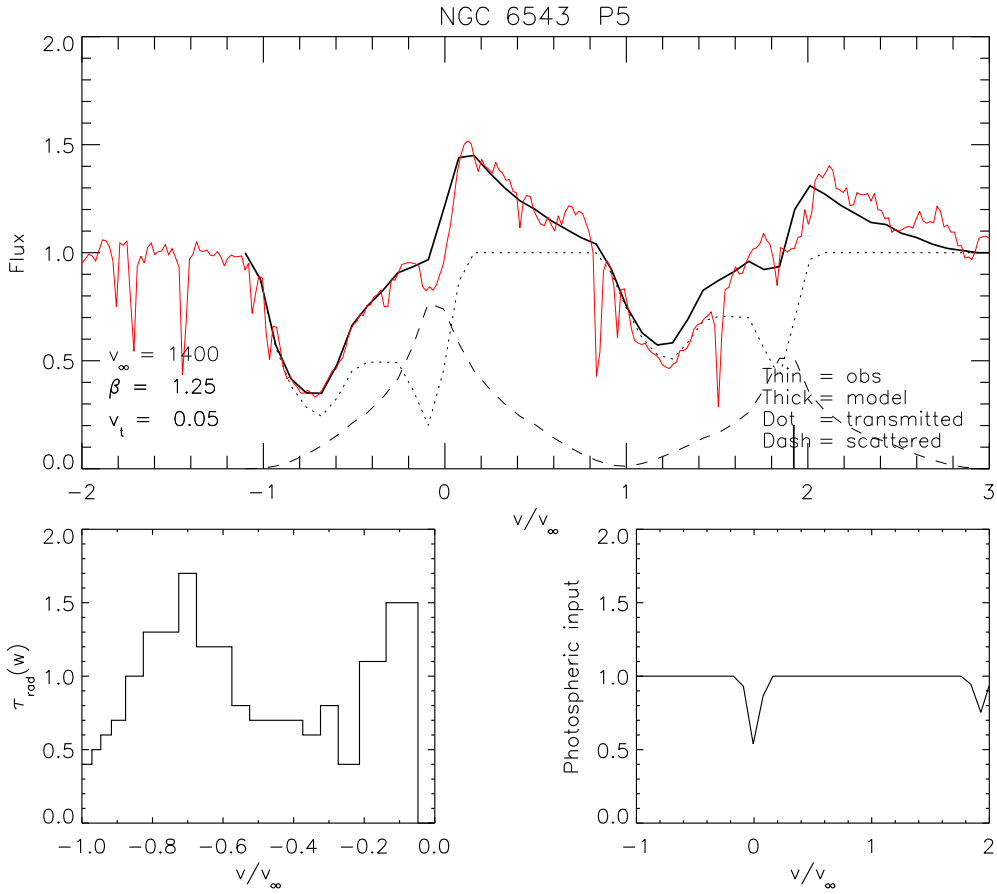

Fig. 2.5. SEI model fit of the mean spectrum from the F034 dataset of the UV spectra of the P V doublet, from the Central Star of PN NGC 6543; see text for detailed descriptions of the individual panels.

produces more scattered light than the observed profile at lower velocities – thereby raising the dashed scattered component line above the observed profile – then even with a further addition of arbitrarily large optical depths at lower velocities will not be able to depress the model line below the position of the scattered component. The only way to deepen the low-velocity absorption in to either strengthen or widen the inputted photospheric line profile, and if that does not improve the fit then the validity of the model's assumption – particularly the spherical symmetry – must be questioned.

• Bottom-left panel:

Here the histogram of optical depth, τ_{rad}, versus normalised velocity function, $w = v_i/v_\infty$, for the 21 independent velocity bins is shown; the optical depths displayed are those giving the above SEI model its final best-fit form.

• Bottom-right panel:

Here can be seen the profile of the photospheric input absorption line which will be ul-

timately modified with its progress through the stellar wind, taken from the TLUSTY model grid for the star's given effective temperature, T_{eff}, and the logarithmic value of its surface gravity, $\log g$; its photospheric depth and width are estimated from the rotationally broadened output of the particular ion absorption line as calculated via the ROTIN programme. The normalised flux of the line is displayed versus the v_∞-standardised velocity, as with the adjacent velocity bin histogram.

Chapter 3

Seeking Structure in UV Spectra of NGC 6543

3.1 Motivations

Investigating the mechanisms of mass-loss is crucial to the study of the development of a stellar system, as the rate at which a star loses its mass is the key factor pertaining to the development of a star, particularly during the latter stages of its life. The rather commonplace existence of a stellar wind became evident from studies of UV data obtained via the *International Ultraviolet Explorer* (*IUE*) satellite, whence the streams of data displayed a wealth of P Cygni profiles from which the stellar wind velocities were measured; and it was shown that the maximum speeds could be up to a few 1000 $\mathrm{km\,s^{-1}}$ and subsequent estimates of the mass-loss rate were shown to range between $\sim 10^{-11}$ and $\sim 10^{-6}$ $M_{\odot}\,\mathrm{yr}^{-1}$(e.g. Perinotto 1989).

From the the earlier evidence of the existence of a stellar wind, it has also been shown that, more often than not, this wind can exhibit a number of varying characteristics: these can found in radial velocity variations (Méndez et al. 1990); also variations have been recorded in the shape-shifting spectra of a star, both in photometric variations of the near-photospheric development stages of the wind as viewed in optical wavelengths (Bell et al. 1994), or in the more fully accelerated outer regions as seen in the blueward UV regions (Patriarchi & Perinotto 1997).

One of the main reasons for seeking evidence for inhomogeneous wind structure is that the stellar wind provides key estimates of the mass-loss rates of its parent star, and so a non-spherically-smooth wind would indicate that current estimates for mass-loss rates are inaccurate as they are based upon models which assume a spherically-smooth wind profile. In fact the presence of inhomogeneity in the wind may indicate that previous mass-loss rates have been over estimated by a factor of at least 3, and perhaps as high as 10 (see Massa et al. 2003; Bouret et al. 2005; Fullerton et al. 2006*b*).

Past studies of fast wind variability spectra have utilised UV data collected by the IUE satellite; but as well as being rather limited in number of exposures available, the UV resonance lines contained therein have been far too saturated to be able to provide sensitive diagnostics – and changes between spectra have been hidden except for the extreme blue edges of the line profiles. Also the IUE exposures were of the order of $\sim 2 - 3$ hours which is comparable to the wind flushing times in such stars. Therefore, in order to get a better perspective on fast wind variability, we have sought to exploit the high-resolution capabilities of the FUSE satellite which is capable of providing high signal-to-noise data over relatively short integration times – as well as providing access to unsaturated resonance line profiles – P V , S IV , S VI , and O VI .

3.1.1 The Target – NGC 6543

This chapter presents a time-series study of the HD 164963, the central star of the planetary nebula NGC 6543, more commonly known as the 'Cat's Eye Nebula'. HST images of the nebula reveal complex bipolar structures which include bubbles and precessing jets (Wesson & Liu 2004).

The HST Wide Field Planetary Camera 2 (WFPC2) images taken via the *Hubble Space Telescope* (*HST*) (Harrington & Borkowski 1994) have provided the source material for a quantitative analysis of the physical and ionisation structures found therein (Balick 2004). The most immediately striking aspect of the HST images of the nebula is its complicated knotted structure: The elliptically-shaped core is $\sim 12''$ along its major axis, and its minor axis of the core has a slightly hourglass appearance. Within this region it is a further two crossed ellipses that give the nebula its nickname of the "Cat's Eye": one connecting the pinched edges of the minor axis of the core; the other aligned along the core's major axis.

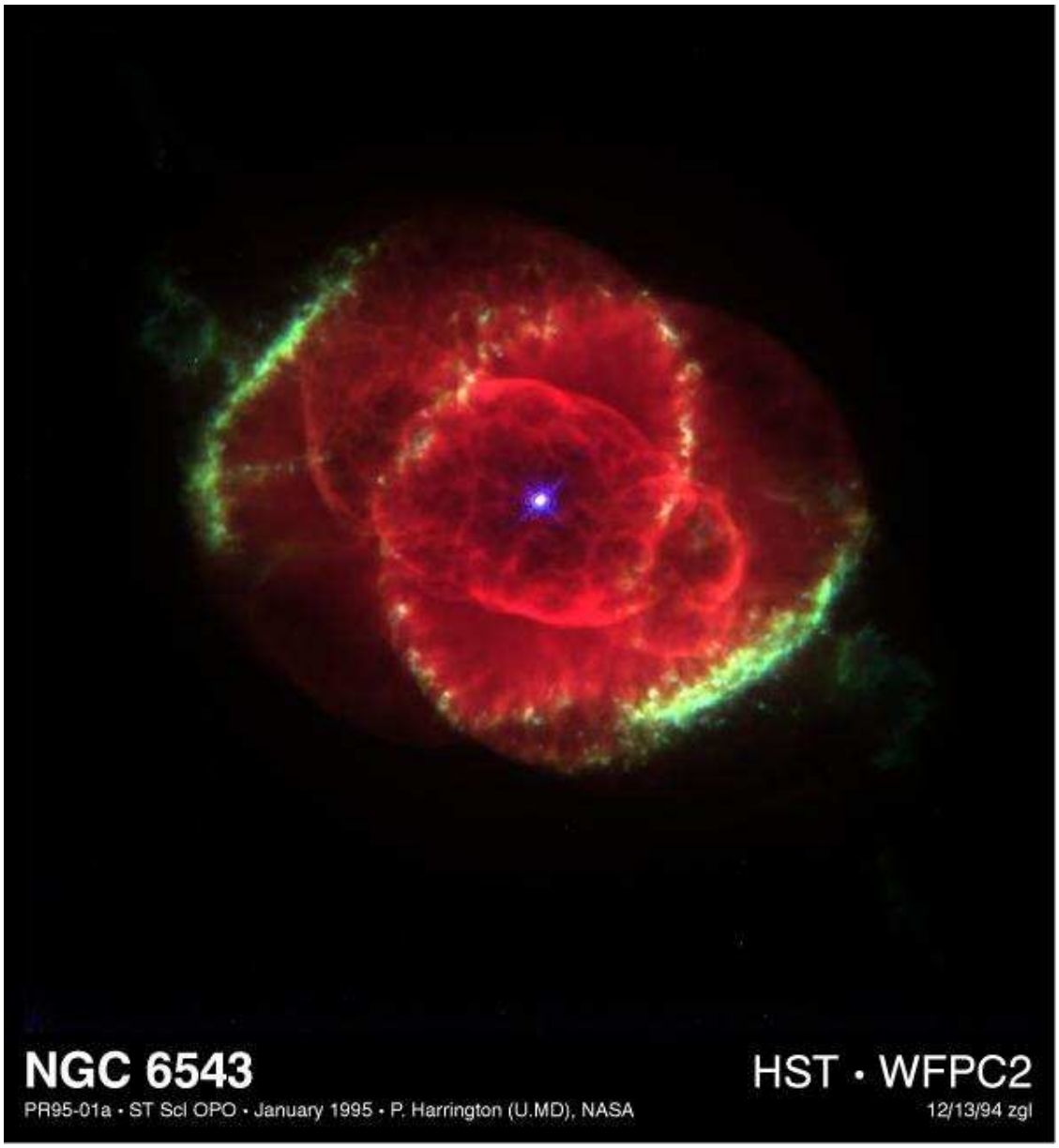

Fig. 3.1. Hubble Space Telescope image of the 'Cat's Eye Nebula': PN NGC 6543 – taken by the HST Wide Field Planetary Camera 2. The Image is a composite of three pictures taken at different wavelengths: red - hydrogen-alpha at 6563 Å; blue - neutral oxygen at 6300 Å; green - ionised nitrogen at 6584 Å: http://chandra.harvard.edu/photo/2001/1220/

In terms of fundamental properties, the central star HD 164963 has been classified in terms of its spectral type as Of-WR (Méndez et al. 1990). This spectral classification is based three main criteria: a strong and broad emission (FWHM > 4Å) in He II $\lambda\,4686$; an Hγ line contaminated with wind emission, particularly in a well developed (or developing) P Cygni line; the He II $\lambda\,4541$ line shows itself to not be in emission, and in the case of NGC 6543 this is both in absorption and also blue-shifted by ~ 100 km s^{-1}.

Wesson & Liu (2004) have carried out a temperature-based analysis of the nebula, mapping the nebula using temperatures derived from ion ratios, while also looking at temperature fluctuations and ion abundances.

Regarding photometry, a difference in flux of approximately 0.01 mag has been measured over a period of roughly a year (Bell et al. 1994). In order to try to uncover a systematic periodicity within the flux, the data were subjected to a time-series analysis algorithm called *PERIOD* which ultimately produces a frequency power spectrum from the Fourier transform of the data. However, each night's data showed frequency peaks related to the observation window for that particular night, thereby masking any potential true periodicity which may have otherwise become apparent. For one night however, JD 2448925, a signal appeared relating to a period of 3.2 h, and when phased to this period, the data showed some indications of periodicity. Also, for JD 2449282 a signal relation to a period of 6.2 h was found, but again, this is very close to the observation window. For the night JD 2449301 a period was found of 2.6 h but this signal was not found in the data for the other nights. They did not find any signal of the order of 1.45 h as derived from apparent periodic shifts of the He II $\lambda\,4868$, as found by Acker (1976), but NGC 6543 does show photometric behaviour similar to that of a 'wind variable' (Méndez 1989).

The variability of the stellar wind of CSPNs is probed further through investigation into the variations on the shape of P Cygni lines found in UV spectra taken from the short (UV) wavelength range via the SWP camera on the IUE satellite (Patriarchi & Perinotto 1995): with a sample of 14 objects evidence was found of changing P Cygni shapes in half the objects, with differences of between 10 – 50% over timescales of years; a parallel is drawn with wind-based variability seen in population I OB stars, and in the case of NGC 6543, there was also evidence of photometric variation.

Later analysis of additional IUE UV data probes the possibility of variability even further (Patriarchi & Perinotto 1997). For each object the data is added together and an average spectrum obtained. Each individual spectrum for a given object is then re-

scaled in comparison with the average, and so when studying the resultant data any differentiation from unity will reveal the presence of possible profile changes, and any change which is greater than 10% is considered a real change, so changes between adjacent spectra can be better analysed and understood. Of particular interest were the regions containing the more noticable P Cygni lines within the UV range: N V $\lambda\lambda$ 1238.82, 1242.80; O IV $\lambda\lambda\lambda$ 1338.60, 1342.98, 1343.51; O V λ 1371.29; Si IV $\lambda\lambda$ 1393.73, 1402.73; C IV $\lambda\lambda$ 1548.20, 1550.77; N IV λ 1718.55Å. The study showed a minimum ± 30 km s^{-1} variation in the blue edge of the P Cygni profiles. Between 1978 and 1993 they report a 15% photometric decrease followed by an increase of 10% between 1993 and 1994 for NGC 6543. In terms of the shape of P Cygni profiles, between 1978 and 1993 there is a 10% decrease in the emission peak of C IV as well as a 170 km s^{-1} decrease in its v_{edge}. Between 1993 and 1994 there is an increase of 170 km s^{-1} of v_{edge} and then again between 1994 and 1995 another 170 km s^{-1} decrease. In comparing these results with similar variations observed in population I OB stars, where the observed blue edge shift is of the order of 10% and the presence of such shifts are attributed to the manifestation of Discrete Absorption Components (DACs): are the CSPNs are exhibiting a similar phenomenon, however, they remain uncertain as they are unable to be sure considering the saturated nature of these CSPN P Cygni lines.

As regards the intensity variations, there appeared changes of between 10 – 30% across the entire P Cygni profile, in both absorption and emission; but in OB stars, although similar levels of variation have been noted in P Cygni lines, the variation has been confined to the absorption part with the emission peaks remaining constant. The lack of large-scale continuum variations lends itself to the theory that those observed are due to variations in the wind (Méndez et al. 1990)

Emission from NGC 6543 has been detected via the Chandra X-ray satellite (see Chu et al. 2001; Guerrero et al. 2001), both from a point source which would appear to be the central star, as well as a substantial quantity of diffuse emission; various mechanisms have been considered by which this diffuse emission could arise. The possibility that the emission could be produced as a result of the stellar wind interacting with the surrounding nebula has been negated, as such a model predicts that the emission will peak close to the inner wall of the interactive region; but for NGC 6543 the diffuse emission appears to be limited to a more immediate region surrounding the central star. An alternative idea is that the X-rays are produced by shock-mechanisms originating within the stellar

wind itself, that is, similar to shocked systems purported to occur within the stellar winds of massive O and B stars (Cassinelli et al. 1994); since NGC 6543 does possess a strong stellar wind (Patriarchi & Perinotto 1991), such a wind-originating shock-mechanism could so produce X-rays.

The possibility of interaction between a compact object and a close binary companion is discarded (Guerrero et al. 2001) as the sizes of the objects involved would produce accretion temperatures of $< 10^5$ K for a mass transfer rate of $< 10^{-7}$ $M_{\odot}$ yr^{-1}, and this is too low a temperature for X-ray emission to occur (Pringle 1981). Alternatively, accretive matter falling directly onto the surface of the compact object could possibly produce X-rays, and for white dwarfs the velocity of the in-falling material is so high that a shock develops above the surface of the star: the in-falling material is heated to a temperature of $\sim 10^8$ K, emitting X-rays. However, the X-ray emission detected from the central star is too 'soft' and does not show the variability associated with high-rate white dwarf accretion. Therefore the accretion of material from a close companion would appear not to be responsible for the observer X-ray emission.

Finally, central star coronal activity is considered, (Guerrero et al. 2001): such activity is caused by the convective and rotational motions of late F-K stars and dMe stars (dwarf M star exhibiting emission), and also evolved stars going from the late-AGB to a proto-PN stage may also have convective envelopes. As a star progresses toward becoming a white dwarf, the ionisation of H and He in its outer envelope ceases at $T_{\rm eff} > 30{,}000$ K, but the central star of NGC 6543 is already a white dwarf, and so this type of coronal activity is unlikely to occur to produce emission of X-rays; on the other hand, the possibility of a close binary companion with such coronal activity is not dismissed and the particularly luminous white dwarf, with L $\sim$ 5600 $L_{\odot}$, could possibly out-shine such a F-M dwarf companion; however, such a companion has yet to be discovered.

In order to uncover some of the basic parameters of the star, the UV and optical spectra of the star have been modelled with a non-LTE unified model atmosphere code ISA-WIND (de Koter et al. 1993), and yielded results of effective temperature, $T_{\rm eff}$, the helium mass fraction, the terminal velocity of the wind, v_{∞}, the wind acceleration, β, and the mass flux $\mathcal{F}_{\dot{M}} = \dot{M}/4\pi R^2$. The L-to-$\dot{M}$ ratio is obtained by being proportional to $T_{\rm eff}4/\mathcal{F}_{\dot{M}}$

The optical spectrum of NGC 6543 has been modelled from an echelle spectrograph, as well as HST spectra for the 1150 – 1400 Å region, and further UV from an IUE spectrum

Table 3.1. Preliminary parameters for NGC 6543

Parameter	Value	Reference
Spectral type	Of-WR (H-rich)	Méndez et al. (1990)
Luminosity	5200 $L_{\odot}$	de Koter et al. (1996)
$T_{\rm eff}$	63000 K	Georgiev et al. (2006)
Radius	0.6 $R_{\odot}$	Georgiev et al. (2006)
Distance	1001 ± 269 pc	Reed et al. (1999)
Mass-loss rate	$\sim 1 \times 10^{-7}$ $M_{\odot}\,{\rm yr}^{-1}$	de Koter et al. (1996)
		Georgiev et al. (2006)
Terminal velocity	1400 $\rm km\,s^{-1}$	This study
Wind flushing time	$\sim$ 45 mins	This study

(Georgiev et al. 2006). With an adopted luminosity of $L = 5200\ L_{\odot}$ (de Koter et al. 1996), the stellar radius was adjusted until the O IV $\lambda\lambda$ 1338, 1343, O IV $\lambda\lambda$ 3560, 3563, and O V λ 1371 lines were reproduced in the model, in which a clumping factor of 0.1 had been introduced as a typical value for massive stars. The mass-loss rate, $\dot{M}$, was determined from the intensities of H I and He II optical lines; the terminal velocity is determined from the blue-ward edges of the UV lines. The best model fit yielded $R = 0.6$ $R_{\odot}$, $T_{\rm eff} = 63{,}000$ K, $\dot{M} = 0.6 \times 10^{-7}\ M_{\odot}\,{\rm yr}^{-1}$ and $v_{\infty} = 1600\ {\rm km\,s}^{-1}$.

Concerning the level of hydrogen deficiency in Wolf-Rayet stars, in particular the intensity decrement of the Pickering ($n \rightarrow 4$) He II lines, where the lines with an even n have a similar wavelength to the hydrogen Balmer lines. However the He II λ 5411 line in the spectrum is much weaker than either the Hβ or Hα lines and so the star cannot be hydrogen poor – in consequence it must be hydrogen rich. The iron abundance, determined in the region 1250 – 1450 Å is well reproduced using solar iron abundance, and so would indicate a level close to the solar value.

In this study fundamental parameters of NGC 6543 have been based upon non-LTE model atmosphere analysis carried out using the *ISA-WIND* code (de Koter et al. 1996), and also *CMFGEN* (Georgiev et al. 2006).

Fundamental parameters are given in Table 3.1.

3.2 FUSE & Time-Series Data

In order to seek out variability and structure in the fast wind of NGC 6543, (F)UV data has been obtained from the archive of the *F*ar *U*ltraviolet *S*pectroscopic *E*xplorer (*FUSE*) satellite.

Table 3.2. UV/FUV ion species

Ion	λ_0 [Å]	$\log \lambda f$	Transition	E_l [eV]	E_u [eV]
Al III	1854.716	3.017	$2p^6 3s$ - $2p^6 3p$	0.0	6.685
Al III	1862.790	2.716	$2p^6 3s$ - $2p^6 3p$	0.0	6.656
C III	977.020	2.872	$1s^2 2s^2$ - $1s^2 2s 2p$	0.0	12.690
C IV	1548.195	2.470	$1s^2 2s$ - $1s^2 2p$	0.0	8.008
C IV	1550.770	2.169	$1s^2 2s$ - $1s^2 2p$	0.0	7.995
N V	1238.821	2.289	$1s^2 2s$ - $1s^2 2p$	0.0	10.008
N V	1242.804	1.988	$1s^2 2s$ - $1s^2 2p$	0.0	9.976
O VI	1031.926	2.137	$1s^2 2s$ - $1s^2 2p$	0.0	12.015
O VI	1037.617	1.836	$1s^2 2s$ - $1s^2 2p$	0.0	11.949
P V	1117.977	2.723	$2p^6 3s$ - $2p^6 3p$	0.0	11.090
P V	1128.008	2.422	$2p^6 3s$ - $2p^6 3p$	0.0	10.991
S IV	1062.662	1.628	$3s^2 3p$ - $3s 3p^2$	0.0	11.667
S IV	1072.973	1.753	$3s^2 3p$ - $3s 3p^2$	0.118	11.673
S VI	933.378	2.615	$2p^6 3s$ - $2p^6 3p$	0.0	13.283
S VI	944.523	2.314	$2p^6 3s$ - $2p^6 3p$	0.0	13.127
Si III	1206.500	3.304	$2p^6 3s^2$ - $3s 3p$	0.0	10.276
Si IV	1393.755	2.855	$2p^6 3s$ - $2p^6 3p$	0.0	8.896
Si IV	1402.770	2.554	$2p^6 3s$ - $2p^6 3p$	0.0	8.839

3.2.1 The Instrument Design

The optical design is based upon a Rowland circle: an imaginary circle drawn at a tangent to the centre of the surface of a diffraction grating, the radius of this circle being half the radius of curvature of the said grating; if an electromagnetic beam passes through a slit located somewhere on this imaginary circle then it will strike the grating and be split, and the consequent beams will be specularly reflected back toward detectors placed at subsequent focus points located upon the same circle, see Figure 3.2. The Rowland circle design incorporates four optical paths or channels – co-aligned so that light from a target object passes through all four simultaneously – each channel consisting of a mirror, a diffraction grating, a Focal Plane Assembly (FPA) which houses the spectrograph apertures, and a portion of an FUV detector. The multi-channel design allows the mirrors and gratings to be coated in such a way as to maximise reflectivity in the wavelength ranges above and below 1020 Å: two mirrors and grating are coated with aluminium with Lithium Fluoride (LiF) overcoat, which provides twice the reflectivity of SiC at wavelengths > 1050 Å but little reflectivity below 1020 Å; the other two mirrors and gratings are coated with Silicon Carbide (SiC) to thus provide a wavelength coverage below 1020 Å. The four channels can be thought to be split onto two sides of the instrument with each side having

a LiF and a SiC channel, each of which produces a spectrum which falls upon a single detector. Each channel has a bandpass of $\sim$ 200 Å, so that the information obtained via two channels, one LiF and one SiC, is needed to cover the $\sim$ 290 Å wavelength range of the instrument (however all four channels cover the 1015 – 1075 Å region).

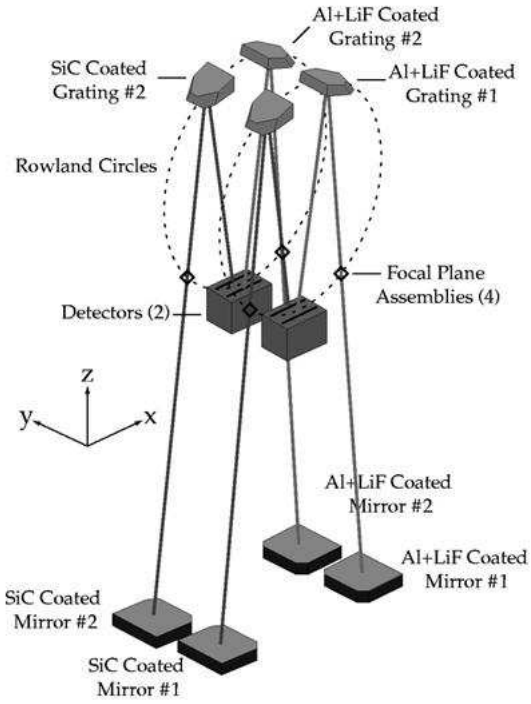

Fig. 3.2. Diagram depicting the Rowland Circle arrangement of gratings and detectors of the FUSE instrument, courtesy of the FUSE website: http://archive.stsci.edu/fuse/instrumenthandbook/

FUSE produces spectra across an overall wavelength range of 905 – 1187 Å. The spectra from the four channels are imaged onto two micro-channel plate detectors, each having one LiF spectra and one SiC spectra imaged onto it, thereby covering the entire wavelength range. The two channels are offset perpendicular to the dispersion direction so as not to allow the spectra to overlap, and also the dispersion direction are opposite for the LiF and the SiC spectra. Each detector is divided into two functionally independent segments, A and B, separated by a small gap ($\sim$ 10 Å). The detectors are also slightly offset with respect to each other so that the gap of each does not fall at the same wavelength region in both detectors. Table 3.3 lists the wavelength coverage of each of the eight detector segment/channel combination segments, whether detector 1 or 2, LiF or SiC, segment A or B:

The LiF channels have a dispersive plate scale of 1.12 Å mm^{-1} and the SiC channels

a scale of 1.03 Å mm^{-1}. With the size of the detector pixels this translates to a scale of $\sim$ 6.7 mÅ $pixel^{-1}$ in the LiF channel and $\sim$ 6.2 mÅ $pixel^{-1}$ for the SiC channel – in the dispersion direction.

Within this thesis, an individual FUSE detector-section combination will be referred to after the fashion of delineation as given in individual FUSE exposure files: for example, in reference to an exposure obtained via the lithium fluoride (LiF)-coated detector number 1, section A – this detector-section-combination will be referred to as "1alif". Therefore, by example, P V doublet lines are usually analysed via the "2alif" exposures, or otherwise those of the "1blif" detector-section.

3.2.2 Observing Modes

The two main observing modes used by FUSE are Time Tag (TTAG) or Histogram (HIST) mode, and each possesses both advantages and disadvantages:

Time Tag (TTAG)

In this mode every photon event recorded by the detectors is sent to the Instrument Data System (IDS), the computer which records the X and Y coordinates of the event upon the detector plus the height of the event pulse; but the arrival time of an individual photon is not recorded. The IDS does not 'tag' every photon event – information from all four detector segments (1A, 1B, 2A, 2B) is sent to the IDS at a maximum rate (for TTAG mode) of $\sim$ 8000 events per second – but the IDS inserts time-tags into the data stream at a nominal rate of once every second, and therefore the (relative) accuracy of photon arrival time in TTAG mode is 1 second.

The advantages of TTAG mode are that it allows the data to be stored with the full detector sampling (6 μm in X and 9.1 - 16.3 μm in Y) which provides the highest spectral resolution to be derived from the data; also data from all apertures is saved and sent to ground as part of the observation dataset. The efficiency of TTAG memory usage is seen best with faint targets as most detector pixels do not experience any events during an exposure; therefore with bright targets the main disadvantage of TTAG is that the spacecraft solid state recorder has only space for $\sim$ 120 MBytes of scientific data, and, for example, a single bright object producing photon events at a rate of 7400 counts s^{-1} would require $\sim$ 60 MBytes of data storage space just for a single 2000 second exposure.

The presence of considerable spectral motion on the detector suggests it is preferable

to make as many observation as possible in TTAG mode. To this end, those observation with an event rate of < 2500 counts s^{-1} TTAG is the default mode – similar to a source producing a flat spectrum of flux $\sim 8 \times 10^{-12}$ erg cm^{-2} sec^{-1} $Å^{-1}$. For higher rates HIST mode is adopted.

Spectral Image or Histogram (HIST)

For an expected count rate of over 2500 counts s^{-1} the IDS is instructed to bin the data in its memory in order to produce a spectral image or histogram (HIST), so the time-tagged facility of TTAG is no longer preserved during exposures; and therefore it is no longer possible to edit spectral images to remove data obtained during periods of high background.

One advantage of HIST mode is that higher data rates are supported – the IDS can process photon event rates up to 32000 events s^{-1} – similar to a source producing a flat spectrum of flux $\sim 8 \times 10^{-11}$ erg cm^{-2} sec^{-1} $Å^{-1}$ – and very close to the $\sim 1 \times 10^{-10}$ erg cm^{-2} sec^{-1} $Å^{-1}$ brightness limit of FUSE. Unfortunately, at full resolution each detector segment is 16384 $\times$ 1024 pixels in size resulting in spectral images which are 32 MBytes each – 128 MBytes for all four segments; also, spectral images are built up in the IDS memory before being sent to the spacecraft recorder and the IDS has only $\sim$ 35 MBytes of memory, which means that the IDS cannot store all data/photon events for the whole detector while in HIST mode; instead only the detector segment containing the spectra taken through the primary aperture are stored in memory.

However, as a means of combating the degradation of data caused by curvature of an astigmatic line spread function (the severity of which is not enough to require high frequency sampling in the Y direction i.e perpendicular to the X direction of the dispersion), the default spectral image mode is to bin the data by a factor of 8 in the Y direction and 1 (no binning) in the X direction, thus reducing the size of the spectral image to < 5 MBytes per exposure. This binning does not affect the resolution at all for most wavelengths, and degrades the nominal spectral resolution by only a few percent.

3.2.3 The In-house FUSE Data Reduction Pipeline

Steps undertaken by the FUSE calibration pipeline – taking raw 2D data and processing it into a set of calibrated 1D spectra – include:

- Data screening (i.e. removing low quality or unreliable data);

Table 3.3. FUSE channels & FUV spectral sections

Channel	Full Range Å	Gap Å	Section A Å	Section B Å
SiC1	1090.9 - 905.0	1003.7 - 992.7	1090.9 - 1003.7	992.7 - 905.0
LiF1	987.1 - 1187.7	1082.3 - 1094.0	987.1 - 1082.3	1094.0 - 1187.7
SiC2	916.6 - 1103.8	1005.5 - 1016.4	916.6 - 1005.5	1016.4 - 1103.8
LiF2	1181.9 - 979.2	1086.7 - 1075.0	1181.9 - 1086.7	1075.0 - 979.2

Table 3.4. NGC 6543 F034 observations

Obs. ID	No. exp	UT Date	MJD (start)	Δt (hours)
F0340105	26	2007-01-13	54113.1260	9.7
F0340106	18	2007-01-14	54114.1097	5.9
F0340107	19	2007-01-15	54115.0933	7.3
F0340108	09	2007-01-16	54116.0680	1.4

- Grating shift correction (i.e. removing spectral motion due to grating motion);
- Drift correction (i.e. calculating image stretch/shift due to thermal effects);
- Background subtraction;
- Flat-field correction;
- Geometric distortion correction (i.e. removing electronic distortions in the delay-line anode);
- Astigmatism correction (i.e. removing curvature perpendicular to the dispersion direction);
- Doppler correction;
- Spectral extraction;
- Wavelength calibration;
- Walk correction (i.e. correcting for pulse-height-dependent errors in the photon location);
- Dead-time correction;
- Flux calibration (counts s^{-1} into erg cm^{-2} s^{-1} $Å^{-1}$);
- Channel co-addition (for simple visual analysis).

3.2.4 The FUSE Time-series Data of NGC 6543

The time-series analyses presented in this chapter are based upon FUSE data from program F034 (PI – DL Massa) obtained between 13^{th} – 16^{th} January 2007, the details of the observations are listed in Table 3.4.

Despite some light lost while using the medium resolution (MDRS) aperture $4^\circ \times 20^\circ$, a total of 72 exposures were taken, and their distribution over the four nights is detailed in Table 3.4. Of these 72, there are 59 adequately captured via the Lif2 channel (segment A: wavelengths 1086 – 1182 Å), where the P V $\lambda\lambda$ 1117.98, 1128.01 is located. Other data from the LiF1 channel (segment A: wavelengths 987 – 1082 Å) giving information on the saturated O VI $\lambda\lambda$ 1031.92, 1037.62. Some limited data – not all FUSE sections managed to obtain sufficient starlight data in all epochs – is also available in the SiC 2 channel (segment A – wavelengths 917 - 1006 Å), namely S VI $\lambda\lambda$ 933.38, 944.52

The mean spectrum for NGC 6543 – F034 (Figure 3.5) provides strong P-Cygni profiles in a number of lines aside from the aforementioned P V , O VI and S VI resonance lines. A possible blueward absorption is shown in the N IV λ 955.34 line and also in C III λ 1175.67.

Apart from the stellar wind-formed lines the spectrum is dominated by narrow interstellar and circumsystem absorptions lines due to atomic species and molecular hydrogen. Also the blue O VI λ 1031.92 component of the doublet is affected by a sharp emission spike from the Ly-β line.

Ionisation details of all UV resonance lines investigated in various degrees in this and the following two chapters are given in Table 3.2.

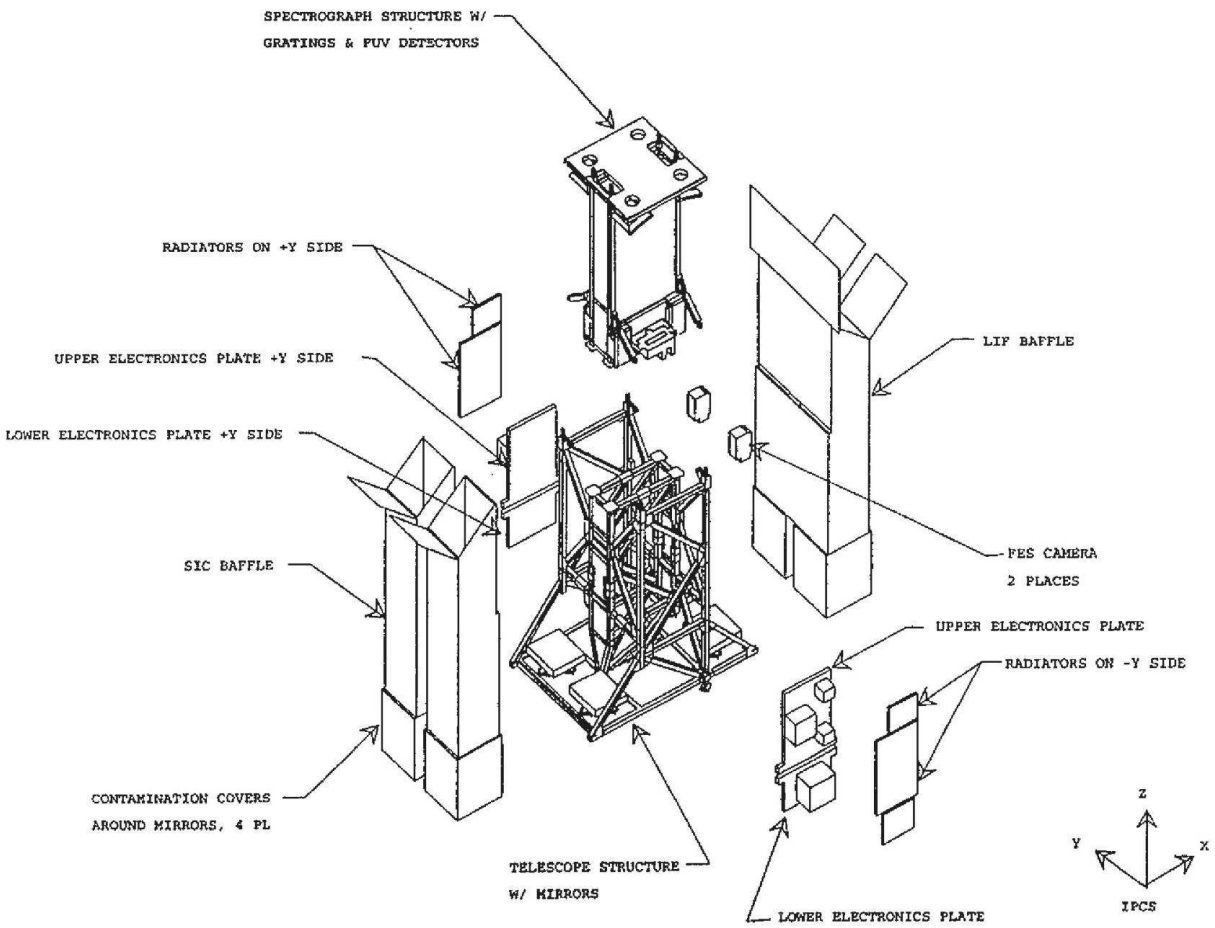

Fig. 3.3. 'Exploded-view' diagram of the FUSE instrument showing the spatial relationships between its mirrors, gratings and detectors; courtesy of the FUSE website: http://archive.stsci.edu/fuse/instrumenthandbook/

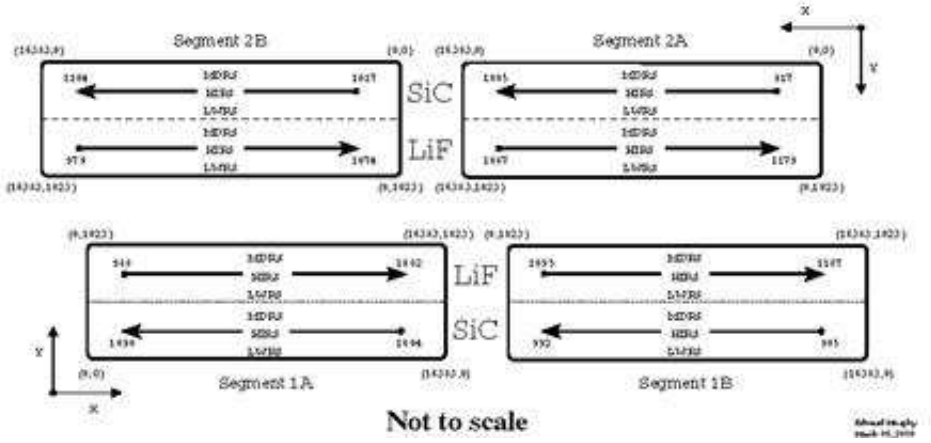

Fig. 3.4. Diagram of the four FUSE detectors indicating their wavelength-dependent arrangement of lithium fluoride and silicon carbide coatings, also courtesy of the FUSE website: http://archive.stsci.edu/fuse/instrumenthandbook/

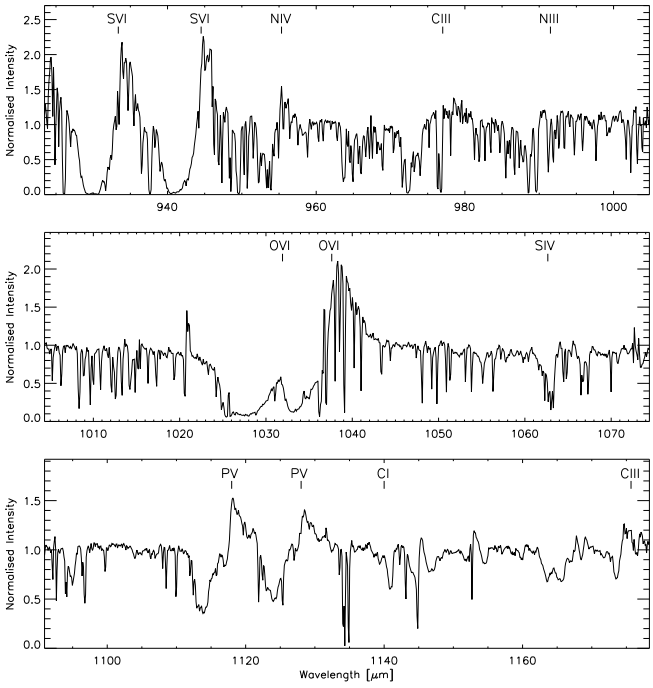

Fig. 3.5. Mean FUSE spectrum of the central star in NGC 6543 taken from the F034 run in January 2007.

3.3 Evidence of Variability

Of the wind lines present within the spectral range afforded by the FUSE data, the P V line appears as a well-developed but crucially *un-saturated* P Cygni profile, and therefore will prove to be the primary diagnostic of the fast wind's physical parameters as well as the prime demonstrator of its variability.

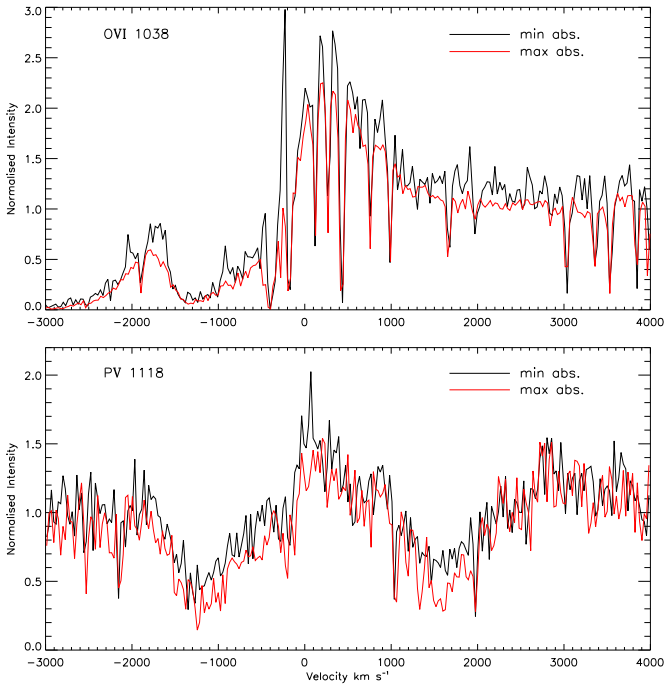

Fig. 3.6. The maximum fluctuation in the P V λ 1117.98 resonance line compared with the more stable low velocity regions of O VI λ 1037.62.

The optically-thick O VI shows minimal variation, but P V shows definite signs of significant variability, the most significant of which occurs between ~ -500 and -1300 km s^{-1} in the blue component, $\lambda_0 = 1117.98$ Å; the red component show variability above the 95 % confidence line bewteen -250 and -1375 km s^{-1}. $\lambda_0 = 1128.01$ Å. The equivalent width of the line is not conserved and varies from as low as ~ 0.3 to $\sim$1.7 Å, giving a mean equivalent width of $\sim$0.8 Å (s.d. of $\sim$0.8 Å), as measured between 1110.5 and 1121.8 Å in the blueward part of the P V doublet, that is to say a variation of $\sim$120%; likewise in the red component the EW also fluctuates, the absorption trough varying between 1.13 and 1.83 Å (mean of 1.47 Å, s.d. of 0.12 Å), the strong emission peak varying between 0.48 and 1.85 Å (a mean of 0.99 Å, s.d. 0.22 Å).

In contrast, the TVS spectrum of the O VI line shows little temporal activity, and the regions wherein P V shows the greatest variance, in O VI the fluctuations in the absorption are minimal at best, with the equivalents widths ranging between ∼8.7 to ∼10.7 Å with a mean of ∼10.2 Å (and s.d. of ∼0.4 Å) as measured between 1021.2 and 1037.2 Å, indicating a variation of no more than 15%, merely an eighth of the variability of the P V resonance line, and would be difficult to quantify due to the highly saturated nature of the absorption.

The application of TVS to time-series of select absorption lines provides further evidence of which of the wind lines possess the greater variability and therefore warrant further investigation. The result of such an analysis are presented below.

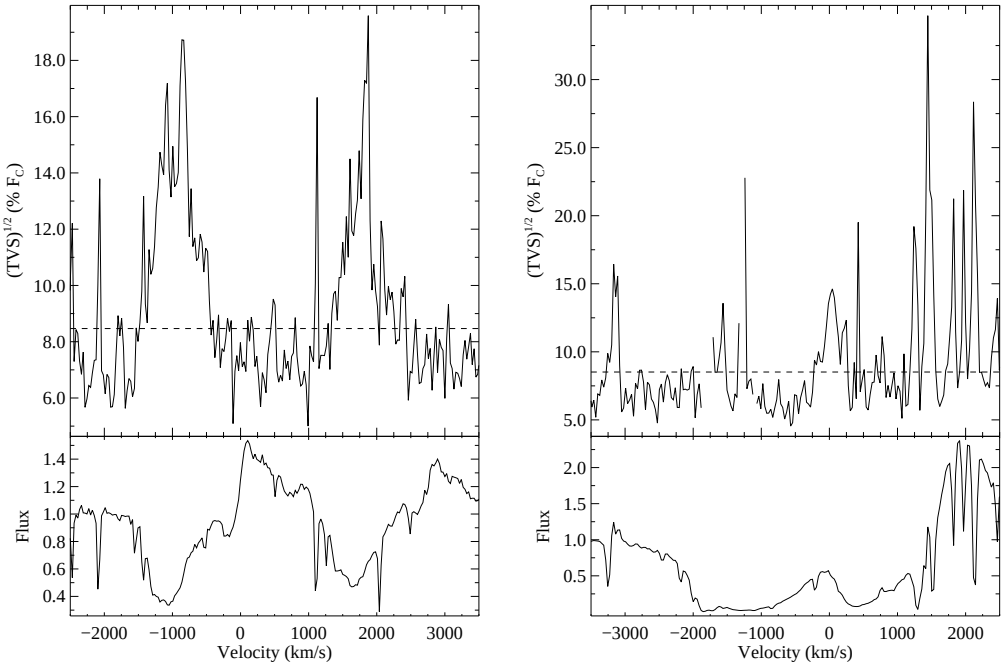

Fig. 3.7. Time Variance Spectra (TVS) of the two most developed P Cygni absorption doublets from the F034 time-series spectra: the well-developed but unsaturated P V $\lambda\lambda$ 1117.98,1128.01 doublet (left) is clearly strongly variable across both the blue and red absorption troughs of the doublet, showing broad peaks above the dotted 95% confidence line; in contrast, the highly saturated O VI $\lambda\lambda$ 1032.97,1038.93 doublet (right) shows a negligible TVS response

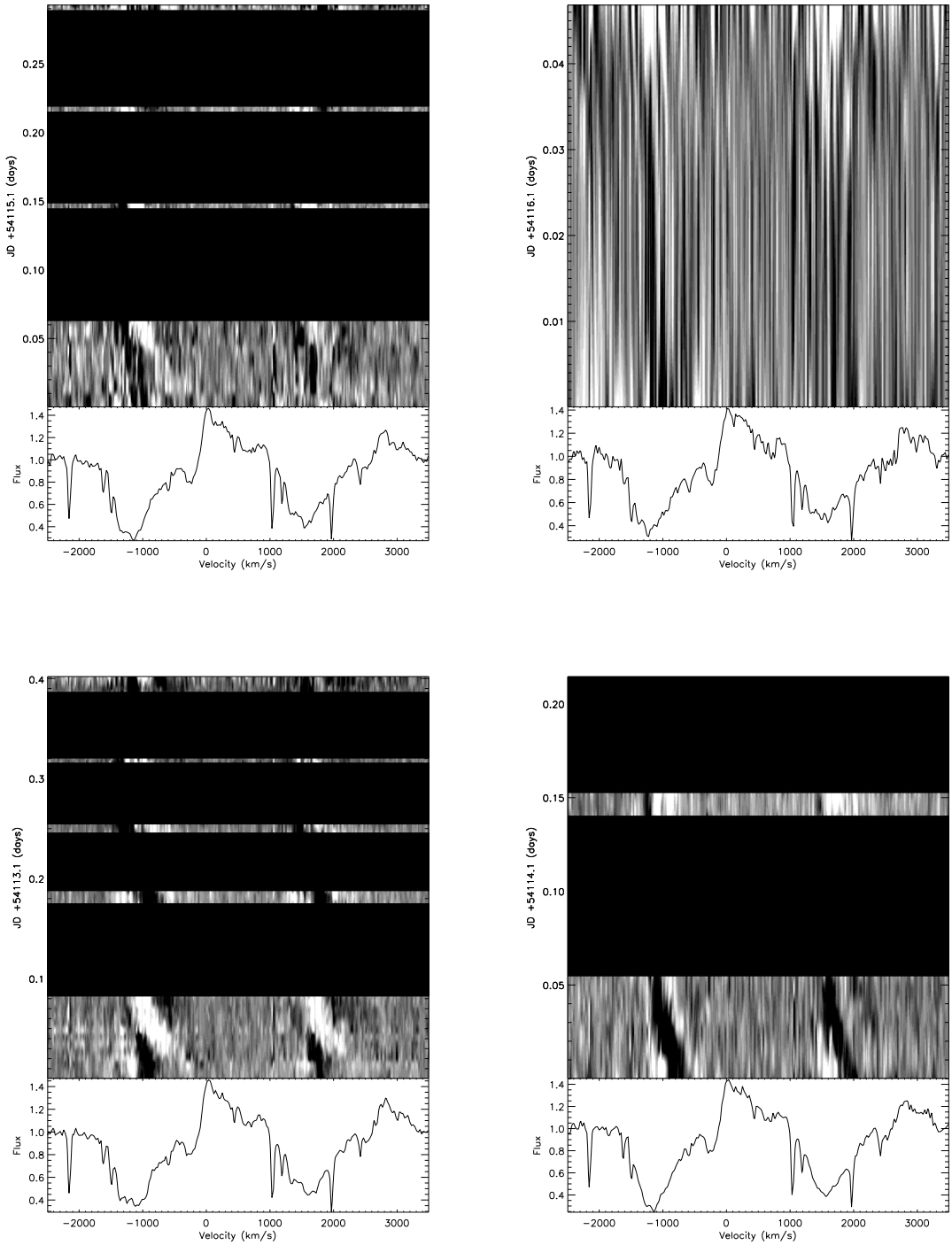

Fig. 3.8. Greyscale images of the four nights' optical spectra (2alif section) from the F034 observation. These are displayed left to right and bottom to top as the the individual greyscale images chronologically proceed from the bottom of the image upwards: 13^{th}, 14^{th} January shown bottom left, right; 15^{th}, 16^{th} January shown top left, right.

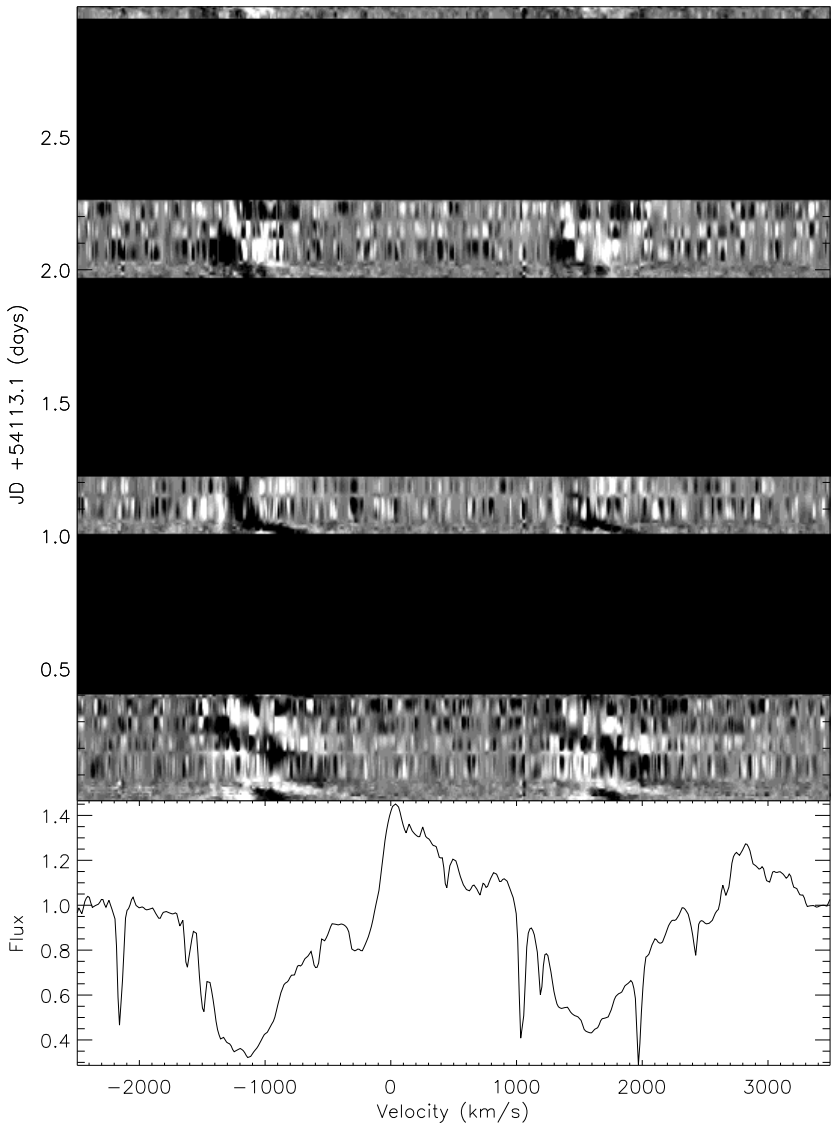

Fig. 3.9. A single greyscale image of the 2alif section spectra of the entire F034 data. Using this singular format, it is easier to observe the cyclic behaviour of the DACs present in the P v doublet.

3.3.1 Discrete Absorption Components

Discrete Absorption Components – referred to throughout this thesis and in the literature as *DACs* – are regions within the confines of an absorption trough of a stellar wind P Cygni line profile and are often found in the spectra of OB stars (Fullerton et al. 2006*b*) where there is a localised enhancement of the optical depth. Through time-series analysis these can be seen to migrate within the resonance line, slowly accelerating with regards to the flow of the wind.

It has been observed in a number of studies of time-series spectra from OB stars that – within the absorption trough of a given P Cygni profile – an 'additional' absorption feature appears at $\sim 0.5\ v_\infty$but has been observed to appear at $\leq 0.3\ v_\infty$ (Prinja et al. 2002). This feature then migrates blueward over several hours or days through the absorption trough, narrowing (in velocity width) as it does so (Cranmer & Owocki 1996). It has also been suggested through further study of time-series IUE data that a connection existed between the periodic appearance of these features and their acceleration and the projected rotation velocity of the star, $v_e sin(i)$ (Prinja 1988).

For an expanding wind the radial optical depth at any position is given by the Sobolev approximation:

$$\tau_{\rm rad}(v) \propto q_{\rm i}\rho \left(\frac{dv}{dr}\right)^{-1} \tag{3.1}$$

(Fullerton et al. 2006*b*)
These enhancements can be achieved by increasing the local ionisation fraction, $q_{\rm i}$, increasing the local wind density, ρ, or by reducing – *flattening* – the local velocity gradient, dv/dr, or by a combination of these inter-related factors.

Using time series spectra taken by the FUSE satellite the appearance of DACs can be observed and the behaviour of different DACs appearing with the resonance profiles of different ions can be studied. It can be shown through time-series greyscale images that the appearances of the DACs repeat in a cyclic manner with a recurrence period of the order of rotation, and in studies of ion doublets, e.g. P V and S IV , the recurrences are in phase. It has also been noted that, as well as in the resonance profiles of the dominant ions, DACs also appear in the profiles of adjacent ions (e.g. P IV , S IV , S VI), and also in trace ions such as O VI .

However, the DAC amplitudes are weaker in the dominant ions and stronger in the profiles of weaker species. This discrepancy in strength between the dominant and less so species would seem to indicate that the velocity gradient cannot be seen as the main cause of the occurrence of DACs, nor can local density enhancements. Also since the DACs can be seen to propagate in phase between different ionisation stages: dominant, weaker, or even in super ions (e.g. S IV , S VI), this would suggest that changes in ionisation levels again cannot be the sole cause of their appearance.

Therefore, instead of the cause being any single parameter of the radial optical depth, $\tau_{\rm rad}(v)$, a DAC's occurrence must be due to a combination of the different factors.

Such a mechanism could be a localised flattening of the velocity gradient, as has been observed via hydrodynamic modelling of *Co-Rotating Interaction Regions (CIRs)* (Cranmer & Owocki 1996), caused initially by localised increases, or decreases, in the radiative force resulting in a bright, or dark, spot near a star's equator. Bright spots generate high-density but slow moving streams, and dark spots provide lower-density but fast moving streams. The CIRs are produced when faster moving material catches up with slower moving material: the leading edge of a fast-moving streams catches up with a slower moving stream, the interaction between the two may steepen into a shocked region. The unperturbed super sonic wind then obliquely impacts upon the CIR, resulting in a "sharp propagating discontinuity" (C & O 1996): a plateau, and where there is a flattening of the velocity gradient there is also an increase in density at similar velocities, but different spatial locations. The fluctuations in density combined with changes in dv/dr result in small variations in the absorption profiles of excited transitions and dominant ions. However, as recombination preferentially increases the abundance of lower ions then DACs are fractionally stronger within them.

A method, somewhat akin to that used by Patriarchi & Perinotto (1997), can be utilised in order to better locate and measure the progression of the DACs as they move through the wind. For each spectral sequence a mean spectrum is created and then this mean is divided into each of the individual spectra in that particular sequence. The aim of this procedure is to produce a second sequence of mean-rectified spectra in which all deviations from the continuum value of unity denote regions where there is a significant deviation from the mean: in this way the appearance of a DAC will be highlighted by a region lower than the continuum, and which, as the sequence progresses, will move further left just as the DAC will travel blueward in the UV time-series spectra as it moves outward

through the wind.

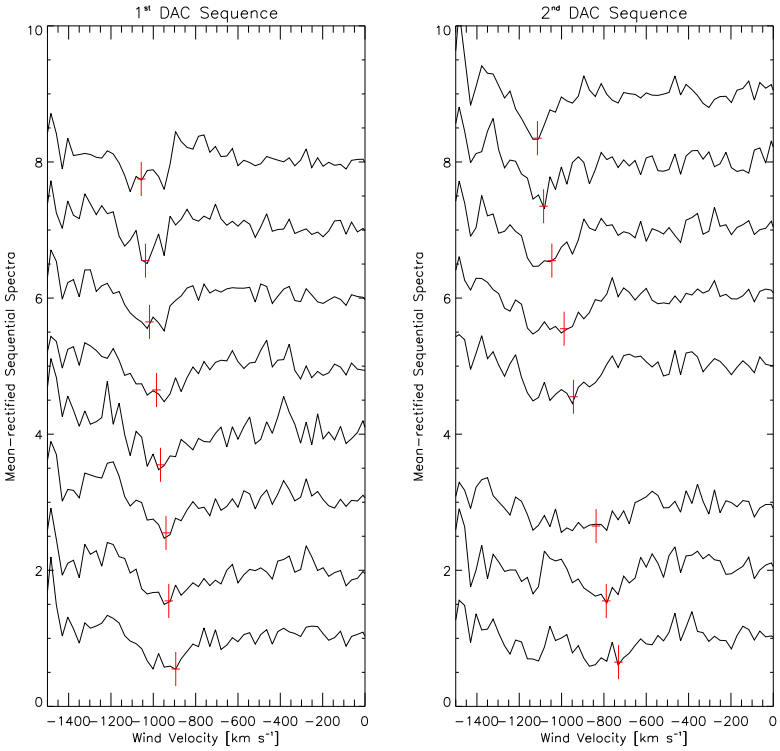

Fig. 3.10. A pair of multi-stacked mean-rectified spectra showing the velocity-space fluctuations from the mean 2alif spectra of the two DAC sequences – this method allows for easier identification of the progression of the DACs through the sequences. The central velocity of each individual blueward DAC is marked with a red tick – this is the position of the individual velocity measurements taken in order to estimate the acceleration of the DAC through the wind.

In Figure 3.10 the two mean-rectified sequences are shown and the progressions of the two significant absorption regions, one in each sequence, and denoted by a red tick mark where the central velocity of each sequential DAC has been estimated. The subsequent velocity measurements can be combined with each corresponding Julian date as set of data coordinates of centralised velocity vs. time, which can then be plotted. The coordinates can also be entered into a least-squares algorithm which will calculate the gradient and y-axis intercept for a least-squares fit through the plotted data – the gradient therefore representing an approximation of the average acceleration of the DAC through the narrow velocity range of its appearance in the greyscale images as it moves through the stellar

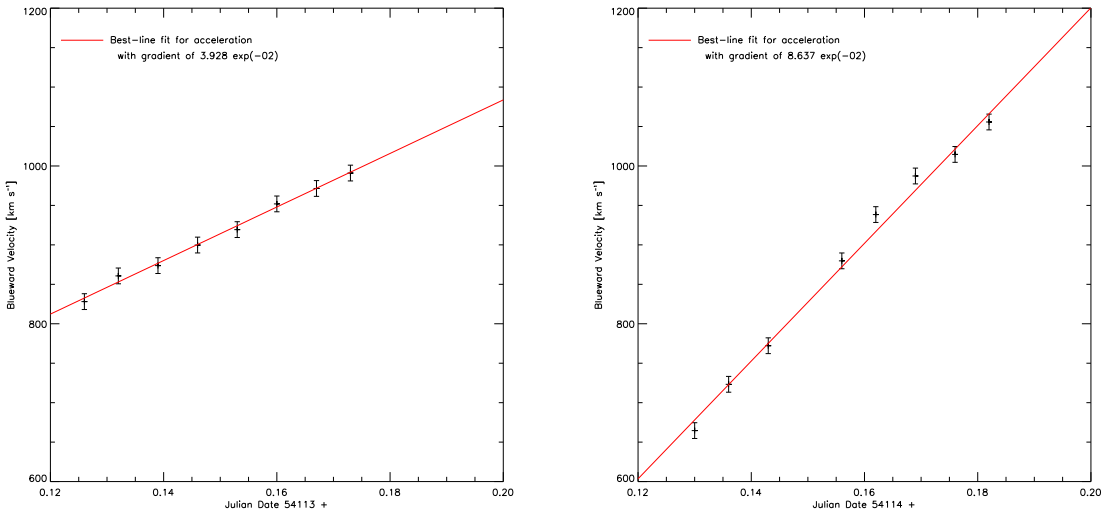

Fig. 3.11. Plotted progressive velocity tracks of two DAC sequences, each overplotted with a least-squares fit of the resultant acceleration.

wind. The first sequence, taken from the first night's data, indicates an acceleration of approximately 3×10^{-3} km s^{-2}; the second sequence, taken from the second night's data, indicating an acceleration of approximately 8×10^{-3} km s^{-2}. The error margin for both is $\sim 10\%$.

3.4 Modulated or Cyclical Behaviour

The behaviour of DACs in OB stars has been demonstrated in several case studies (Massa et al. 1995; Kaper et al. 1996; Fullerton et al. 1997; de Jong et al. 2001; Prinja et al. 2002): these are modulated and may related to the rotation period of the stellar wind source star. A similar study of wind variability is therefore of interest in that emanating from the central star of NGC 6543. In particular the optical depth changes, as mentioned above in terms of maximum and minimum values, may also exhibit a cyclic behaviour.

In order to try to uncover any inherent cyclic behaviour the time-series spectra are submitted to a Fourier-based periodogram analysis to uncover the quantitative nature of any repetitive behaviour. The Fourier method involved utilises the CLEAN algorithm (Roberts et al. 1987), as described in Chapter 2, to diminish false frequency signatures as might evolve from the underlying noise, as well as aiming to eliminate as much as possible the window function – the duration period of the nightly observations which, due to the repetitive nature of the observing run, might imprint itself upon the resultant frequency power spectrum.

To this end a gain of 0.5 over 200 iterations was undertaken of a select velocity range of the time-series, in the blueward wind velocity between -600 to -1100 $\mathrm{km\,s^{-1}}$ which is approximately the extent of the range of the selected DACs as seen in the greyscale images.

The resulting power spectrum shows a number of peaks across a frequencies range of between 0 and the maximum frequency (as inputted as a parameter in the Fourier algorithm) of 20 cycles per day – see Figure 3.12. However there appears a strong power peak at 5.8125 cycles per day – corresponding to a period of ~ 0.172 d, or ~ 4.129 h (4 hours 8 minutes) – see Figure 3.13. A subsequent greyscale image of the P V wavelength ranged, phased to a period of 0.172 d illustrates this repetitive modulation over three cycles, and this is shown in Figure 3.14. There does appear to be some coherence between this period value and the DAC progression within the wind across the estimated range of -600 to -1400 $\mathrm{km\,s^{-1}}$.

IUE data, which is the following section provides a measure of the terminal wind velocity for the SEI line profile fitting programme, can also be used as an alternative source of evidence of line variability, given a sufficient number of exposures. Taking *low resolution* IUE spectra – where R $\sim$ 300 – from the ESA archive, where a sequence of 39

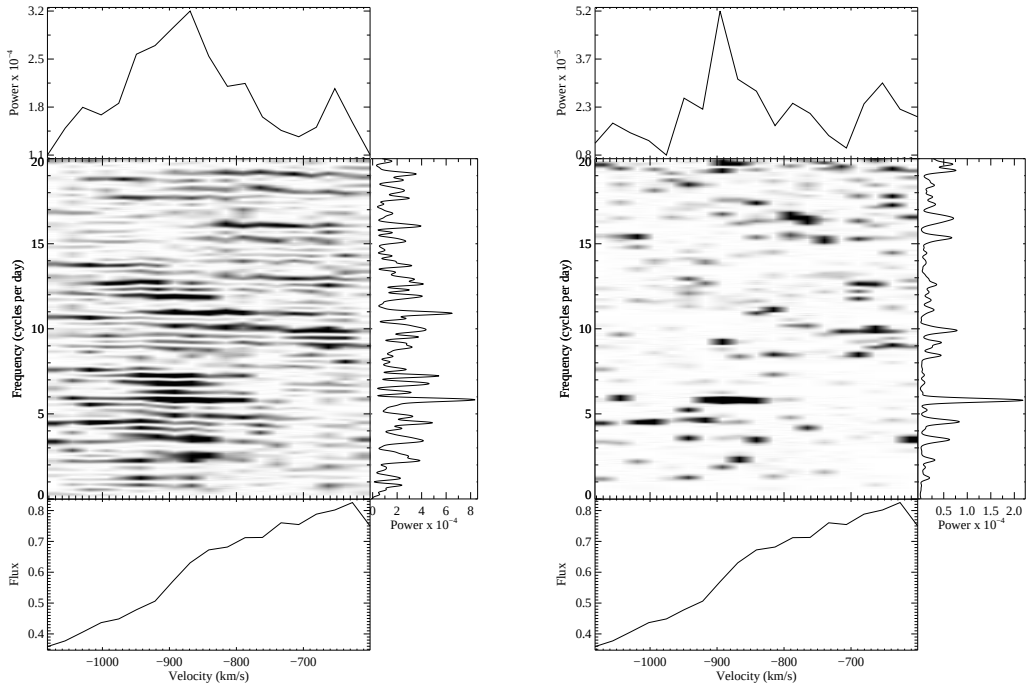

Fig. 3.12. Full-panel displays of Fourier-based frequency analysis of the blue trough of the P V doublet, as seen in the F034 spectra, analysed between −600 – −1100 km s^{-1}, with the 'dirty' analysis on the left, and the 'clean' analysis (gain = 0.500) on the right.

exposures, SWP54865 to SWP54961, taken over 4.2 days, these spectra show a significant level of variability in the blue wing of the C IV line, even though the line is quite saturated.

The variance of the C IV line is shown in Figure 3.15, and there appears to be something of a double peak in the TVS of the absorption part of the P Cygni profile as well as a third peak on the red emission side. Taking the range −1000 – −2000 km s^{-1} as probably covering the fluctuations in the extreme blue edge of the absorption, the 39 spectra are passed through the time-series Fourier (CLEAN) analysis to try an uncover an underlying periodicity in the variance.

3.5 Line Synthesis & Optical Depths

The physical properties of the DACs present within a stellar wind can be estimated through the use of the SEI absorption profile modelling method. As detailed in Chapter 2, the radial optical depth of the profile is treated as 21 independent velocity bins (each ~ 0.05 v_∞ wide) in order to provide a flexible means by which to match absorption optical depths

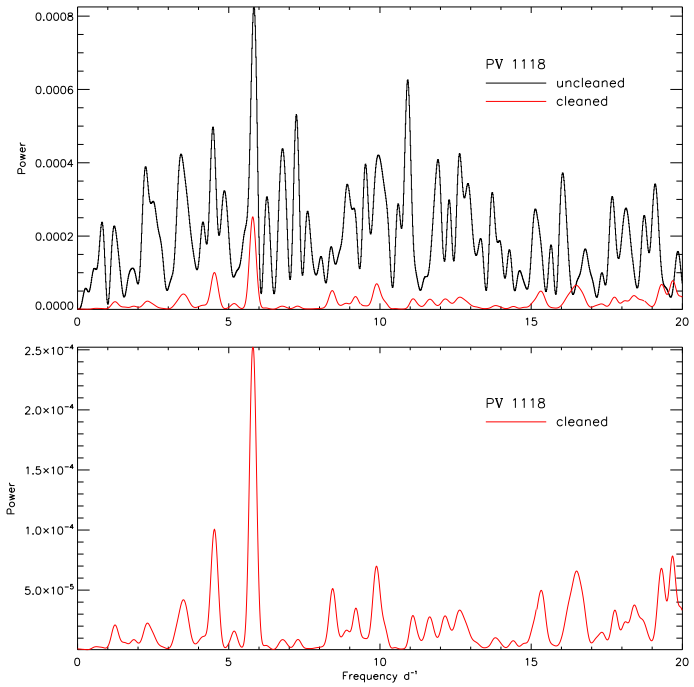

Fig. 3.13. Extracted power spectrum output of a Fourier-based frequency analysis of the F034 spectra, analysed between -600 to -1000 km s^{-1}(the velocity range across which the DACs appear to traverse): the top panel shows the power spectra derived from the 'dirty' analysis in black, with the 'cleaned' analysis (gain = 0.500) superimposed in red; the bottom panel shows the cleaned analysis on its own in red, with the highest peak indicating a strongest signal occurring at $\sim$ 5.8125 cycles per day.

in a structured wind affected by variable features such a DACs. The method assumes a standard parametrised velocity law:

$$w = w_0 + (1 - w_0)(1 - 1/x)^{\beta} \tag{3.2}$$

where $w = v/v_\infty$ and $x = r/R_\star$ i.e. the parametrised wind velocity and radial distance.

The presence of the initial photospheric spectrum in the SEI profile is approximated by a Gaussian of $FWHM = 200$ km s^{-1}: this has the effect of improving the line fit at the lower radial velocity end ($\leq 0.2\ v_\infty$) of the absorption profile under investigation, here P v . The dimensions of the input photospheric Gaussian, for the specific ion being modelled in SEI, are derived from the corresponding photospheric line profile taken from the a specific

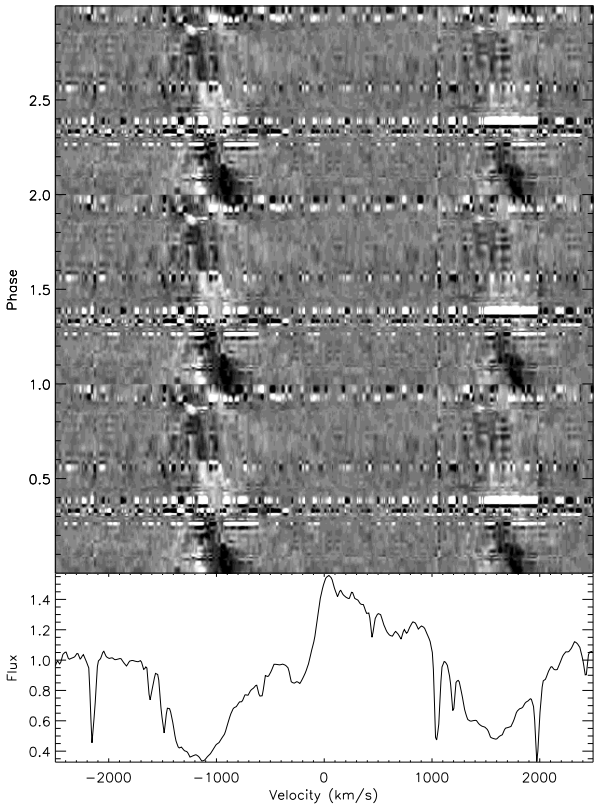

Fig. 3.14. Greyscale representation of the F034 P v doublet folded over a period of 0.172 days – here displayed over three cycles.

photospheric spectrum chosen from the TLUSTY model grid; the specific spectrum chosen for the parameters of $T_{\rm eff}$ and $\log g$ closest to those of the object being modelled, in this case NGC 6543, for which the grid spectrum for $T_{\rm eff}$= 55,000 K and $\log g = 4.00$ is chosen as being the closest approximate photospheric model for the corresponding parameters of NGC 6543: $T_{\rm eff}$ = 63,000 K, $\log g$ = 4.2 (Georgiev et al. 2006). The chosen TLUSTY grid model spectrum is then fed into a simple algorithm, ROTIN3, which rotationally-broadens a user-specified wavelength range about the central wavelength of ion intended for modelling (e.g. P v λ 1118); the subsequent rotationally broadened range is then outputted as a simple ASCII file which can then be fed into DIPSO, and thence the optical depth and velocity FWHM can be measured and these dimensions then applied as the SEI photospheric input parameters.

The model fit for the mean P v profile is shown to have a very good fit with parameters:

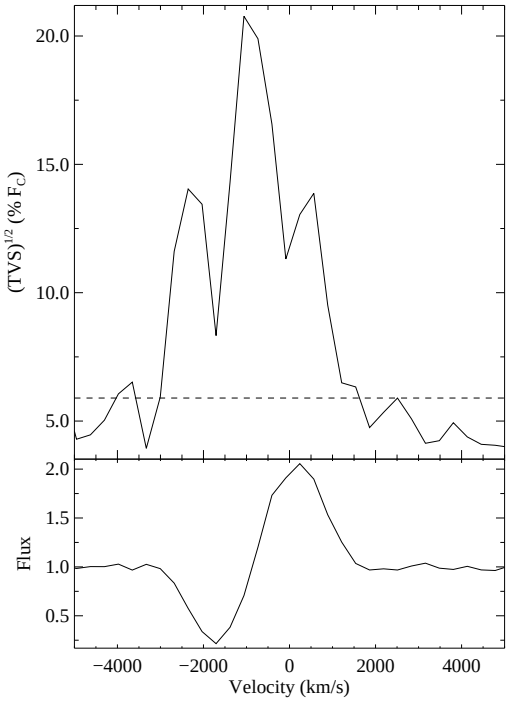

Fig. 3.15. TVS analysis of IUE data of the C IV $\lambda\lambda\,1548, 1550$ doublet – note the double/triple nature of the variability response.

v_∞= 1400 km s^{-1}, and $v_{\rm turb}$ (the small scale (turbulent) velocity dispersion parameter) = 0.05. Although an earlier SEI modelling had been undertaken with a velocity acceleration factor of $\beta = 1.0$ (Prinja et al. 2007), in the modelling undertaken for this thesis it was found that a revised factor of $\beta = 1.25$ provided a better overall fit, while not necessarily making much difference to the absorption profile fit, the increased factor gave a better fit to the redward emission part of the profile.

The values derived for the average $\dot{M}q(\mathrm{P}^{4+})$ – measured between 0.2 and 0.9 v_∞ – for the mean spectra of each night of the observing run, as well as an overall 'average' measure, for the entire observation, are listed in Table 3.5.

It should be noted however that the SEI modelling code assumes a spherically-symmetric wind, and as such, the models often predict excess forward-scattered emission in the low velocity part of the absorption trough, that is below 0.25v_∞, and so, for NGC 6543 with v_∞ = 1400 km s^{-1}, the model fit below $\sim$ 350 km s^{-1} cannot be relied upon. This excessive prediction is inherent in the code as one attempts to model higher velocity absorption by increasing the optical depth, thereby reducing the transmitted flux of the more blueward velocity bins; then the model compensates by increasing the forward scattered component

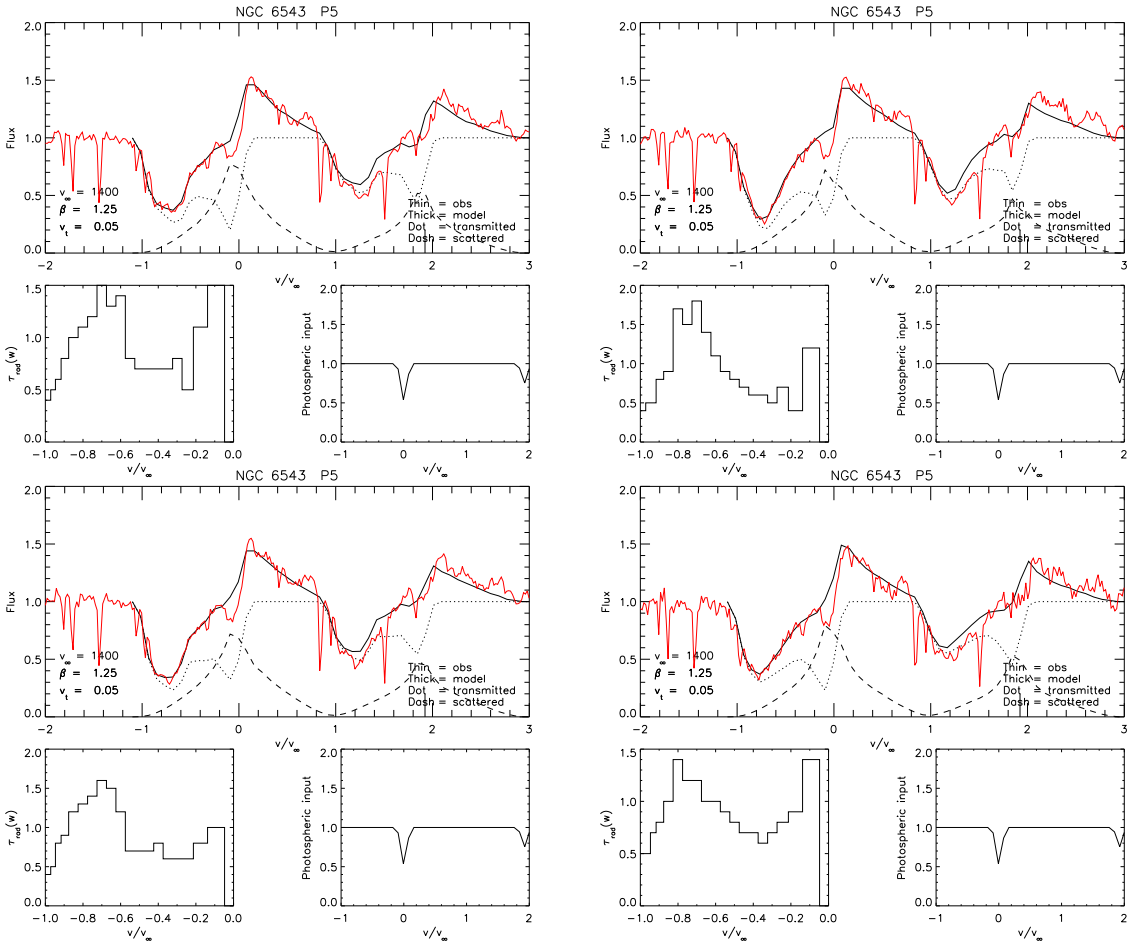

Fig. 3.16. SEI fits to the mean P v resonance profiles of the 4 consecutive nights of the F034 run: 13^{th}, 14^{th} January 2007, top left, right; 15^{th}, 16^{th} January 2007, bottom left, right.

at lower velocities (Massa et al. 2003). There may come a time when the model thereby predicts more scattered light than is observed in the spectrum, then even if one attempts to increase the optical depths of the lower velocity bins – even by some arbitrarily large optical depths far greater than those assigned to the higher velocity end – the low-velocity part of the profile will not deepen. Unfortunately the scale of the excess scattering has a correlation with the line strength and so is prevalent in deeper absorption lines, particularly strongly saturated ones. A readjustment of depth and FWHM width of the inputted photospheric ion profile may be attempted, but then there is the risk of introducing dimensions which cannot be adequately wind-rectified in the subsequent P Cygni profile. Therefore the validity of the SEI model assumptions has to be questioned, particularly the fundamental assumption of a spherically symmetrical wind and its apparent homogeneity (Massa et al. 2003).

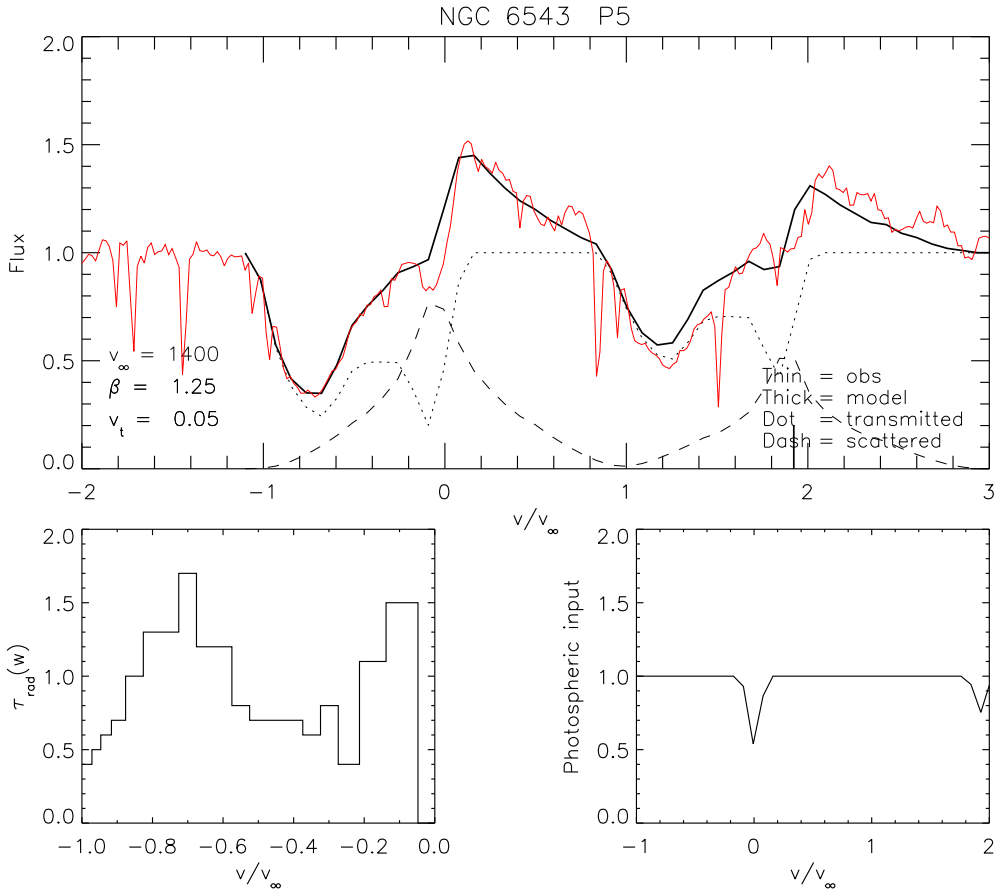

Fig. 3.17. SEI model fit of the mean spectrum from the F034 observation.

As well as the spherically symmetric models predicting too much low velocity scattering, the inability of the model to match the shape of the observed profile may reflect an unaccounted-for 'clumpiness' in the wind. An inhomogeneous, 'clumped' wind would lead to the derivation of low ionisation fractions – such as those obtained for B supergiants (Prinja et al. 2002). Also, if the wind if actually composed of dense clumped regions separated by less dense spaces, then each constant velocity surface will not fully contribute to the emission, and similarly the surface of the star will not be completely covered by optically thick material: in fact it would be relatively porous. This would lead to the absorption regions would not be very deep – appearing less deep than in reality – thus appearing less saturated than they should. When fitting the apparent absorption profile, the optical depths, and subsequent $\dot{M}q$ values assumed, would not be optically as deep as if the wind was homogeneous (Oskinova et al. 2007).

Table 3.5. NGC 6543 F034 $\dot{M}q$ results

Obs. ID	UT Date	MJD (start)	Minimum $M_\odot\,\mathrm{yr}^{-1}$	Maximum $M_\odot\,\mathrm{yr}^{-1}$	Av.$(0.2 - 0.9v_\infty)$ $M_\odot\,\mathrm{yr}^{-1}$
05	2007-01-13	54113.1260	1.1e-09	1.2e-08	5.5e-09
06	2007-01-14	54114.1097	1.4e-09	1.5e-08	5.9e-09
07	2007-01-15	54115.0933	1.3e-09	1.2e-08	5.8e-09
08	2007-01-16	54116.0680	1.8e-09	1.3e-08	5.3e-09
Mean	–	–	9.0e-10	1.3e-08	5.5e-09

3.5.1 Errors Inherent in SEI $\dot{M}q_i(w)$ Calculations

As detailed in Chapter 2, the SEI code calculates a velocity dependent mass-loss rate-ionisation fraction product, $\dot{M}q(w)$, as well as also providing an average $\dot{M}q$ figure as integrated between 0.2 and 0.9 of the normalised velocity function, w, thus:

$$\dot{M}q_i(w) = \frac{m_e c}{\pi e^2}\frac{4\pi\mu m_H}{f\lambda_0 A_E} R_\star v_\infty^2 x^2 w \frac{dw}{dx}\tau_{rad}(w), \tag{3.3}$$

and therefore, in simplifying the above equation the $\dot{M}q$ value obtained can be simply expressed as a proportionality relation with the essential parameters used by SEI in order to calculate the $\dot{M}q$, thus:

$$\dot{M}q_i(w) \propto R_\star v_\infty^2 \frac{dw}{dx}\tau_{rad}(w), \tag{3.4}$$

Temperature of stars are usually given to the nearest thousand degrees Kelvin and so, with temperatures ranging between $\sim$ 30,000 and $\sim$ 45,000 K, the largest fractional error margin can be approximated to 1000/30000 i.e $\sim$3%; similarly error margins of luminosity can be estimated at being around the 10% mark. Therefore in combining the error fractions of both luminosity and temperature to derive an error for stellar radius, the resulting percentage error for the stellar radius is $\sim$6%. The terminal velocity as measured via the blue edge of staurated P Cygni profiles can be derived to within $\pm$50 $\mathrm{km\,s^{-1}}$, therefore for wind speeds in the range of -500 – -1500 $\mathrm{km\,s^{-1}}$ the greatest error margin is of the order of 10%.

As well as these error margin estimates of the SEI code input parameters, there are also

the more manually-based errors of manipulation inherent in the modelling of the profiles themselves.

The error calculation corresponding to the simpler proportionality relation of $\dot{M}q$ given above in Equation 3.4, is as follows:

$$\left(\frac{\Delta\dot{M}q}{\dot{M}q}\right)^2 = \left(\frac{\Delta R_\star}{R_\star}\right)^2 + 2\left(\frac{\Delta v_\infty}{v_\infty}\right)^2 + \left(\frac{\Delta\beta}{\beta}\right)^2 + \left(\frac{\Delta\tau_{\rm rad}}{\tau_{\rm rad}}\right)^2 \tag{3.5}$$

where the error in the stellar radius, $\Delta R_\star$, is derived from the errors of L and $T_{\rm eff}$, as SEI uses the input parameters of luminosity and stellar effective temperature to calculate the subsequent stellar radius. From the stellar luminosity-temperature relationship:

$$L_\star = 4\pi {R_\star}^2 \sigma {T_{\rm eff}}^4 \Longleftrightarrow R_\star = \sqrt{(L_\star/(4\pi\sigma {T_{\rm eff}}^4))} \tag{3.6}$$

and hence the subsequent error in the stellar radius can be derived:

$$\left(\frac{\Delta R_\star}{R_\star}\right)^2 = \frac{1}{2}\left[\left(\frac{\Delta L_\star}{L_\star}\right)^2 + 4\left(\frac{\Delta T_{\rm eff}}{T_{\rm eff}}\right)^2\right] \tag{3.7}$$

As the SEI modelling procedure is able to match the overall morphology of the P V absorption profile, through the normalised velocity bin-by-bin adjustment of optical depths, it therefore allows one to model profiles from individual exposures. Consequently, it has been possible to match the P V absorption profiles for a couple of sequences of individual spectra from the F034 dataset, namely the spectra of exposures F03401050012 to F03401050082 (1^{st} night) and from F03401060042 to F03401060122 (2^{nd} night): these sequences correspond to the appearance and migration of the DAC-like features as shown in the lower panels of Figure 3.16. The variation in the fits to these spectra is due to the occurrences of DACs, and therefore can be compared to a non-DAC spectrum (such as the profile of F03401080072) which provides a representation of a maximum flux/minimum absorption over most velocities (i.e. between 0.0 and 1.0 v_∞).

The SEI fits to these two spectral sequences are shown in Figure 3.18 where it is ably depicted that the manipulation of the individual velocity bin's optical depth, in order to match the varying morphology of an absorption profile as it were frame by frame, is a

excellent means by which one can demonstrate that the wind profiles of CSPNs (as with OB stars) can be structurally distorted by such DAC-like features migrating through the wind.

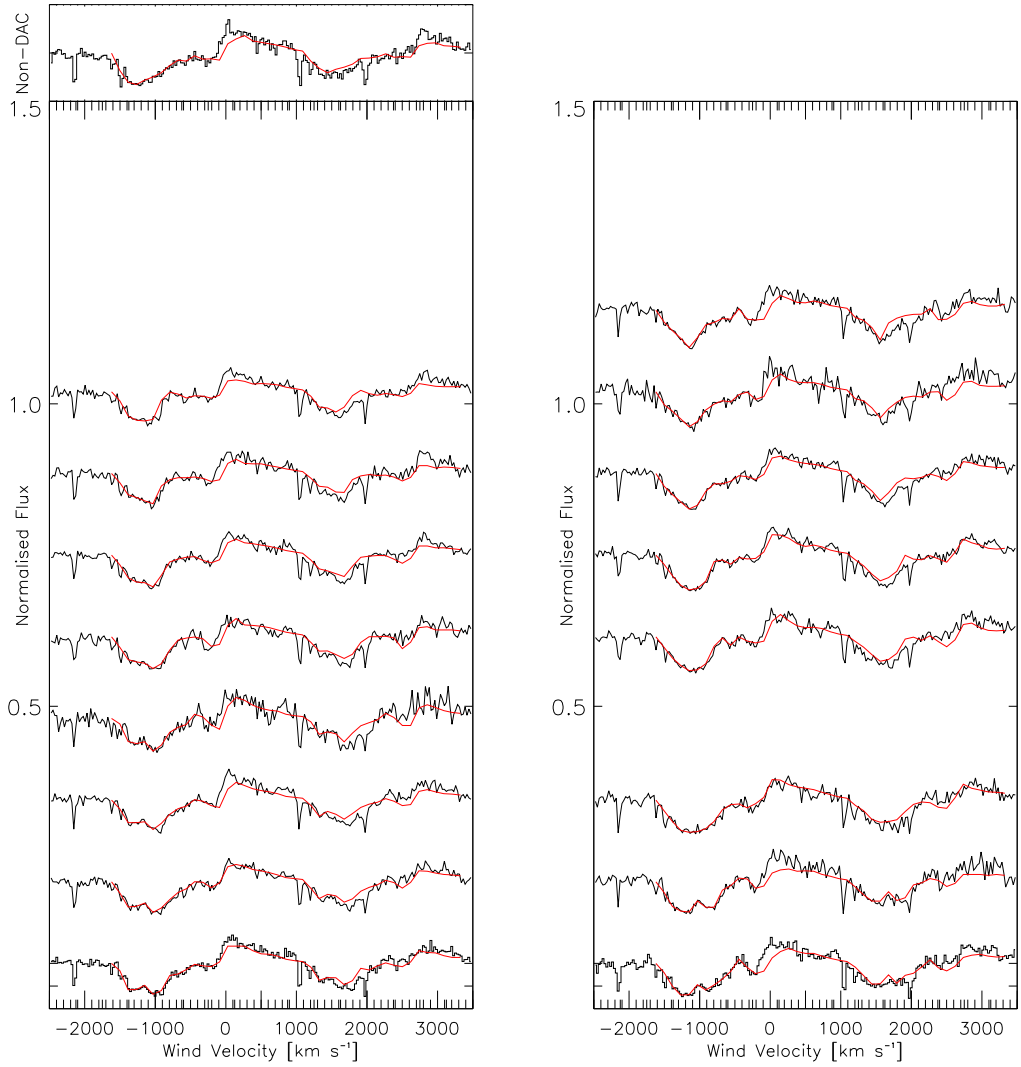

Fig. 3.18. A pair of multi-stacked spectra showing the velocity-space progression of P V doublet DACs for two sequences.

From these SEI model sequences one is then able to extract optical depths at specific velocity of these migrating DACs (as described in Section 3.3, and illustrated in Figures 3.8 and 3.9), and therefore examine the variation and progress through the wind of optical depth features at their migrating central velocities. These central velocity-localised DAC

optical depths can also be 'normalised' by dividing each within the sequence by the corresponding optical depth in the non-DAC case. The resulting ratios of τ_{DAC}/τ_{min} from the two sequences can be plotted as a function of normalised velocity, w, as illustrated in Figure 3.19. This plot shows how the optical depth ratio for the two independent sequences develops as the DACs move through the wind. In each case the ratio increases from ∼1.5 to a maximum of ∼4.0 at around 0.6 v_∞ and then drops down to ∼1.0 at around 0.7 v_∞. It them seemingly begins to increase a second time toward 0.8 v_∞ before the DAC(s) fade out.

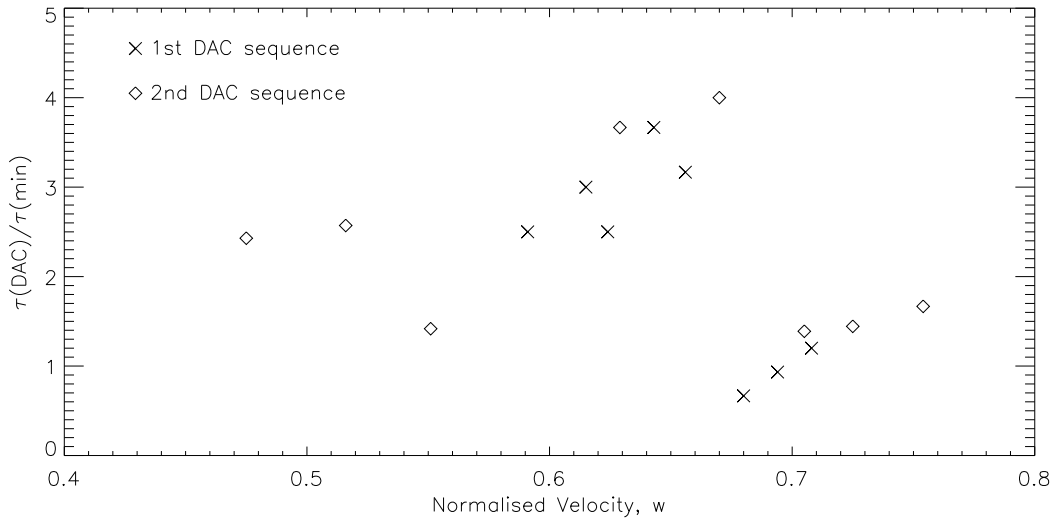

Fig. 3.19. Plot showing the changes of the radial optical depth ratios, τ_{DAC}/τ_{min}, for the two DAC sequences.

3.5.2 The Case for Clumping via CMFGEN

A better insight into the effects of a clumpier structure to the wind can be gained via the unified atmosphere code CMFGEN (Hillier & Miller 1998), which calculates non-LTE models of the entire stellar atmosphere from the photosphere right out to the extremities of the outflow of spherically-symmetric winds with multi-level ions.

Whereas TLUSTY assumes plane-parallel geometry in order to provide an accurate model of a fully line-blanketed photosphere, CMFGEN employs spherical-symmetry in order to extend the nLTE line-blanketed atmosphere into the stellar wind beyond. This unified-wind-atmosphere code was written by Hillier (1990) and later developed by Hillier & Miller (1998) whereupon the effects of iron species line blanketing were applied to the

original 1990 code.

The prime directive of the code is the solving of the radiative transfer equation for stars with a spherically-extended atmosphere outflow using the Sobolev approximation or the full solution of the co-moving-frame radiative transfer equation. The original iteration code takes a tridiagonal Newton-Raphson operator, which is based upon the complete linearisation method forwarded by Auer & Mihalas (1969), but without limitation upon the number of energy level transition it is able to deal with. In essence, a partial linearisation method is employed, not unlike that of the approximate lambda operator as seen in the TLUSTY methodology, with similar convergence. Like TLUSTY, the ultimate aim is the inclusion of a many blanketing lines as possible in the model while at the same time reducing the computations involved to a minimum; again as with the iterative TLUSTY lambda operators, radiative transfer in the lines is treated 'exactly' as no opacity redistribution or sampling techniques are used.

While extending the radiative transfer equation solutions into line-blanketing, the concept of (Anderson's) superlevels reduces the number of energy levels that need to be solved explicitly.

The populations of the superlevel ${}^{S}n$ are include in the solution of the rate equations; the population of an individual atomic level in the full model atom ${}^{F}n$ but which possess similar departure coefficients as their 'parent' superlevel.

$$\sum_{i}^{F} n_{ij} =^{S} n_j \tag{3.8}$$

$$\sum^{F} n^*_{ij} =^{S} n^*_j \tag{3.9}$$

where * denotes LTE population, ${}^{S}n_j$ is the population density of superlevel j and ${}^{F}n_{ij}$ is the population density of the full level i which is a member of the superlevel j.

$$b = \frac{{}^{F}n_{ij}}{{}^{F}n^*_{ij}} = \frac{{}^{S}n_j}{{}^{S}n^*_j} \tag{3.10}$$

The linearisations are performed by replacing ${}^{F}n_{ij}$ by:

$$^{F}n_{ij} =^{S} n_j \left(\frac{^{F}n^*_{ij}}{^{S}n^*_j} \right) \tag{3.11}$$

Here, $^{F}n_{ij}$ is temperature-dependent as it depends upon $^{F}n^*_{ij}/^{S}n^*_j$. Also using superlevels in this way extends LTE which assumes a single superlevel to describe all ionisation stages; in an nTLE environment each ionisation stage is represented by many levels.

However, in order to avoid the innumerable lines overlapping and merging near series limits, one of the improvements to the original 1990 code includes an approach similar to that of Hubeny et al. (1994) – adopting an occupation formalism probability of Hummer & Mihalas (1988) – is used, along with other opacity redistribution functions. The approach is the defining of a level occupation probability of w_i and that of a higher level is w_j: for transitions between state i and j the occupation probability for state j is assumed to be w_j/w_i as state i is undissolved; but if state i is dissolved then the occupation probability of state j goes to zero – this is because if the lower energy state is to be dissolved then the higher state must be also being closer to the continuum.

Other enhancements to the 1990 code include dealing with potential resonances in photo-ionisation cross sections, as well as the effects of such as regards Auger ionisations (see Hillier & Miller 1998 for details).

The code was run by Miguel Urbaneja (of the Institute for Astronomy, Hawai'i – obtained via private communication), using the fundamental parameters as listed in Table 3.1, with the addition of $\log g = 4.2$ and a He/H abundance ratio of 0.1 (e.g. Georgiev et al. 2006). A parametric treatment of wind clumping form part of the CMFGEN modelling: this is calculated via a volume filling factor f, defined as:

$$f = f_\infty + (1 - f_\infty) exp(-v/v_{cl}), \tag{3.12}$$

where v_{cl} is the velocity at which clumping starts – adopted as 35 $\mathrm{km\,s^{-1}}$ – above the sonic point. Although CMFGEN can be used to model the entire stellar atmosphere, the main issue for this investigation was to see the effects of clumping in CMFGEN models upon the fast wind of NGC 6543; and so fittings were limited to a few key lines and not the entire atmospheric spectra.

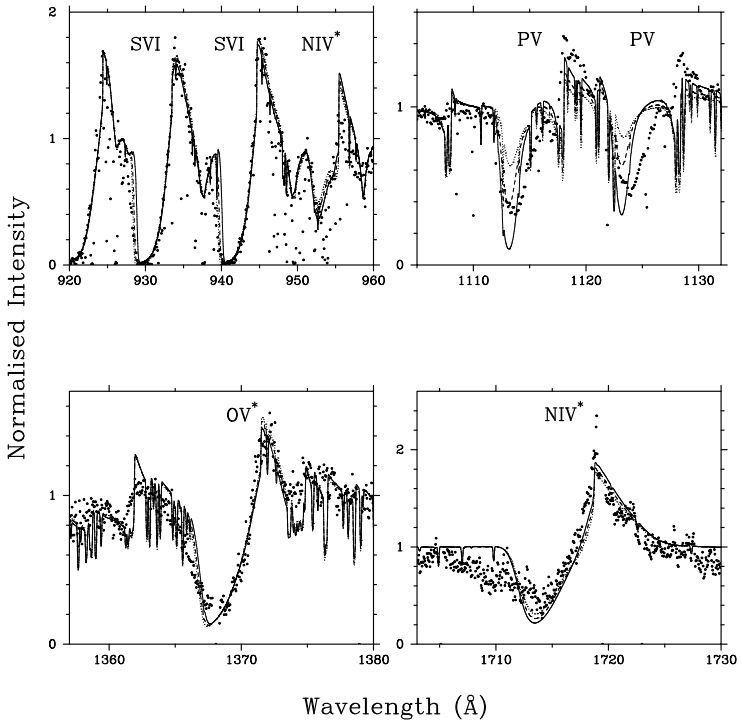

Fig. 3.20. CMFGEN model fits of key diagnostic lines for NGC 6543 are shown (from FUSE and high-resolution IUE spectra), where the superimposed models have filling-factors of $f_\infty = 0.06$ (solid line), 0.08 (dashed line), and 0.10 (dotted line). Courtesy of Miguel Urbaneja (via private communication).

A selection of models have been run with varying volume filling – "clumping" – factors, with $f_\infty = 0.06$, 0.08 and 0.10, and the resultant synthesised spectra then compared to a few key line profiles as detailed in FUSE and high-resolution IUE data of the central star, as shown in Figure 3.20. Taking a mass-loss rate of $6 \times 10^{-8} M_\odot\,\mathrm{yr}^{-1}$, the models show good overall fits to the observed resonance and excited line profiles, with the P V line more sensitive to clumping factor than O V and N IV . The best-fit case is for the filling factor of $f_\infty = 0.08$ but this is based upon (F)UV line fitting only and does not incorporate diagnostic optical lines for the central star of NGC 6543 such as He II λ 4686 or C IV λ 5801.

In Figure 3.21 the ionisation fraction of the P^{3+} P^{4+} and P^{5+} ion species are displayed as function of wind velocity for each of the three clumping factors. It can be seen that the ion fraction of P^{5+} shows a dominance at low velocities, and it is this dominance which results in the lower velocity mis-match of the model for the P V resonance line.

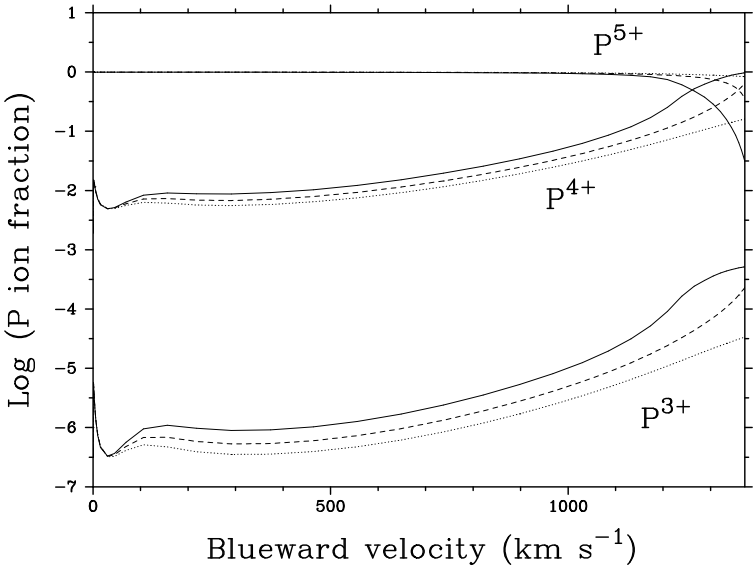

Fig. 3.21. Log plots of the P IV , P V and P VI ion fractions as functions of the blueward wind velocity, for the filling-factor cases of $f_\infty = 0.06$ (solid line), 0.08 (dashed line), and 0.10 (dotted line). Courtesy of Miguel Urbaneja (via private communication).

Although not dominant, the ion fraction of P^{3+} and P^{4+} both increase with velocity across all velocities with evidence of recombination from P^{5+} to P^{4+} at the approach to the terminal wind velocity.

Other CMFGEN models predict that the dominant ions are those of C^{4+} and P^{5+} – i.e. $q_\mathrm{i} > 0.97$ over ~ 0.2 to 0.9 v_∞ and S^{5+} and O^{4+} close to a dominant level – 0.6 and 0.2 respectively.

P V is therefore sensitive of small-scale clumping in the fast wind, coupled with the presence of larger scale structures as evident with the appearance of the DACs.

3.6 Conclusion

In this chapter evidence has been found in the FUSE UV data of NGC 6543 that the outflow emanating from its central star is variable on a time-scale of hours; also this variability is attributable to the appearance of recurrent additional optical depth absorption features which are seen to migrate blueward through the absorption troughs of the UV P Cygni profiles. In depicting such temporal behaviour in the profile of the P V resonance

Table 3.6. Comparison of NGC 6543 and mid O-star properties

DAC measure	NGC 6543	O stars (e.g. O7 III)
$v_{initial}$	$\sim 0.3\ v_\infty$	$\leq 0.3\ v_\infty$
Recurrence	yes (over $\sim$ hours)	yes (over $\sim$ days)
$(dv/dt) \times (R_\star/v_\infty)$	$\sim$ 12–24 km s^{-1}	$\sim$ 10 km s^{-1}
maximum τ(DAC)/τ(min)	~ 4	~ 5
Quasi-periodic	yes; P $\sim$ 0.14 days	yes; P $\sim$ days
FWHM/v_∞(initial)	$\sim 0.15\ v_\infty$	$\sim 0.3\ v_\infty$
FWHM/v_∞(final)	$\leq 0.05\ v_\infty$	$\leq 0.1\ v_\infty$

lines of NGC 6543, it has been observed that such behaviour is similar to that exhibited by the presence of DACs in UV data of hot, luminous OB stars. In comparing the 'DAC-like' properties of NGC 6543, as seen in this study, to those formerly observed in various studies of OB stars (e.g. Kaper et al. 1996; Prinja 1998; Fullerton et al. 2006*b*), it is noted that such parameters are remarkably similar for the two different stellar systems: these are compared in Table 3.6. In terms of the initial DAC detection within the absorption profile is similar for the two. Although it is noted that the velocity dispersion of the two DAC-type structures differ in that the approximate FWHM velocity measurements of the DACs of NGC 6543, which range between $\sim$0.15 v_∞ at their initial appearance before narrowing to $\sim$0.05 v_∞ or less as they migrate, are half the width of the similar measurement for O stars (initially at $\sim$0.3 v_∞ and then narrowing to $\sim$0.1 v_∞ with migration); conversely the flow-time-scaled linear accelerations for NGC 6543 (which must be taken as estimated 'average' values because of the velocity-law dependence of the model acceleration of the wind), are perhaps, at the higher measure of $\sim$26 km s^{-1}, as much as double the similarly-scaled acceleration of O stars, at $\sim$10 km s^{-1}. Despite these immediate differences, the velocity dispersions and the estimated (linear) accelerations, are of the same order for NGC 6543 and O stars.

It has been suggested that the appearance of DAC structures in the stellar wind and their quasi-periodic behaviour is a manifestation effect of *Co-Rotating Interaction Regions (CIRs)* (Cranmer & Owocki 1996), which are instigated by localised increases (bright spots) and decreases (dark spots) in a star's equatorial radiative force. Bright spots generate high-density but slow moving streams, and dark spots provide lower-density but fast moving streams. The CIRs are produced when faster moving material catches up with slower moving material: the leading edge of a fast-moving streams catches up with a slower moving stream, the interaction between the two may steepen into a shocked region.

Then unperturbed super sonic wind then obliquely impacts upon the CIR, resulting in a "sharp propagating discontinuity": a plateau, and where there is a flattening of the velocity gradient there is also an increase in density at similar velocities, but different spatial locations.

The proposed physics behind the appearance of DACs – namely the collisional shock-effect upon optical depths through development of a radial velocity plateau – can be explained by the mechanisms behind the CIR model, and it is the co-rotating structure which enables these variations in absorption to occur over far greater time-scales than that attributed to the flow-time of the wind itself.

*S*obolev with *E*xact *I*ntegration (SEI) code provides a measure of the $\dot{M}q_i$ product for a given model, which for dominant ion species with $q_i \sim 1$, the results can therefore go toward providing a measure of the mass-loss rate itself, $\dot{M}$. However SEI code assumes a smooth wind, and does not take into account any degree of clumpiness which may be present within the outflow material, and which could have an affect upon the $\dot{M}q$ values obtained via the model. With this understanding one must therefore tale into consideration the 'clumping' filling factor of f_∞ ∼0.08 implied in the results of the CMFGEN analysis as carried out by Miguel Urbaneja (IoA, Hawai'i) and presented in Section 5 of this chapter; especially considering the inherent sensitivity of the P V resonance lines to clumping factors as well as to mass-loss. Studies of O-type stars by Bouret et al. (2005) and Fullerton et al. (2006*b*) have formulated a reduction factor by which mass-loss measured via smooth-wind studies (such as SEI), should be reduced: by a factor of $\sim 1/\sqrt{f_\infty}$, i.e. for a clumping factor of $f_\infty \sim 0.08$, the reduction factor for the mass-loss of NGC 6543 would be $1/\sqrt{0.08} \sim 4$. It should also be noted that in optical studies of CSPNs, Kudritzki et al. (2006) undertook analysis to establish the clump filling factors required to improve stellar emission fits of Hα and He II λ 4686, and it was shown that the adoption of filling factors improved fits of their FASTWIND code.

However, Oskinova et al. (2007) argue that the introduction of clumping factors to address the unreal homogeneity of stellar wind models (which are considered to cause an over-estimation of mass-loss rates) has generalised the issue by an assumption of the optical thinness of the clumps, with the result that the subsequent reduction of mass-loss rate calculations by a factor of ∼3 actually results in an *under*-estimation of mass-loss values. Their opinion is that the spatial separation of the clumps – the *porosity* of the wind material – must be taken into account, and that modelling which incorporates larger

separations of optically-*thick* clumps is better able to fit the emission line profiles which have now been detected in X-ray spectra of O stars.

Given the connection being established between wind models and mechanisms of O stars and O-type CSPNs, this is yet another branch of spectroscopic research which can help towards a further understanding and appreciation of the inherent astrophysics of CSPNs.

Chapter 4

Structure in Fragmented FUSE UV Time-Series Spectra

The structure observed in the wind of NGC 6543, as detailed in the previous chapter, gives rise to speculation of NGC 6543 being unique among CSPNs, or whether it is possible to see DAC-like forms in the winds of other CSPN objects; and to this end a selection of objects was made with view to analyse further FUSE-based data. However the extent of data in the archive is limited, and often disappointingly noisy or off-target. In this chapter the focus will be upon four objects which, although posessing limited time-series data, can still provide useful information upon general parameters for hydrogen-rich CSPNs.

From the STSci archive of data obtained via the FUSE satelitte it was necessary to seek out data which fulfilled certain criteria necessary to undergo similar time-series analysis as had been carried out on the UV data obtained for NGC 6543. Of primary importance was that a given object must possess a number of sequential spectra, and not just one or two. Also, the spectra must present clearly defined P Cygni profiles, the key signatures of a expanding stellar atmosphere; what is more, the P Cygni profiles found within a given object's UV spectra need to be *unsaturated* in order to modelled as accutaely as possible and obtain, via the SEI code, a measure of the mass-loss-ionisation-fraction product, $\dot{M}q$. The data selected is listed below in Table 4.1.

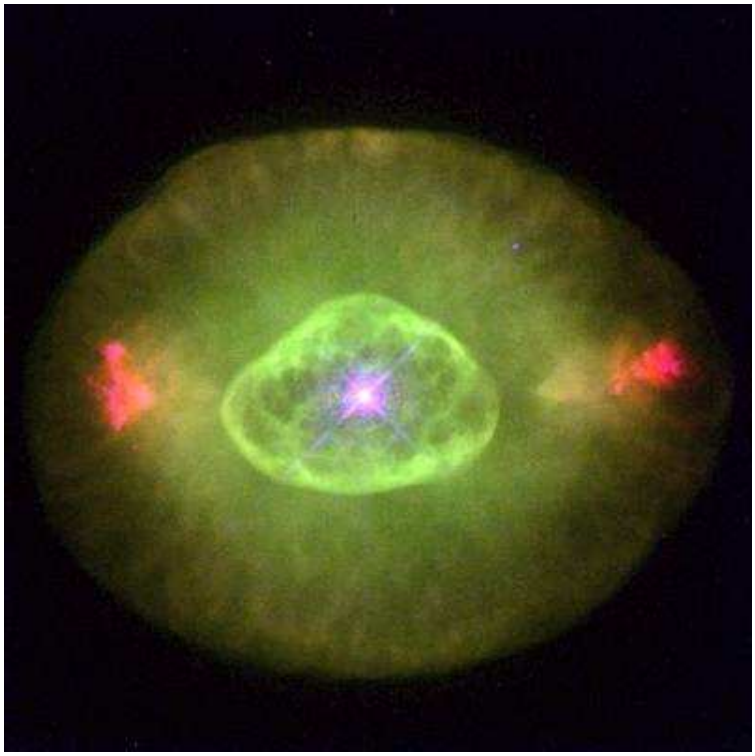

Fig. 4.1. HST WFPC2 image of PN NGC 6826 (the 'Blinking Nebula'), showing the nebula's gaseous composition with nitrogen (red), hydrogen (green), and oxygen (blue): http://apod.nasa.gov/apod/image/9712/

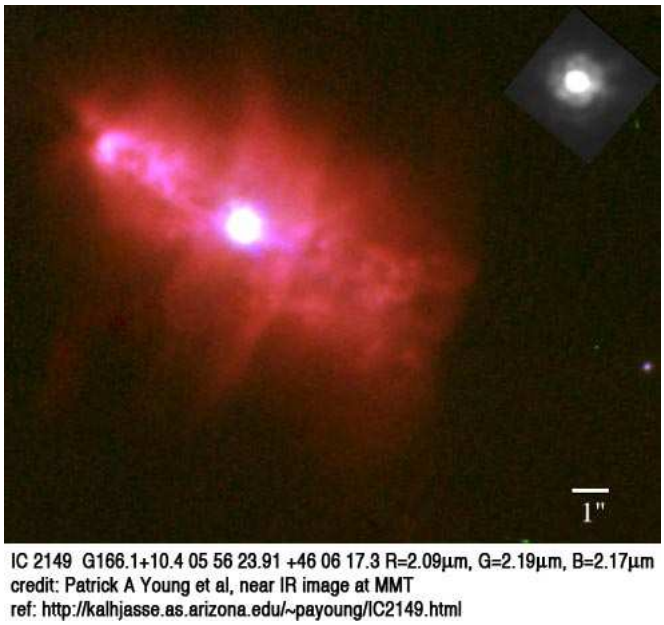

Fig. 4.2. Composite MMT near-infrared image of PN IC 2149, made up of exposures taken via red (2.09 μm), green (2.19 μm), and blue (2.17 μm) filters: http://www.williams.edu/astronomy/research/PN/ nebulae/search/nebimages/

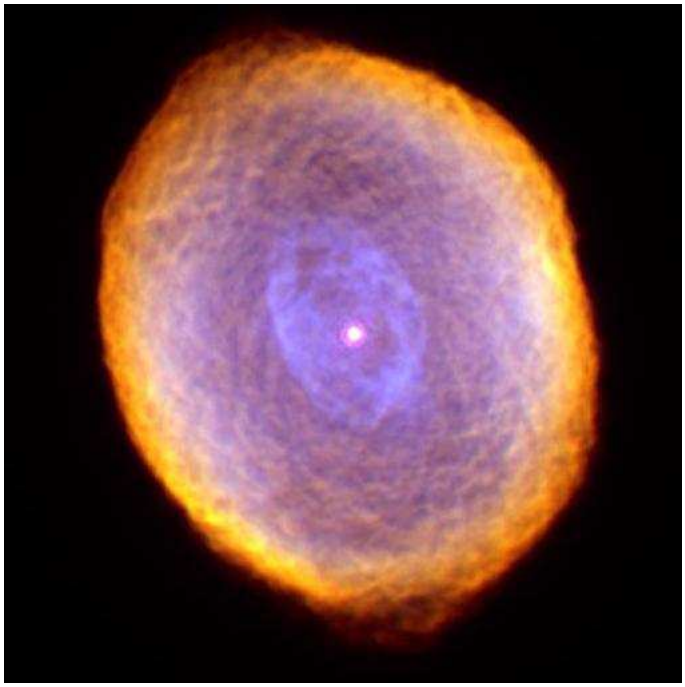

Fig. 4.3. HST WFPC2 image of PN IC 418 (the 'Spirograph Nebula'), showing the nebula's gaseous composition with nitrogen (red), hydrogen (green), and oxygen (blue): http://www.astro.yale.edu/astro120/

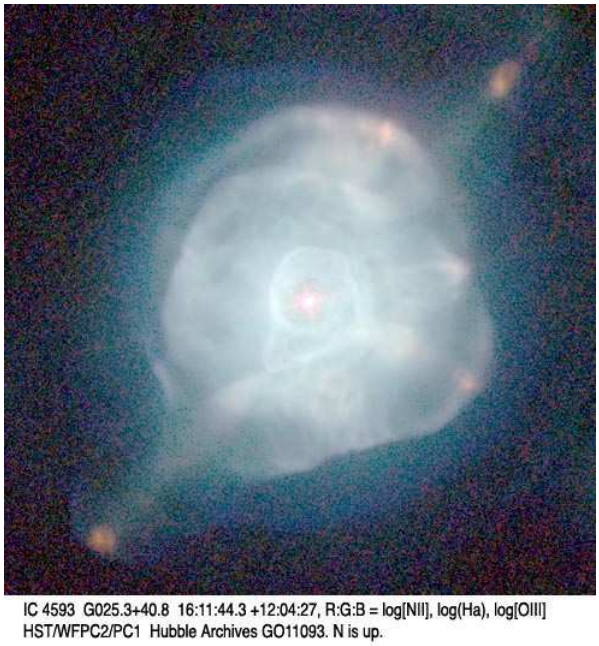

Fig. 4.4. HST WFPC2 image of PN IC 4593, with filters depicting different nebula gases, namely nitrogen ([N II] - red), helium (Hα - green), and oxygen ([O III] - blue): http://hubblesite.org/gallery/album/entire/pr2007033d/largeweb/npp/all/

Table 4.1. FUSE objects – details of observations

Object	NGC 6826	IC 2149	IC 418	IC 4593
Dataset	P1930401	P1041401	P1151111	B0320102
No. Exposures	12	8	9	4
UT Date	2000-08-07	1999-12-02	2001-12-02	2001-08-03
MJD (start)	51763.950	51514.132	52245.100	52124.645
ΔT	1.6	6.1	1.2	0.5

4.1 Fragmented Time-series Objects

4.1.1 NGC 6826

A study of NGC 6826 (along with NGC 6543) (Perinotto et al. 1989) depitcs an early use of the original SEI method (Lamers et al. 1987). Using the SEI method model fits were obtained for the P Cygni profiles of C IV , N IV and N V , O IV and O V . From the SEI fits, the product of the mass-loss rate, $\dot{M}$, and the averaged ionisation fraction q_i, i.e. $\dot{M}q_i$, is derived by intergrating between 0.2 and 0.8 of the normalised wind profile, $w = v/v_\infty$. In order to obtain a value for the mass-loss rate itself, $\dot{M}$, the ionisation hypothesis that $q(\mathrm{O\,IV}) + q(\mathrm{O\,V}) = 1$ is used, from which NGC 6826 is assigned a mass-loss rate of $\dot{M}$ $= 5.2 \times 10^{-8}\ M_\odot\,\mathrm{yr}^{-1}$ (with $4.0 \times 10^{-8}\ M_\odot\,\mathrm{yr}^{-1}$ for NGC 6543). Once $\dot{M}$ is obtained then the averaged ion fractions of the investigation ion profiles can be calculated.

4.1.2 IC 2149

IC 2149 possesses a perculiar morphology and is another of those PN which have benefitted from the PN of the last twenty years or so whose investigations into various kinematic scenarios have provided possible means by which numerous PNs have evolved their elaborate shapes (Sahai & Trauger 1998)

The prescence of a stellar wind is discerned from the appearance of P Cygni profiles observed in the UV spectra (Perinotto et al. 1982), the terminal velocity of which is taken from the edge of the saturated blue component of the C IV λ 1548.20, 1550.77 doublet.

Despite the indications of the manifestation of a stellar wind, as far as a possessing a variable outflow, this latter phenomenon has not been observed (Patriarchi & Perinotto 1997).

4.1.3 IC 418

Simultaneous spectroscopic and photometric exposures have been taken of the central star of IC 418 with the aim of assessing the variability observed (Méndez et al. 1986), in an atttempt to discern the cause whether due to hidden binarity or to (mono-)stellar pulsations; it had already been noted that the photometric velocity varied on a timesacle of a few hours (Méndez et al. 1983). The variations were on too short a scale to indicate being the result of a binary-system interaction; due to the compartively low-level fluctuations of surface temperature, radial pulsations are not a likely cause; also non-radial pulsations are not though of as a likely source of the variations as these do not appear to be sinusoidal in nature, which would otherwise indicate the presence of waves traveliing non-radially across the stellar surface. Therefore, the observed fluctuations are cause by variations of the stellar outflow rate at the level of the photosphere, namely variations in the optical thickness (depth) of the outflowing material, which because of the apparent lack of temperature fluctuations, must be attributed to fluctuations in density, possibly be caused by some unknown mechanism which switches on/off the mass at the bottom of the expanding atmosphere, and with the continuing mass-loss above, there is a subsequent drop in density, thus resulting in a drop in optical thickness.

The original format of the SEI method of modelling P Cygni profiles has been utilised to model UV resonance lines from IUE data, and from these models the mass-loss rates, $\dot{M}$, can be estimated (Cerruti-Sola & Perinotto 1989): input parameters used are taken from non-LTE hydrogen and helium model atmospheres giving temperature and gravities for certain CSPNs. With both high- and low-resolution IUE data, Zanstra temperatures were obtained, the theoretical stellar continuums have been compared to those observed to gain futher temperature-based information, and the final temperatures have then been used to estimate further stellar parameters.

An assumption utilised by Castor et al. (1981), that $q(\mathrm{O\,IV}) + q(\mathrm{O\,V}) = 1$, could not be used as not both these ions were measurable for IC 418; however an alternative assumption, gives that $q(\mathrm{N\,IV}) + q(\mathrm{N\,V}) = 1$ also, and using the measured $\dot{M}q$ for the N IV and N V ions, the mass-loss rate for IC 418 was estimated to be $\dot{M} = 6.3 \times 10^{-9}$ $M_{\odot}\,\mathrm{yr}^{-1}$.

4.1.4 IC 4593

The fast winds of IC 4593 had also been investigated (Cerruti-Sola & Perinotto 1989) (CS) using the (then) fairly recent wind analysis method, SEI (Lamers et al. 1987). Employing a multi-parameter grid method, whereby varying input parameters were employed in the construction of the SEI model, they (CS) were able to assess which combination produced the best-fit model and therefore drew the conclusion that this was because the input parameters were the optimum for that paticular object. The adoption of the grid method was used instead of applying an input phospheric absoprtion line and not applying such wind law parameters as termianl velocity, and a β acceleration parameter in order to manipulate the photosperic absorption trough into shape-shifting into a P Cygni profile.

In estimating the mass-loss rate, $\dot{M}$, from the SEI derived $\dot{M}q$, one, of couse, has to have a value for the ionisation fraction, q of the ion modelleled. The assumption made by Castor et al. (1981), that $q(\mathrm{O\,IV}) + q(\mathrm{O\,V}) = 1$, could not be used as IC 4593 does not possess line profiles for both these ions in its spectra; however the second assumption that $q(\mathrm{N\,IV}) + q(\mathrm{N\,V}) = 1$, could be used as both these ions can be identified as lines in the spectra, and so CS were able to predict a values for the mass-loss rate of the star, $\dot{M} = 4.2 \times 10^{-8}\ M_{\odot}\,\mathrm{yr}^{-1}$.

4.2 Time-Averaged Spectra & SEI Modelling

As with NGC 6543 in the previous chapter, the mean spectrum of each object was subjected to SEI modelling, and again as with NGC 6543, the parameters of optical depth and velocity FWHM have been estimated from rotationally-broadened spectral absorption lines from photosperic spectra obtained via the TLUSTY T_{eff} –$\log g$ grid of models. Each P Cygni profile has been modelled with SEI and the resulting $\dot{M}q$ values from the radial optical depth fits have been recorded, as well as the average $\dot{M}q$ value integrated between the radial velocity bins 0.2 – 0.9 v_{∞}.

The input parameters – see Table 4.2 – listed for NGC 6826, IC 418 and IC 4593 used for the SEI modelling procedure in this chapter, namely the individual objects' wind's terminal velocities, as well as their individual values for luminosity and effective temperature (from which the respective stellar radii can be derived the code), have been taken from the wind-analysis results of Kudritzki et al. (2006). The parameters list for IC 2149 have been taken from Perinotto et al. (1982). Although the terminal velocity for the

Table 4.2. FUSE objects – central star parameters

Object	NGC 6826	IC 2149	IC 418	IC 4593
v_∞[km s^{-1}] ±100	1200	1000	700	950$_*$
$T_{\rm eff}$[K] ±1000	46000	35000	36000	40000
$\log L/L_\odot$ ±0.01	4.11	3.24	4.38	4.05
Radius, $R/R_\odot$	1.8	2.0	4.0	2.2
Abundance, A_E	solar	solar	solar	solar
Radial velocity [km s^{-1}] (Schneider et al. 1983)	−6.2 ±0.6	−30.7 ±2.1	+61.9 ±0.5	+22.0 ±0.5

stellar wind of IC 4593 is given by Kudritzki et al. (2006) as 900 km s^{-1}, it was found that in the SEI modelling of the blue component of P V , the blue edge of the absorption trough was better aligned with the underlying spectral absorption trough if the model's terminal velocity was adjusted up to 950 km s^{-1} *. The chemical abundances of the CSPNs have been assumed to be solar.

4.2.1 Data Source & Ion Species – NGC 6826

The FUV spectra for NGC 6826 are taken from the P193 Program (PI – T.P. Snow), obtained on 7^{th} August 2000: 12 exposures were obtained over ∼1.6 hours (5796 s) via the Lif2 Channel (segment A: 1087 – 1182 Å) from which information on the P V λλ 1117.98, 1128.01 doublet can be derived; likewise 12 exposures were obtained via the Lif2 Channel (segment B: 979 – 1075 Å) for the O VI λλ 1031.93, 1037.62 doublet.

In Figure 4.5 P Cygni profiles can be seen in the doublets of P V and O VI ; also in the non-resonance line of C III λ 1175.66 there appears a P Cygni-like absorption trough - emission peak pairing in its spectral profile.

4.2.2 SEI Model Fits – NGC 6826

P V λλ *1117.98, 1128.01*

The SEI models for different ion species found in the outflow of NGC 6826 exhibit a wide range of dgrees of development and saturation, see Figure 4.6. An SEI model fit has been acheived for the unsaturated P V profile by applying a v_∞ of −1200 km s^{-1} and $\beta = 1.25$

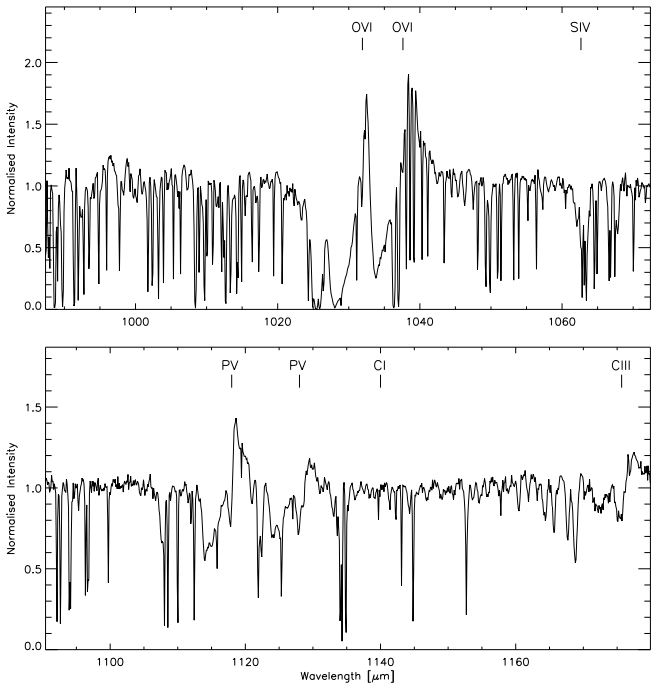

Fig. 4.5. Mean FUSE spectra for NGC 6826 highlighted with key resonance lines

upon a photospheric input Gaussian profile with a FWHM of ∼200 km s^{-1}; however, the absorption profile of P V λ 1117.98 is relatively shallow and in exhibiting the geneneral shape of a P Cygni profile with the extent of the depth of the absorption trough being echoed in the height of the emission peak, this peak is similarly weak. In terms of the radial optical depths the $\tau_{\rm rad}$(w) values range from 0.4 at $w = 0.25$ to 0.9 at $w = 0.90$. In terms of the average $\dot{M}q(\mathrm{P}^{4+})$, as integrated over 0.2 to 0.9 v_∞, the SEI model predicts a value of $\sim 6.8 \times 10^{-9}$ $M_\odot\,\mathrm{yr}^{-1}$, and over the limited data available the $\dot{M}q(\mathrm{P}^{4+})$ ranges from a minimum of $\sim 5.3 \times 10^{-9}$ $M_\odot\,\mathrm{yr}^{-1}$ and a maximum of $\sim 7.8 \times 10^{-9}$ $M_\odot\,\mathrm{yr}^{-1}$.

O VI $\lambda\lambda$ 1*031.93, 1037.62*

In contrast the P Cygni profile for the O VI λ 1031.93 line has a much deeper absorption trough and a subsequently stronger peak in emission: the SEI fits has been achieved with a similar v_∞ and β for a photospheric input Gaussian profile of FWHM ∼200 km s^{-1}. The P Cygni profile is highly saturated with the absorption trough reaching down to zero flux; however it is not as saturated as to proceed to flatten out to the extent seen in C IV λ 1548.20. Aside from the blending of the top of the blue edge of the absorption profile

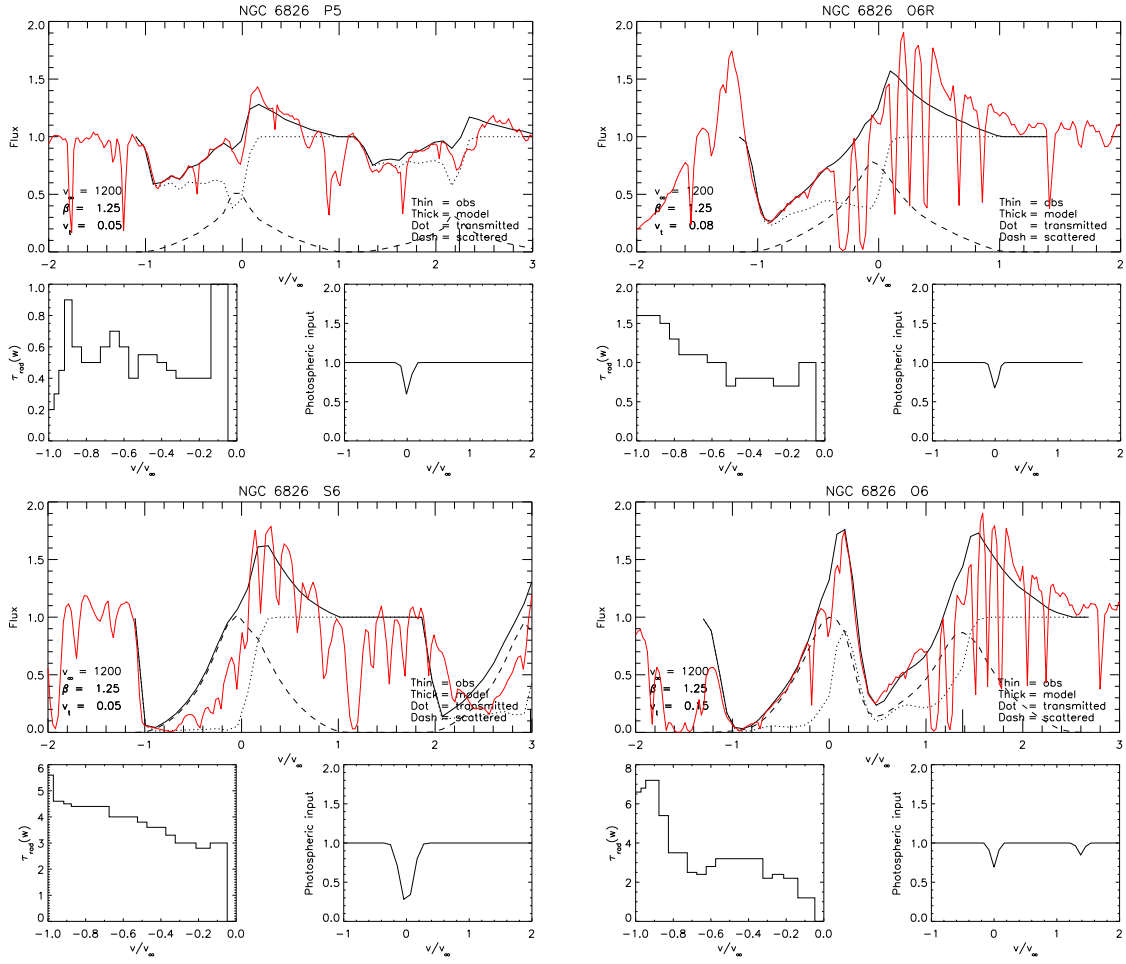

Fig. 4.6. NGC 6826: SEI model fits for the mean spectra for the P V (l) and O VI (r) resonance lines shown above, with model fits for S VI (l) and C III (r) shown below.

becoming blended with the adjacent absorption of Ly-β, thus preventing the blue O VI component from merging back into the continuum, the SEI model is reasonable matched; despite the saturation towards to blue edge of the absorption trough, the increased forward scattering of the model does not move beyond the red edge of the absorption trough, although it does appear to coincide. The optical depth histogram records a minumum optical depth of 0.45 at $w \sim 0.2$, increasing steadily to ~ 3.5 up to $w = 0.8$ from where the depth increses rapidly to a maxiumum of 7.4 at $w = 0.9$, after which it drops slightly before the trough becomes blended with the Ly-β absoprtion. The red component of O VI at λ 1037.62 possesses a better defined blue edge which is well matched by the model but in the lower velocities ($w \leq 0.4$), and beyond into emmission, the profile is affected by interstellar ansorption, although at first glance the model appears to match the (albeit

estimated) shape of the P Cygni profile. The optical depth histogram shows a minimum of 0.7 at $w \sim 0.2$, increasing to 1.6 at $w \geq 0.9$.

S VI λ 933.38

The blue component of the S VI $\lambda\lambda$ 933.38, 944.76 doublet is highly saturated, and although possessing a clearly defined blue edge, the saturation in the absorption has forced the model to produce excessive forward scattering which extend to the blue edge of the trough: the subsequent optical depth histogram is unlikely to reflect the true nature of the absorption in terms of the τ_{rad} values it displays which can only be taken as the lower limit of the radial optical depths.

4.2.3 Data Source & Ion Species – IC 2149

The FUV spectra for IC 2149 are taken from the P104 Program (PI – Warren Moos), obtained on 2^{nd} December 1999: 8 exposures were obtained over ∼6.1 hours (21910 s) via the Lif2 Channel (segment A: 1087 – 1182 Å) for the P V $\lambda\lambda$ 1117.98, 1128.01 doublet; 8 exposures were obtained via the Lif2 Channel (segment B: 979 – 1075 Å) for the O VI $\lambda\lambda$ 1031.93, 1037.62 doublet; and 8 exposures also obtained via the Sic2 Channel (segment A: 917 – 1006 Å) for the S VI $\lambda\lambda$ 933.38, 944.52 doublet.

Under the P104 Program 9 exposures were also obtained over ∼4.5 hours (16228 s) on 25^{th} November 1999, and a further 12 exposures over ∼4.8 hours (17171 s) on 14^{th} January 2000; however, when this data was applied to the TVS algorithm, the power output showed limited variance above the 95% confidence level – Figure 4.21 below – and so was not investigated further.

In Figure 4.7, as well as P V and O VI a vague P Cygni appears at S VI λ 933.38 but not at S VI λ 944.52, as well as a contaminated P Cygni at C III λ 977.03; although it does show a blueward absorption. C III λ 1175.66 has a slight redward emission peak but is rather shallow and therefore not a strong P Cygni profile, but again there is a strong blueward (unsaturated) absorption trough.

4.2.4 SEI Model Fits – IC 2149

P V $\lambda\lambda$ 1*117.98, 1128.01*

As seen in Figure 4.8, the SEI model of the P V profile of IC 2149 – modelled using $v_\infty = -1000\ \mathrm{km\,s^{-1}}$ and $\beta = 1.25$ upon an input Gaussian of FWHM $\sim 200\ \mathrm{km\,s^{-1}}$ – is similar to that of NGC 6826 in that the profile is unsaturated to the extent of appearing a weak line - but in contrast to NGC 6826 the adopted optical depth profile $\tau(w)$ peaks at 0.9 at a the lower (normalised) velocity of $w = 0.25$, with the profile becoming shallower towards the wind terminal velocity, dropping to a low $\tau(w)$ of 0.05 at $w = 0.93$. The average $\dot{M}q(\mathrm{P}^{4+})$, (integrated, as before, over 0.2 to 0.9 v_∞), gives a value of $\sim 1.5 \times 10^{-9}\ M_\odot\,\mathrm{yr}^{-1}$, and over the limited data available the $\dot{M}q(\mathrm{P}^{4+})$ ranges (to a much lesser extent than seen in NGC 6826) from a minimum of $\sim 1.3 \times 10^{-9}\ M_\odot\,\mathrm{yr}^{-1}$ and a maximum of $\sim 1.7 \times 10^{-9}\ M_\odot\,\mathrm{yr}^{-1}$.

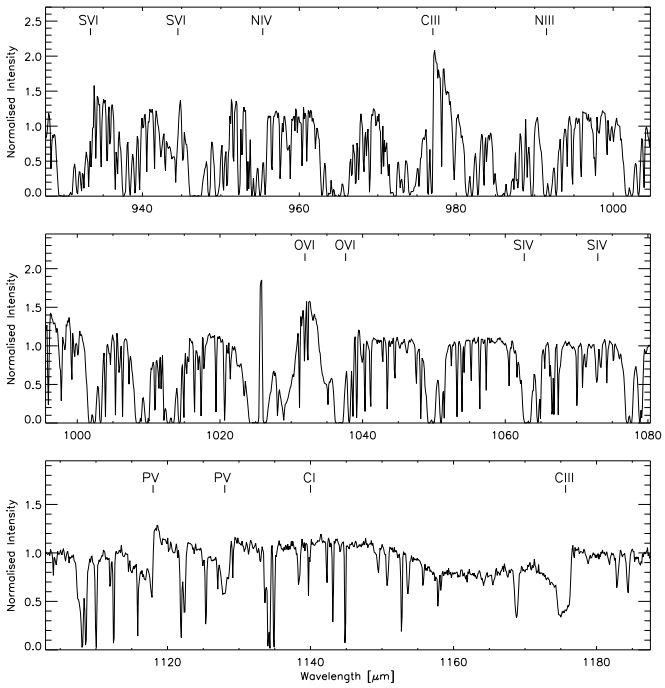

Fig. 4.7. Mean FUSE spectra for IC 2149 highlighted with key resonance lines

O VI λλ 1*031.93, 1037.62*

The blue component of the O VI λλ 1031.93, 1037.62 doublet is blended with the red edge of the Ly-β interstellar line and so aligning the blue edge of the O VI model – upon an input Gaussian profile of FWHM $\sim$ 300 km s^{-1} – is at best a rather rough estimate; otherwise the remainder of the absorption trough is well matched. Although strong in absorption the trough does not appear saturated and there is no excessive scattering to affect the model, therefore the profile is well matched as far back as the emission peak which although affected by interstellar absorption is also well matched by the model. The $\tau_{\rm rad}$ histogram shows that the optical depth is lowest at low velocity with $\tau(\sim 0.2) = 0.5$, rising to $\tau(0.85) = 2.4$; blue edge values of optical depth are unreliable however, because of the interstellar absorption from $w > 0.8$. The red O VI component is excessively affected by interstellar absorption and so, unlike with NGC 6826, no attempt has been made to model its profile.

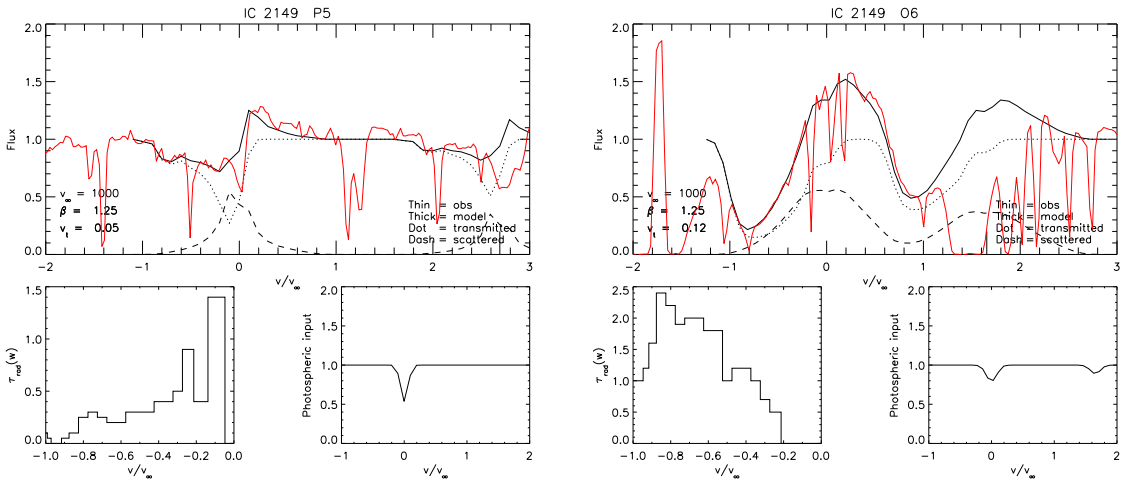

Fig. 4.8. IC 2149: SEI model fits for the mean spectra for the P V (l) and O VI (r) resonance lines.

4.2.5 Data source & Ion Species – IC 418

The FUV spectra for IC 418 are taken from the P115 Program (PI – Michael Shull), obtained on 2^{nd} December 2001: 9 exposures were obtained over ∼1.2 hours (4423 s) via the Lif2 Channel (segment A: 1087 – 1182 Å) for the P V $\lambda\lambda$ 1117.98, 1128.01 doublet can be derived; 9 exposures were obtained via the Lif1 Channel (segment A: 987 – 1082 Å) for the O VI $\lambda\lambda$ 1031.93, 1037.62 doublet; and 9 exposures also obtained via the Sic2 Channel (segment A: 917 – 1006 Å) for the S VI $\lambda\lambda$ 933.38, 944.52 doublet.

P Cygni profiles can be seen in Figure 4.9 for P V $\lambda\lambda$ 1117.98, 1128.01 and O VI $\lambda\lambda$ 1031.97, 1037.62 but not for S VI $\lambda\lambda$ 933.38, 944.52 simply saturated absorption. P Cygni profiles can also be seen at C III λ 977.03 (saturated), S IV λ 1072.97 (unsaturated), and also at C III λ 1175.66 (strong absorption but not quite saturated).

There is also strong blueward absorption at N IV λ 955.34 and S IV λ 1062.66 but not the full absorption-emission P Cygni profile.

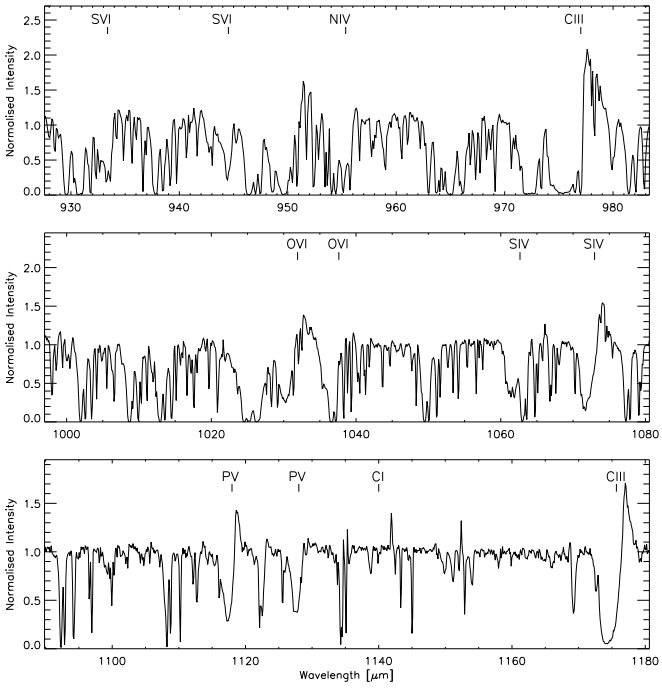

Fig. 4.9. Mean FUSE spectra for IC 418 highlighted with key resonance lines

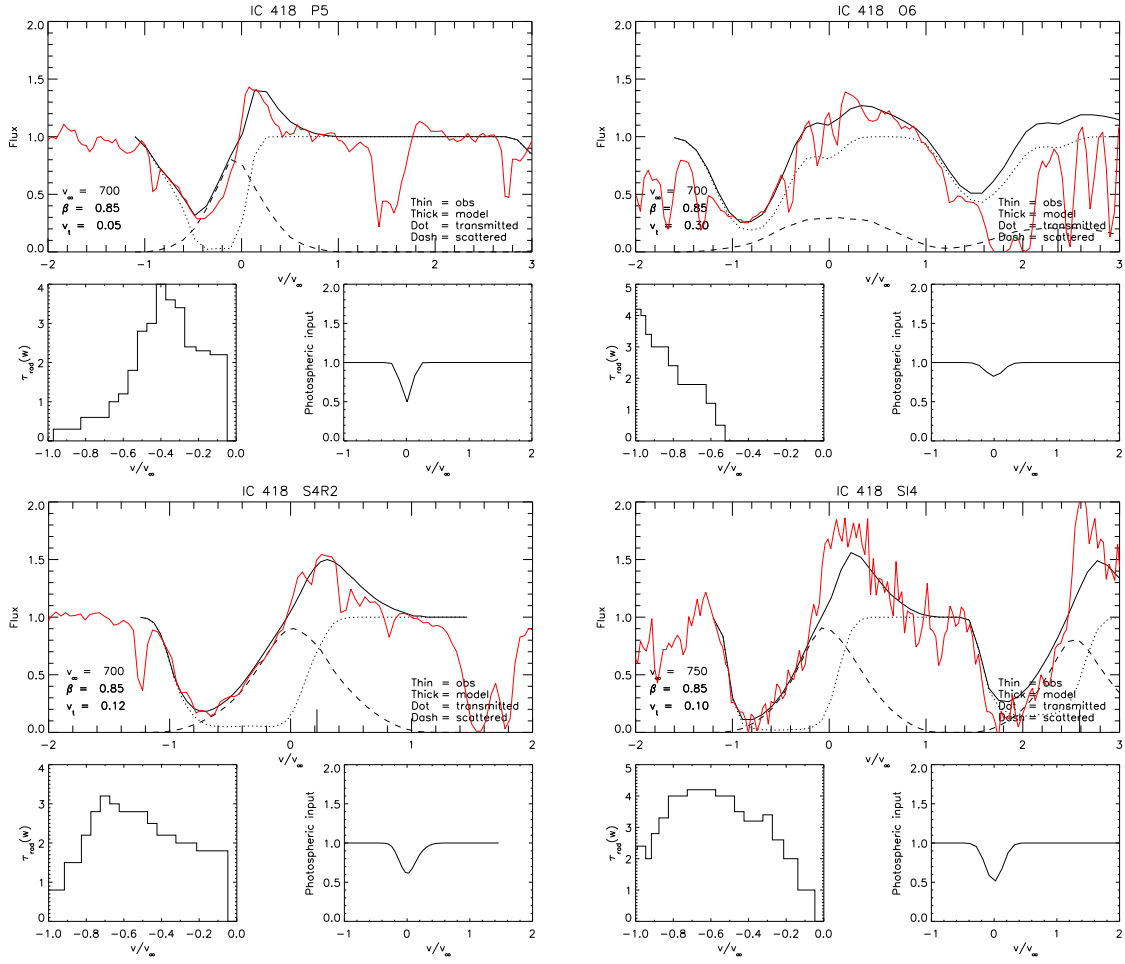

Fig. 4.10. IC 418: SEI model fits for the mean spectra for the P V (l) and O VI (r) resonance lines shown above, with model fits for S VI (l) and C III (r) shown below.

4.2.6 SEI Model Fits – IC 418

P V $\lambda\lambda$ 1117.98, 1128.01

The SEI model of the P V profile of IC 418 is modelled using $v_\infty = -700$ km s^{-1}, but now the P V profile is fitted with a faster acceleration profile for $\beta = 0.85$ (upon an photospheric input Gaussian of FWHM ~ 200 km s^{-1}). As seen in Figure 4.10, IC 418 possesses a much stronger P Cgyni profile to either that of NGC 6826 or IC 2149 but still unsaturated. The optical depth profile $\tau(w)$ peaks at 0.9 at a the lower (normalised) velocity of $w = 0.25$, with the profile becoming shallower towards the wind terminal velocity, dropping to a low $\tau(w)$ of 0.05 at $w = 0.93$. The average $\dot{M}q(\mathrm{P}^{4+})$, (over 0.2 to 0.9 v_∞), gives a value of $\sim 1.2 \times 10^{-8}$ $M_\odot$ yr^{-1}, and over the limited data available the $\dot{M}q(\mathrm{P}^{4+})$ ranges (to a much lesser extent than seen in NGC 6826) from a minimum of $\sim 1.3 \times 10^{-9}$ $M_\odot$ yr^{-1} and

a maximum of $\sim 2.4 \times 10^{-9}\ M_{\odot}\,\mathrm{yr}^{-1}$.

O VI λ1031.93

An attempt has been made to model the blue component of the O VI λλ 1031.93, 1037.62 doublet ($v_{\infty} = -700$ km s^{-1}, $\beta = 0.85$, photospheric input Gaussian of FWHM ~ 350 km s^{-1}); however the blue edge of the absorption trough (and also the continuum further bluewards) has been too much affected by interstellar line absorption to achieve a confidently modelled profile, indeed even a high dispersion parameter of $v_{\mathrm{turb}} = 0.30$ cannot match the blue edge which has been all but removed by the interstellar lines. The corresponding histogram shows a low value of $\tau(w)$ in the velocity range $0.00 \leq w < 0.50$, from where the rest of the histogram shows a steady increase from $\tau(0.55) = 0.5$ to $\tau(1.00) = 4.2$. The red component is much worse affected by interstellar absorption and subsequently any P Cygni profile that might otherwise exist has been hidden.

S IV λ1072.97

In contrast, the red component of the S IV λλ 1062.66, 1072.97 doublet is minimally affected by interstellar line absorption and so the P Cygni profile has been well matched with similar wind law parameters (v_{∞}, β) as P V above (photospheric input Gaussian: FWHM ~ 300 km s^{-1}), requiring only a slight increase in the wind dispersion of $v_{\mathrm{turb}} = 0.12$ to match the blue wall of the model with that of the absorption trough underneath. The corresponding τ_{rad} histogram shows a steady increeas in optical depth from 1.8 at $\sim \tau(0.2)$ to a maximum $\tau(0.7) = 3.2$ before decreasing again to 0.8 in the velocity range of the blue edge, $0.90 \leq w < 1.00$.

Si IV λ1393.76

In addition, the blue component of the Si IV λλ 1393.76, 1402.77 has been modelled, the spectrum obtained via the IUE archive (SWP 37763). Again with similar velocity parameters (v_{∞}, β, photospheric input Gaussian: FWHM ~ 350 km s^{-1}) the profile has been well matched by the model; however a slightly higher v_{∞} of 750 km s^{-1} had to be adopted in order to align the blue edge of the SEI model absorption component with that of the observed line profile, with only a slight increase of velocity dispersion to $v_{\mathrm{turb}} = 0.10$. The τ_{rad} histogram shows that from 2.0 at $\sim \tau(0.2)$ the optical depth increases to a maximum

of 4.2 between $0.60 \leq w \leq 0.70$ before decreasing again to 2.4 at the blue edge, $0.90 \leq w < 1.00$.

4.2.7 Data Source & Ion Species – IC 4593

The FUV spectra for IC 4593 are taken from the B032 Program (PI – Robert Gruendl), obtained on 3^{rd} August 2001: only 4 exposures were obtained over ∼0.5 hours (1933 s) via the Lif2 Channel (segment A: 1087 – 1182 Å) for the P V $\lambda\lambda$ 1117.98, 1128.01 doublet can be derived; 3 exposures were obtained via the Lif1 Channel (segment A: 987 – 1082 Å) for the O VI $\lambda\lambda$ 1031.93, 1037.62 doublet; and 3 exposures also obtained via the Sic2 Channel (segment A: 917 – 1006 Å) for the S VI $\lambda\lambda$ 933.38, 944.52 doublet.

P Cygni profiles can be seen for P V $\lambda\lambda$ 1117.98, 1128.01 and O VI $\lambda\lambda$ 1031.97, 1037.62 and very subtley for S VI $\lambda\lambda$ 933.38, 944.52 the second line of which shows only the smallest redward emission peak. P Cygni profiles can also be seen at C III λ 977.03 (saturated) and C III λ 1175.66 (strong but unsaturated).

Strong blueward absorption can also be seen at N IV λ 955.34 and although there may be blueward absorption at S IV λ 1072.97 but it is weak and indistinct.

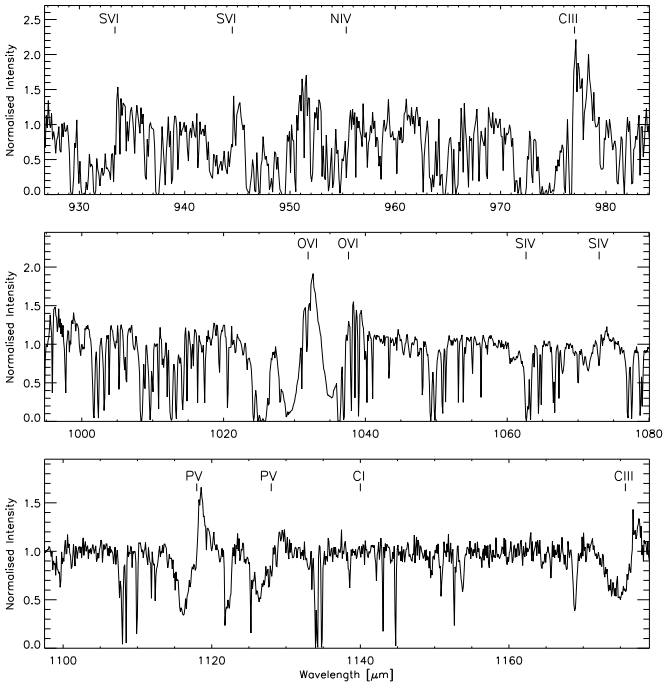

Fig. 4.11. Mean FUSE spectra for IC 4593 highlighted with key resonance lines

4.2.8 SEI Model Fits – IC 4593

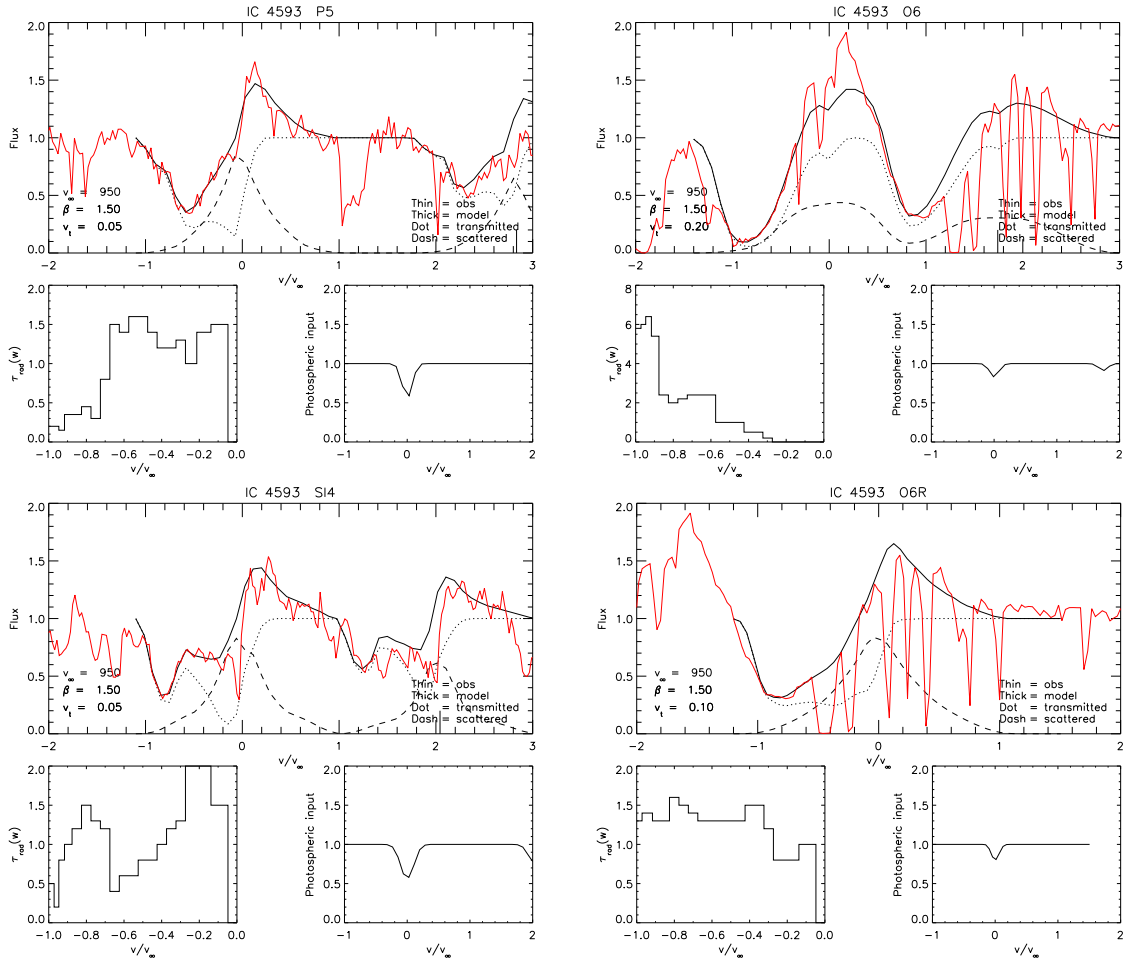

Fig. 4.12. IC 4593: SEI model fits for the mean spectra for the P V (l) and O VI (r) resonance lines shown above, with model fits for S VI (l) and C III (r) shown below.

P V $\lambda\lambda$1117.98, 1128.01

An SEI model of the P V profile of IC 4593 was initially attempted using $v_\infty = -900$ km s^{-1}(Kudritzki et al. 2006), however a much better fit, with the blue edge of the model aligning itself closer with that of the underlying spectra, was acheived with $v_\infty = -950$ km s^{-1} (which is 50 km s^{-1} higher but within the $\pm$ 100 km s^{-1} error limit of Kudritzki), upon a photospheric input Gaussian of FWHM $\sim$ 250 km s^{-1}. Also the β factor of the wind's acceleration profile possesses has been increased from 1.25 of NGC 6826 and IC 2149 (and NGC 6543 in chapter 3) to a factor of $\beta = 1.50$. IC 4593 has a much stronger P Cgyni profile to either that of NGC 6826 or IC 2149 but still unsaturated. The optical

depth profile $\tau(w)$ peaks at 0.9 at a the lower (normalised) velocity of $w = 0.25$, with the profile becoming shallower towards the wind terminal velocity, dropping to a low $\tau(w)$ of 0.05 at $w = 0.93$. The average $\dot{M}q(\mathrm{P}^{4+})$, (over 0.2 to 0.9 v_∞), gives a value of $\sim 1.2\times10^{-8}$ $M_\odot\,\mathrm{yr}^{-1}$, and over the limited data available the $\dot{M}q(\mathrm{P}^{4+})$ ranges (to a much lesser extent than seen in NGC 6826) from a minimum of $\sim 1.3 \times 10^{-9}$ $M_\odot\,\mathrm{yr}^{-1}$ and a maximum of $\sim 2.4 \times 10^{-9}$ $M_\odot\,\mathrm{yr}^{-1}$.

O VI $\lambda\lambda$ 1*031.93, 1037.62*

The P Cygni profile at O VI λ 1031.93 has also beem modelled with $v_\infty = -950\,\mathrm{km\,s^{-1}}$ and β = 1.50 (photospheric input Gaussian: FWHM $\sim 250\,\mathrm{km\,s^{-1}}$), but an increased dispersion parameter of 0.30 in order to better fit the blue edge of the model; unfortuately as high v_{turb} parameters have a tendency to smooth out the model profile this has had the effect of lowering the emission peak in the model and so this aspect of the P Cygni is matched less satisfactorily. The edge of the blue component of the O VI doublet is also affected by interstellar line absorption (particularly the adjacent Ly-β) which has effectively removed the contiuum bluewards of O VI and so modelling the blue component is often difficult; however a SEI fit of the red component, O VI λ 1037.62 has been acheived, again with v_∞ $= -950\,\mathrm{km\,s^{-1}}$ and $\beta = 1.50$ (photospheric input Gaussian of $\sim 200\,\mathrm{km\,s^{-1}}$), but a lesser dispersion parameter of $v_{\mathrm{turb}} = 0.10$, and despite significant interstellar line interference the underlying emission peak is better matched by the model.

Si IV λ 1*393.76*

An additional P Cygni profile is found in an IUE spectrum (SWP 17948) for the blue component of the Si IV $\lambda\lambda$ 1393.76, 1402.77 doublet: this is well match by the parameters of $v_\infty = -950\,\mathrm{km\,s^{-1}}$, $\beta = 1.50$ (photospheric input Gaussian: FWHM $\sim 350\,\mathrm{km\,s^{-1}}$) and a low dispersion $v_{\mathrm{turb}} = 0.05$. Despite minimal interstellar lines and the model predicting slightly excessive forward scattered emission between 0 and 0.2 v_∞, the model is fitted satisfactorily in the velocity range $0.25 \leq w < 1.00$. The τ_{rad} histogram seems to comprised of two components in that $\tau(w)$ steadily decreases from 1.3 at $w = 0.3$ to 0.4 at $w = 0.65$, before rapidly increasing to 1.5 at $w = 0.8$, and again falling to 0.2 at $w = 0.93$. Of these two 'components', the former is interesting as it resembles (perhaps only superficially) the pattern of the τ_{rad} fitting seen in that of the blue P V component in the sequential time-series spectra of NGC 6543 in chapter 3, where such a relatively deep absorption

Table 4.3. FUSE objects average mass-loss-ionisation fractions [$M_{\odot}\,\mathrm{yr}^{-1}$]

Object	P V 1118	O VI 1032	O VI 1037	S VI 933	S IV 1073	Si IV 1394
NGC 6826	6.8 e-09	6.7 e-11	4.2 e-11	8.1 e-10	–	–
IC 2149	1.5 e-09	1.4 e-11	–	–	–	–
IC 418	1.2 e-08	1.5 e-11	–	–	2.4 e-09	1.8 e-10
IC 4593	9.3 e-09	3.1 e-11	4.3 e-11	–	–	2.1 e-11

in the lower velocity part of the absorption profile could be attributable to a DAC-like feature, especially at the feature was seen to migrate bluewards before fading into the deeper absorption closer to the blue edge of the trough; unfortunately the IUE archive does not possess such time-series spectra as might be able to display such a DAC-like migration, and so this must remain speculation.

All average $\dot{M}q$ values across all modelled P Cygni profiles are listed in Table 4.3, and as with the $\dot{M}q$ calculations via SEI code for NGC 6543 as detailed in Chapter 3, the estimated error in of the order of $\sim 20\%$.

4.3 Time Variability Characteristics

The information as regards variability which can be obtained from such in-extensive data is limited. Although one can attempt TVS analyses upon the time series data for each object, due to the limited exposures available, the resulting TVS spectra may not reflect the true extent of the variability. Indeed for IC 4593 there are only four FUSE exposures available and so TVS analysis of such a limited sample is inconclusive. As regards further Fourier-based analyses upon the data, again the limited number of exposures over narrow timescales is far too sparse to be able to produce any Fourier power spectra of any value regarding the revelation of modulation periods. Instead, until such extensive data becomes avaliable, the initial TVS analysis will at least provide information as the to velocity range across which any variability becomes apparent; the corresponding greyscale plots may, as in the previous chapter, reveal the presence of large scale structures within the wind, which migrate bluewards through the wind over time.

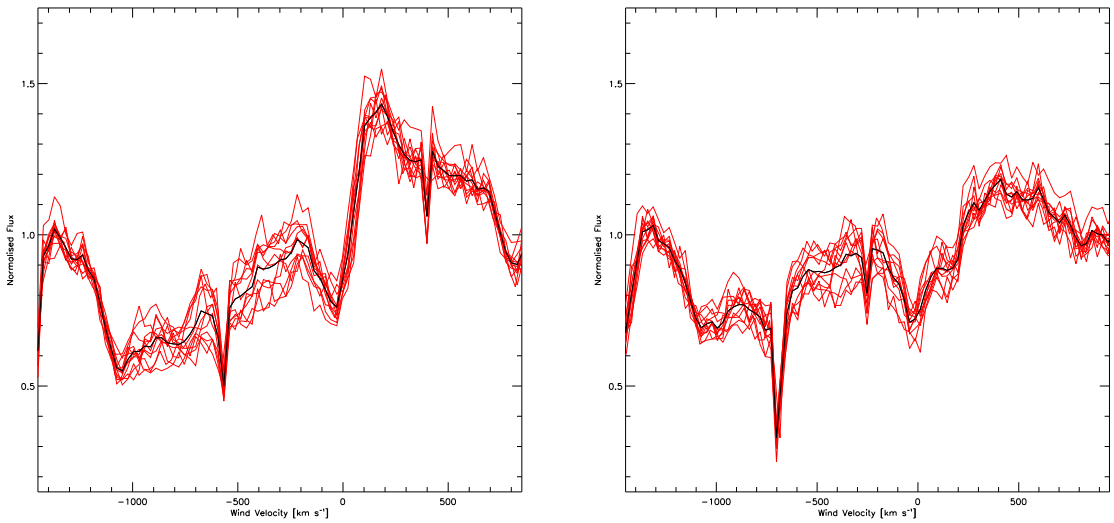

Fig. 4.13. NGC 6826: Overplot of P v doublet spectra illustrating the variable nature of the resonance profile: P v λ 1117.98 on the left and P v λ 1128.01 on the right.

4.3.1 Time Variability – NGC 6826

The overplot of spectra depicting minimum and maximum absorption – Figure 4.14 – shows a significant variation in the absorption trough of P v λ 1117.98, as well as a narrow variable margin in the emission peak; also in the absorption trough of P v λ 1128.01 but across a narrower velocity range than its more blueward counterpart.

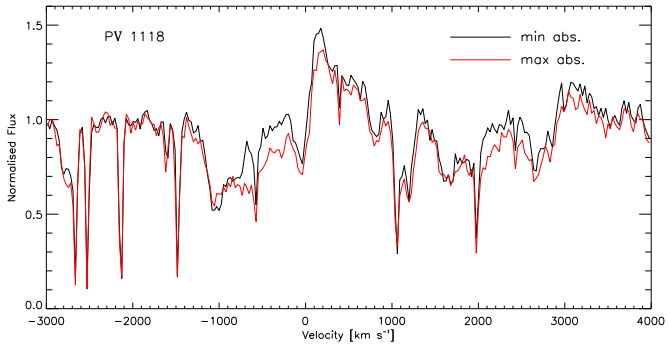

Fig. 4.14. NGC 6826: Dual spectra plot depicting P V doublet with minimum (black) and maximum (red) absorption.

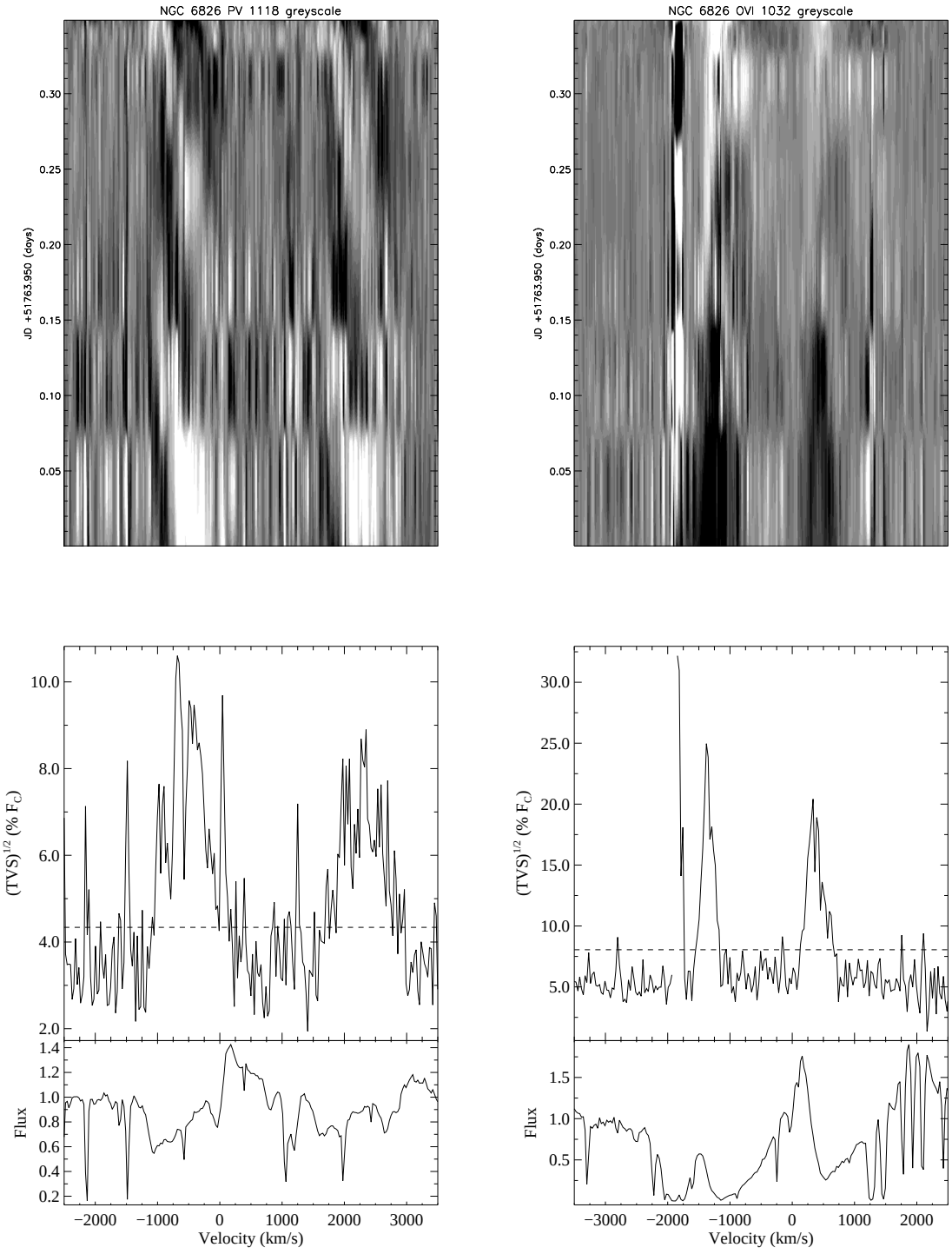

Fig. 4.15. TVS analysis plots (below) of the P Cygni profiles of the P V $\lambda\lambda$ 1117.98, 1128.01 (l) and O VI $\lambda\lambda$ 1031.93, 1037.62 (r) UV doublets of NGC 6826, where the upper panel of each TVS profile depicts the variance statistic, with changes above the 95% significance level (dotted line) highlighted. The corresponding greyscale depiction of each line profile's time-series spectra is also shown (above) depicting the temporal changes in the (vertically stacked) individual spectra, all normalised by the corresponding mean profile as shown in the lower panel beneath the TVS significance profile; the dynamical range of the greyscales on this page – and all subsequent greyscales in this chapter – is 0.95 (black) to 1.05 (white).

The TVS displays in Figure 4.15 show variation in the absorption of the P V $\lambda\lambda$ 1117.98, 1128.01 doublet, which for the blue component extends over an approximate range of -750 – 0 km s^{-1}; for the red componet the TVS shows significant variability between -1000 – $+250$ km s^{-1}; the TVS also indicates a narrow spike in the region of the blue component emission peak, across an approximate (maxiumum) range of between 0 – $+100$km s^{-1}. Not so in the TVS display for the O VI λ 1031.93, 1037.62 doublet, only in the emission peaks which unfortunately tends to mask any possible blue-edge variation of the O VI λ 1031.93 saturated absorption trough.

The equivalent width of the absorption trough in the blue component, as measured between 1112.8 and 1118.2 Å, is also variable between exposures, varying between a minimum of 0.8 Å to a maximum of 1.3 Å, with a mean of 1.1 Å (s.d: 0.2 Å); the emission peak, as measured between 1118.0 and 1120.9 Å, varies between 0.5 and 0.7 Å, with a mean of 0.6 Å (s.d: 0.1 Å).

Figure 4.15 illustrates the problem with greyscale images based upon a limited number of exposures: as the few spectra available are stitched together by the greyscale imaging algorithm, the result is a smearing effect as the time-axis limits of each exposure are merged to produce a continous display across the entire duration of the observation (i.e. the scale of the y-axis). It is therefore difficult pinpoint with a cursor precise loci of apparently migrating DAC-like features in terms of changing velocity and the corresponding time-reference. One solution is to reduce the resolution level of the time-axis from the greyscale (from the default setting of 500 to the low level of 10): this has the effect, as seen in Figure 4.16 of producing a stacked series of low resolution spectral strips which therefore allow for slightly more accurate estmations of the DAC's progressions in velocity and time which otherwise would not be possible; it also provide a clearer means by which one can estimate the errors of v and t.

Thus using such low-resolution greyscale images a series of esimated velocity-time coordinates can be obtained and consequently an estimate of the average accelerations of select DAC-like features can be derived from a least-squares method. The velocities of two such features have in the low-res. greyscale of the blue component of the P V doublet have been estmated – see Table 4.4 – and the resulting velocity-time coordinates have been plotted and superimposed by the subsequent least-squares average acceleration, as shown in Figure 4.17: both DAC-like features have an estimated average acceleration of $\sim 2 \times 10^{-2}$ km s^{-2} (with an estimated error of around 10%).

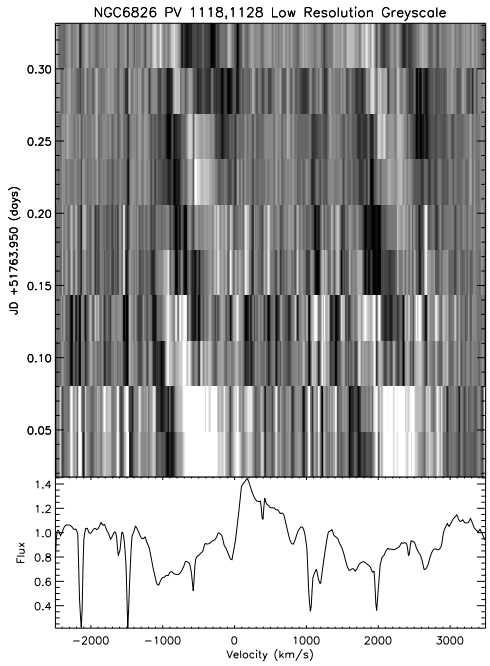

Fig. 4.16. Low-resolution greyscale of P V doublet from which approximate mesurements can be taken of both velocity and time index of the blueward progression of the DAC-like features observed in the greyscale display of the P1930401 data of PN NGC 6826 in order to estimate the albeit (linear and therefore approximate) acceleration of the 'DACs'.

Unfortunately this P1930 observation was unable to produce any clearly-defined spectra in either the 2asic or the 1bsic ranges i.e. for the $\sim$ 900 - 1000 Å wavelength range; however, an alternative dataset, that of the F160 Program, does exhibit clear spectra in this range as well, but unfortunately it shows little variability – for S VI $\lambda\lambda$ 933.38, 944.52, N IV λ 955.34, C III λ 977.02 – when investigated for time-variance.

4.3.2 Time Variability – IC 2149

Earlier studies of IUE UV data, have reported that no variability in the apparent stellar wind can be detected (Patriarchi & Perinotto 1997), so it is with a sense of intrigue that one applies the temporal-variability analysis techniques to the FUV data from FUSE, which provides spectral data over three nights.

As can be seen below in the TVS outputs of Figure 4.21, from P1041402 (1^{st} observation: UT date 1999-11-25) and P1041403 (3^{rd} observation: UT date 2000-01-14), the TVS doesn't show any significant varaiability across the P V doublet, only the narrow-

Table 4.4. NGC 6826 P V DAC progress

Blueward Velocity km s^{-1}	Time [MJD 51764 +]
892	0.03
962	0.06
1055	0.10
1126	0.13
1137	0.16
564	0.13
670	0.16
775	0.19
845	0.22
857	0.25
903	0.28

est peaks which could simply reflect the random variability in noise levels. However, for the P1041401 data (2^{nd} observation: UT date 1999-12-02), a greater spread of variability across the doublet is indicated, see Figure 4.20: between approximately -100 – -500 km s^{-1} in the blueward component ($\lambda_0 = 1117.98$ Å), and (approximately) across a range between -400 – 0 km s^{-1} with regard to the red component ($\lambda_0 = 1128.01$ Å).

The equivalent width of the absorption trough of the blue component of P V , as measured between 1113.6 and 1118.1 Å, varies between 0.8 and 0.9 Å (mean 0.9 Å, s.d. 0.1 Å); the emission peak, as measured between 1117.9 and 1121.5 Å, varies between 0.3 and 0.5 Å (mean 0.4 Å, s.d. 0.1 Å).

As with NGC 6826, the TVS for the P V doublet of IC 2149 – Figure 4.20 – shows a tendency for variability in the absorption troughs: between -1000 – 0 km s^{-1} in the blue component, and between -400 – 0 km s^{-1} in the red component. For the O VI doublet however the TVS is dominated by the strong variance peak for the Ly-β emission peak, but even with this dominating the TVS output, some variability in the O VI doublet could exist in the absorption trough of O VI λ 1031.93 and perhaps in the blue-edge of O VI λ 1037.62.

In the image of the minimum absorption (maximum flux) overplotted with the spectrum of maximum absorption (minimum flux) – Figure 4.19 – there is only an obvious difference between the two spectra across the lower velocities of the P V λ 1117.98 resonance line; the other seems to possess little difference between the two extreme cases.

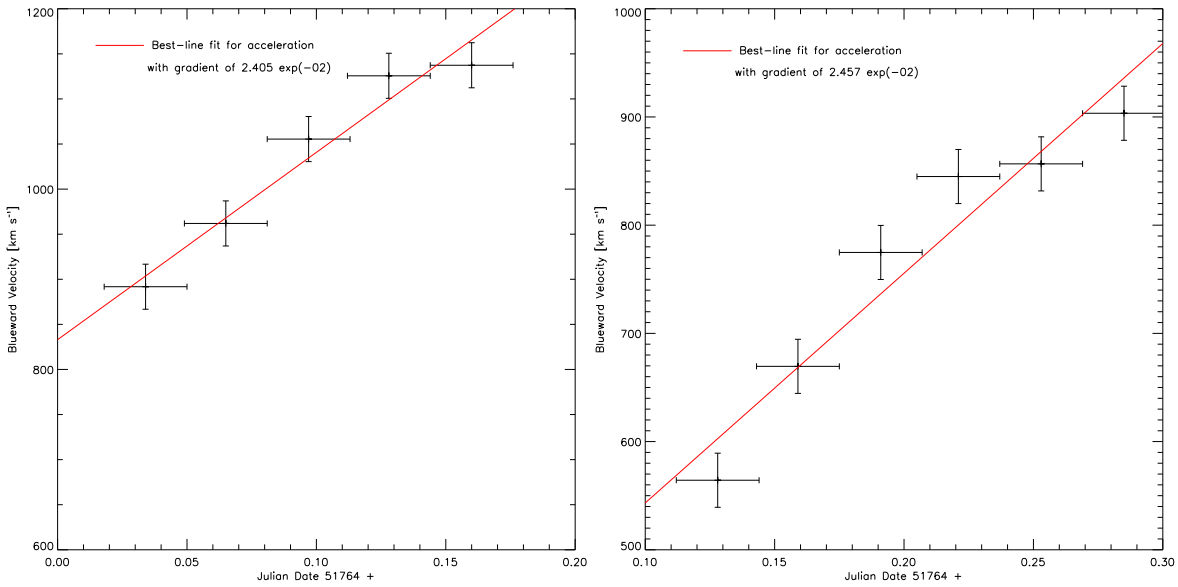

Fig. 4.17. The two sets of velocity-time coordinates of the DAC-like feature observed in the low-resoultion greyscale of the NGC 6826 P1930401 UV data are plotted and a least-squares algorithm has calculated the gradient of the best-fit line through the points: the acceleration of the first DAC-like feature is approximated at $\sim 2.4 \times 10^{-2}$ km s^{-2}; the acceleration of the second is similarly fitted and approximated at $\sim 2.5 \times 10^{-2}$ km s^{-2}.

As in the initial greyscale image of the P v doublet of NGC 6826, the lack of exposures for the IC 2149 data of P1041401 is also blended in an attempt to display the changing spectral profile across the duration of the night's observation. As well as with NGC 6826 the time resolution of the greyscale has been reduced (again to the low level of 10) with the result of a stacked series of spectra from which one can estimate the velocity-time loci of a blueward-progressing DAC-like feature seen in the absorption trough of the blue component of the P v doublet – see Table 4.5.

Again, as with the DAC-like features in NGC 6826, the velocity-time estimates for the DAC in the P v doublet can be applied to a least-squares algorithm and a subsequent average acceleration can be derived: this is shown in Figure 4.23 where the acceleration is estimated as $\sim 2 \times 10^{-2}$ km s^{-2} (again with an error of around 10%).

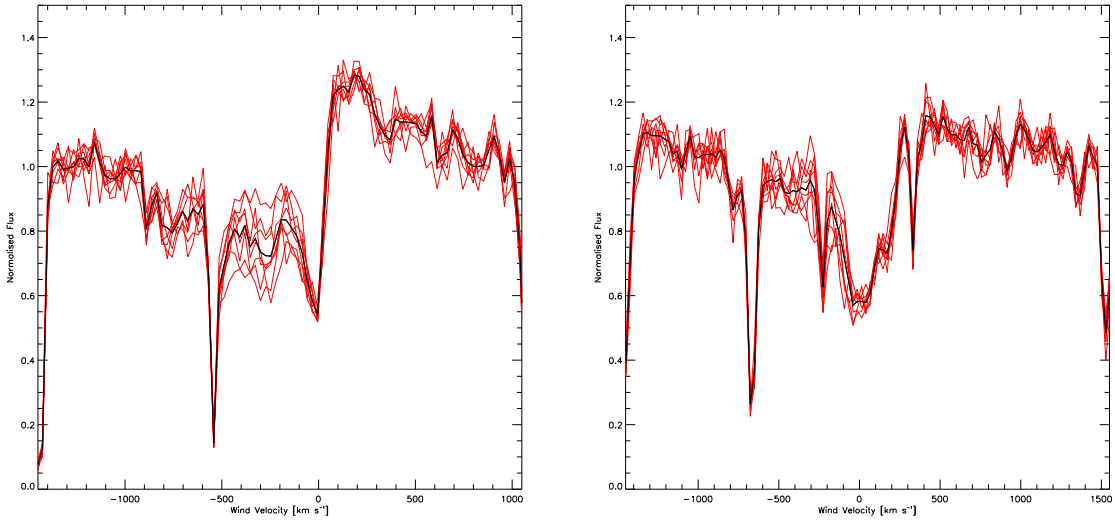

Fig. 4.18. IC 2149: Overplot of P V doublet spectra illustrating the variable nature of the resonance profile: P V λ 1117.98 on the left and P V λ 1128.01 on the right.

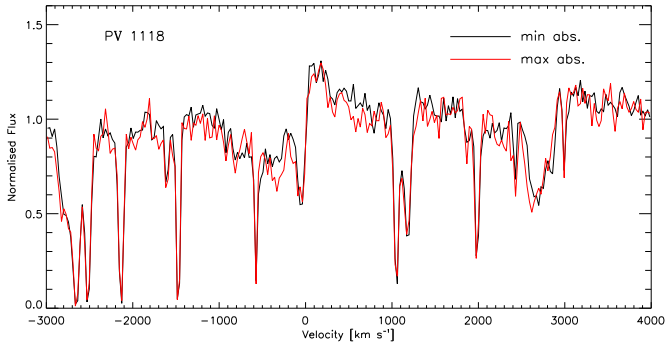

Fig. 4.19. IC 2149: Dual spectra plot depicting P V doublet with minimum (black) and maximum (red) absorption.

Table 4.5. IC 2149 P V DAC progress

Blueward Velocity km s^{-1}	Time [MJD 51514 +]
190	0.05
213	0.09
319	0.13
389	0.17
436	0.21
588	0.25
646	0.29
716	0.34
740	0.38

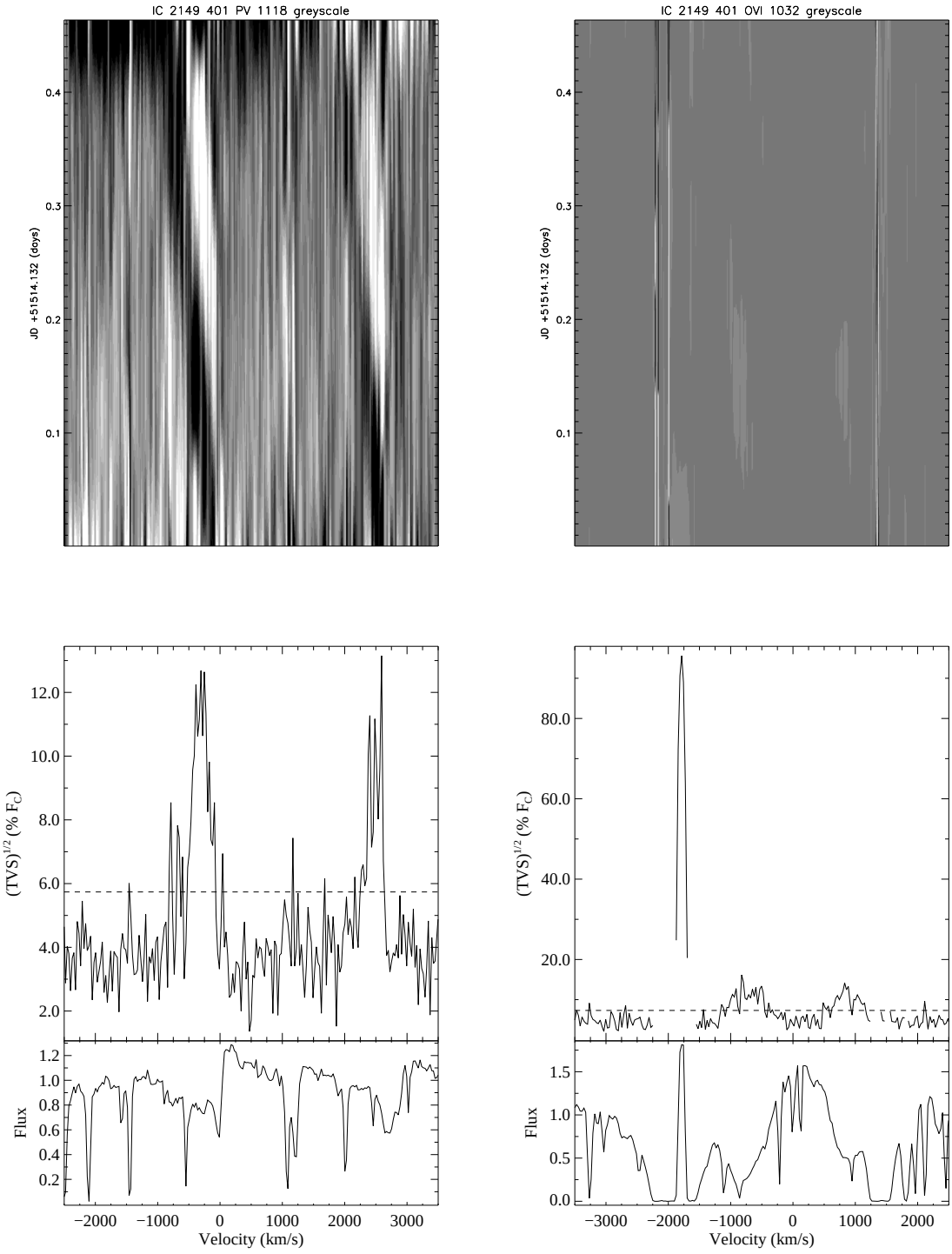

Fig. 4.20. TVS analysis plots (below) of the P Cygni profiles of the P V $\lambda\lambda$ 1117.98, 1128.01 (l) and O VI $\lambda\lambda$ 1031.93, 1037.62 (r) UV doublets of IC 2149; the corresponding greyscale depiction of each lines time-series spectra is also shown (above).

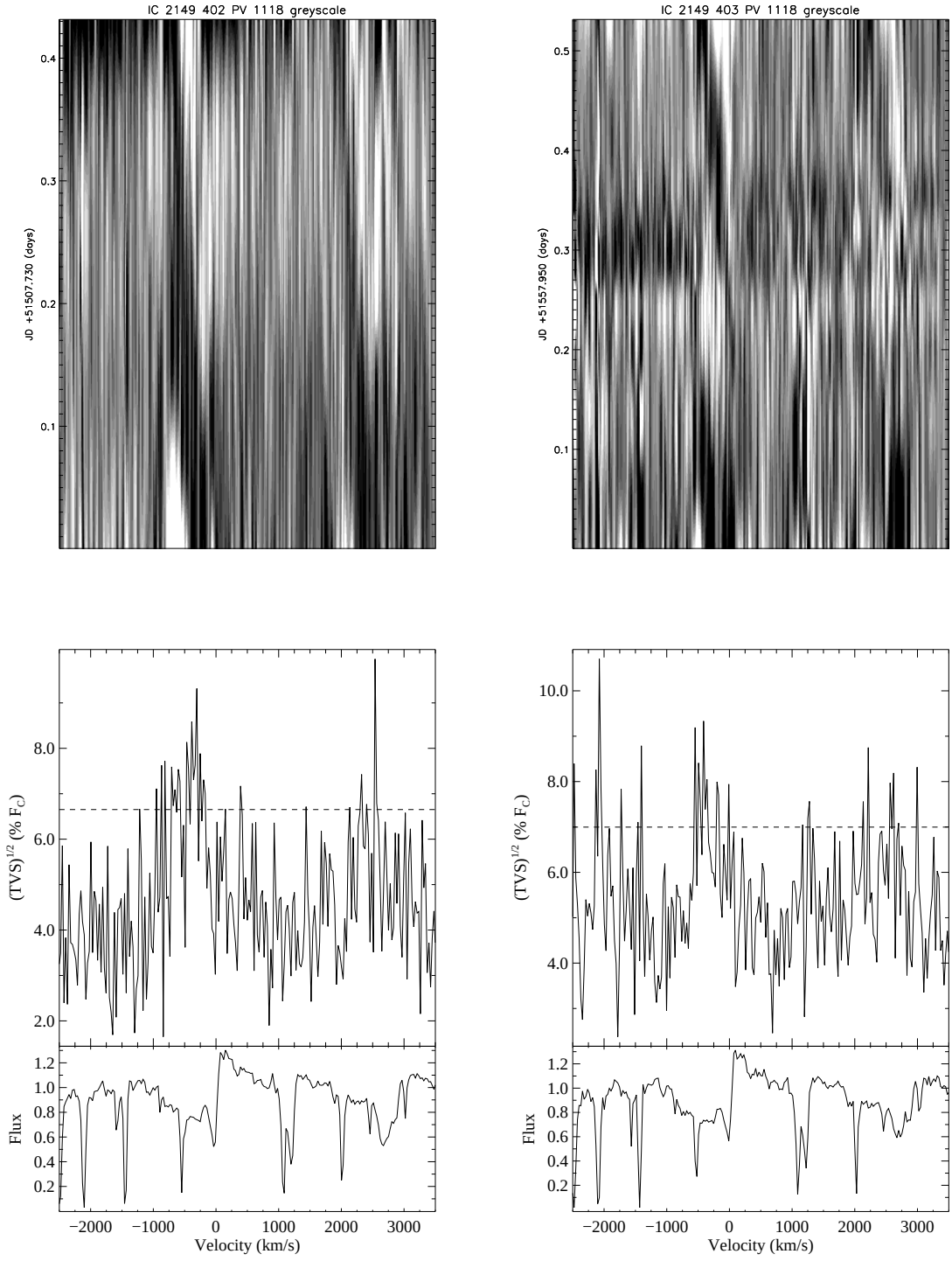

Fig. 4.21. IC 2149: TVS & greyscale outputs for the P v doublet of the 1^{st} (l) and 3^{rd} (r) nights' data.

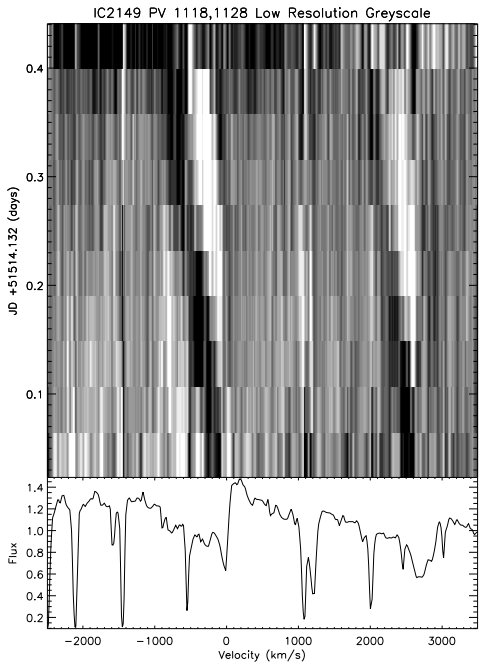

Fig. 4.22. A low-resolution greyscale of P V doublet from which an approximate measurement can be taken of both velocity and time index of the blueward progression of the DAC-like feature observed in the greyscale display of the P1041401 data of PN IC 2149 in order to estimate the albeit (linear and therefore approximate) acceleration of the 'DAC'.

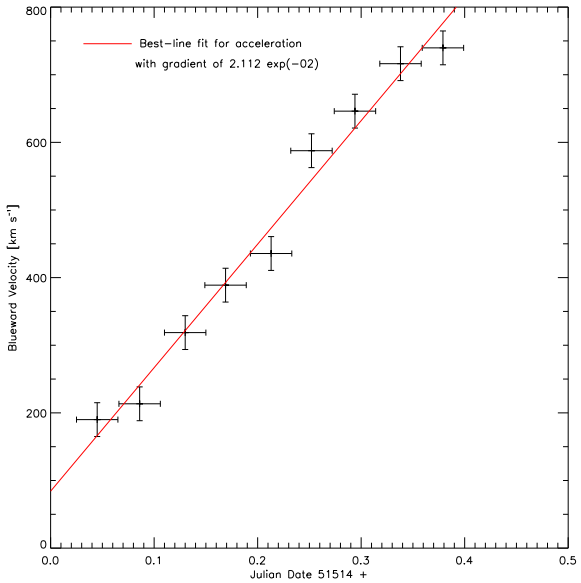

Fig. 4.23. The velocity-time index coordinates as measured from the low-resolution greyscale of the IC 2149 P1041401 UV data are plotted and a least-squares algorithm has calculated the gradient of a best line fit through the points: the linear (and therefore approximate) acceleration of the DAC-like feature is therefore estimated at $\sim 2.1 \times 10^{-2}$ km s^{-2}.

4.3.3 Time Variability – IC 418

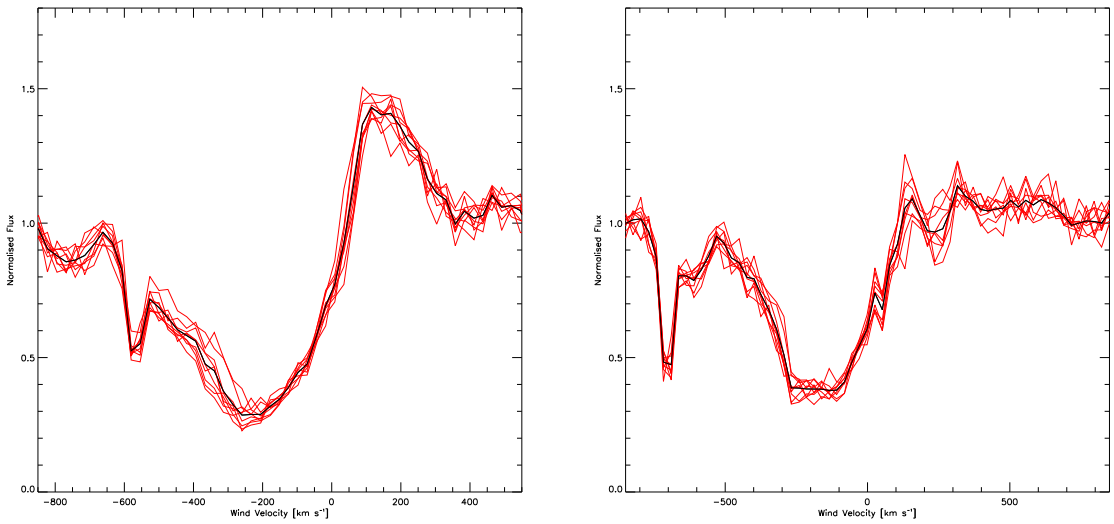

Fig. 4.24. IC 418: Overplot of P V doublet spectra illustrating the variable nature of the resonance profile: P V λ 1117.98 on the left and P V λ 1128.01 on the right.

The overplot of minimum (black) and maximum (red) absorption in the P V doublet – Figure 4.25 – taken from the 2alif spectra, shows the extremes of the flux levels but does not satisfactorily reproduce the relative low level of variance as picked up by the TVS.

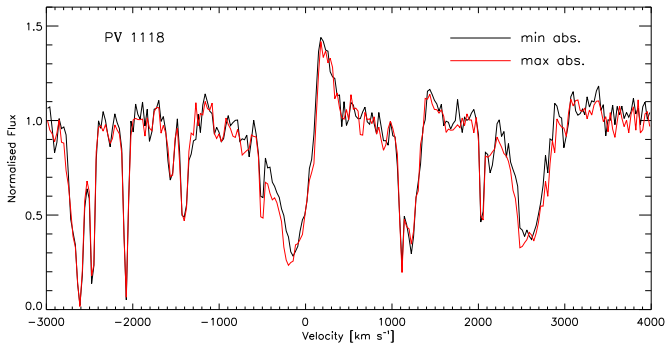

Fig. 4.25. IC 418: Dual spectra plot depicting P V doublet with minimum (black) and maximum (red) absorption.

The TVS outputs for IC 418 in Figure 4.26 show a little variability in the P V doublet: a narrow margin in absorption, between -50 – -25 km s^{-1}, and between 0 – $+25$ km s^{-1} in emission for the blue component (λ_0 = 1117.98 Å); the red component (λ_0 = 1128.01

Å) shows variation over a narrow -300 – -200 km s^{-1} margin in the absorption trough, and three significance peaks across approximately 0 – $+300$ km s^{-1} in the (relatively low) emission peak. There is no real indication of any variation in the saturated O VI doublet (only a strong TVS peak in the region of the Ly-β emission spike).

In terms of equivalent width, the blue P V component absorption trough, as measured between 1113.8 and 1118.5 Å, varies between 1.2 and 1.4 Å (mean 1.3 Å, s.d. 0.1 Å); the EW of the emission peak, measured between 1118.3 and 1121.1 Å, varies between 0.2 and 0.5 Å (mean 0.3 Å, s.d. 0.1 Å).

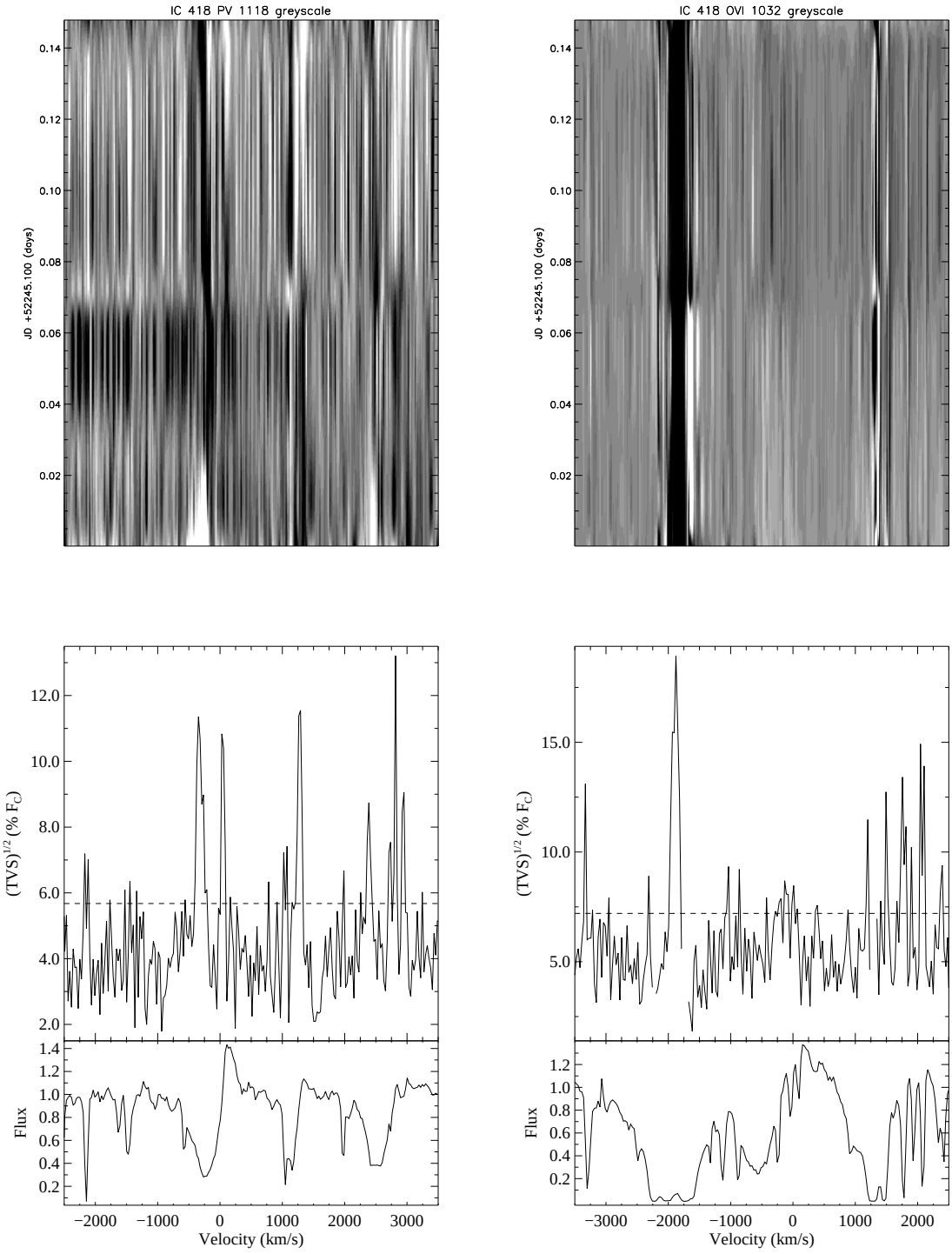

Fig. 4.26. TVS analysis plots (below) of the P Cygni profiles of the P V $\lambda\lambda$ 1117.98, 1128.01 (l) and O VI $\lambda\lambda$ 1031.93, 1037.62 (r) UV doublets of IC 418; the corresponding greyscale depiction of each lines time-series spectra is also shown (above).

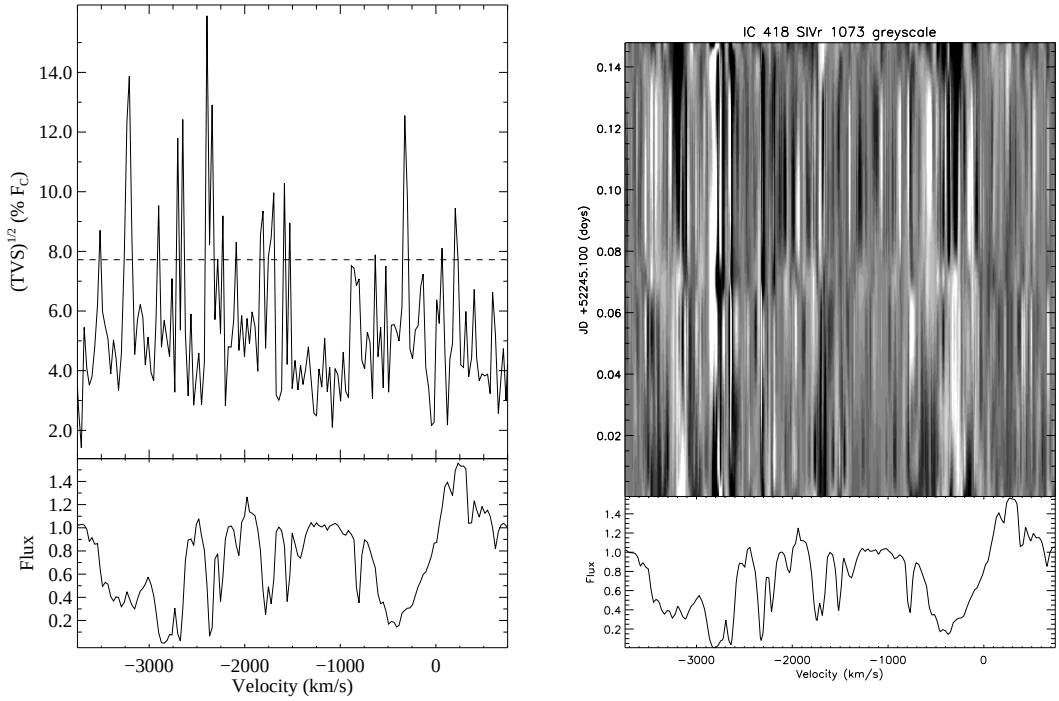

Fig. 4.27. IC 418: TVS & greyscale outputs, centred on the stronger red component of the S IV $\lambda\lambda$ 1062.66, 1072.97 doublet.

4.3.4 Time Variability – IC 4593

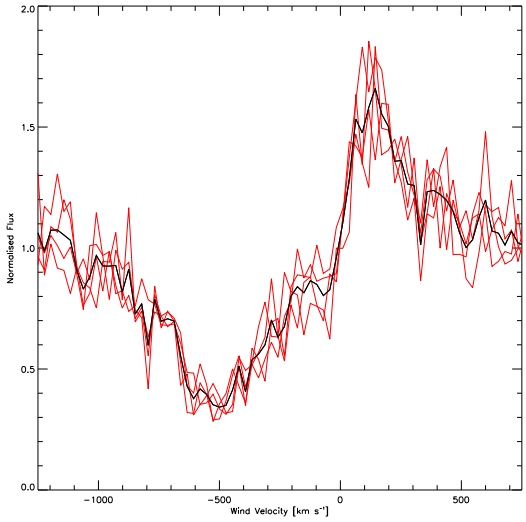

Fig. 4.28. IC 4593: Overplot of P V doublet spectra illustrating the variable nature of the resonance profile: P V λ 1117.98

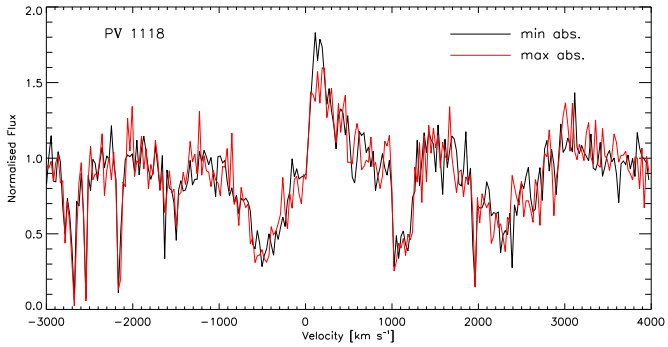

Fig. 4.29. IC 4593: Dual spectra plot depicting P V doublet with minimum (black) and maximum (red) absorption.

For the central star of IC 4593, in terms of the FUSE data, there is an extremely limited number of exposures: only four from B0320102. With so few spectra it is impossible to detect any indication of any variability in the limited data; indeed, even in the image of the over plotted spectra – Figure 4.29 – it is difficult to determine whether the fluctuations are true variability or simply noise. The TVS outputs of Figure 4.30 for both the P V and the O VI doublets fail to show any significant variance.

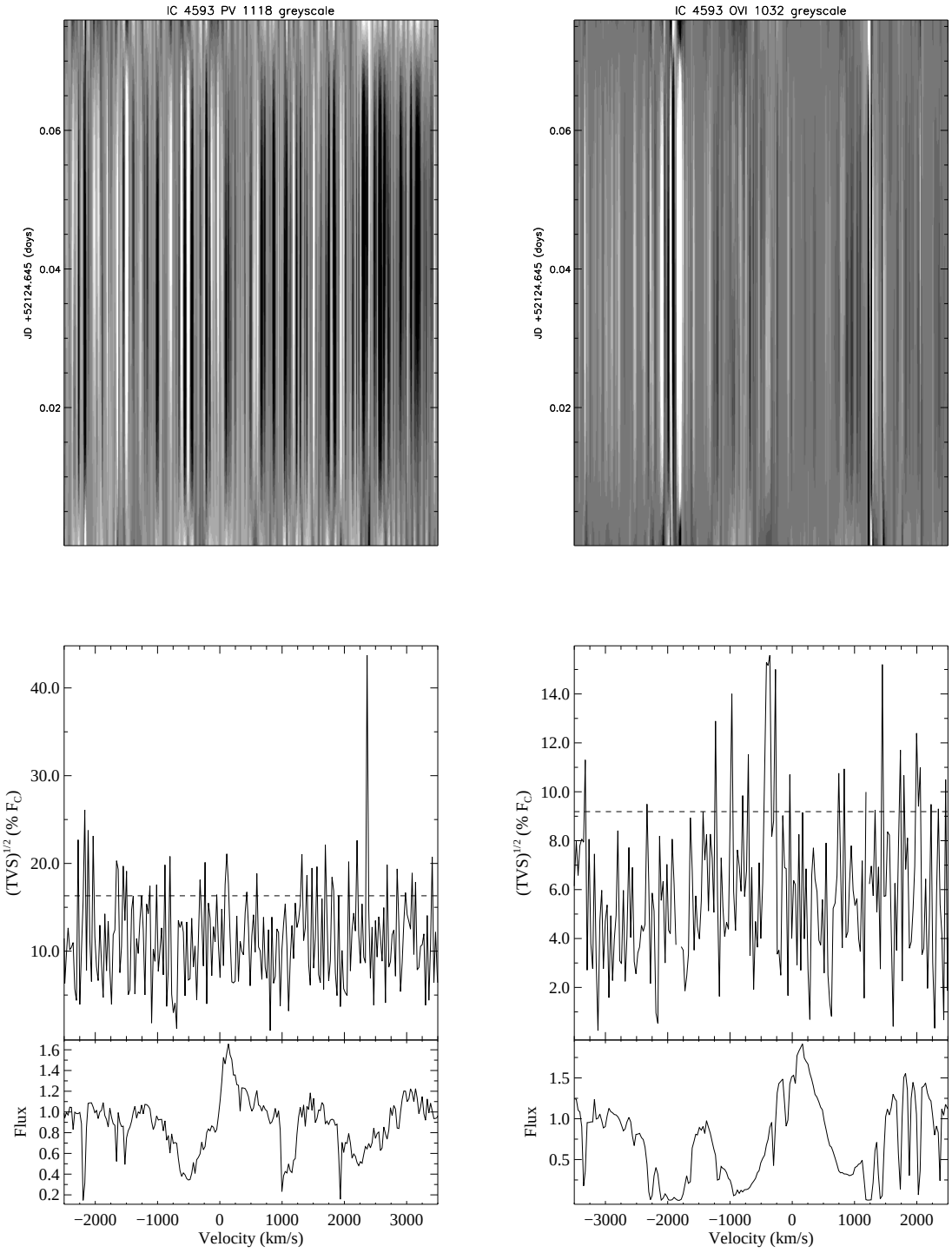

Fig. 4.30. TVS analysis plots (below) of the P Cygni profiles of the P V $\lambda\lambda$ 1117.98, 1128.01 (l) and O VI $\lambda\lambda$ 1031.93, 1037.62 (r) UV doublets of IC 4593; the corresponding greyscale depiction of each lines time-series spectra is also shown (above).

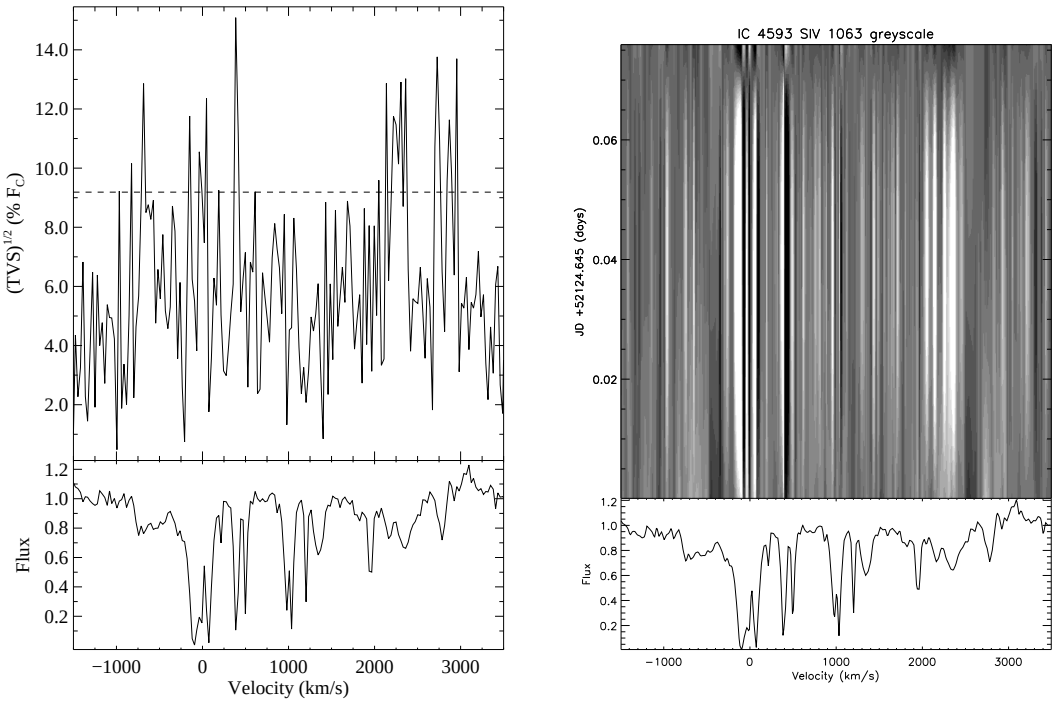

Fig. 4.31. IC 4593: TVS & greyscale outputs for the S IV $\lambda\lambda$ 1062.66, 1072.97 doublet.

4.4 Summary

The main aim of this chapter has been to try to replicate some of the results of the analysis of NGC 6543 in the previous chapter: to examine whether the structure found within the outflow of NGC 6543 – particularly the DAC-like feature seen migrating bluewards within the absorption troughs of the P V $\lambda\lambda$ 1117.98, 1128.01 doublet – could be observed in the outflows of other CSPNs. The unfortunately-limited FUSE UV spectra of four other CSPNs has been subjected to similar time-variance analysis techniques: the TVS analysis had been applied to the time-series spectra available and subsequent greyscale displays have provided image-based representations of any variabilty contained therein. As well, SEI modelling has been applied to certain P Cygni profiles contained in the UV spectra and measures of $\dot{M}q$ have been obtained. The variablilty exhibited in the shapes of the P Cgyni profiles, particularly the blue component of the P V doublet, of these four CSPNs, is reflected in the fluctuations in the measured value of the blue P V components' equivalent widths, details of which are collated in Table 4.6.

Table 4.6. FUSE objects' P V equivalent width measurements [Å]

Object	Wavelength Range [Å]	Min EW – Max EW	Mean EW	SD
NGC 6826	1112.8 – 1121.4	0.31 – 0.92	0.62	0.20
IC 2149	1113.5 – 1121.5	0.35 – 0.67	0.47	0.10
IC 418	1113.6 – 1120.0	0.83 – 1.12	0.98	0.11
IC 4593	1113.4 – 1121.7	0.53 – 0.73	0.63	0.08

The TVS analysis of the FUSE spectral sections containing the *unsaturated* P V doublet have shown the greatest variability across a wider velocity range than other P Cygni profiles such as the more saturated O VI $\lambda\lambda$ 1031.93, 1037.62 doublet; the extent of the P V doublet variability, as measured in terms of the central velocity of each component, is detailed below in Table 4.7 for each of the four fragmented time-series targets.

Table 4.7. FUSE objects' P V TVS (approximate) variability ranges [km s^{-1}]

Object	Variance Detected	Blue Component $\lambda_0 = 1117.98$ Å	Red Component $\lambda_0 = 1128.01$ Å
NGC 6826	yes	-750 – 0	-1000 – $+250$
IC 2149	yes	-1000 – 0	-400 – 0
IC 418	yes	-50 – -25 & 0 – $+25$	-300 – -200 & 0 – $+300$
IC 4593	no	–	–

The P1930401 data of NGC 6826 and the P1041401 data of IC 2149 have demonstrated higher levels of variability, and this can be seen in the resulting greyscales which appear to show DAC-like features which migrate towards the blue edge of the absorption troughs of their respective P Cygni profiles: from the NGC 6826 P1930401 data, the two DACs migrate between ~ -900 and ~ -1150 km s^{-1} and between ~ -550 and ~ -900 km s^{-1}; the DAC seen in the IC 2149 P1041401 data appears to migrate between ~ -200 and ~ -750 km s^{-1} (see Table 4.8 below). The limited number, and non-uniform time index spacing of the exposures in such data proves a handicap when trying to observe the blueward migration of these DAC-like features: only a reduced resolution of the time-axis can help towards a rough estimate of the average acceleration of the DAC-like features. For the two DACs seen within the NGC 6826 data, and also the DAC observerd in the IC 2149 data, the average acceleration is $\sim 2 \times 10^{-2}$ km s^{-2}, which when re-scaled by the $R_\star/v_\infty$ flow-time factor of each object respectively, gives a $(dv/dt)(R_\star/v_\infty)$ of ~ 25 km s^{-1} for NGC 6826 and ~ 29 km s^{-1} for IC 2149 – both of which compare favourably with the upper $(dv/dt)(R_\star/v_\infty)$ factor for NGC 6543 of ~ 26 km s^{-1}, as shown in the previous chapter – and all three are of a similar order to that given for the O7 III star example mentioned in Chapter 3, namely ~ 10 km s^{-1}.

Table 4.8. FUSE objects' P v DAC migration

DAC	Velocity Range [km s^{-1}]	ΔT	Acceleration [km s^{-2}]	$\times R_\star/v_\infty$
NGC 6826 A	-900 – -1150	$\sim$0.13 d	2.4 $\times 10^{-2}$	$\sim$25 km s^{-1}
NGC 6826 B	-550 – -900	$\sim$0.15 d	2.5 $\times 10^{-2}$	$\sim$25 km s^{-1}
IC 2149	-200 – -750	$\sim$0.33 d	2.1 $\times 10^{-2}$	$\sim$29 km s^{-1}

The lack of extensive datasets for these CSPNs – in terms of a large number of exposures – prevents one from subjecting such time-series data to a proper Fourier analysis in order to try and uncover any potentially periodic modulation of such structures. However this chapter has shown that the existence of DAC-like features, as seen within the spectra of NGC 6543 in the previous chapter, is not an isolated phenomenon; but whether this is a common feature of CSPN outflows or not, can only be properly investigated with a sufficiently extensive wealth of time-series data.

However, it should be pointed out that despite the lack of time series data available for CSPNs, this study has managed to present evidence of DAC-like stuctures in the outflows of three (possibly four) central stars; and therefore this might suggest that structured

winds may be as prevalent in CSPN outflows as they appear to be in the UV spectra of the stellar winds of O stars.

Chapter 5

ESO Optical Spectra of Young CSPNs

5.1 Introduction – ESO Time-series Objects & their observation

In March 2006 observations were carried out of three young H-rich (O star type) planetary nebulae: Hen 2-138, Hen 2-131, and NGC 2392 (commonly known as the Eskimo Nebula). The main aim of the run was to obtain time-series optical spectra over 3 nights of observing, the data from which would be used to seek out structure within the stellar winds emanating from the central stars of these nebulae; and to uncover the nature of any modulated behaviour. The monitoring of such structural modulation would aid the understanding of the possible causes of such behaviour, including the occurrence of non-radial pulsations (NRPs) which it has been suspected may be a direct precursor of co-rotating interaction regions (CIRs) which themselves create large-scale structure in the winds of massive OB stars (Cranmer & Owocki 1996). Therefore any signs of modulated structure with the outflow of these CSPNs would suggest further similarities between the behaviour of H-rich CSPNs and OB stars.

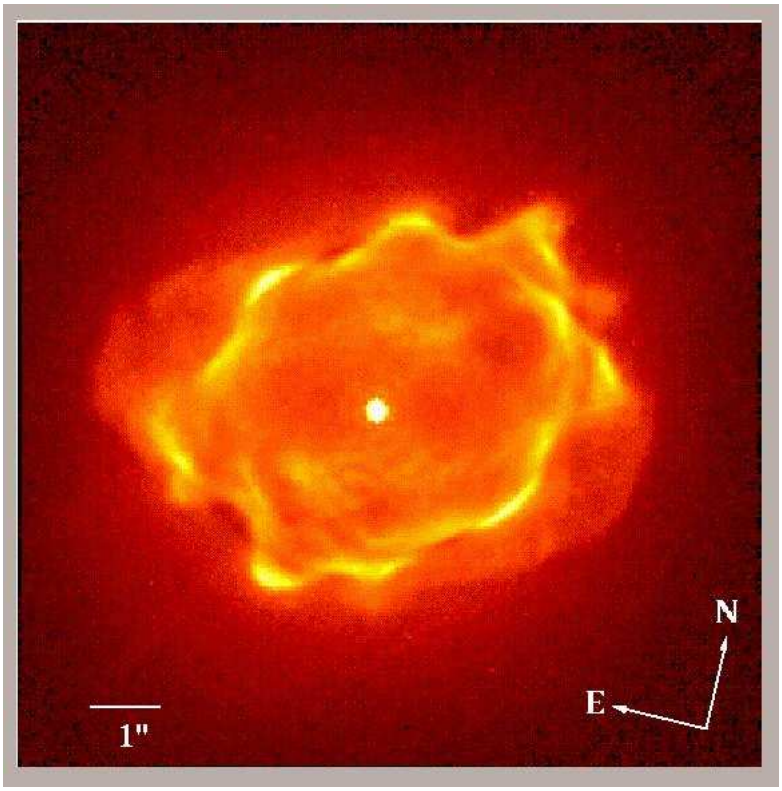

Fig. 5.1. HST WFPC2 image of PN Hen 2-138, captured via the Hα filter: http://www.aip.de/groups/sternphysik/stp/PN/cdrom/images/

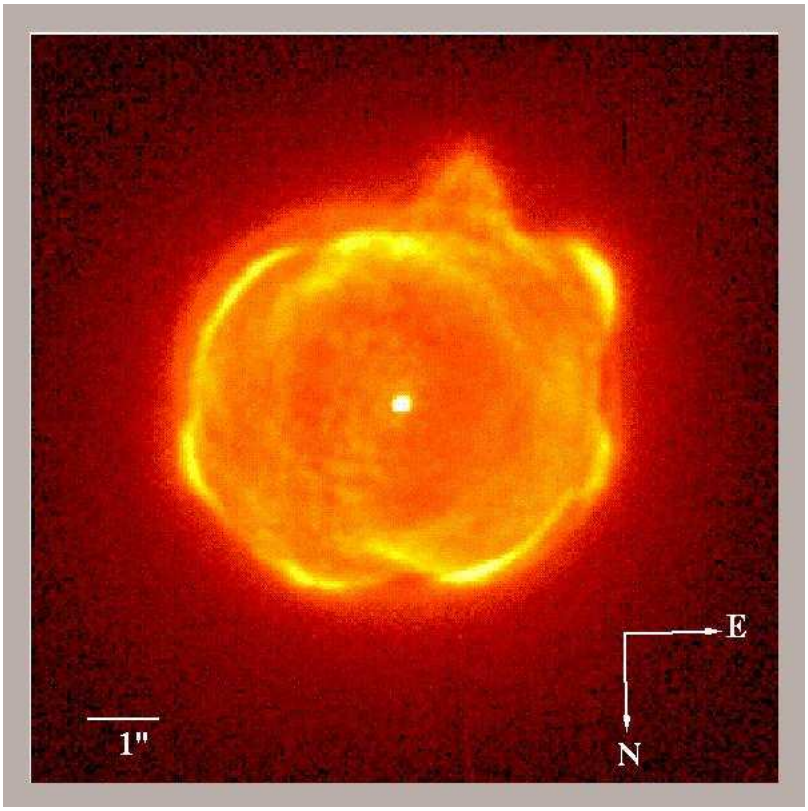

Fig. 5.2. HST WFPC2 image of PN Hen 2-131, captured via the Hα filter: http://www.aip.de/groups/sternphysik/stp/PN/cdrom/images/

Fig. 5.3. HST WFPC2 image of PN NGC 2392: the different colours of the image highlight different gases comprising the nebula: nitrogen (red), hydrogen (green), oxygen (blue), and helium (violet): http://www.stsci.edu/ inr/thisweek1/thisweek029.html

Table 5.1. Hen 2-138 central star parameters

Parameter	Value	Ref.
Sp. type	Of (H-rich)	Mendez et al. (1998)
T_{eff}	28000 ± 2000 K	This study
Log g	2.9 ± 0.2	This study
Mass	0.60	This study
Log $(L/L_{\odot})$	3.87	This study
Distance	3.5 kpc	Zhang (1995)
Radial velocity	-47 km s^{-1}	Schneider et al (1983)

5.1.1 Hen 2-138

The nebula possess a complicated knotted appearance, with bubble-like structures arranged in a fairly symmetrical manner about an overall elliptical morphology. The central star of Hen 2-138 (HD 141969) has been analysed in the search for photometric variations as a result of positive results occurring in similar studies in other CSPNs (Hutton & Mendez 1993): the variations found were on the time scale of hours, and were therefore similar to those found in the photometric observations of the central stars of IC 418 (Méndez et al. 1986) and IC 4593 (Bond & Ciardullo 1989). Both HD 141969 (the central star of Hen 2-138) and HD 138403 (the CS of Hen 2-131) have exhibited fluctuations in magnitude of between 0.10 and 0.15 mag over the timescale of hours. These four central stars are also similar in other parameters: they all possess relatively low effective temperatures of between 27,000 and 40,000 K (Méndez et al. 1988, 1990) as well as radial velocity variations (Méndez 1989; Méndez et al. 1990), and also changes in emission and P Cygni profiles (Méndez et al. 1988, 1990; Méndez 1991).

5.1.2 Hen 2-131 & NGC 2392

These two planetary nebulae and their respective central stars HD 138403 (Hen 2-131) and HD 059088 (NGC 2392) have previously been studied extensively with the aim of testing the validity of radiatively driven wind theory (see Kudritzki et al. 1997; Pauldrach et al. 2003; Kudritzki et al. 2006).

A prime motivation was to see whether the plane-parallel models used, based upon the model fitting of Balmer lines, can sufficiently match the observed wind profile with a degree of success comparable to that previously achieved in similar modelling the winds of O, B, and A stars.

Despite a lack of reliable CSPN distance measures, earlier efforts involved plotting the

positions of CSPNs upon the $\log g$ – $\log T_{\rm eff}$ diagram and comparing these to plots of post-AGB tracks obtained via the $\log L$ – $\log T_{\rm eff}$ diagram: in this way the stellar masses could be read in the $\log g$ – $\log T_{\rm eff}$ diagram, and hence the corresponding luminosities could be calculated; also, with knowledge of de-reddened apparent magnitudes, stellar distances could even be derived (Kudritzki et al. 1997). The results of this analysis seemed to echo the success previously achieved with the CSPN results forming a relatively small scatter about the wind-momentum–luminosity relation diagram for O, B and A supergiant stars, but extrapolated back for the lower luminosities of the CSPNs.

An alternative modelling approach, based upon a homogeneous, spherically-symmetric, radiatively-driven atmospheric outflow, involved solving hydrodynamic and nLTE problems concerning rate equations and radiative transfer (Pauldrach et al. 2003). These problems are solved iteratively, whereby a synthesised spectrum is calculated and then compared with the observed spectrum and, as necessary, subsequent adjustments are made to stellar parameters (radius, terminal velocity, and then mass) in order to improve the fit.

When this latter iterative technique was applied to spectra of the central stars of Hen 2-131 and NGC 2392, some interesting (and rather conflicting) results were thrown up.

The directly-measured terminal velocity of Hen 2-131, given at $\sim 500\,{\rm km\,s^{-1}}$ fits neatly between post-AGB evolution tracks of masses 0.565 and 0.625 $M_{\odot}$, and so seemingly indicating a mass of $\sim 0.6\ M_{\odot}$, but this mass should be consistent with a mass-loss rate of $\sim 10^{-8}\ M_{\odot}\,{\rm yr^{-1}}$, but is in fact estimated to be 100 times as much, and such a mass-loss rate of $\sim 10^{-6}\ M_{\odot}\,{\rm yr^{-1}}$ should only emanate from a central star of a mass $\sim 0.9\ M_{\odot}$.

With NGC 2392, its measured terminal velocity (as similarly compared to the post-AGB tracks) indicated a mass of $\sim 0.9\ M_{\odot}$ but the observed mass-loss rate of $\sim 10^{-8}\ M_{\odot}\,{\rm yr^{-1}}$ was too small for this large a mass, and conversely indicated a smaller mass of $\sim 0.6\ M_{\odot}$.

Alternatively, taking the the mass-loss rates determined via the post-evolution mass-luminosity tracks as a starting point, would seem to predict terminal velocities which differ by a factor of 2 or 3 from the values obtained by *direct measurement*.

The observed UV spectra of Hen 2-131 provided an indication of the success of any particular assumed parameter value through the direct comparison of the modelled profile when superimposed upon that observed. With a preliminary mass ($0.6\ M_{\odot}$) derived from the directly-measured terminal velocity, the subsequent mass-loss rate and hydrodynamical

model was too low to be able to accurately match the observed profile, with the result that the luminosity had to be increased as this had a direct bearing on the mass-loss rate which itself had to increase in order for the model to better reproduce the observed spectrum, while also adjusting the mass (up to 0.9 $M_{\odot}$) in order to maintain the same directly-observed terminal velocity.

With the UV spectrum of NGC 2392, however, as the initial mass-loss rate (and resultant mass of 0.9 $M_{\odot}$) was too high to match the observed spectrum and so had to be lowered through the adjustment of the luminosity (and subsequent mass down to 0.6 $M_{\odot}$) in order to match the observed spectrum.

However, other parameters were also taken from observed quantities, for example $T_{\rm eff}$ was derived from the ionisation equilibrium of Fe ions in the UV spectra, which for the weak-winded NGC 2392 is 40,000 K. Its low terminal velocity of $-400\,{\rm km\,s^{-1}}$ coupled with its lowered luminosity (reduced in order to better match the model spectral profile with that of the observed UV) resulted in a small radius of $\sim 1.5\ R_{\odot}$, which together with the measured v_{∞} gave a stellar mass of $\sim 0.4\ M_{\odot}$ – less than half the $\sim 0.9\ M_{\odot}$ mass that was predicted earlier via the mass-luminosity relationship.

For Hen 2-131, the mass-luminosity relationship suggested a stellar mass of $\sim 0.6\ M_{\odot}$ for the measured terminal velocity of $-500\,{\rm km\,s^{-1}}$ and temperature of 33,000 K, but for these measured values the UV model under-predicted the mass-loss rate as compared to the observed spectrum and so the luminosity needed to be increased to raise the observed mass-loss rate leading to a much larger stellar radius of 5.5 $R_{\odot}$, and hence an increase of stellar mass from the M-L relationship-derived 0.88 $M_{\odot}$ to an even larger 1.39 $M_{\odot}$ – almost at the Chandrasekhar limit.

When applied to the wind-momentum–luminosity relation diagram, the results if the latter hydrodynamical analysis provide a narrower spread of plotted points about the extrapolated wind-momentum–luminosity relation as defined by the more massive and hotter stars.

5.2 European Southern Observatory 3.6 m Telescope & the HARPS Spectrograph

The *H*igh-*A*ccuracy *R*adial velocity *P*lanet *S*earcher (*HARPS*) spectrograph was chosen because of its high resolving power, R = 111,000 over the 4000-7000 Å wavelength range,

Table 5.2. Hen 2-131 & NGC 2392 central stars' parameters

Parameter	Hen 2-131	NGC 2392	Ref.
Sp. type	Of	Of	Mendez et al. (1998)
T_{eff} [K]	32000	44000	Kudritzki et al. (2006)
Log g	3.2	3.6	Kudritzki et al. (2006)
Mass [$M_{\odot}$]	0.71	0.86	Kudritzki et al. (2006)
Log ($L/L_{\odot}$)	4.07	4.30	Kudritzki et al. (2006)
Distance [kpc]	3.3	2.8	Kudritzki et al. (2006)
Radial velocity [$\mathrm{km\,s^{-1}}$]	-1	$+75$	Schneider et al. (1983)

Table 5.3. ESO 3.6 m & HARPS specifications

Parameter	Value
Wavelength range	4000–7000 Å
Resolving power, R	110,000
Signal-to-noise, S/N	≥ 40

thus enabling the observer the opportunity to view and subsequently analyse spectral lines at a different point in the wind. The clarity of the P Cygni profiles observed is aided by the high signal-to-noise ratio, with S/N ≥ 40 for the 30 minute duration of the exposures.

Located at the La Silla observatory on the edge of the Atacama desert in northern Chile and at an altitude of 2400 m above sea level, the 3.6 m telescope is equatorially-mounted and uses a Cassegrain focus (f8) to direct light via towards the HARPS spectrograph. It has a pointing accuracy to within 5 arcsec (RMS) and a PSF of $\sim$ 0.7-0.8.

The HARPS spectrograph is an eschelle spectrograph, contained within a vacuum vessel which help to reduce the velocity drift otherwise caused by variations in temperature and air pressure. It is fed by a pair of fibres, one of which collects the starlight while the other is directed toward a Thorium-Argon lamp to record a reference spectrum.

5.2.1 Data Reduction Pipeline

The HARPS Consortium have developed software which allows for the entire data reduction procedure to be carried out in near real-time; the reduction depends on the observing mode as well as the spectral type of the star – these parameters are received by the pipeline from the FITS header information of the raw data.

Reduction results include:

- dark current values,
- order localisation,

- flat fields,
- dispersion solution for calibrations;
- extracted spectra for all modes;
- precise radial velocity – for simultaneous Th reference only;
- cross correlation function – for simultaneous Th reference only.

The pipeline runs automatically for all spectra at the telescope with no intervention required by the user; warning pop-up windows are handled by the support astronomer.

5.2.2 ESO Time-series Optical Data

The time-series data under investigation was taken with the 3.6m optical telescope at the La Silla observatory in Chile, and the data collected upon the HARPS spectrograph, over three nights between March 24^{th} and March 26^{th} 2006 (BJD 2453818.67601 to 2453820.90567), with a total of 18 spectra being taken, 6 over each of the consecutive nights.

Details of exposure times (UT and MJD), targets, and duration are listed in Table 5.4

Table 5.4: ESO La Silla observation log summary.

UT Date &	Time (start)	MJD (start)	Target	Exposure [s]
2006 March 24	00:02:28.611	53818.5139	NGC 2392	1800
	00:33:30.717	53818.5354	NGC 2392	1800
	01:04:29.464	53818.5569	NGC 2392	1800
	01:35:13.489	53818.5783	NGC 2392	1800
	02:06:02.195	53818.5997	NGC 2392	1800
	02:36:53.142	53818.6211	NGC 2392	1800
	03:23:03.749	53818.6527	Hen 2-131	1800
	03:56:26.961	53818.6760	Hen 2-138	1800
	04:28:46.776	53818.6983	Hen 2-131	1800
	05:00:16.016	53818.7203	Hen 2-138	1800
	05:31:59.367	53818.7422	Hen 2-131	1800
	06:04:31.504	53818.7650	Hen 2-138	1800
	06:48:41.041	53818.7955	Hen 2-131	1800
	07:20:49.895	53818.8180	Hen 2-138	1800

cont. on next page

Table 5.4 cont.

UT Date &	Time (start)	MJD (start)	Target	Exposure [s]
	07:52:49.869	53818.8400	Hen 2-131	1800
	08:24:26.479	53818.8621	Hen 2-138	1800
	08:56:12.511	53818.8840	Hen 2-131	1800
	09:27:32.849	53818.9060	Hen 2-138	1800
2006 March 24	23:53:08.599	53819.5073	NGC 2392	1800
2006 March 25	00:23:42.093	53819.5285	NGC 2392	1800
	00:54:18.288	53819.5498	NGC 2392	1800
	01:24:52.872	53819.5710	NGC 2392	1800
	01:55:28.396	53819.5923	NGC 2392	1800
	02:26:02.530	53819.6135	NGC 2392	1800
	03:09:54.575	53819.6436	Hen 2-131	1800
	03:42:20.360	53819.6663	Hen 2-138	1800
	04:14:57.797	53819.6888	Hen 2-131	1800
	04:47:49.226	53819.7118	Hen 2-138	1800
	05:19:24.135	53819.7335	Hen 2-131	1800
	05:50:59.656	53819.7556	Hen 2-138	1800
	06:34:59.712	53819.7860	Hen 2-131	1800
	07:06:29.371	53819.8081	Hen 2-138	1800
	07:38:19.213	53819.8300	Hen 2-131	1800
	08:09:45.773	53819.8520	Hen 2-138	1800
	08:41:26.884	53819.8738	Hen 2-131	1800
	09:12:59.965	53819.8959	Hen 2-138	1800
2006 March 26	00:02:33.378	53820.5138	NGC 2392	1800
	00:33:10.742	53820.5350	NGC 2392	1800
	01:03:45.048	53820.5562	NGC 2392	1800
	01:34:18.601	53820.5775	NGC 2392	1800
	02:04:52.147	53820.5987	NGC 2392	1800
	02:35:28.409	53820.6199	NGC 2392	1800
	03:22:15.952	53820.6522	Hen 2-131	1800
	03:54:13.135	53820.6746	Hen 2-138	1800

cont. on next page

Table 5.4 cont.

UT Date &	Time (start)	MJD (start)	Target	Exposure [s]
	04:28:22.441	53820.6981	Hen 2-131	1800
	04:59:54.791	53820.7202	Hen 2-138	1800
	05:31:57.055	53820.7423	Hen 2-131	1800
	06:04:52.014	53820.7653	Hen 2-138	1800
	06:48:15.745	53820.7953	Hen 2-131	1800
	07:19:52.106	53820.8174	Hen 2-138	1800
	07:51:38.468	53820.8393	Hen 2-131	1800
	08:23:31.900	53820.8616	Hen 2-138	1800
	08:55:19.142	53820.8835	Hen 2-131	1800
	09:26:56.383	53820.9057	Hen 2-138	1800

All data for each of the three objects have been corrected for their respective system's Helio-centric radial velocity: $-47\ \mathrm{km\,s^{-1}}$ for Hen 2-138; $-1.2\ \mathrm{km\,s^{-1}}$ for Hen 2-131; $+75\ \mathrm{km\,s^{-1}}$ for NGC 2392 (Schneider et al. 1983).

5.3 Time-Averaged Fast-Wind Characteristics

5.3.1 Variety of Absorption Lines

The spectrum is comprised of stellar lines and nebular emission – rest velocity He I lines, metal absorption profiles lines – blue-shifted absorption, P-Cygni profiles, and nebular lines, see Figure 5.5.

The evidence for stellar wind activity is mainly attributed to the appearance of a significant P Cygni line for the He I λ 5875.57 line – which corresponds to the $2^3\mathrm{pP}^0$ - $3^3\mathrm{D}$ shift. Further information about the physical nature of the wind can be extracted from a study of UV data, and to this end a variety of wind lines have been taken from *FUSE*, *IUE* and *HST* spectra, see Figure 5.6.

5.3.2 Ion species: Hen 2-138

Among these are certain low-ionisation species, such as C II λ 1334.53, Al III $\lambda\lambda$ 1854.72, 1862.79, Mg II $\lambda\lambda$ 2795.53, 2802.70 and C III λ 1175.66, and also the high-ionisation species S IV $\lambda\lambda$ 1062.66, 1072.97, Si IV $\lambda\lambda$ 1393.76, 1402.77 and C IV $\lambda\lambda$ 1548.20, 1550.77. Notable absences from the range of identifiable lines are N V $\lambda\lambda$ 1238.82, 1242.80 and O VI $\lambda\lambda$ 1031.93, 1037.62 which are often ascribed to shocked gas in hot star winds.

Velocity space spectra for each of the ions shows a disparity in the blue wind-shifted velocity of these wind lines – those of the lower ions show blueward absorption in the range ~ -100 – -300 km s^{-1} whereas the higher ions are blueward shifted to lie within the range ~ -500 – -700 km s^{-1}. Altogether the lines show strong, often saturated, optical depths in the low to intermediate velocity range, and from these UV lines, as well as the P Cygni of He I λ 5875.62, one would conclude that the wind of Hen 2-138 is a dense and comparatively slow moving one. The denseness of the wind is further emphasised if one examines the spectra of the Si III λ 1300 triplets – see Figure 5.7 – lines which form in particularly dense atmospheres and which here show blueshifts of between ~ -60 km s^{-1} and -80 km s^{-1}, indicating the presence of the radial outflow right at the base of the wind.

5.3.3 SEI Model Fits – Hen 2-138

In order to uncover some of the physical parameters of Hen 2-138, the Sobolev with Exact Integration (SEI) method was employed, but due to the lack of extensive UV time series data, the code will only be applied to single exposures as an suggestive representation of an 'average' moment. As in the two previous chapters the underlying photospheric spectrum has been derived from the TLUSTY plane-parallel grid of models – specifically that for $T_{\rm eff} = 27{,}500$ K and $\log g = 3.00$ – and this photospheric input Gaussian (representing the underlying absorption profile) is rotationally broadened by 100 km s^{-1}. The resultant models are converted into the product of $\dot{M}$ and the (specific) ionisation fraction $q_{\rm i}$, $\dot{M}q_i(w)$, and the mean $< \dot{M}q_i >$, averaged over the $0.2 \leq w \leq 0.9$ normalised velocity range, is subsequently derived and presented for each ion species modelled.

Presented in Figure 5.8 are the SEI model fits for the ions Si IV λ 1393.76, C IV λ 1548.20, S IV λ 1072.97, and Al III λ 1854.72. The first thing to note is that the higher ionisation species of Si IV and C IV require a higher terminal velocity parameter of -700 km s^{-1} in order for the models to be derived, but the lower ionisation species of Al III and S IV

Table 5.5. SEI-derived mass-loss and wind ionisation parameters

Ion	$< \dot{M} q_i >$ $[M_\odot\,\mathrm{yr}^{-1}]$	$< q_\mathrm{i} >$
Al^{2+}	7.7×10^{-10}	6×10^{-3}
S^{3+}	2.5×10^{-9}	2×10^{-2}
Si^{3+}	2.4×10^{-10}	2×10^{-3}
C^{3+}	1.1×10^{-10}	9×10^{-4}

require a terminal velocity parameter of only -300 km s^{-1}. Assuming a solar abundance and using the parameters detailed in Table 1, and derived via CMFGEN analysis carried out by Miguel Urbaneja (described below), the models obtain values for the averaged mass-loss rate – ionisation fraction product $< \dot{M} q_i >$, which are listed in Table 5.5.

Another general point is that the SEI models all underestimate the strengths of the ionisation component of the UV P Cygni profiles for Hen 2-138, this despite the adoption of significantly slow wind laws with the acceleration parameter $\beta = 3.00$.

Al III λ 1854.72

As the broad absorption profile of the blue component of the C IV doublet does not present a clear blue edge from which one would normally measure the terminal velocity of the outflow, then the much more clearly defined blue edge of the Al III λ 1854.72 P Cygni was used to obtain a measure of the terminal velocity which (to the nearest 10 km s^{-1}) was measured to be $v_\infty = -300$ km s^{-1}. The wind acceleration parameter, β, has to be raised to a relatively high value of $\beta = 3.00$ (and hence describes a slowly accelerating velocity law) in order for the projected P Cygni emission peak of SEI model to approach that of the underlying spectra. These velocity law parameters of v_∞ and β are applied to a photospheric Gaussian profile with a FWHM of $\sim$ of 200 km s^{-1} and a central optical depth of 0.500. Despite the strong P Cygni shape of the profile the absorption trough does drop to saturated levels between w $\sim$0.6 and w $\sim$0.8; also the model predicts excessive forward scattering which prevents accurate modelling across the width of the absorption trough. The optical depth is high across almost the entire trough, increasing from 2.8 at $w \sim 0.2$, increasing to 4.6 at $w = 0.8$, before dropping rapidly to a low of 0.8 at $w > 0.9$.

S IV λ 1072.97

An SEI model fit has been achieved for the red component of the S IV $\lambda\lambda$ 1062.66, 1072.97 doublet by applying a similar velocity law, $v_\infty = -300$ km s^{-1}, $\beta = 3.00$ to a photospheric Gaussian profile with FWHM $\sim$325 km s^{-1} and a central optical depth of 0.850; an increased turbulence/smoothing parameter of $v_{\rm turb} = 0.16$ is required to align the blue edge of the model to that of the broad spectral absorption trough. The spectral absorption profile approaches saturation between $w \sim$0.6 and $w \sim$0.8, and also the model also predicts excessive forward scattering across the entire absorption range; again the optical depth is therefore high across the entire width of the absorption and rises from 2.2 at $w \sim 0.2$ to a maximum of 5.8 at $w = 0.85$ before dropping back to 2.0 towards the blue edge ($w > 0.9$).

Si IV λ 1393.76

In applying the same velocity law parameters of $v_\infty = -300$ km s^{-1} and $\beta = 3.00$ (upon an input photospheric Gaussian of FWHM $\sim$ 575 km s^{-1}) for the blue component of the S IV $\lambda\lambda$ 1393.76, 1402.77 it became clear that this terminal velocity did not allow the blue edge of the SEI model to match that of the spectral absorption trough underneath, and it was through a trial-and-error process of gradually increasing the velocity to $v_\infty = -700$ km s^{-1} that an alignment was achieved. The absorption of the profile approaches saturation between $w \sim$0.2 and $w \sim$0.5, where the blue edge occurs and from where the profile then becomes progressively shallower: this is reflected in the optical depths of the model which rapidly increase from 2.4 at $w \sim$0.2 to a maximum of 7.0 at $w = 0.5$ (this range is also where the model shows excess forward scattering); the optical depth then drops off sharply to a much lower level of $\sim$0.4 for $w > 0.6$.

C IV $\lambda\lambda$ 1548.20, 1550.77

The broad blue and red components of C IV $\lambda\lambda$ 5148.20, 1550.77 are both saturated and blended with each other to an extent that the emission peak of the blue component has been removed by the absorption of the red. This makes this doublet extremely difficult to model, however a vague degree of alignment was achieved, but again with the higher terminal velocity of $v_\infty = -700$ km s^{-1} ($\beta = 3.00$, and $v_{\rm turb} = 0.15$ to allow for the broadness of the profile, the input Gaussian of which has a FWHM of $\sim$ 400 km s^{-1}). The high

saturation of the absorption and excess forward scattering are reflected in the optical depths of the model which rise from 3.0 at $w \sim 0.2$ to 6.0 at $w = 0.6$, and then sharply drop to a low of 0.1 at $w = 0.75$, rising again to between 1.0 and 1.5 for $w > 0.9$.

5.3.4 CMFGEN Analysis of Hen 2-138

In order to obtain more fundamental parameters from the time-averaged UV spectra, it has been modelled by Miguel Urbaneja (IfA, Hawai'i), using the unified non-LTE, line-blanketed model atmosphere code CMFGEN (Hillier & Miller 1998). The model is defined by the stellar radius, the luminosity, the mass-loss rate, the wind terminal velocity, the stellar mass, and by the abundances of the species included in the calculations. The code does not solve for the hydrodynamical structure and so requires the velocity field has to be defined. To this end, the output of a plane-parallel model (such as that provided by TLUSTY) is used to define the pseudo-static photosphere, connected to just below the solar point of a β-type velocity law – such as that used in SEI – to describe the wind regime.

The effective temperature of the system is derived from the ionisation balance of He, where only the He I lines of the spin system and those He II lines present in the optical are used. In this case He II lines react strongly to temperature changes of $\pm$ 1000 K, whilst the He I lines remain unaffected. The surface gravity is determined by the fitting of the Balmer lines series. More weight is given to the higher lines as stellar wind effects and contamination by ionised gas are less important. The photospheric structure is linked to the stellar mass and so different values would result in changes. These would be very small, however, for this target object.

The final model is shown in Figure 5.9 where most of the features of the FUV/UV spectrum are successfully reproduced. However, the wide absorption troughs of the Si IV and C IV profiles are not well matched, and it under-predicts the strengths of the Al III lines. Low ionisation species require a lower effective temperature but then it is found that this will not produce the observed He I /He II ionisation balance; conversely, high ionisation features present in the optical spectrum, such as the O III and C IV lines, require a higher effective temperature, but again, that would not successfully reproduce the correct ionisation balance.

This two-temperature requirement is consistent with a similar situation in the SEI modelling: $v_\infty = -300\,\mathrm{km\,s^{-1}}$ is adequate for the Al III and S IV (red component); whereas

$v_\infty = -750$ km s^{-1} is required for the S IV and C IV lines.

Since these modelling codes assume spherically-symmetric winds, the problems observed here in being forced to adopt different parameters to be able to match both high and low ionisation lines, coupled with discrepancies in matching the absorption and emission strengths of P Cygni profiles, would seem to suggest that the wind and its terminal velocity and mass-loss are latitude-dependent. Low velocity, low ion species forming in the cooler equatorial regions of an asymmetric outflow that is viewed almost pole-on – the higher speed, high ions of Si IV and C IV are being driven out from the hotter polar regions of the outflow.

For a v_∞ of 300 km s^{-1}, $T_{\rm eff} = 29{,}000$ K, adopted central star mass of $\sim 0.6\ M_\odot$, and a $\log(L/L_\odot) \sim 3.9$, the CMFGEN model yields a mass-loss parameter $\log Q \sim$ -11.45 dex (where $Q = \dot{M}(R_\star v_\infty)^{-1.5}$) and hence a mass-loss rate of $\sim 1.2 \times 10^{-7}\ M_\odot$ yr^{-1}. The model is for a smooth wind with clumping being unconstrained here, but it is noted as being very low. The wind momentum value, $\log\ (M_\odot v_\infty {R_\star}^{0.5})$, of $\sim$ 26.6 dex is within the scatter of the wind momentum-luminosity relation observed/derived for CSPNs and predicted by line-driven wind theory (see e.g. Kudritzki et al. 2006); although in the CSPN region alone, there is not a convincing relation between wind momentum and luminosity.

In comparing the CMFGEN-derived mass-loss rate with those derived from the empirical line SEI models results $< \dot{M}q >$, the empirical analyses would suggest that none of the SEI-modelled ion species are dominant in the wind, however in the CMFGEN base model that S^{3+} and Si^{3+} ionisation fractions are dominant in the wind (i.e. $\sim$ 90%): this would suggest that either the CMFGEN-derived mass-loss rate is *over*-estimated or the SEI-derived product of $\dot{M}q$ is *under*-estimated. For a mass-loss rate of $\sim 1.2 \times 10^{-7}$ $M_\odot$ yr^{-1}, the corresponding ion fractions are also listed in Table 5.5.

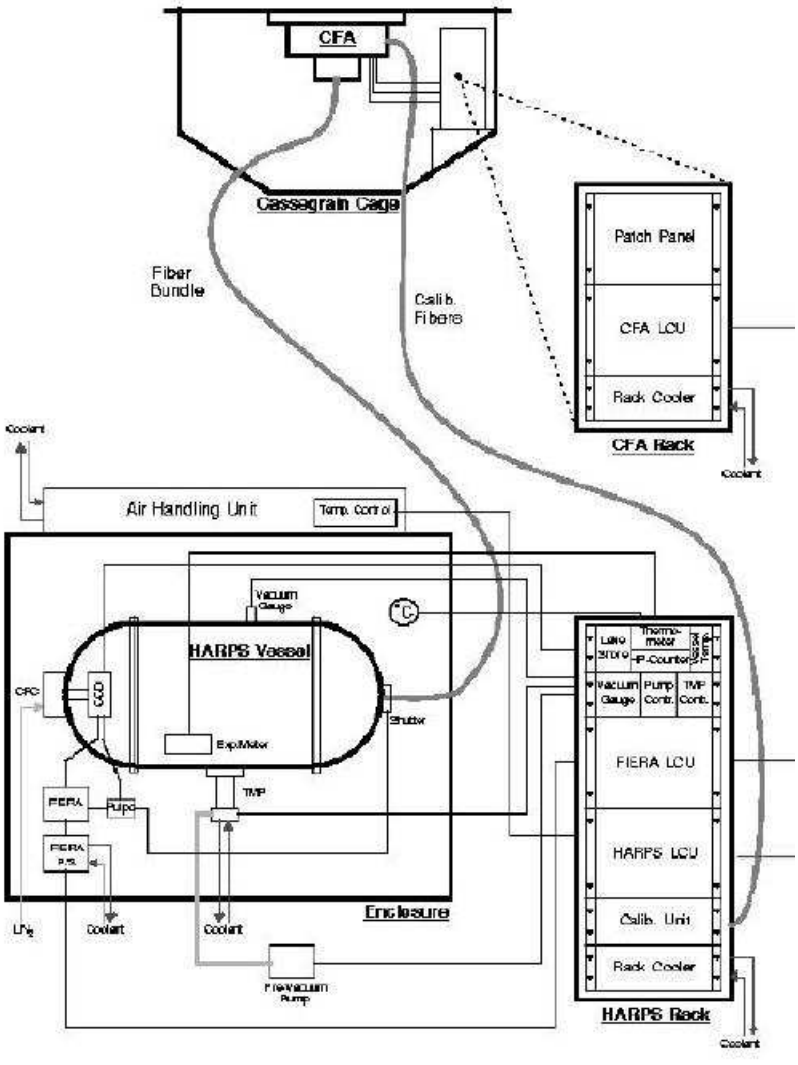

Fig. 5.4. Diagram of the ESO HARPS spectrograph system, courtesy of the ESO website: http://www.eso.org/sci/facilities/lasilla/instruments/harps/inst/description.html

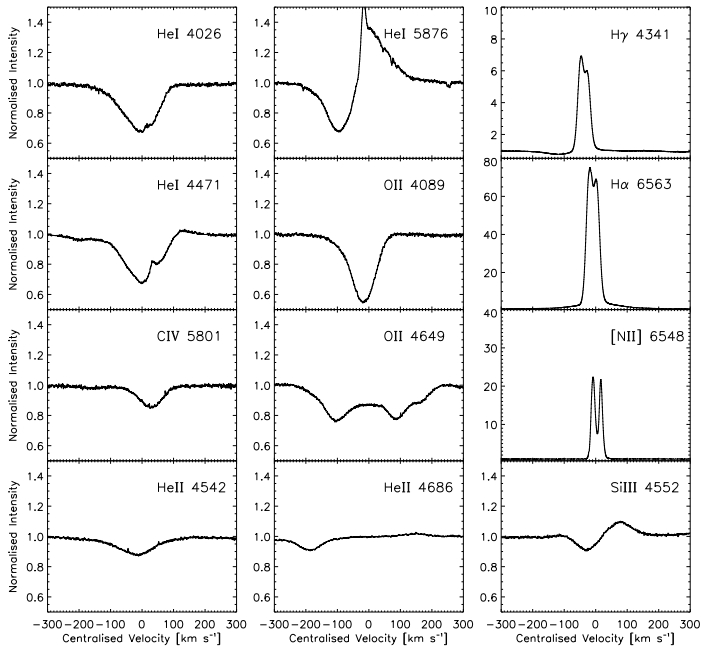

Fig. 5.5. Mean ESO optical spectral lines of photospheric, fast wind and nebula regions of Hen 2-138.

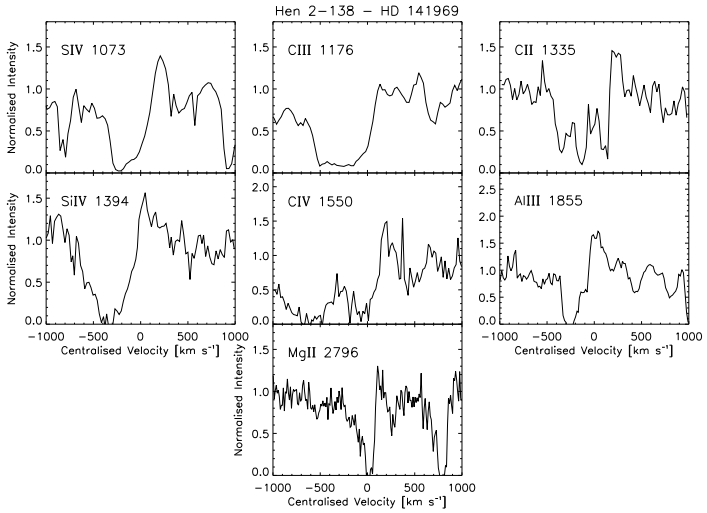

Fig. 5.6. Mean far UV spectral lines depicting fast wind features from FUSE & IUE data of Hen 2-138.

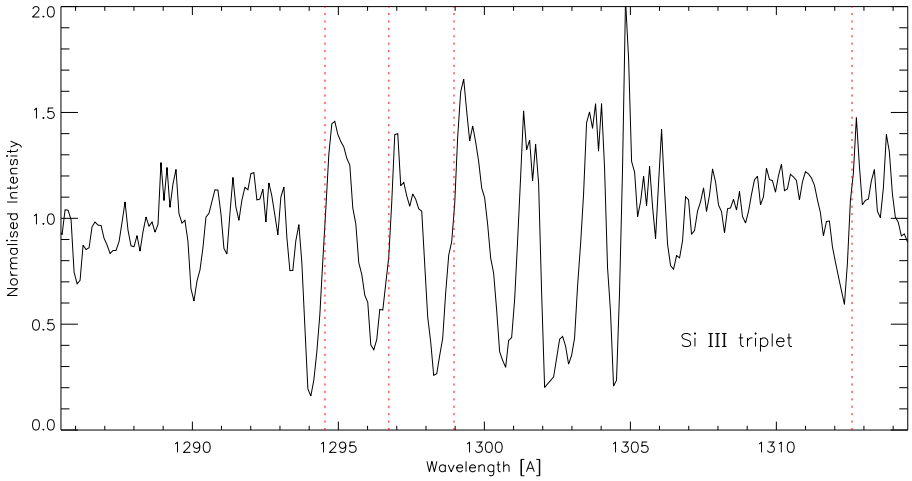

Fig. 5.7. Hen 2-138 UV spectrum (IUE) showing blueward shifted Si III triplets – with Si III singlet at 1312 Å also shown – the vertical dashed lines indicate the spectral rest positions.

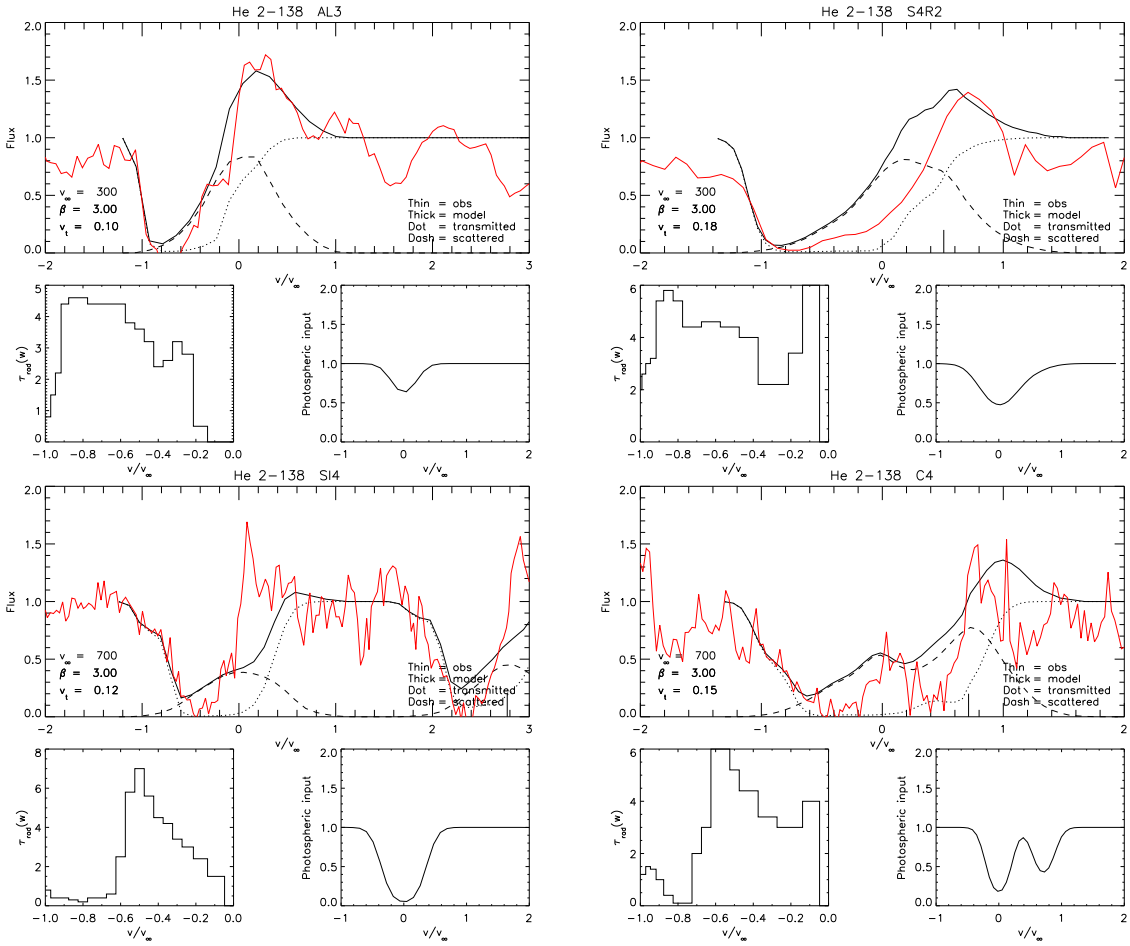

Fig. 5.8. SEI fits to the Hen 2-138 UV P Cygni profiles of (left to right, top to bottom: Si IV λ1394, C IV λ1548, S IV λ1073, and Al III λ1855. The larger panels display the SEI model fit overlaid upon the observed spectra, and the smaller panels depict the input photospheric spectra (right) and the derived radial optical depth profile shown as a function of normalised velocity (left). The two higher ionisation species (above) require a higher terminal velocity of 700 km s^{-1}, whereas the two lower ionisation species (below) only require a terminal velocity of 300 km s^{-1}.

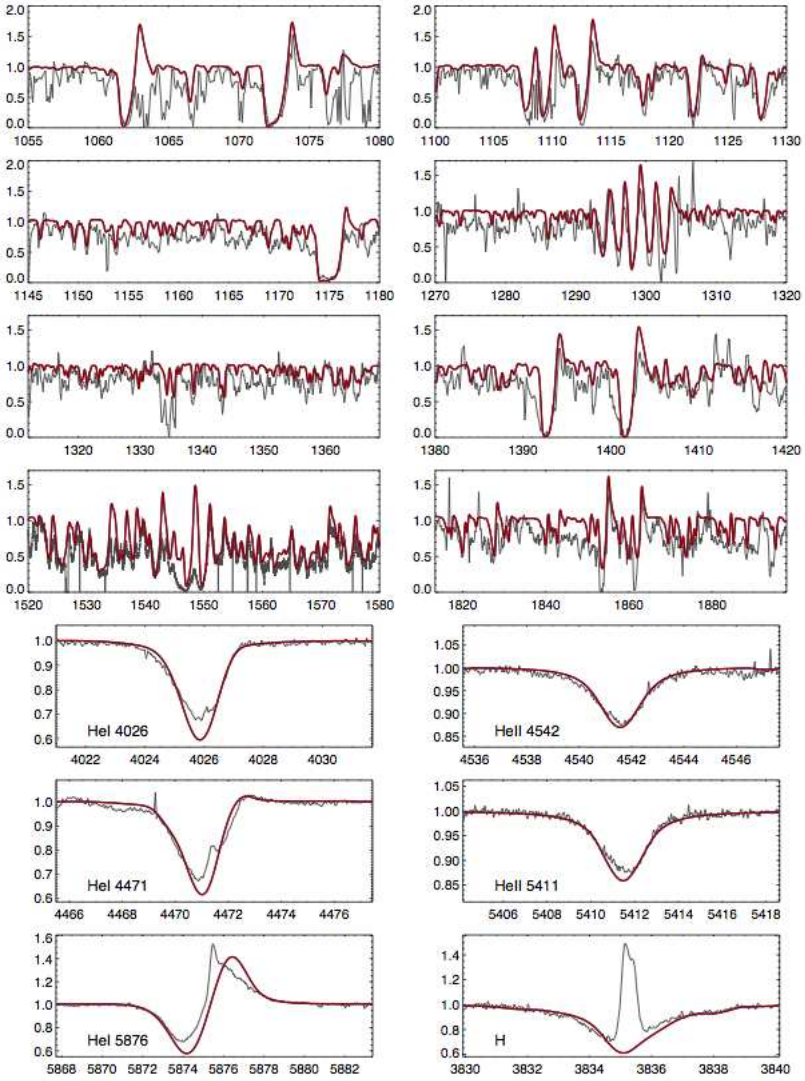

Fig. 5.9. CMFGEN model fits for Hen 2-138

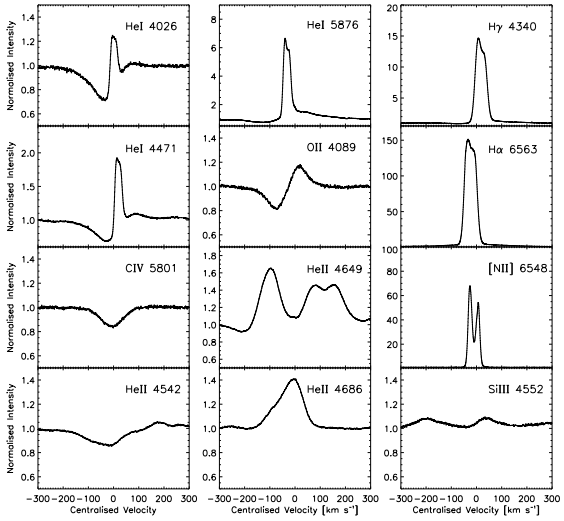

Fig. 5.10. Mean ESO optical resonance lines of photospheric, fast wind, and nebula regions of Hen 2-131.

5.3.5 Ion Species - Hen 2-131

The optical spectra of Hen 2-131 also includes the low-ionisation species, such as C II λ 1334.53, Al III $\lambda\lambda$ 1854.72, 1862.79, Mg II $\lambda\lambda$ 2795.53, 2802.70 and C III λ 1175.66, as well as the high-ionisation species S IV $\lambda\lambda$ 1062.66, 1072.97, Si IV $\lambda\lambda$ 1393.76, 1402.77 and C IV $\lambda\lambda$ 1548.20, 1550.77. The blue edges of the stronger absorption troughs of the species appear within a -200 – -500 km s^{-1} range.

Again, as with Hen 2-138, the shocked gas wind lines of N V $\lambda\lambda$ 1238.82, 1242.80 and O VI $\lambda\lambda$ 1031.93, 1037.62 are absent. However the P V λ 1117.98 component – not present in the UV spectra of Hen 2-138 – can be seen in the spectra, although its emission peak is not as strong as its blueward absorption trough.

As with the outflow of Hen 2-138, the Si III λ 1200 triplet is examined for any indications of blueshift and in the UV spectrum of Hen 2-131 the triplet lines of are blueshifted by a far greater velocity than those of Hen 2-138: in Hen 2-131 the blue shift is between -160 and -220 km s^{-1}, which in contrast to the outflow of Hen 2-138, would suggest a less dense wind, but slow-moving.

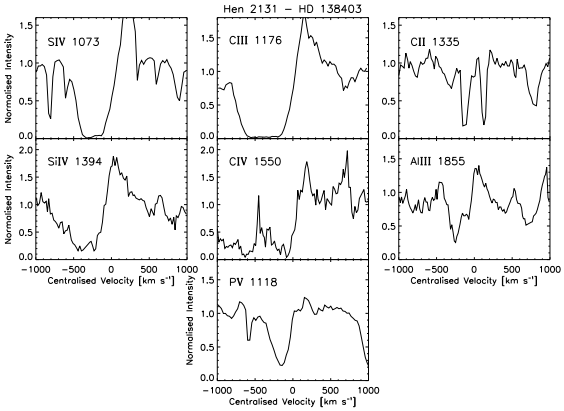

Fig. 5.11. Mean far UV spectral lines depicting fast wind features from FUSE & IUE data of Hen 2-131.

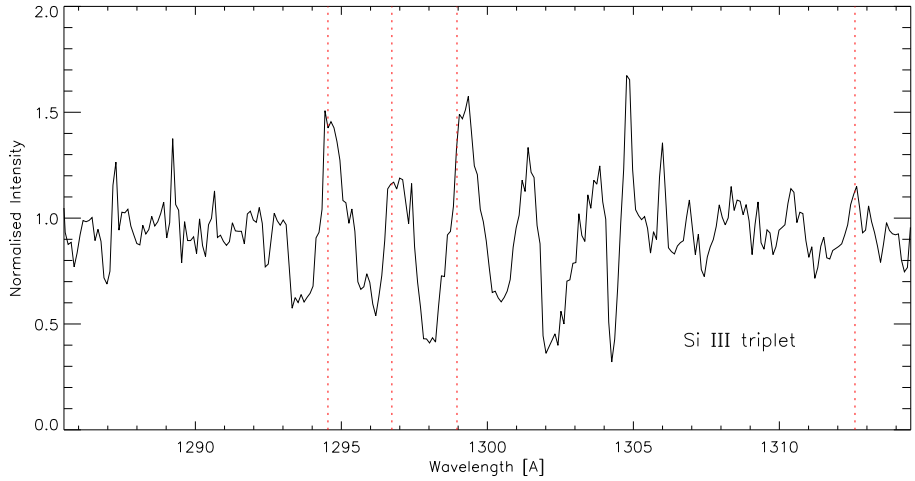

Fig. 5.12. Hen 2-131 UV spectrum (IUE) showing blueward shifted Si III triplets - with Si III singlet at 1312 Å also shown - the vertical dashed lines indicate the spectral rest positions.

5.3.6 SEI Model Fits - Hen 2-131

P V λ 1117.98

The blue component of the P V $\lambda\lambda$ 1178.98, 1128.01 doublet is modelled with a terminal velocity of $v_\infty = -400$ km s^{-1} (Kudritzki et al. 2006) – upon a Gaussian input profile of FWHM = 250 km s^{-1}, central optical depth of 0.800 – and a similar wind law β factor of 3.00 ($v_{\rm turb}$ was initially given the low value of 0.05 and it was found that this did not need to be increased in order to align the blue edge of the absorption). The high β appears to over predict the emission peak of the profile but not excessively, and indeed the apparent emission of the profile is unusually weak. Also the forward scattering as predicted by the

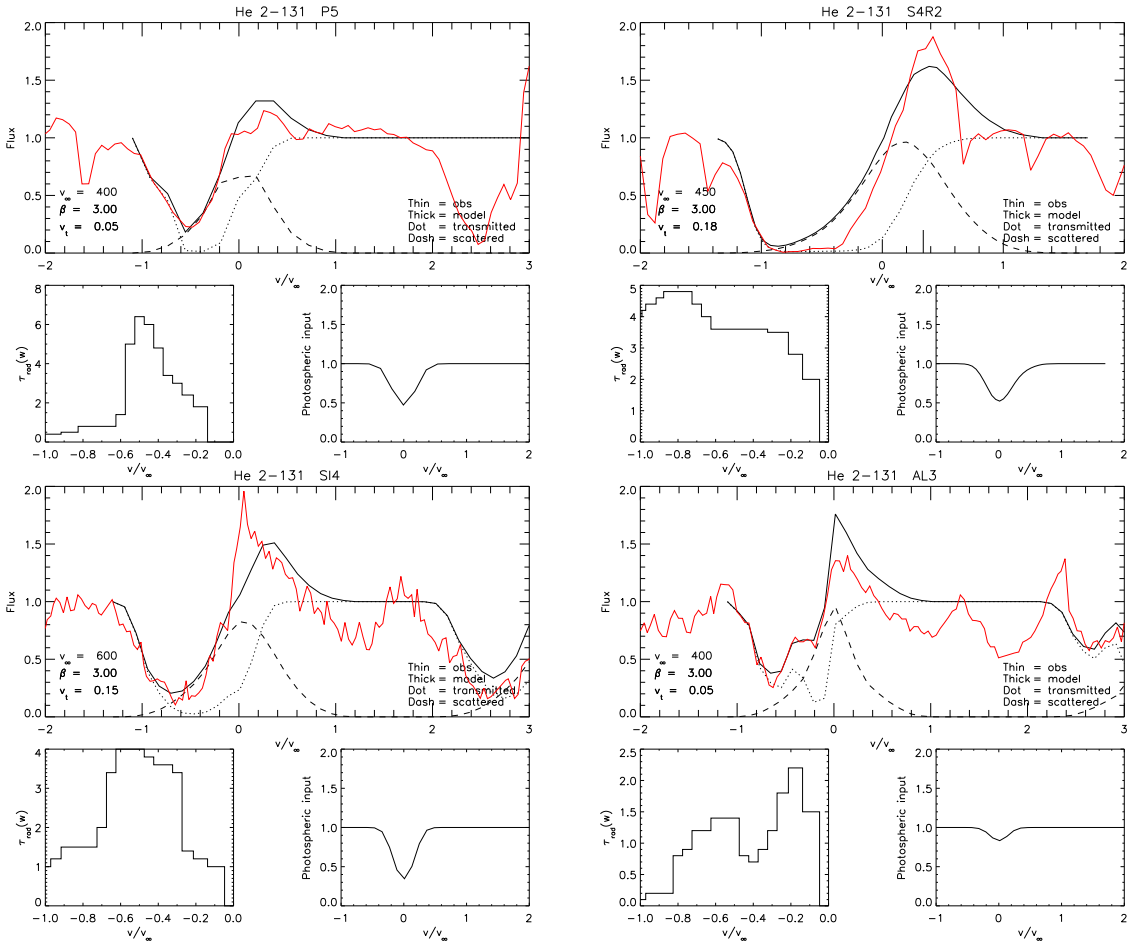

Fig. 5.13. SEI model fits to the Hen 2-131 P Cygni resonance profiles of P V λ1118, S IV λ1073, Si IV λ1394, and Al III λ1855.

model does not overlap with the lower velocity absorption but the edge of one appears to coincide with the edge of the other. This being so the optical depths adopted to model the absorption profile are reasonable high despite the profile being unsaturated: rising from ∼2.0 at w ∼0.20 to 5.6 at w ∼0.50; the optical depths are then much lower across the bluer half of the trough, dropping towards 1.0 at w ∼0.75 and then less than half again for w >0.90.

S IV λ1072.97

The P Cygni-like red component of the S IV 1062.66, 1072.97 doublet is highly saturated in absorption to the extent that it flattens out along the zero-flux level. This high saturation cannot be replicated in the model ($v_\infty = -400$ km s^{-1}, $\beta = 3.00$, $v_{\rm turb} = 0.16$, upon a photospheric Gaussian of FWHM = 300 km s^{-1}, central optical depth = 0.650), which for the full extent of the absorption trough is hampered by the forward scattering component.

The optical depths therefore are necessarily high in order to bring the model down as far as to meet the forward scattering and are of the order of ∼3.6 for $\sim 0.20 > w > 0.60$, further increasing to a maximum of 4.8 at w ∼0.80, and falling slightly to 4.0 at the terminal velocity.

Si IV λ 1393.76

The modelling of the P Cygni of the blue component of the Si IV 1393.76, 1402.77 doublet (input Gaussian: FWHM = 325 km s^{-1}, central optical depth of 1.100), could only be achieved by increasing the terminal velocity to $v_\infty = -600$ km s^{-1} while still retaining β = 3.00 (and increasing $v_{\rm turb}$ to 0.15 to align the model with the slope of the blue edge). Whether this indicates a similar two-component outflow, such as described above for Hen 2-138, is uncertain, as the terminal velocity required for all other modelled P Cygni profiles for Hen 2-131 was that of 400 km s^{-1}, as assigned by Kudritzki et al. (2006). As the absorption approaches near saturation levels in the range $0.30 > w > 0.70$ the optical depths again can only bring down the model's flux level to that of the encroaching forward scattering in this velocity range where the optical depth range from a minimum of 3.4 to a maximum of 4.0; for $w > 0.70$ the optical depths fall to ∼1.5 up to $w = 0.90$ and then, as the flux rises toward the continuum level, drop to 1.0 at terminal velocity.

Al III λ 1854.72

The unsaturated Al III 1854.72 has had its input Gaussian profile (FWHM = 200 km s^{-1}, central optical depth = 0.200) modelled using a wind law (similar to that used for the unsaturated P V profile) of $v_\infty = -400$ km s^{-1}, $\beta = 3.00$, and the low $v_{\rm turb} = 0.05$. The lack of saturation has not brought the flux levels within the level of the model's forward scattering prediction, therefore the optical depths adopted more accurately reflect the absorption of the profile: from ∼2.0 at w ∼0.20 they drop to 0.8 at $w = 0.45$, before increasing to a maximum of 1.4 at $w = 0.50$, then falling slightly towards 0.8 at $w = 0.80$ from where the optical depth drops again, but sharply, to an average of ∼0.2 for $w > 0.80$.

5.3.7 Ion Species - NGC 2392

Here there are the low-ionisation species, such as C II λ 1334.53, Al III $\lambda\lambda$ 1854.72, 1862.79, Mg II $\lambda\lambda$ 2795.53, 2802.70 and C III λ 1175.66, and the high-ionisation species S IV $\lambda\lambda$ 1062.66, 1072.97, Si IV $\lambda\lambda$ 1393.76, 1402.77 and C IV $\lambda\lambda$ 1548.20, 1550.77. Again, like similar species

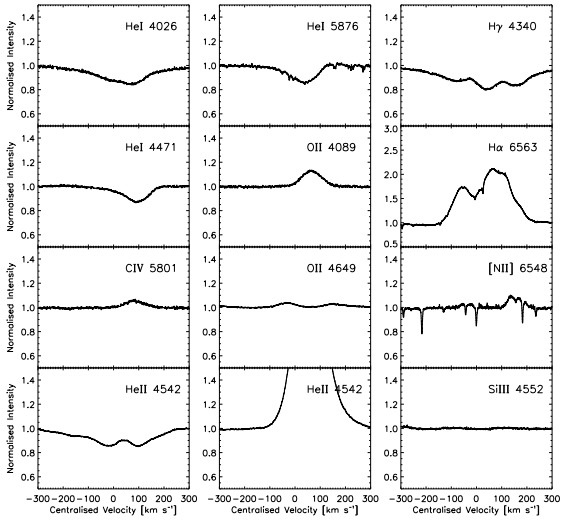

Fig. 5.14. Mean ESO optical resonance lines of photospheric, fast wind, and nebula regions of NGC 2392.

of Hen 2-131, the blue edges of the stronger species appear within a -200 – -500 km s^{-1} range.

Unlike the UV spectra of Hen 2-138 and Hen 2-131, the doublets of N V $\lambda\lambda$ 1238.82, 1242.80 and O VI $\lambda\lambda$ 1031.93, 1037.62 are present and would therefore indicate the presence of shocked gas in the wind. Also, as in the spectra of Hen 2-131, the P V λ 1117.98, 1128.01 doublet is also present.

The Si III λ 1200 triplet – seen in Figure 5.16 – appears to be blueshifted only by between -10 and -30 km s^{-1}, which is even slower than that measured for Hen 2-138, but the examination of the blue-shifted triplet is hampered by the appearance of rather weak absorption lines – not nearly as strong as the similar lines of the other two ESO objects – and it is difficult to pick out the absorption profiles from the noise of the continuum, despite the triplet rest wavelength positions being marked. The small blueshift of the triplet would indicate a dense wind, but the shallowness of the absorption lines, particularly in both the ESO optical data, as well as the lack of strongly saturated UV profiles from IUE and FUSE would indicate a relatively weak wind.

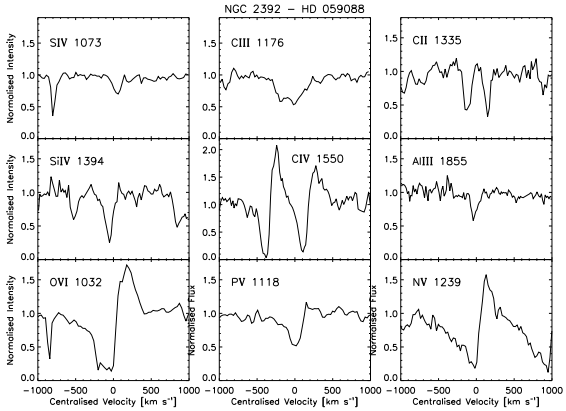

Fig. 5.15. Mean far UV spectral lines depicting fast wind features from FUSE & IUE data of NGC 2392.

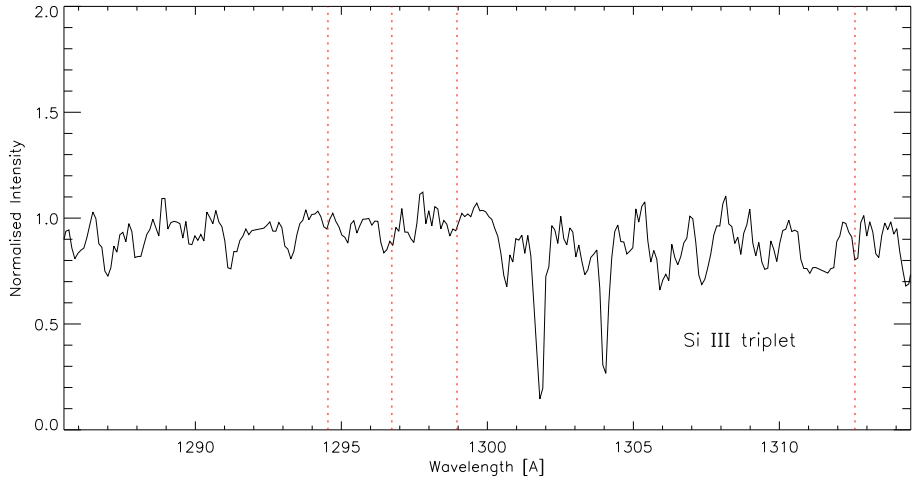

Fig. 5.16. NGC 2392 UV spectrum (IUE) showing blueward shifted Si III triplets - with Si III singlet at 1312 Å also shown - the vertical dashed lines indicate the spectral rest positions.

5.3.8 SEI Model Fits - NGC 2392

O VI λ 1031.93

With a wind terminal velocity of $v_\infty = -400$ km s^{-1} (Kudritzki et al. 2006), the strong P Cygni profile of the blue component of the O VI $\lambda\lambda$ 1031.93, 1037.62 doublet was modelled upon a Gaussian photospheric input absorption of FWHM = 200 km s^{-1}, and a central optical depth of 0.400; again the velocity law β acceleration parameter is set as high as 3.00 in order to match the high emission peak of the profile, with $v_{\rm turb} = 0.10$ to align the model to the slope of the blue edge of the absorption. Although the profile's absorption is not saturated it does present a flattened trough and so between w ∼0.30 and w ∼0.60 the

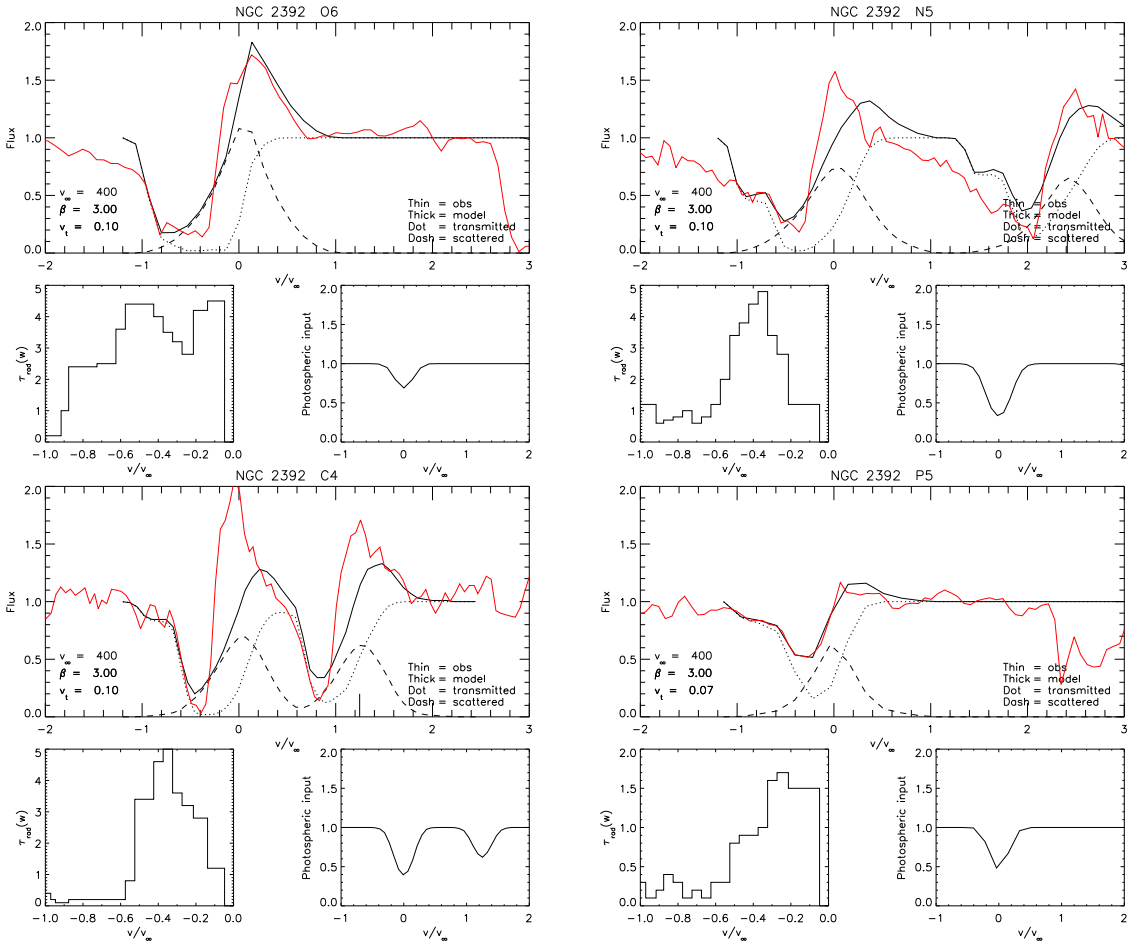

Fig. 5.17. SEI model fits to the NGC 2392 P Cygni resonance profiles of O VI λ 1032, N V λ 1239, C IV λ 1548, and P V λ 1118.

spectra does fall beneath the model's level of forward scattering, and as such, the optical depth levels cannot push the profile of the model as far as the underlying absorption would require: the optical depth rises from 3.2 at $w = 0.30$ to a high of 4.4 at $w = 0.55$; beyond the excessive forward scattering, $0.60 < w < 0.90$ the optical depth drops to ∼2.4 and then sharply drops again to 0.2 for $w >$0.90.

N V λ 1238.82

Using similar velocity law parameters ($v_\infty = -400$ km s^{-1}, $\beta = 3.00$, $v_{\rm turb} = 0.10$), the blue component of the N V $\lambda\lambda$ 1238.82, 1242.80 doublet had also been modelled (upon a photospheric Gaussian input profile of FWHM = 250 km s^{-1}, with a central optical depth of 1.15), but despite the high β factor, the model falls short of the emission peak presented in the P Cygni profile. As with the previous model, although the absorption is not saturated, the more redward side of the spectral trough requires a deeper optical

depth than can be allowed by the excessive forward scattering component of the model, affecting the absorption profile in the region $\sim 0.50 > w >\sim 0.30$ in which the optical depths of the model range between 3.4 and 4.8 (at $w = 0.35$). Further towards the blue, i.e. $w > 0.60$, the optical depth remains of the order of ~ 1.0 as the absorption trough becomes shallower, with no definite edge.

C IV λ1548.20

The blue component of the C IV $\lambda\lambda$1548.20, 1550.77 doublet presents a noticeably narrow absorption trough, so much so that using the velocity law parameters of $v_\infty = -400$ km s^{-1}, $\beta = 3.00$, $v_{\rm turb} = 0.10$ as for the above NGC 2392 P Cygni profiles (upon an Gaussian photospheric input profile of FWHM = 200 km s^{-1}, central optical depth = 1.00), the model predicts a broader absorption trough; also the high emission peak of the profile is much underestimated by the model despite the high β factor of 3.00. The saturation of the absorption in the region $\sim 0.30 > w >\sim 0.50$ is again affected by excessive forward scattering where the optical depths range from 3.4 to a maximum of 5.0 (at $w = 0.35$). In the region $w > 0.60$ the absorption trough possesses a steep edge; the shallowness of the trough further blueward is reflected in the low optical depth of the model of ~ 0.2 as the absorption merges into the continuum.

P V λ1117.98

The unsaturated profile of the P V $\lambda\lambda$1117.98, 1128.01 doublet of NGC 2392 is noticeably weak, with the blue component comprising a shallow absorption trough and a significantly small emission peak, but even so, is only marginally overestimated by the high $\beta = 3.00$ factor of the adopted wind law (again with $v_\infty = -400$ km s^{-1}, but a slightly reduced $v_{\rm turb}$ of 0.07 to match the blue edge slope, upon a Gaussian photospheric input profile of FWHM = 200 km s^{-1}, central optical depth = 0.80). The relatively shallow, unsaturated nature of the absorption prevents the level of forward scattering, as predicted by the model, from overlapping the trough; therefore the levels of optical depth adopted in order to model the absorption reflect the optical depths of the spectral profile much more accurately than those of the more saturated profiles described above. The optical depths are highest at $\sim$1.6 at $w \sim$0.20, then drop to $\sim$0.9 for $0.30 > w > 0.50$, and then drop down to marginally fluctuate around 0.2 for $w > 0.50$ as the absorption again starts to merge into the level of the continuum.

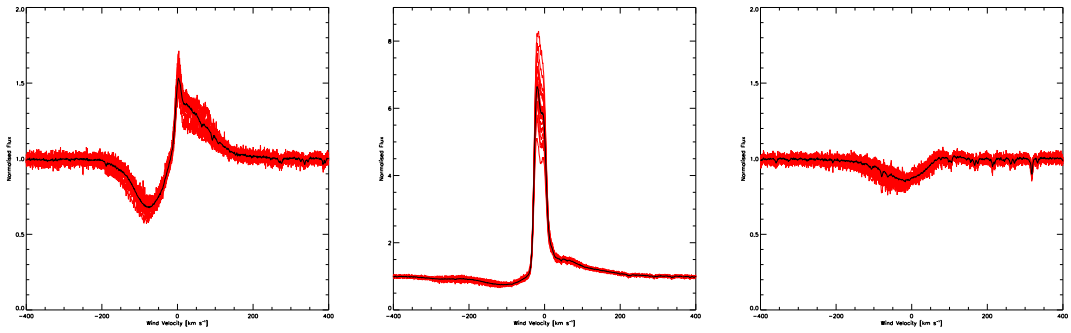

Fig. 5.18. Three 18 exposure over-plots of the He I λ 5876 line for (l-r) Hen 2-138, Hen 2-131, NGC 2392, the individual exposures, taken over $\sim$ 2.2 days, are plotted in red, and the mean profile is overlaid in black, so as to further emphasise the variable nature of the P Cygni profile.

5.4 Time Variable Characteristics of the CSPN Winds

5.4.1 Equivalent Width Measurements – Hen 2-138

After studying the time-averaged data of the central star winds of these three objects, the more time-dependent nature of the PNs winds can be explored. The initial indications of the variable nature come from time-dependent variations in the P Cygni profile of the He I λ 5875.62, see Figure 5.18. Here 18 time-series exposures for each object, obtained over $\sim$ 2.2 days are simultaneously plotted in red with the mean spectrum superimposed upon the others in black, thereby allowing the extent of the variability to be estimated. The absorption profile shows variation up to an extent of ~ -200 km s^{-1}. Also, time-variable changes of the optical lines of He I λ 4026.19, He I λ 4471.48, and the more deep-bedded C IV λ 5801.33 are studied, lines which show behaviour more akin to changes in lower regions close to the photosphere than in the more developed wind.

More quantitative evidence can be obtained from equivalent width measurements of the profiles, and these are shown in Table 5.6. The maximum and minimum EW measurements for both absorption troughs and emission peaks for the He I λ 5875.62 P Cygni are listed (along with the mean EW and the standard deviation of the EW range) as measured between the given wavelengths, which indicate the estimated extremities of the troughs/peaks before merging back into the continuum. Also listed are the max./min. EW measurements (along with mean EW and SD) for the He I λ 4026.19 and He I λ 4471.48 optical lines as well as the deep-seated C IV λ 5801.33 line. As can be seen in the table the

Table 5.6. Hen 2-138 equivalent width measurements [Å]

Spectral Line	Wavelength Range [Å]	Min – Max	Mean	SD	Max % Diff.
He I λ 4026	4020.0 – 4030.0 a.	0.59 – 0.78	0.68	0.06	32
He I λ 4471	4465.5 – 4472.0 a.	0.58 – 0.77	0.67	0.06	33
He I λ 5876	5870.0 – 5874.4 a.	0.45 – 0.78	0.59	0.09	71
He I λ 5876	5874.3 – 5880.0 e.	0.48 – 0.91	0.75	0.11	88
C IV λ 5801	5795.0 – 5804.0 a.	0.29 – 0.37	0.33	0.02	27

He I λ 5875.62 profile shows the greatest variation in EW, varying between $\sim$ 0.45Å and 0.78Å in its absorption trough and between $\sim$ 0.48Å and 0.91Å in its emission peak. It has also been observed that these variations are correlated between the absorption and emission sections in that they vary together: the deepest absorption troughs are accompanied by the strongest emission components, and likewise for the shallowest/weakest of each. The other (non-P Cygni) optical lines also exhibit variable EW measurements but not quite to the extent of the aforementioned P Cygni profile: the absorption trough of He I λ 4026.19 varies between $\sim$ 0.59Å and 0.78Å, that of He I λ 4471.48 varies between 0.58Å and 0.77Å; the deep-seated C IV λ 5801.33, also in absorption, varies in EW (although to a lesser extent) between 0.29Å and 0.37Å.

5.4.2 Equivalent Width Measurements – Hen 2-131

The P Cygni profile of He I λ 5875.62 as observed within in the outflow from the central star of Hen 2-131 is much less even distributed between its absorption trough and its emission peak: whereas the EWs of absorption/emission of this line in Hen 2-138 are reasonably similar, the emission peak of He I λ 5875.62 is much higher and its EW much greater than that of the absorption trough, the variation in EW in the emission peak is roughly five times that of the absorption trough, varying between $\sim$ 0.51Å and 0.90Å, as opposed to the emission peak where the EW varies between $\sim$ 3.66Å and 5.68Å. Where the lines He I λ 4026.19 and He I λ 4471.48 existed only in absorption in the outflow of He 2-138, in the outflow of Hen 2-131 they both exhibit variable absorption troughs and emission peaks: for the He I λ 4026 line the EW varies between $\sim$ 0.29Å and 0.47Å in absorption, and between $\sim$ 0.02Å and 0.17Å in emission; for the He I λ 4471 line the EW varies between $\sim$ 0.30Å and 0.58Å in absorption, and between $\sim$ 0.42Å and 0.67Å in emission. The deep-seated C IV λ 5801 line only shows an absorption trough which itself varies in EW between $\sim$ 0.23Å and 0.49Å.

Table 5.7. Hen 2-131 equivalent width measurements [Å]

Spectral Line	Wavelength Range [Å]	Min – Max	Mean	SD	Max % Diff.
He I λ 4026	4021.0 – 4025.8 a.	0.29 – 0.47	0.38	0.04	64
He I λ 4026	4025.8 – 4026.4 e.	0.02 – 0.17	0.08	0.04	682
He I λ 4471	4466.5 – 4471.0 a.	0.30 – 0.58	0.46	0.07	92
He I λ 4471	4471.0 – 4476.2 e.	0.42 – 0.67	0.58	0.11	58
He I λ 5876	5868.5 – 5874.8 a.	0.51 – 0.90	0.72	0.12	76
He I λ 5876	5874.7 – 5881.5 e.	3.66 – 5.68	4.75	0.54	55
C IV λ 5801	5796.5 – 5803.2 a.	0.23 – 0.49	0.34	0.08	110

Table 5.8. NGC 2392 equivalent width measurements [Å]

Spectral Line	Wavelength Range [Å]	Min – Max	Mean	SD	Max % Diff.
He I λ 4026	4020.0 – 4033.0 a.	0.49 – 0.76	0.58	0.07	55
He I λ 4471	4468.5 – 4474.5 a.	0.19 – 0.34	0.24	0.04	82
He I λ 5876	5871.8 – 5878.5 a.	0.20 – 0.56	0.38	0.10	173
C IV λ 5801	5800.7 – 5804.5 e.	0.07 – 0.13	0.09	0.02	79

5.4.3 Equivalent Width Measurements – NGC 2392

In the outflow of NGC 2392, the three He I lines all appear in absorption only – even the He I λ 5875.62 line appears to show only an absorption trough: the region to the immediate right of the absorption trough may be ever so slightly raised (in terms of flux) above the continuum level but it is too subtle a change to be properly quantifiable. Any wind emanating from the central star must be very weak indeed. Despite the lack of significant P Cygni profiles in the helium lines, they do exhibit variability: He I λ 4026.19 varies in EW between $\sim$ 0.49Å and 0.76Å, He I λ 4471.48 varies between $\sim$ 0.19Å and 0.34Å; but the greatest variation in EW is shown in the He I λ 5875.62 wind line, between $\sim$ 0.20Å and 0.56Å. Of the metal lines, C IV λ 5801.33 shows the greatest relative variability: between 0.07Å and 0.13Å.

5.4.4 Time Variance Spectra (TVS) – Hen 2-138

All optical absorption lines of potentially significant variability were submitted to the Time Variance Spectra (TVS) analysis algorithm with the aim of singling out those lines which show a significant level of variability and thus require further investigation: only those with considerable activity above the TVS confidence level line would perhaps reveal a periodic frequency in later Fourier analysis.

After studying the time-averaged qualities of the central star winds of these three

objects, now the time-dependent nature of the PNs' winds can be explored. The higher wind He I λ 5875.62 line and the more photospherically dominated lines of He I λ 4026.19, He I λ 4471.48 and the much more closely-photospheric, deep-seated C IV λ 5801.33 are now subjected to the more rigorous time-variance analysis of the TVS algorithm.

In He I λ 5875.62 there is a clearly strong TVS response from both the absorption and emission components of the P Cygni profile, with the absorption variance extending out to ~ -200 km s^{-1} blueward; slightly further than the redward emission, the variance of which extends to between $\sim +100$ km s^{-1} and $+150$ km s^{-1}. A broad absorption enhancement appears during the 2^{nd} night's data but the extent of the observation is not long enough to be able to discern whether this forms part of a migrating DAC, such as those observed in the UV spectra of OB stars, or indeed as observed within the FUV data of NGC 6543 as discussed in Chapter 3 of this thesis (and also by Prinja et al. 2007).

The near-photospheric lines also show variability, but not quite to the extent of the higher wind line: the TVS profile only extends to $\sim \pm 100$ km s^{-1} above the 95% confidence line. Also in both the He I λ 4026.19 and the He I λ 4471.48 lines the variability of the profiles is revealed to be on a scale of hours by strong blue-to-red features appearing within the 3^{rd} night's data, as seen in the uppermost greyscale strip, and hence are not correlated with the 2^{nd} night's enhanced absorption component in He I λ 5875.62. An outward flowing wind – where absorption enhancements (as with those of NGC 6543) would be expected to migrate from red-to-blue – is seemingly not detected in the deeper near-photospheric regions. Within the TVS profiles for the photospheric lines the response is stronger in the redward 'half' of the TVS than in the blueward 'half', as well there being a drop in the TVS response at about the rest velocity. The localised structures observed migrate across the absorption troughs in an estimated 0.3 – 0.4 days. The EW of these profiles can vary by as much as $\sim 25\%$. Similar TVS features are observed in the C IV λ 5801.33 line, which is narrower than the He I lines – close to the projected rotational velocity – ± 100 km s^{-1} – and hence are probably formed much closer to, or even at the photosphere.

Table 5.9 describes the extents in velocity of the varying absorption and emission feature of the four lines under TVS analysis.

5.4.5 Time Variance Spectra (TVS) – Hen 2-131

The ESO time-series variance studies of a range of photospheric resonance lines from the central star of PN Hen 2-131 are presented along with their accompanying greyscales:

Table 5.9. Hen 2-138 TVS velocity ranges

Spectral Line	TVS Velocity Range [km s^{-1}]
He I λ4026	−175 – +125
He I λ4471	−175 – +150
He I λ5876	−250 – +125
C IV λ5801	−75 – +125

Table 5.10. Hen 2-131 TVS velocity ranges

Spectral Line	TVS Velocity Range [km s^{-1}]
He I λ4026	−200 – +100
He I λ4471	−200 – +125
He I λ5876	−325 – +125
C IV λ5801	−125 – +125

the TVS analysis of He I λ4026.19 shows a response above the 95% continuum line between −200 and +100 km s^{-1}; the He I λ4471.48 line between −200 and +125 km s^{-1}; the wind line of He I λ5875.62 has a response between −325 and +125 km s^{-1}; and the deep-photosperic C IV λ5801.33 line also, in the range of ±125 km s^{-1}, see Table 5.10.

5.4.6 Time Variance Spectra (TVS) – NGC 2392

Likewise, the TVS images of the photospheric helium lines of NGC 2392 are presented along with their accompanying greyscale images, as well as the TVS/greyscale images of the He I λ5875.62 wind line and the deep-photospheric C IV λ5801.33 line: the photospheric helium lines of He I λ4026.19 and He I λ4471.48 give 95% confidence responses between −200 and +150 km s^{-1} and −250 and +150 km s^{-1} respectively; the He I λ5875.62 wind line shows a response between −250 and +100 km s^{-1}; and the C IV λ5801.33 line gives a response in the ±100 km s^{-1} range, see Table 5.11.

Table 5.11. NGC 2392 TVS velocity ranges

Spectral Line	TVS Velocity Range [km s^{-1}]
He I λ4026	−150 – −50
He I λ4471	−150 – +100
He I λ5876	−200 – +100
C IV λ5801	+50 – +100

5.4.7 Fourier Analysis & Signal Selection

The optical time-series spectra is fed into the Fourier2d analysis code (as used with the UV time-series spectra of NGC 6543 in Chapter 3), where each ion species previously analysed via TVS is now investigated for possible indications of variability modulation. The velocity range for the Fourier analysis for each individual ion species is restricted to the approximate range for which the TVS analysis indicated a response above the 95% confidence line; this restriction of the velocity range will focus specifically on the extent of the variance and so should therefore limit the amount of noise undergoing the Fourier analysis and so the power spectra outcome should be optimally devoid of noise-based interference which might otherwise produce misleading frequency signals.

Once the Fourier power spectra have been obtained then follows the task of examining all the Fourier responses from all absorption lines investigated to see whether any potential modulation signals can be uncovered. In order to do this a selection strategy has to set in motion, whereupon the frequency signals obtained for each absorption are subjected to key questions, and depending whether such criteria are met or not, each power spectra peak is either forwarded for further consideration or abandoned.

The key questions are:

• Has the peak in power (at said frequency) been derived from a Fourier analysis response from within the wavelength/velocity range of the absorption trough itself, and not from 'outside' where the peak may have originated due to fluctuations in noise-levels?

• Does the power spectra peak appear at (or within ± 0.2 (d^{-1})) any potential window functions?

• Does the particular peak frequency appear in the Fourier analysis results of more than one line?

• Does the frequency – and hence the subsequent time period – lend itself to a greyscale reproduction of a coherently time-modulated signal?

The window functions are those significant time periods of the observation windows from which the corresponding frequencies can become imprinted upon the Fourier-based analysis. For instance the data gathered for this optical analysis was gathered over three nights and so the frequency corresponding to the period of 3 days (i.e $f \sim 0.33$ d^{-1}) might produces an strong response which would be undesirable as it would not reflect any true modulation periods within the object(s) being studied. Similarly as each period

Table 5.12. Hen 2-138: Fourier power spectra peak frequencies

Spectral Line	Strongest Frequency Signals [d^{-1}]		
He I λ 4026	1.31250	1.72500	3.02500
He I λ 4471	1.27500	1.70000	2.90000
He I λ 5876	1.32500	2.13750	2.77500

of observation is begun at approximately the same time each evening, the frequency corresponding to the times period of 24 hours (i.e. $f \sim 1.00$ d^{-1}) might also produce an misleading response. The duration of an individual objects observation might produce yet another false frequency, or rather a short range of frequencies which one must be wary of: on each night NGC 2392 was observed for 3-3.5 hours ($6.85 < f < 8.00$ d^{-1}); Hen 2-131 and Hen 2-138 were observed (alternating between the two) over a total period of 6-6.5 hours ($3.69 < f < 4.00$ d^{-1}).

Only when a suspected frequency power peak can satisfy the above criteria can it be put forward as an indication of a possible modulation period in the absorption profile variability.

5.4.8 Fourier Analysis – Hen 2-138

Considering the Fourier output power spectra, having been passed through the CLEAN algorithm (Roberts et al. 1987), the peaks remaining may suggest periodic frequencies if potential modulation within the outflow of Hen 2-138, particularly of similar frequencies appear for more than one absorption line under analysis (assuming that the frequency noted has not been imposed upon the output by any possible window functions). The central frequency values of any given peak are read of an out ASCII file which lists in two columns the frequency (in steps of 0.01250 d^{-1}) and its corresponding power value so that one can track where a particularly strong peak rises to a maximum power before falling back down again. Although the peak frequency can be thus ascertained to the nearest 0.01250 step, an error margin can be estimated from a given peak's FWHM i.e. an error of $\pm$ HWHM, which amongst the peaks observed give FWHMs of between 0.3 and 0.4, suggesting a maximum error margin in frequency of $\pm$ 0.2 d^{-1}.

Listed in Table 5.12 are three peak power frequencies observed in the Fourier output power spectra for the photospheric lines of He I λ 4026.19 and He I λ 4471.48, as well as the optical wind line of He I λ 5875.62. The output spectra for photospheric helium lines as well as other metal lines in the optical spectra are shown in Figure 5.25. It was

observed that the strongest peaks were obtained for the helium lines, both from the near photospheric region as well as the base of the wind; other metal lines tended to produce much shallow peaks whose relative power was at least an order of magnitude less than that of the stronger helium signals. Therefore it was decided that the search for modulation frequencies/periods would focus upon the stronger helium lines. The difference in relative strength between the power spectra outputs for the stronger helium lines and, by way of example, the output for the metal line of C IV λ 5801.33 is shown in Figure 5.26.

As discussed above in the key questions that need to be addressed when seeking strong modulation signals, it is necessary to observe a given peak frequency in more than one line before the signal can be seriously considered. This appears to be the case with the lines of He I λ 4026.19 and He I λ 4471.48, with both showing strong peaks at approximately 1.3 and 1.7 d^{-1}: these frequencies correspond to periods of 0.77 d and 0.58 d respectively. A third shallower peak is also visible for both lines at around 3.0 d^{-1} for the former line, and at around 2.9 d^{-1} for the latter: likewise corresponding to periods of 0.33 d and 0.35 d respectively. These last two peak frequency values are noticeably close to one another, within less than the ± 0.2 d^{-1} error margin of the Fourier power spectra display: it is therefore reasonable to 'average' their corresponding periods of 0.33 d and 0.35 d – resulting in a third potential modulation test-period of 0.34 d.

In earlier research (Prinja et al. 2010), it was reported that there are alias peaks at 1.4 and 2.8 d^{-1}, but this result has not exactly been repeated in more recent analysis. However it should be noted that the lower twin peaks lie either side of an average peak at approximately 1.4 d^{-1} and the latter two peaks lie either side of an average of 2.8 d^{-1}. Perhaps this second analysis has produced power spectra of a greater resolution, that is the earlier analysis being of a lower resolution has contrived to suggest alias frequents which on closer inspection may not be as coincidental as at first thought, although the more recent peaks lie within a reasonably close distance to the former values of these 'aliases'.

5.4.9 Fourier Analysis – Hen 2-131

As in the Fourier analysis of Hen 2-138, the strongest power spectra responses for Hen 2-131 arose in the analyses of the photospheric helium lines of He I λ 4026.19 and He I λ 4471.48 and the wind line of He I λ 5875.62: as detailed in Table 5.13 the two photospheric lines provide peak power signals at frequencies at ~ 2.4 d^{-1}, ~ 3.5 d^{-1}, and ~ 4.4 d^{-1}, which correspond to potential modulation periods of 0.43, 0.30, and 0.23 d respectively. Likewise

Table 5.13. Hen 2-131: Fourier power spectra peak frequencies

Spectral Line	Strongest Frequency Signals [d^{-1}]		
He I λ 4026	2.35000	3.47500	4.38750
He I λ 4471	2.35000	3.55000	4.50000
He I λ 5876	2.77500	3.62500	4.51250

the He I λ 5875.62 wind line shows its peak frequencies at $\sim$ 2.8 d^{-1}, $\sim$ 3.6 d^{-1}, and $\sim$ 4.5 d^{-1} which, within the $\pm$ 0.2 d^{-1} error of the FWHM of the power spectra peaks for the photospheric absorption lines, and hence, correspond to similar periods.

A better comparison of the separate power spectra for the different lines is afforded when the power spectra are superimposed upon one another to see whether frequency peaks can be found in roughly the same positions for different resonance lines.

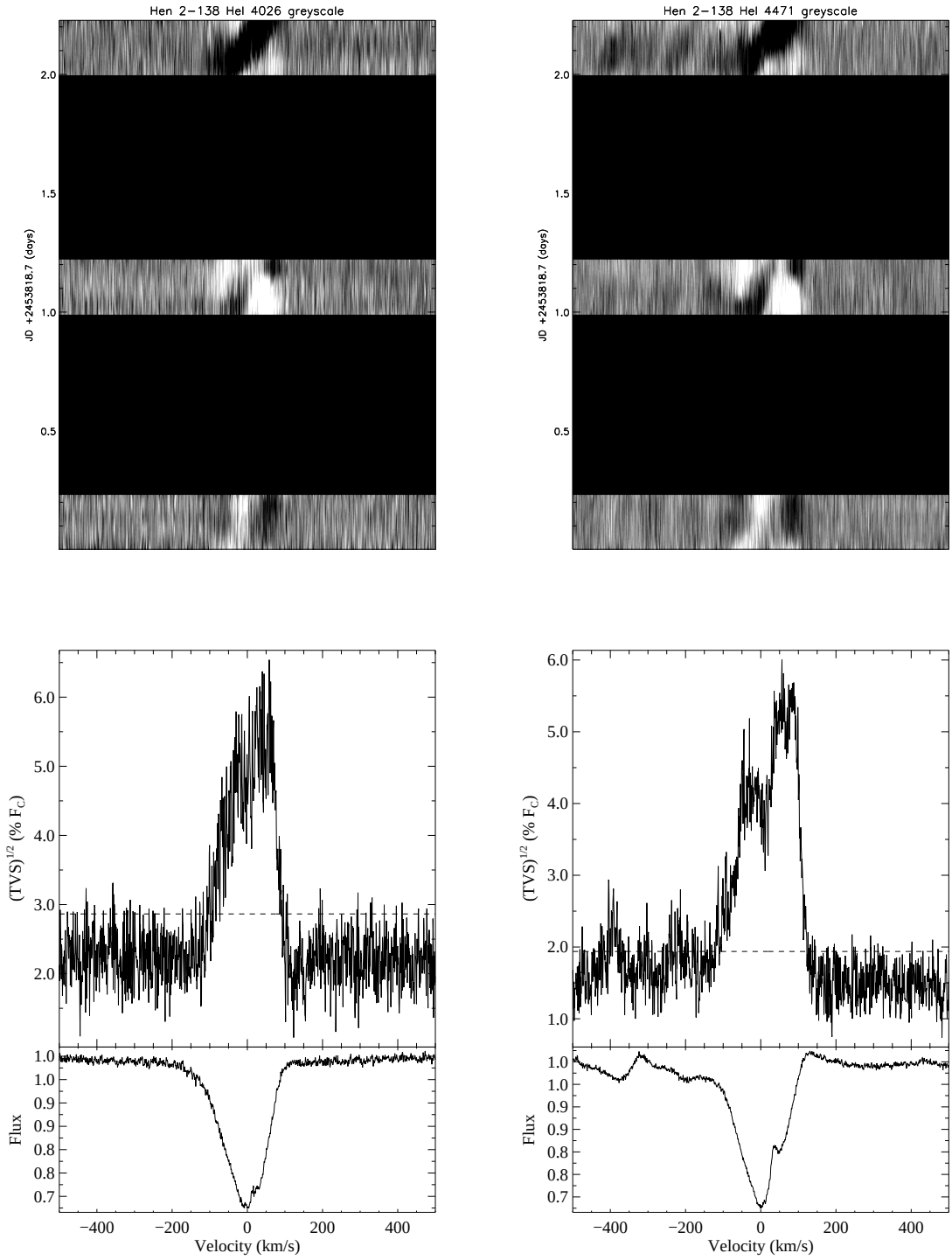

Fig. 5.19. TVS analysis plots (below) of the absorption profile of the He I λ 4026 (l) and He I λ 4471 (r) optical lines of Hen 2-138, where the upper panel of each TVS profile depicts the variance statistic, with changes above the 95% significance level (dotted line) highlighted. The corresponding greyscale depiction of each line profile's time-series spectra is also shown (above) depicting the temporal changes in the (vertically stacked) individual spectra, all normalised by the corresponding mean profile as shown in the lower panel beneath the TVS significance profile; the dynamical range of the greyscales on this page – and all subsequent greyscales in this chapter – is 0.95 (black) to 1.05 (white).

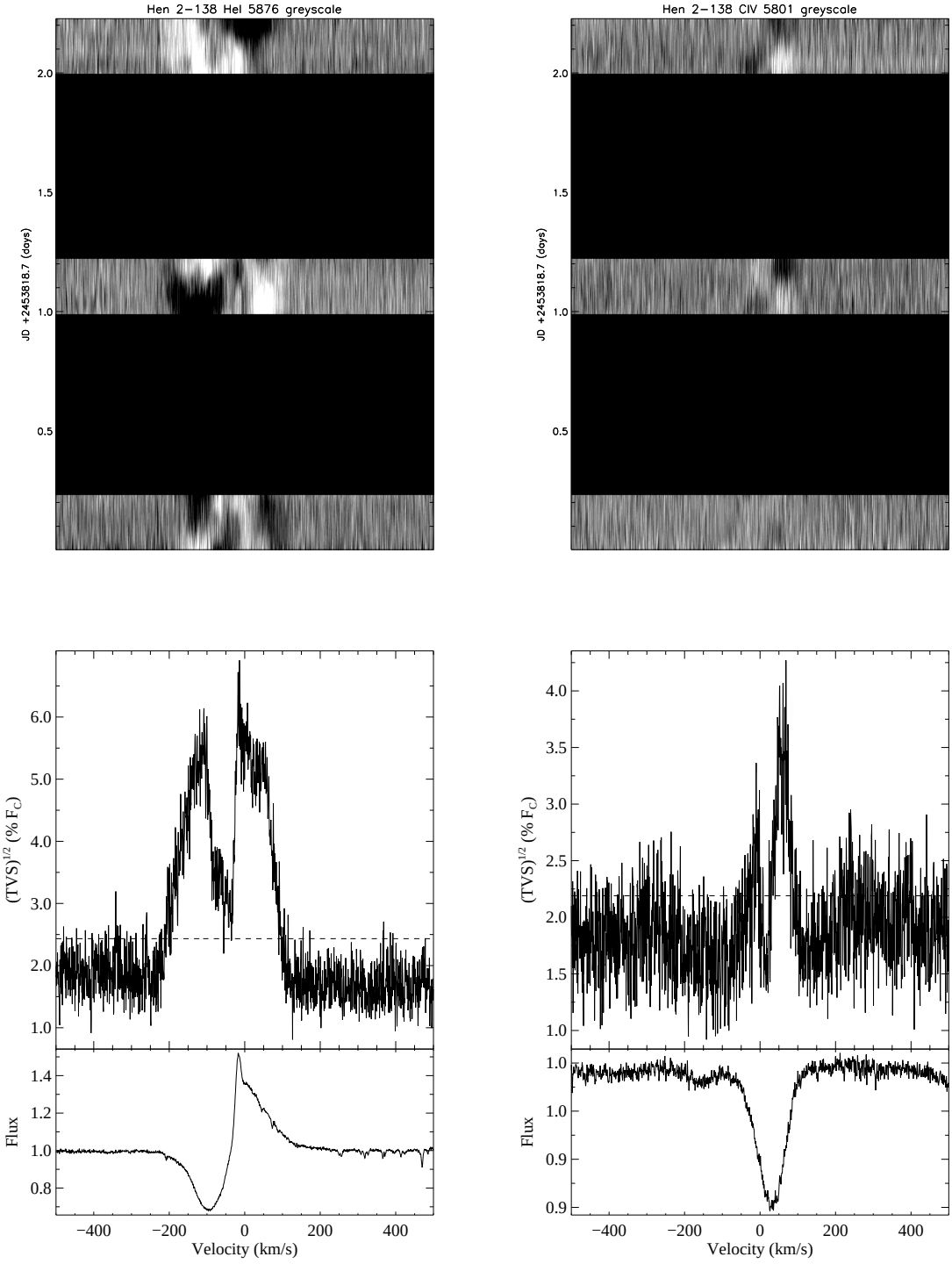

Fig. 5.20. TVS analysis plots (below) of the absorption profile of the He I λ5876 (l) and C IV λ5801 (r) optical lines of Hen 2-138; the corresponding greyscale depiction of each lines time-series spectra is also shown (above).

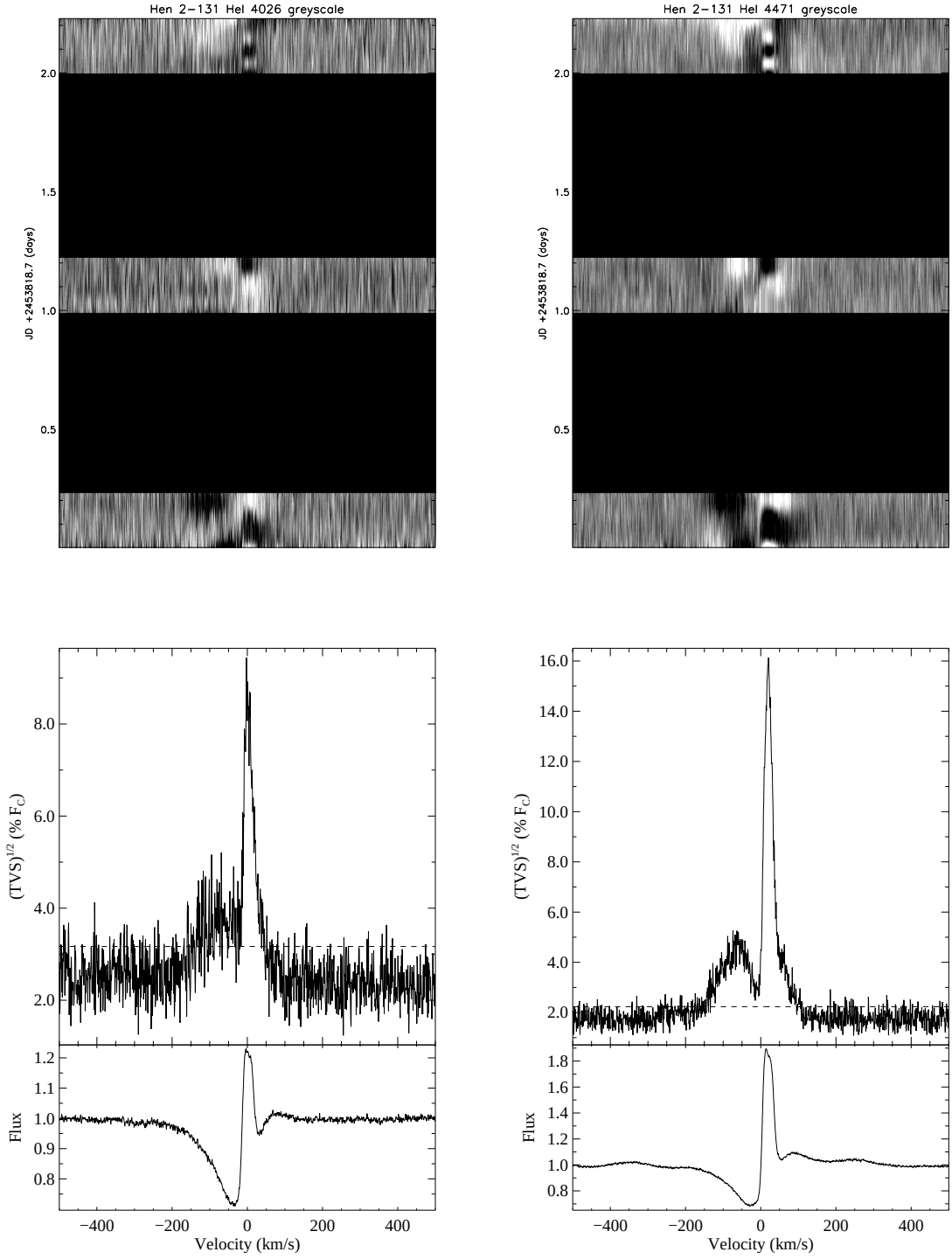

Fig. 5.21. TVS analysis plots (below) of the absorption profile of the He I λ 4026 (l) and He I λ 4471 (r) optical lines of Hen 2-131; the corresponding greyscale depiction of each lines time-series spectra is also shown (above).

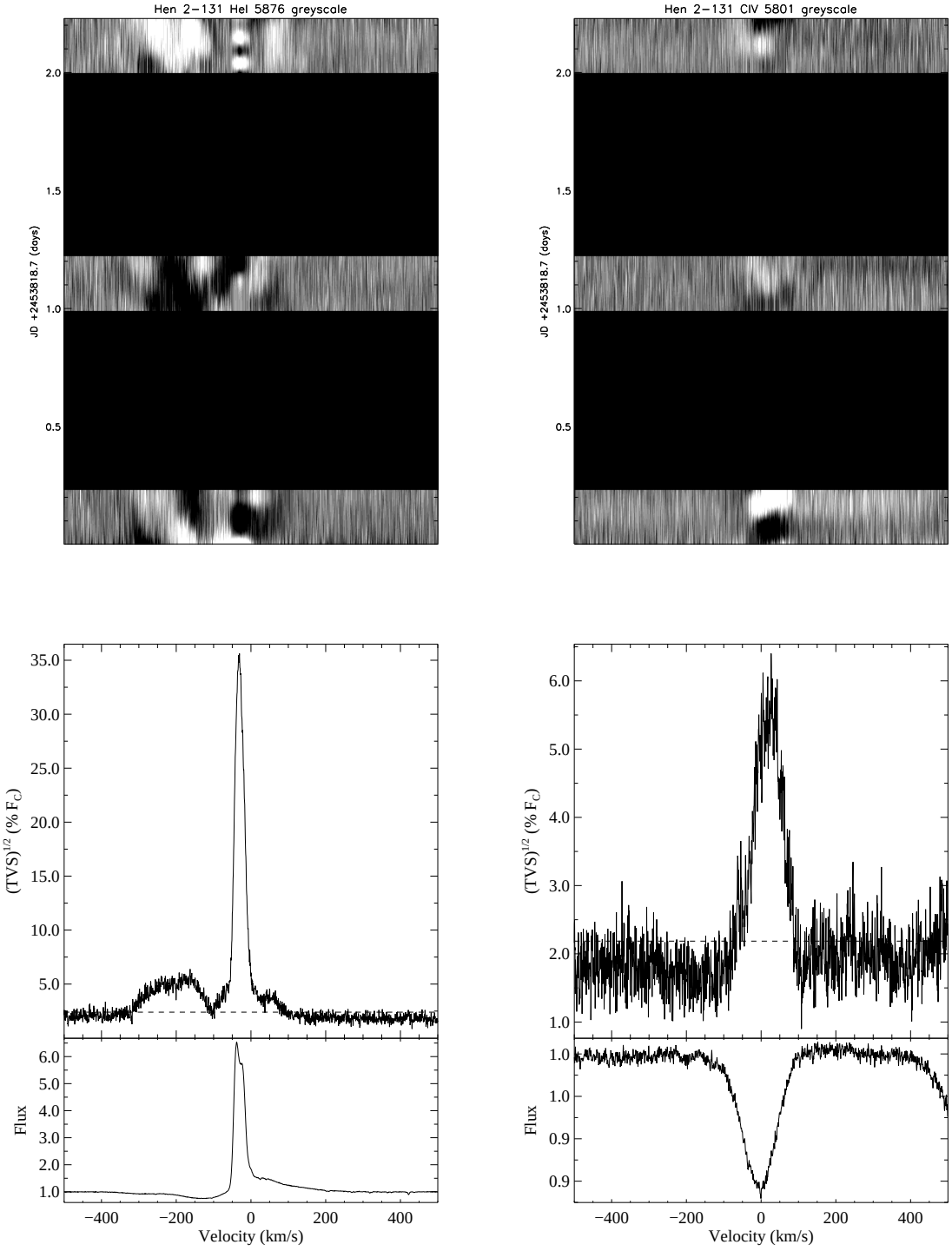

Fig. 5.22. TVS analysis plots (below) of the absorption profile of the He I λ5876 (l) and C IV λ5801 (r) optical lines of Hen 2-131; the corresponding greyscale depiction of each lines time-series spectra is also shown (above).

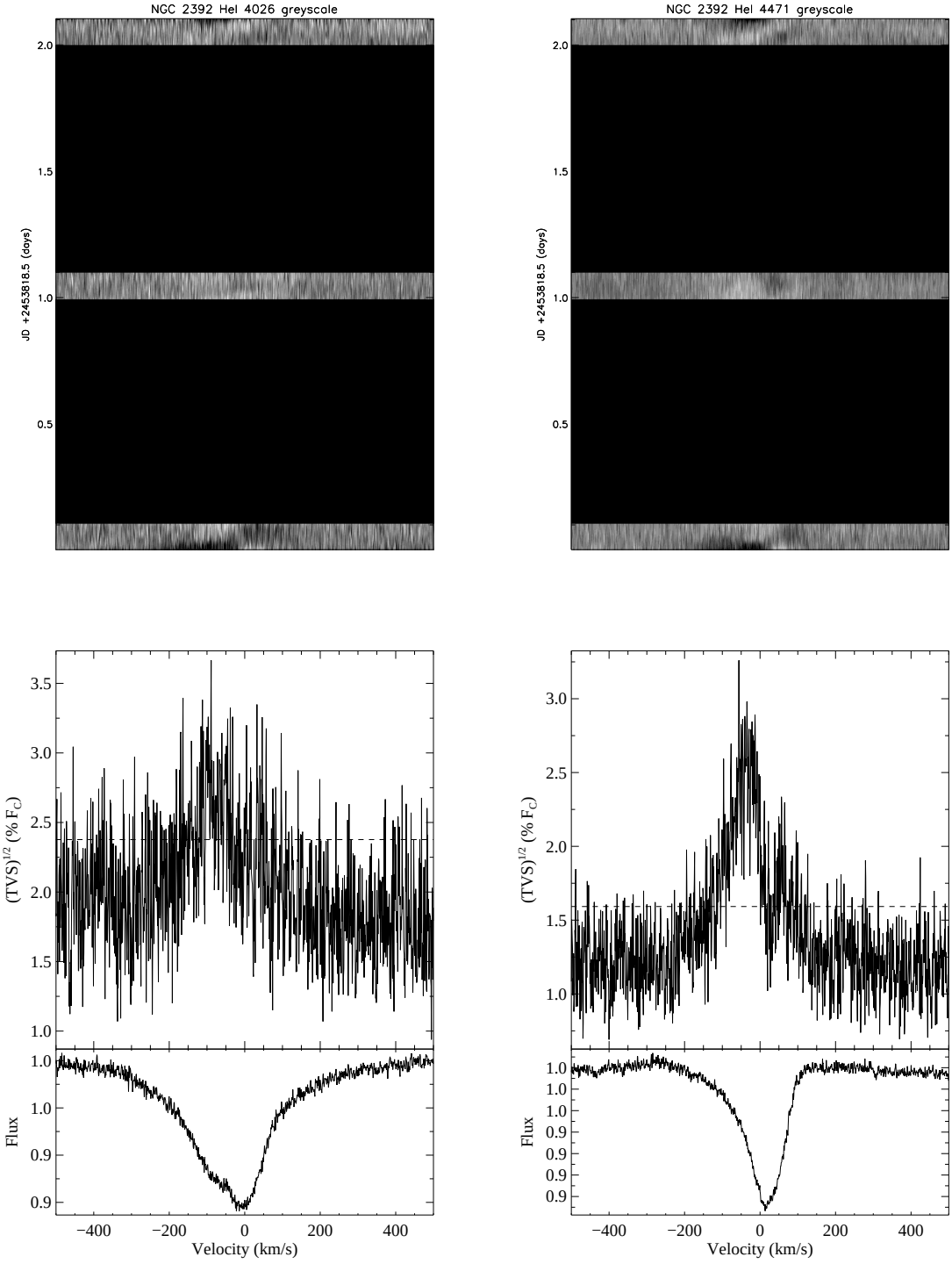

Fig. 5.23. TVS analysis plots (below) of the absorption profile of the He I λ 4026 (l) and He I λ 4471 (r) optical lines of NGC 2392; the corresponding greyscale depiction of each lines time-series spectra is also shown (above).

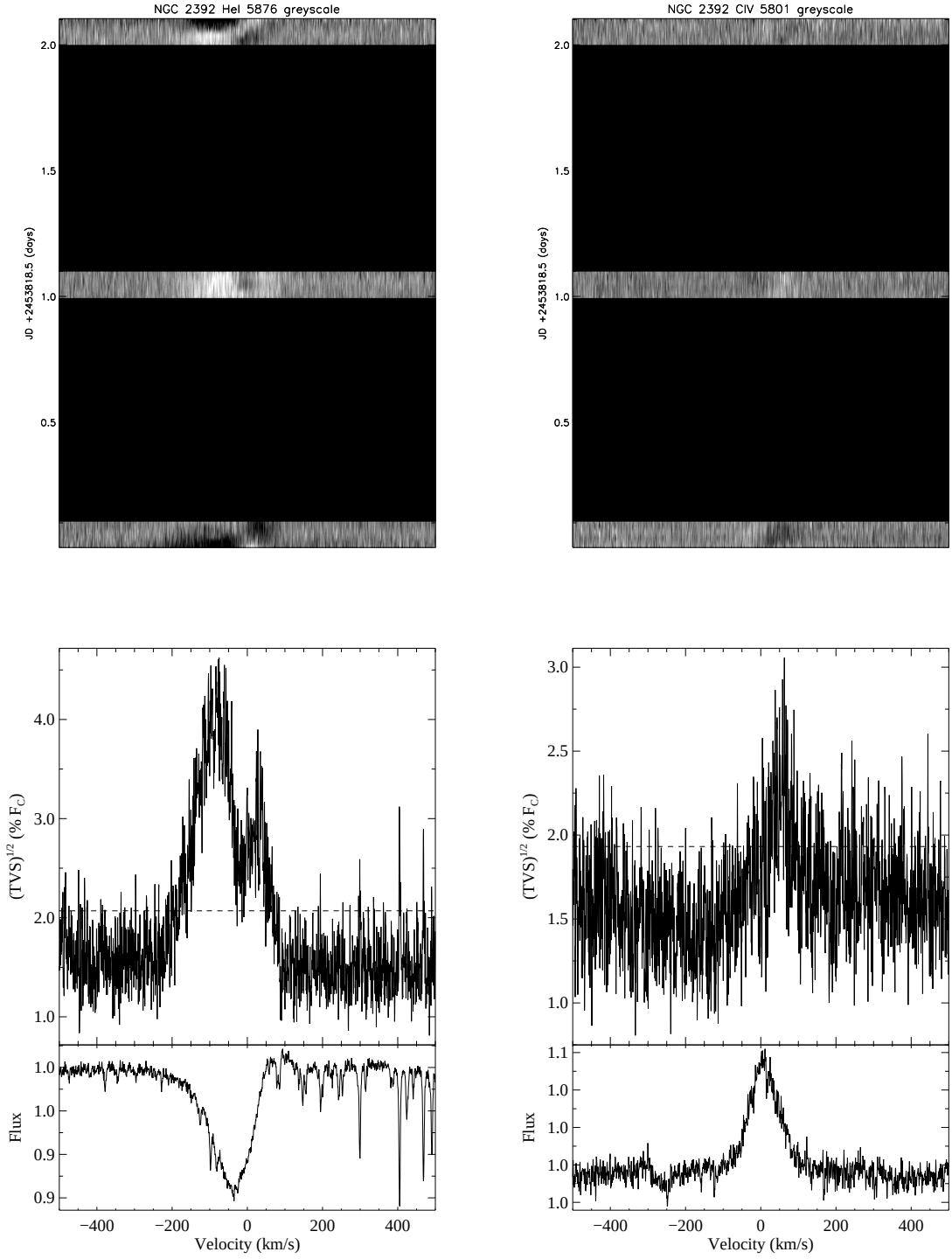

Fig. 5.24. TVS analysis plots (below) of the absorption profile of the He I λ5876 (l) and C IV λ5801 (r) optical lines of NGC 2392; the corresponding greyscale depiction of each lines time-series spectra is also shown (above).

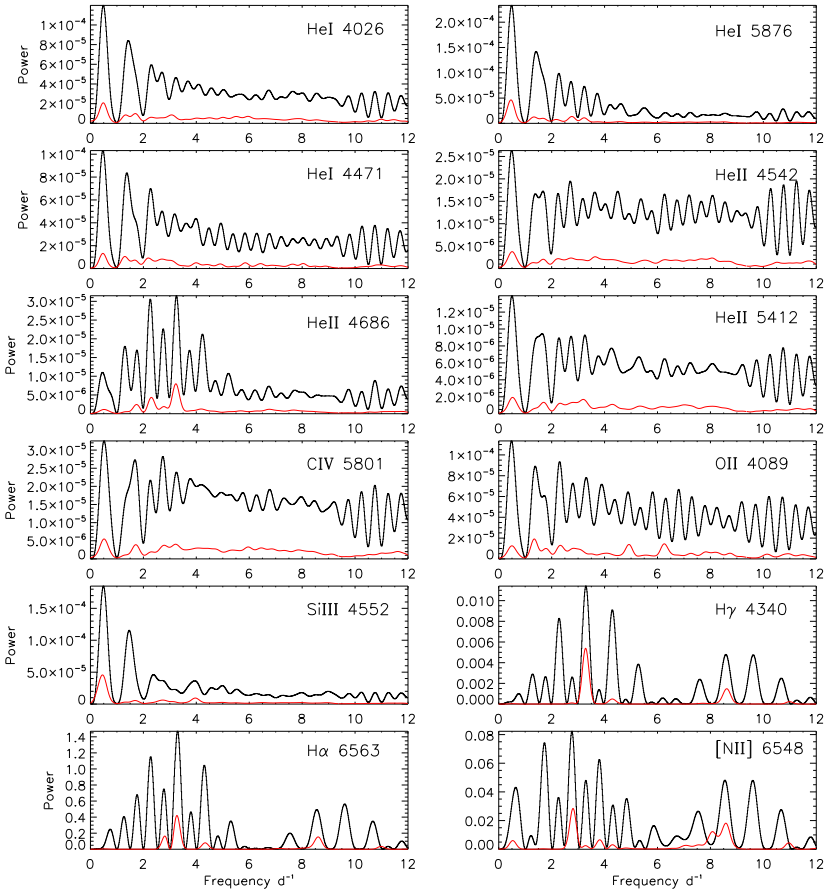

Fig. 5.25. A display of Fourier power spectra for the optical resonance lines of Hen 2-138: the black shows the uncleaned power spectra and the red shows the cleaned power spectra.

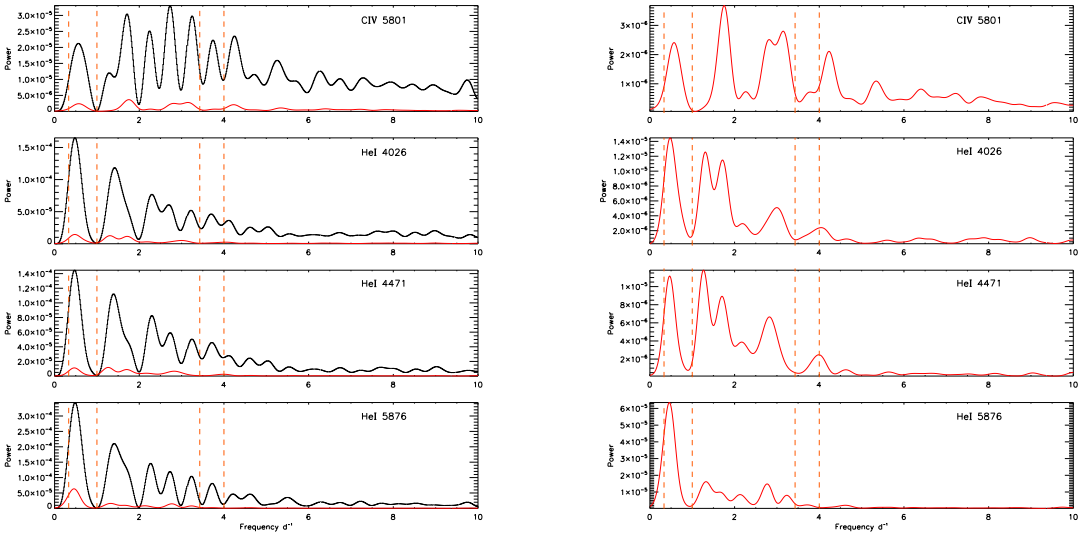

Fig. 5.26. Fourier power spectra (left) of the C IV λ 5801 deep photospheric line, and the He I λ 4026, He I λ 4471 and He I λ 5876 deep-wind lines of Hen 2-138: the uncleaned power spectra is shown in black, with the corresponding cleaned spectra superimposed in red; Cleaned power spectra of the aforementioned optical lines are also shown separately (right). The dotted lines indicate the window function frequencies which may provide false power peaks.

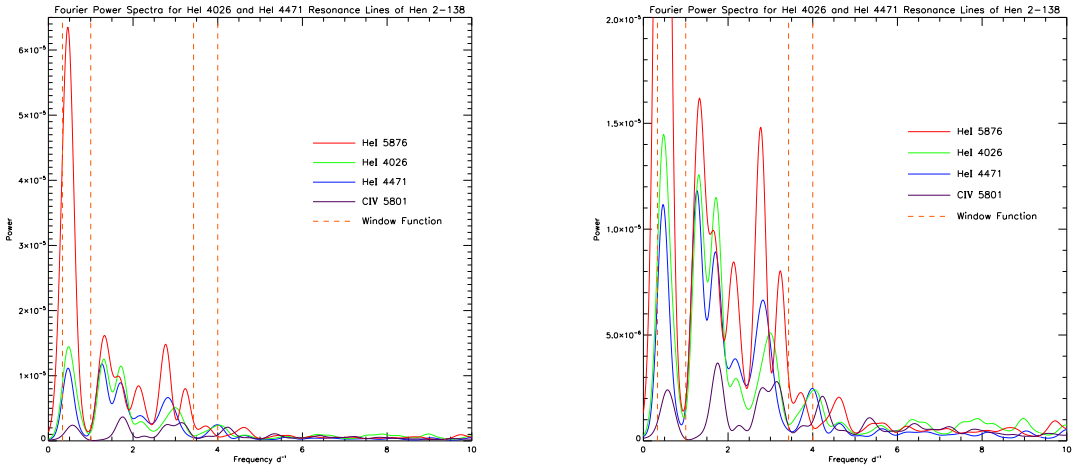

Fig. 5.27. A display of the cleaned power spectra of the C IV λ 5801, He I λ 4026, He I λ 4471, He I λ 5876 optical lines of Hen 2-138 *over*-plotted upon each other – the aim is to strengthen any potential periodicity in the variability by identifying a peak frequency in more than one line.

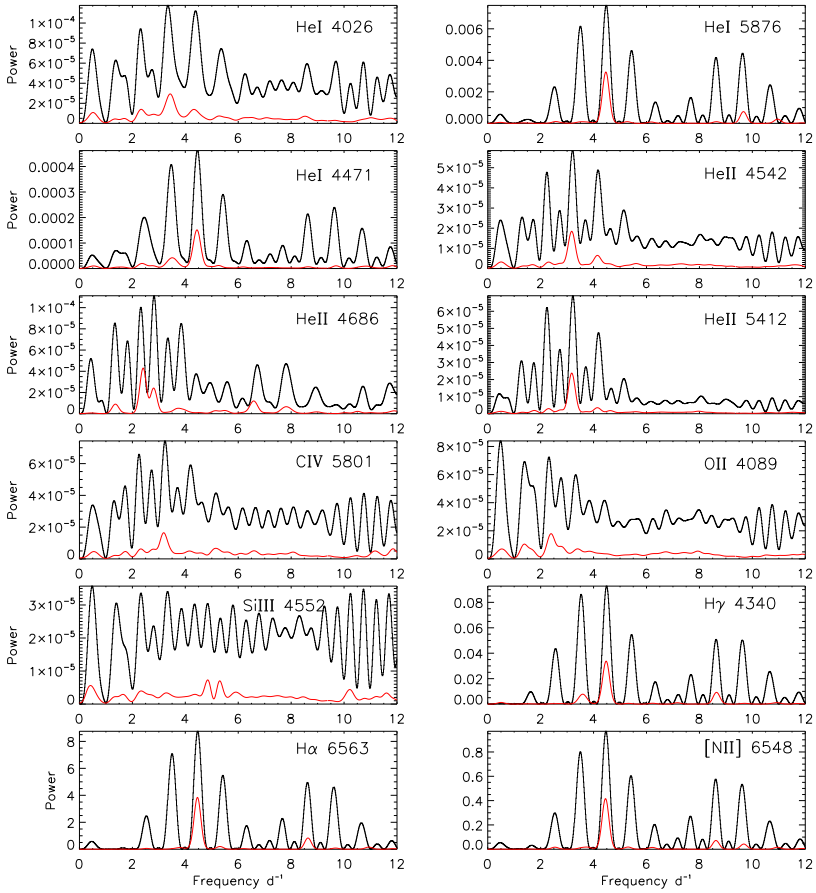

Fig. 5.28. A display of Fourier power spectra for the optical resonance lines of Hen 2-131: the black shows the dirty power spectra and the red shows the cleaned power spectra.

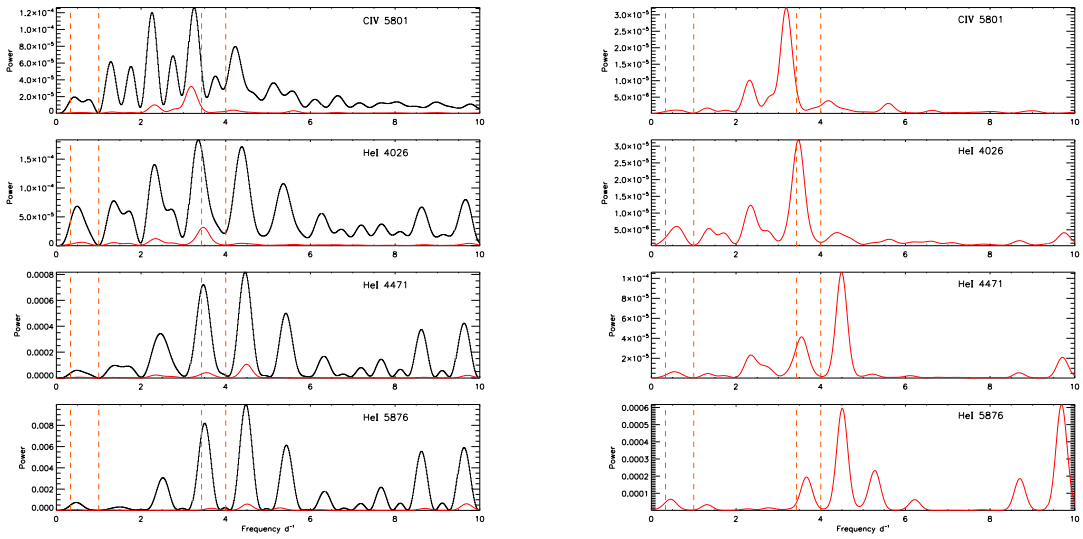

Fig. 5.29. Fourier power spectra (left) of the C IV λ 5801 deep photospheric line, and the He I λ 4026, He I λ 4471 and He I λ 5876 deep-wind lines of Hen 2-131: the uncleaned power spectra is shown in black, with the corresponding cleaned spectra superimposed in red; Cleaned power spectra of the aforementioned optical lines are also shown separately (right). The dotted lines indicate the window function frequencies which may provide false power peaks.

Table 5.14. NGC 2392: Fourier power spectra peak frequencies

Spectral Line	Strongest Frequency Signals [d^{-1}]		
He I λ 4026	2.35000	3.31250	4.28750
He I λ 4471	2.35000	3.31250	4.27500
He I λ 5876	2.63250	3.31250	4.26250

5.4.10 Fourier Analysis – NGC 2392

PN NGC 2392 is similarly analysed and the results presented below. In initial analysis this appears to show a very strong correlation in the power spectra for all lines, at a frequency of approximately 7.5 d^{-1}. In actual fact the obvious correlation is rather too strong and so a close look at the frequency value for the strongest peaks is required, and it it noted that the resultant value is actually closely attuned to the times the observations of the data were undertaken over the three nights of the run. As exposures were taken of this object during the first 3 – 3.5 hours of the nights session for three nights this repetition has embedded itself in the data, as this ∼3 hour window function had imposed this ∼ 7.5 d^{-1} frequency upon the power spectra, thereby overpowering any actual true modulation frequency/periodicity which might otherwise make a greater impression upon the analysis tool.

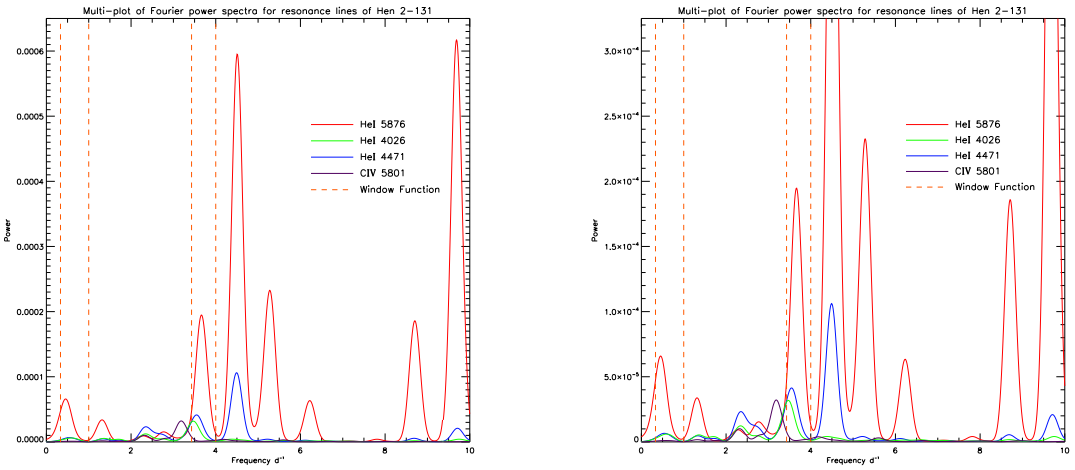

Fig. 5.30. A display of the cleaned power spectra of the C IV λ 5801, He I λ 4026, He I λ 4471, He I λ 5876 optical lines of Hen 2-131 *over*-plotted upon each other – the aim is to strengthen any potential periodicity in the variability by identifying a peak frequency in more than one line.

However, repeated analysis, but with a higher maximum frequency of 20 d^{-1}, has not produced such a strong response as the above window function, especially when one plots the power spectra for only the range up to 10 d^{-1} in order to focus upon lower frequencies of the photospheric helium lines which, in the other PNs of this chapter, have demonstrated relatively strong peaks within the 0 – 5 d^{-1} range in the other Fourier analyses of their respective optical time-series spectra. There are strong frequency response from both the He I λ 4026.19 and He I λ 4471.48 photospheric lines at $\sim$ 2.4 d^{-1}, $\sim$ 3.3 d^{-1}, and at $\sim$ 4.3 d^{-1}. The He I λ 5875.62 low wind line produces a slightly different lowest frequency response at $\sim$ 2.6 d^{-1} but this is within the $\pm$ 0.2 d^{-1} margin indicated by the FWHM of the frequency responses; the other two strong responses are similar to the corresponding responses from the photospheric helium lines, of $\sim$ 3.3 d^{-1}, and at $\sim$ 4.3 d^{-1}. Consequently, these frequencies give corresponding (potential) modulation periods of 0.43, 0.30, and 0.23 d.

5.4.11 Greyscale Representations of Phased Periods – Hen 2-138

The time-series spectra of Hen 2-138 of the key helium line profiles are again fed into the greyscale algorithm, but now the pictorial output can be phased over the key periods indicated by the peak frequencies as displayed in their respective Fourier power spectra. Each of the three aforementioned potential modulation periods: 0.77 d, 0.58 d, and 0.34

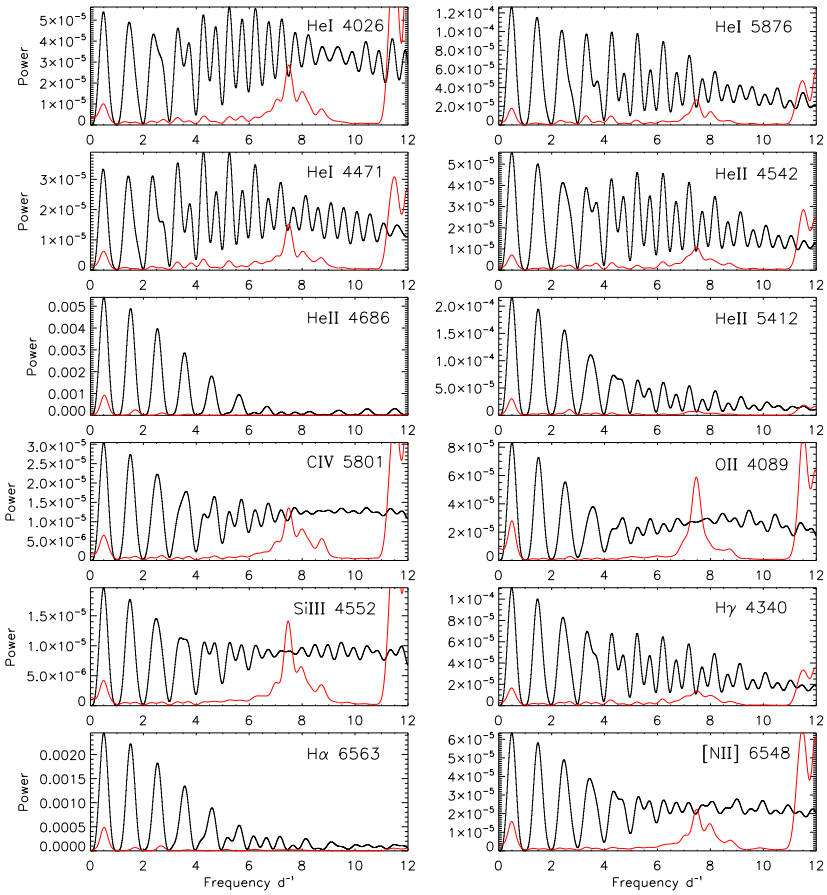

Fig. 5.31. A display of Fourier power spectra for the optical resonance lines of NGC 2392: the black shows the uncleaned power spectra and the red shows the cleaned power spectra.

d, are thereby 'greyscale-tested'. The period which demonstrates the greatest coherency is the latter 0.34 d period, see Figure 5.34: both the He I λ 4026.19 and the He I λ 4471.48 lines appear to exhibit a periodic consistency in their features migrating from bluer to redder velocities over this repeated period; the higher wind He I λ 5875.62 line, on the other hand, does not show a similar degree of coherency – it appears relatively fragmented over this period – and so it cannot be concluded that its structural changes are modulated over this timescale.

This shorter 0.34 d period would be repeated approximately 6 times over the 2.2 d of the observation.

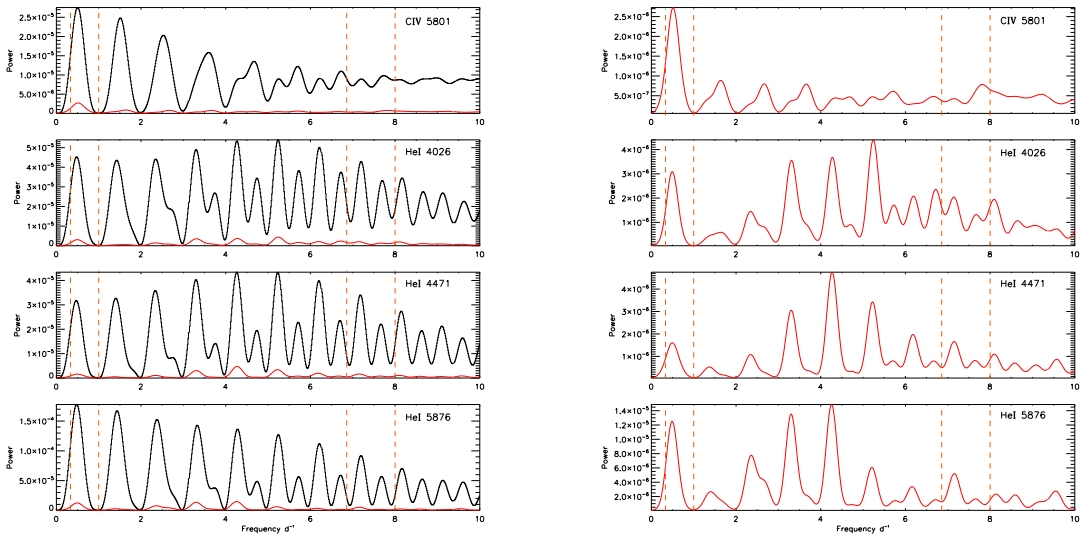

Fig. 5.32. Fourier power spectra (left) of the C IV λ 5801 deep photospheric line, and the He I λ 4026, He I λ 4471 and He I λ 5876 deep-wind lines of NGC 2392: the uncleaned power spectra is shown in black, with the corresponding cleaned spectra superimposed in red; Cleaned power spectra of the aforementioned optical lines are also shown separately (right). The dotted lines indicate the window function frequencies which may provide false power peaks.

5.4.12 Greyscale Representations of Phased Periods – Hen 2-131

The time-series spectra of the individual line profiles of Hen 2-131 are similarly inputted into the greyscale algorithm and phased over each of the potential modulation periods corresponding to the stronger frequencies observed in the Fourier analysis of the helium lines. The resulting representation which shows the greatest degree of coherency is that data which has been phased over the period of 0.43 d, see Figure 5.35. As in the similar phased greyscale image of Hen 2-138 it is possible to observe dark absorption features migrating towards the red. Also, in the He I λ 5875.62 wind line, one observes features which appear to migrate in opposite directions: one from blue to red (as seen in the photospheric lines of Hen 2-138); but also a feature which migrates from redder to bluer velocities – in a similar fashion to the DAC-like features observed in the UV spectra of the two previous chapters.

For Hen 2-131, a modulation period of 0.43 d would be repeated approximately 5 times over the 2.2 d duration of the observation.

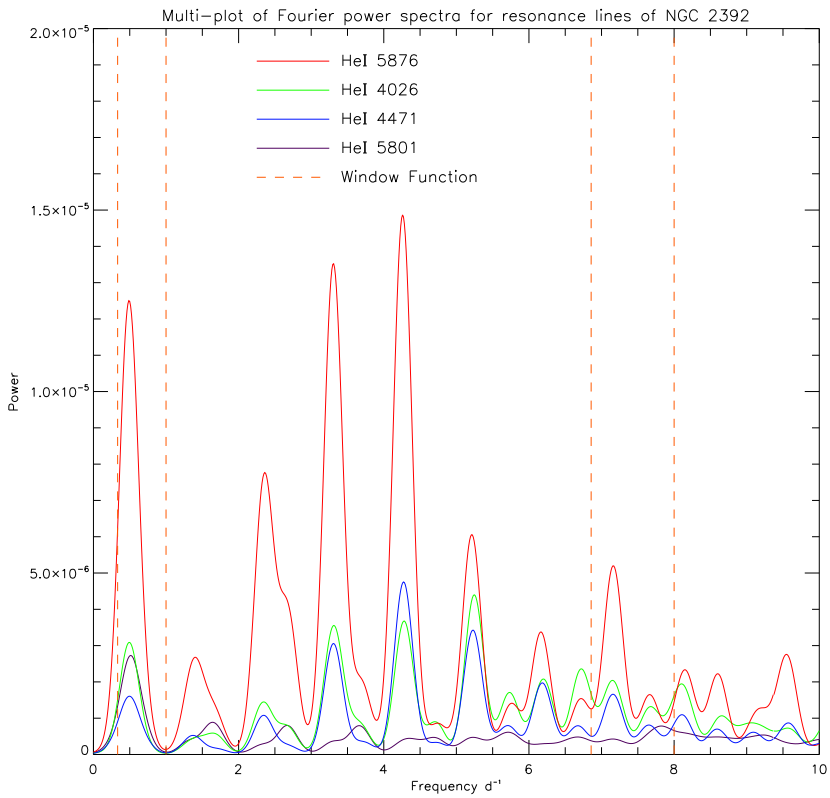

Fig. 5.33. A display of the cleaned power spectra of the C IV λ 5801, He I λ 4026, He I λ 4471, He I λ 5876 optical lines of NGC 2392 *over*-plotted upon each other – the aim is to strengthen any potential periodicity in the variability by identifying a peak frequency in more than one line.

5.4.13 Greyscale Representations of Phased Periods – NGC 2392

When the time-series quotient line profiles for the He I λ 4026.19, He I λ 4471.48 and He I λ 5875.62 lines are once again reproduced via greyscale, but with the representations phased over each prospective modulation period, the more coherent images of the travelling of feature within the profiles are those phased on the 0.23 d period, shown in Figure 5.36. However, in contrast to the similar representations of the line profiles of Hen 2-138, this coherency is stronger in the 3-cycle greyscale of the He I λ 5875.62 profile; the corresponding greyscale images of the photospheric helium lines are not as well reproduced.

Similar greyscale representations are also shown of the similar profiles – Figure 5.37 – but phased over a period of 0.30 d, where again the He I λ 5875.62 profile shows the greater coherency over this period.

The modulation period of 0.23 d would be repeated approximately 9 times over the 2.2 d duration of the observation; the 0.30 d period would be repeated approximately 7 times.

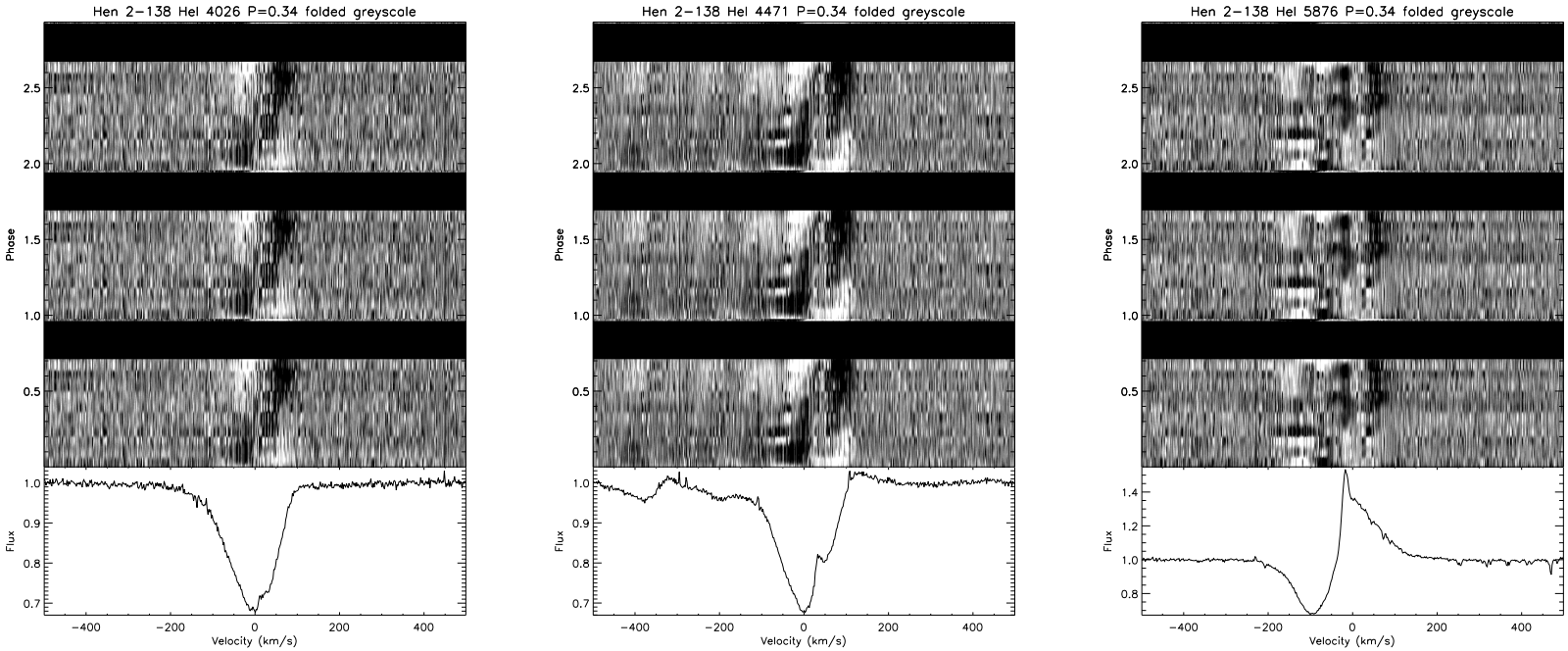

Fig. 5.34. Greyscale display of the He I λ 4026 (l), He I λ 4471 (c), and He I λ 5876 (r) deep-wind lines of Hen 2-138, in which the data has been 'folded' over a period of 0.34 days.

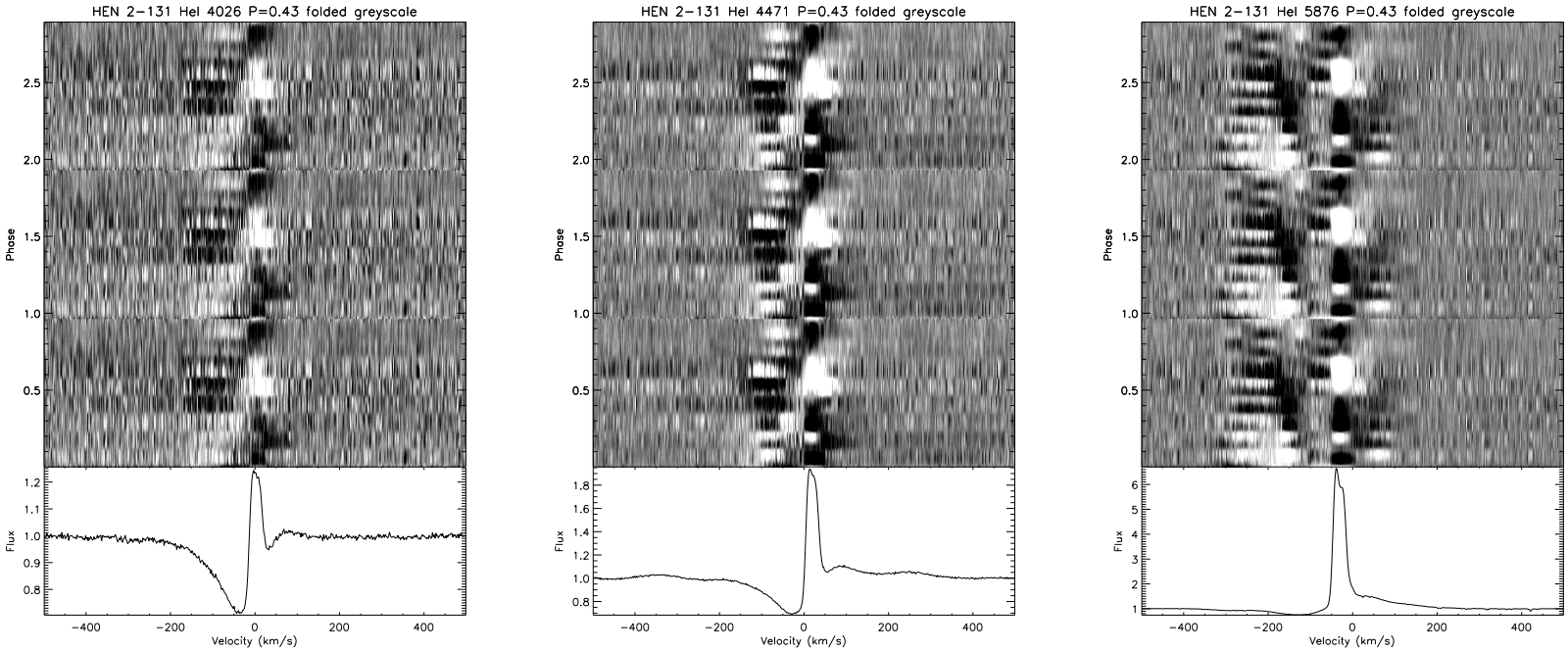

Fig. 5.35. Greyscale display of the He I λ 4026 (l), He I λ 4471 (c), and He I λ 5876 (r) deep-wind lines of Hen 2-131, in which the data has been 'folded' over a period of 0.43 days.

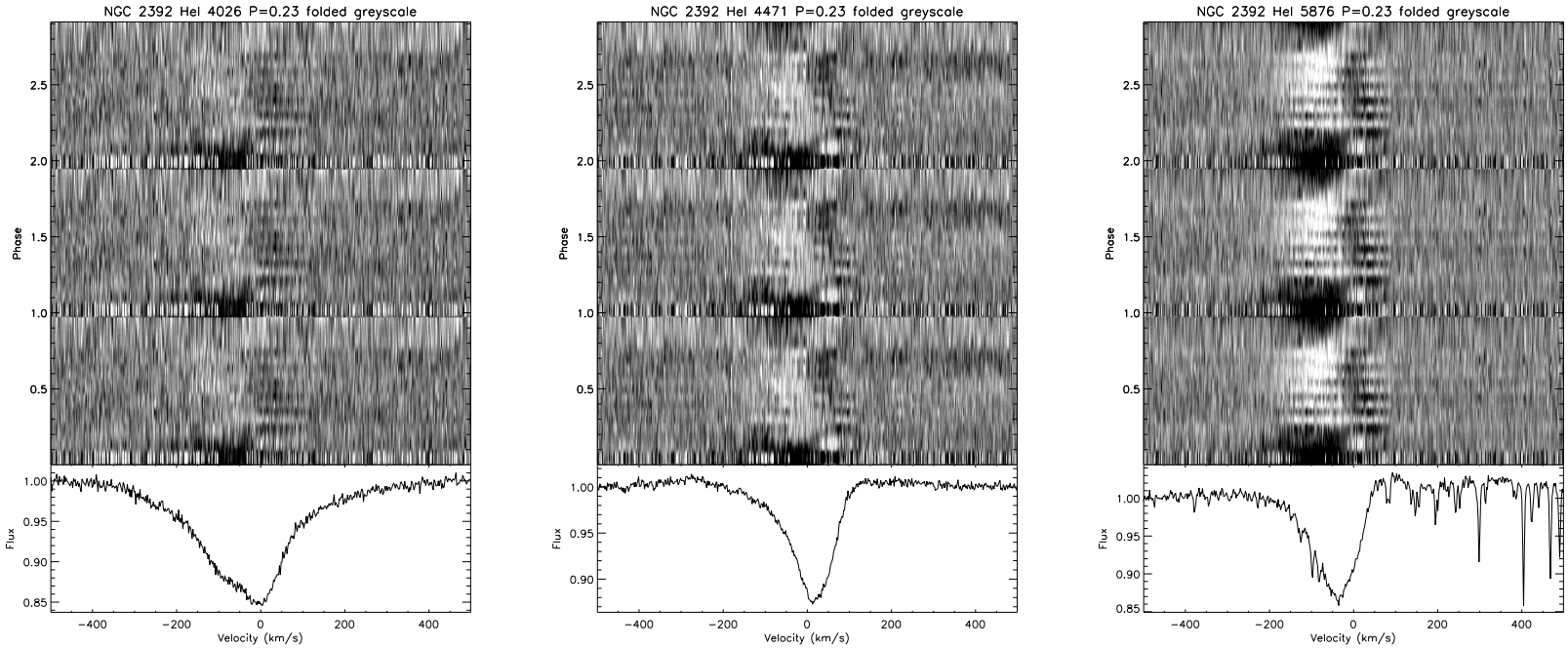

Fig. 5.36. Greyscale display of the He I λ 4026 (l), He I λ 4471 (c), and He I λ 5876 (r) deep-wind lines of NGC 2392, in which the data has been 'folded' over a period of 0.23 days.

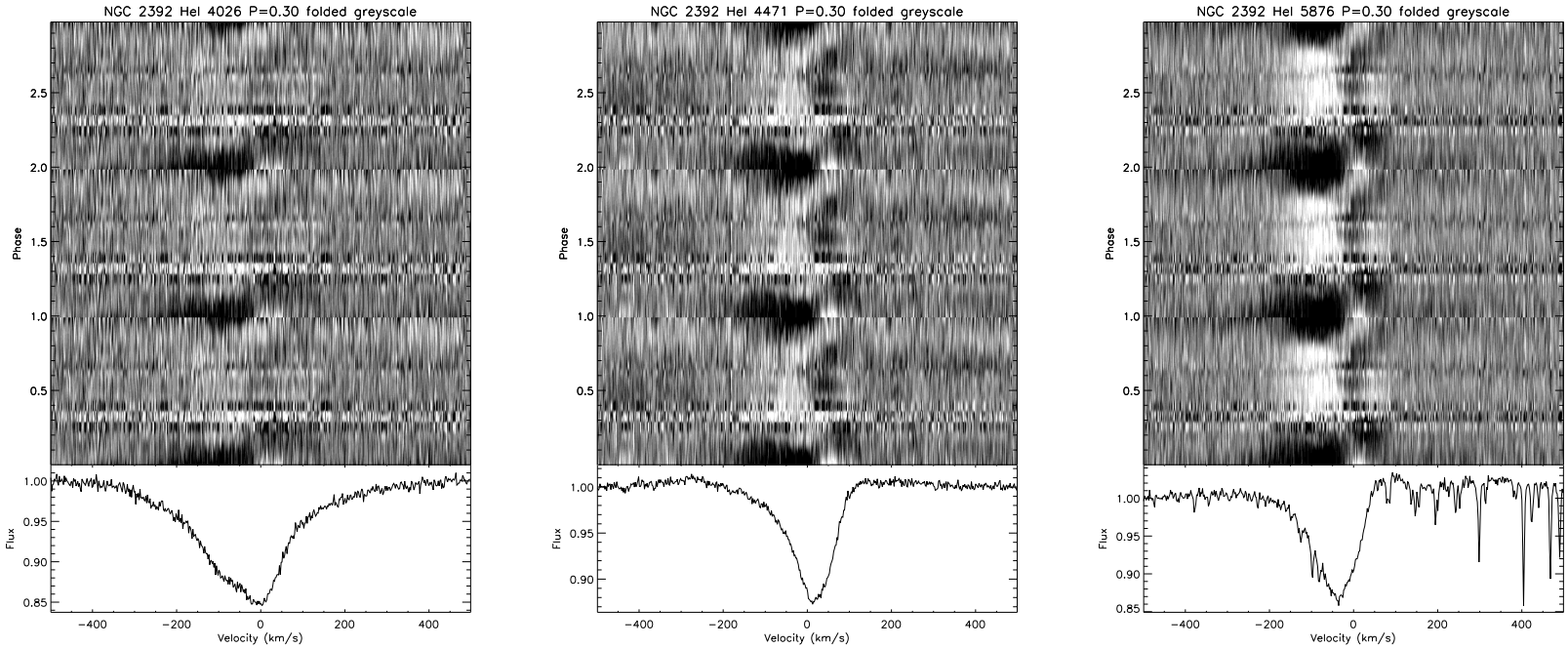

Fig. 5.37. Greyscale display of the He I λ 4026 (l), He I λ 4471 (c), and He I λ 5876 (r) deep-wind lines of NGC 2392, in which the data has been 'folded' over a period of 0.30 days.

5.5 Discussion

From a desire to obtain more data upon other CSPNs – promoted by the lack of available time-series data for such objects – I have been given the opportunity to observe and analyse temporal phenomena with a deeper (nearer-photospheric) region of the stellar wind, where as well as the wind P Cygni line of He I λ 5875.62, the data has provided the means – through the (in-house) reduction and subsequent analysis of more photospheric helium species, particularly the absorption lines of He I λ 4026.19 and He I λ 4471.48, as well as photospheric metal lines e.g. C IV λ 5801.33.

The various analyses presented in this chapter indicate that the PN He 2-138 possesses a dense, slow moving outflow indicated by the blueshifted Si III triplet found in the densest super-photospheric regions of a stellar atmosphere. Whereas similar blueshifted Si III triplet profiles are observable in the UV spectra of Hen 2-131 and suggest a similar conclusion; the UV spectra of NGC 2392 show much shallower/weaker absorption profiles, with the Si III triplet exhibiting little in the way of P Cygni-type wind signature, although possible marginally blueshifted.

The SEI resonance line model fits suggest that Hen 2-138 possesses a dual-component wind: the lower ion species of Al III λ 1854.72 and S IV λ 1072.97 are modelled with a wind terminal velocity of 300 km s^{-1}, whereas the higher ion species of C IV λ 1548.20 and Si IV λ 1393.76 required the requisite wind terminal velocity parameter for SEI stepped up to 700 km s^{-1} in order for a decent model fit.

Similar SEI modelling undertaken on UV data (from IUE and FUSE) of the central stars of Hen 2-131 and NGC 2392 have been carried out with, for the most part, a terminal wind velocity of 400 km s^{-1}; the only exceptions were a slight increase to v_∞= 450 km s^{-1} for the S IV λ 1072.97 (red) component, and a larger increase to 600 km s^{-1} for the Si IV λ 1393.76 (blue) component. These being the only exceptions, there was not enough evidence to suggest the existence of a dual-velocity nature to the wind of either central star, and indeed such a conclusion has not been seen in any of the literature pertaining to these two objects.

Further line synthesis modelling of Hen 2-138, via CMFGEN, has indicated that the outflow has a dual-component nature: the CMFGEN analysis for a temperature of a hotter component ($>$ 29,000 K) provides a better fit to the near-photospheric C IV and O III lines, but at the same time predicting too much He II and not enough He I ; in

contrast, a cooler component ($\sim$ 25,000 K) is required to better fit the low ionisation lines (including C II and Al III), but these models subsequently predict too much photospheric He I and therefore not enough/is too weak in He II . The CMFGEN model is unable to reproduce the relative strengths between the absorption and emission components of P Cygni profiles, particularly those of the Si IV $\lambda\lambda$ 1393.76, 1402.77, the C IV $\lambda\lambda$ 1548.20, 1550.77, and the Mg II $\lambda\lambda$ 2795.53, 2802.70 doublets. If this suggests the presence of dual-nature to the outflow, this would seem to be confirmed in the SEI modelling of some of the P Cygni resonance lines: for the UV Al III λ 1854.72 and the S IV λ 1072.97 which as a lower abundance surrogate to the S IV line in the range if ionisation potential, these lines can only be modelled with a terminal velocity of 300 km s^{-1}, whereas a more than double terminal velocity is required for the modelling of the blue component of the S IV $\lambda\lambda$ 1062.66, 1072.97 doublet, as with the similar component of the C IV $\lambda\lambda$ 1548.20, 1550.77 doublet. It is important to note that although the P Cygni profiles modelled have been taken from a variety of different sources (IUE, FUSE), and hence different epochs, there has been no recorded shift in the blue edge/wings of the resonance lines which is more than 100 km s^{-1}.

Hybrid winds can often be seen emanating from Be stars, where dual layer outflows have been modelled: a hotter and higher velocity wind emanates from the polar regions of the star, its presence revealed through the appearance of strong UV high-excitation (resonance) absorption profiles; a cooler, lower velocity wind ($<$ 100 km s^{-1}) emerges from the more equatorial regions, and described by narrow low-excitation emission lines (Zickgraf et al. 1985). Subsequently the increase from the slower velocity of 300 km s^{-1} for the Al III and S IV lines to the much higher (more than double) velocity of the C IV and Si IV lines suggest a spatial distribution of similarly latitude-dependent outflow which here is being viewed pole-on. However the apparent absence of the N V $\lambda\lambda$ 1238.82, 1242.80 doublet in IUE data lets down this analogy as in a Be star's wind this doublet would appear strongly in emission.

Asymmetric wind properties, such as have been considered in this chapter, add to the ongoing debate concerning the often non-spherical appearance of an increasing number of young planetary nebulae, many of which exhibit axi- and point-symmetries (Sahai & Trauger 1998). If the occurrence of the high mass-loss superwind towards the end of the AGB stage is asymmetric then the subsequent interaction between the wind and the circumstellar material will likewise be asymmetric, which may result in a complex

nebula. The HST images of Hen 2-138 and Hen 2-131 both show non-spherically symmetric formations: the former has an overall elliptical shape with many bubble-like structures along its outer edge, appearing in a point-symmetry arrangement around the central star; the latter is less elliptic, also with bubble-like structures along its edge, but not in as complex an arrangement as in Hen 2-138.

One theoretical mechanism leading to an asymmetric outflow is the creation of a sub-surface magnetic dynamo, born out of a significant differential rotation between the contracting core and expanding envelope of an AGB star, with a transfer of angular momentum speeding up the core's rotation while slowing down that of the envelope (Blackman et al. 2001). The effect of rapid rotation upon line-driven outflows can lead to a latitude dependent mass-loss rate, which is itself dependent upon the surface radiative flux and effective surface gravity which, when gravity darkening is taken into account, is much greater at the poles than at the equator (Dwarkadas & Owocki 2003; Dwarkadas 2004), causing an asymmetric outflow and evolving into a bipolar nebula. Indeed, the apparent asymmetry of the Hen 2-138 outflow might be attributed to the central star being a rapid rotator, with the added dichotomy of the CMFGEN fitting possibly indicating that one is observing the central star from a point somewhere between the hotter, faster polar wind, and the cooler, slower equatorial outflow.

It has been suggested that the formation and evolution of non-spherical nebulae may sometimes be caused by binary systems, and that around 15% of planetary nebulae are part of a short period (< 3 days) binary system (Bond 2000); however other radial velocity-based survey of CSPNs have provided binary system estimates of around 40-60% (Sorensen & Pollacco 2003), or even over 90% (De Marco et al. 2004). The deep-seated near-photosperic lines studied in this chapter have shown that although they exhibit clear variability in that their enhanced absorption features migrate from the blue towards the red, seen particularly in the temporal variability exhibited by Hen 2-138 and the patterns displayed for the He I λ 4026.19, He I λ 4471.48 lines, these do not possess the more sinusoidal side-to-side pattern of a more regular radial velocity shifts. Instead these may depict prograde non-radial pulsations (NRPs), and indeed, as the migration shown is blue-to-red, such features cannot be attributed to the effects of a stellar wind which would cause absorption feature migration from red-to-blue velocities; the prescence of the wind can only be seen in the more clearly defined P Cygni profiles as seen in the He I λ 5875.62 line and the UV resonance lines of the IUE (UV) and FUSE (FUV) spectra.

The temporal analysis of three nights' time-series data, obtained from the ESO 3.6m optical telescope and the HARPS spectrograph, have enabled the investigation into temporally-variable phenomena located towards the near-photospheric base of the wind. Indeed, structure has been observed in this region for all three objects, and for each Fourier periodogram analysis has been applied to the time-series data of the helium lines as well as other metal lines (e.g. the deep-wind C IV λ 5801.33 absorption line). The strongest power responses of potential modulation frequencies were attributable to the photospheric helium lines, and through a stepped selection process, subsequent modulation periods have been tested via their application to a period-phased greyscale imaging process. This has had the result that the aforementioned helium lines of Hen 2-138 have been greyscale-phased over a period of $\sim$0.34 days; Hen 2-131 over a period of $\sim$0.48 days; and NGC 2392 over a period of $\sim$0.23 days, with a second potential modulation period of $\sim$0.30 days.

It has been observed that these time-series studies of young, H-rich CSPNs have provided evidence of potentially modulated structures within the lower wind regions, and, as seen in the blue to red migrations of lines He I λ 4026 and He I λ 4471, if such features are evidence of non-radial pulsations (NRPs), these might provide the origins of photospherically-originating structures, carried outwards from the central star via co-rotating interaction regions (CIRs). Fullerton et al. (1996) observed a prolific manifestation (77% of their sample) of variability in photosperic absorption line profiles in optical spectra of O stars, variability which quite possibly arises from NRPs; and in considering the similarly wide proliferation of O stars exhibiting variable winds, demonstrated by the appearances and migrations of DACs in UV P Cygni profiles, the possibility of a physical connection between the two is proposed. Cranmer & Owocki (1996) have also considered a connection between photospheric disturbances and the appearances and migrations of DACs further out in the stellar wind: their proposed mechanism is the aforementioned CIRs – the interface between co-rotating 'streams' of higher and lower density material, spreading out spirally from the stellar surface, caused by so-called bright spots (low velocity - high density), and dark spots (high velocity - low density); the fast streams collide with the slower streams, the resulting shock interaction producing a plateau in the velocity gradient, and a subsequent localised increase in the absorptive optical depth.

de Jong et al. (2001) speculate upon the action of CIRs providing a connection between their role in the manifestation and recurrence of DACs in UV resonance line profiles and similarly varying, i.e. coincidental in phase, with maxima in blue-shifted Hα profiles – a

connection which leads to the suggestion that the variability observed in the stellar wind must originate near the stellar surface, and that the action of the CIR model is a viable mechanism by which to transport the density-related markers of such surface disturbances. They consider small magnetic field structures as a possible cause of the perturbation effects upon the surface, however their magnetic field measurements prove inconclusive; likewise in considering the possibility of NRPs providing the causal mechanism for the surface density disturbances – to be carried into the UV wind regions via CIR spirals – these results are also inconclusive in that the recorded NRP period of around 3.5 hours is much faster than the modulation period observed in the appearance of DACs, at around 2.1 days.

Chapter 6

Conclusion

6.1 Structure in Stellar Winds

The prime motivation for this thesis was to explore whether the stellar outflows of H-rich central stars of planetary nebulae possessed a degree of structure such as that has been observed within the outflows of the hotter and more massive O stars.

Firstly, time-series UV spectra obtained for the Cat's Eye Nebula, NGC 6543, from the archive of the Far Ultraviolet Spectroscopic Explorer was examined for evidence of stellar wind variability and it was found that the outflow emanating from the central star is exhibits unsaturated P v P Cygni profile variability on a time-scale of hours in the form of recurrent additional optical depth absorption features which are seen to migrate blueward through the absorption troughs. This DAC-like behaviour is similar to that exhibited by the presence of DACs in UV data of hot, luminous OB stars. In comparing the 'DAC-like' properties of NGC 6543, as seen in this study, to those formerly observed in various studies of OB stars (e.g. Kaper et al. 1996; Prinja 1998; Fullerton et al. 2006*b*), the parameters are remarkably similar, including the flow-time-scaled (linear) acceleration of ~ 26 km s^{-1} for NGC 6543, when the similar acceleration of an example O star is of the same order at ~ 10 km s^{-1}.

In order to investigate whether this similarity in the physicality of the respective outflows is just coincidental for NGC 6543 alone, or not, the following chapter was concerned with trying to observe similar variable phenomena – the blueward-migrating DAC-like fea-

tures appearing within the absorption troughs of the P V $\lambda\lambda$ 1118, 1128 doublet – could be observed in the outflows of other CSPNs. However time-series UV spectra is limited and so of four other CSPNs has been subjected to similar time-variance analysis techniques: the TVS analysis had been applied to the time-series spectra available and subsequent greyscale displays have provided image-based representations of the variability contained therein. Of the four central stars examined, blueward migrating DACs were observed in the temporal greyscale images of the (limited) UV spectra for two objects, namely NGC 6826 and IC 2149, the DAC-like structures of both of which were measured as to their blueward velocity migration in time, and for which the former was shown to possess a flow-time-scaled approximate (linear) acceleration of $\sim$25 km s^{-1}, and $\sim$29 km s^{-1} for the latter – both close to the $\sim$ 26 km s^{-1} measured for NGC 6543. The similarities of flow-time acceleration suggest that might be a typical value i.e. $\sim$ 20 km s^{-1} for CSPNs in general, but without more extensive time-series – certainly not the wealth of UV spectra as available for O stars – this would be difficult to prove. Nevertheless, it does goes further to suggest the possibility of a common frame of reference for CSPN DAC-like behaviour.

The lack of extensive UV time-series data available for CSPNs has prompted the investigation into the optical wavelength range and therefore able to observe and analyse temporal phenomena in the nearer-photospheric region of the stellar wind. Here the sole P Cygni wind line is that of He I λ 5875.62, however analysis of other photospheric helium lines within this region, particularly the absorption lines of He I λ 4026.19 and He I λ 4471.48, as well as photospheric metal lines e.g. C IV λ 5801.33 allow the investigation of potential variability at the base of the wind.

The SEI resonance line model fits (of single UV exposures only) suggest that Hen 2-138 possesses a dual-component wind: the lower ion species of Al III λ 1854.72 and S IV λ 1072.97 are modelled with a wind terminal velocity of -300 km s^{-1}, whereas the higher ion species of C IV λ 1548.20 and Si IV λ 1393.76 required the requisite wind terminal velocity parameter for SEI stepped up to -700 km s^{-1}. Subsequent analysis by Miguel Urbaneja (IfA, Hawai'i), using CMFGEN, confirms a higher/lower velocities are required to match higher/lower ion species, hinting at a laterally-dependent outflow or 'hybrid' wind. SEI modelling for the central stars of Hen 2-131 and NGC 2392 have not provided evidence to suggest a dual-component wind of either central star, both allowing (for the most part) modelling of wind profiles with a terminal velocity of $v_\infty = -400$ km s^{-1}.

However, the temporal analysis of three night's time-series data, obtained from the

ESO 3.6 m optical telescope and the HARPS spectrograph, has enabled the investigation into temporally-variable phenomena located towards the near-photospheric base of the wind. Indeed, structure has been observed in this region for all three objects and for each Fourier periodogram analysis has been applied to the time-series data of the helium lines as well as other metal lines (e.g. the deep-wind C IV λ 5801.33 absorption line). The strongest power responses of potential modulation frequencies was attributable to the photospheric helium lines and subsequent modulation periods have been tested via their application to a period-phased greyscale imaging process with the result that the aforementioned helium lines of Hen 2-138 have been greyscale-phased over a period of $\sim$0.35 days; Hen 2-131 over a period of $\sim$0.48 days; and NGC 2392 over a period of $\sim$0.23 days, and also a second potential modulation period of $\sim$0.30 days.

The modulation of the seemingly blue-to-red structures, as observed in the phased greyscales of Hen 2-138, are interesting in that they might suggest the manifestation of Non-Radial Pulsations (NRPs), which may or may not provide the photospheric mechanism responsible for the density fluctuations which travel through the stellar outflow via Co-Rotating Interaction Regions (CIRs). As movement of these regions in the outer wind are observed by the motions of Discrete Absorption Components (DACs) which are observed to migrate through the absorption troughs of UV spectra. The modulated movements of these structure have been observed ubiquitously in the UV spectra of winds from OB stars. The outflows of CSPNs have also demonstrated variable winds in that UV spectroscopic exposures, taken months or years apart, have also shown changing absorption profiles of UV resonance lines. However, without extensive time-series UV data, investigations into wind-born structures have not been carried out to the extent that they have been for OB stars (although similarities between the winds of H-rich CSPNs and OB stars has been suspected since the initial discoveries of the changing shape of the CSPN P Cygni resonance line profiles). With the availability of FUSE time-series UV data, the more temporally-based spectroscopic study of the variable stellar wind of CSPNs has begun, and the early indications are that, in terms of the modulated behaviour of their UV outflow, central stars are more closely akin to OB stars than previously thought.

6.2 Future Work

It has also become apparent in recent years that a quantitative of the clumped nature of a stellar wind would confirm the suspicion that it is the existence of structure within a porous wind – and therefore not smooth as previously assumed – that is a key ingredient in the manifestation of such phenomena as XUV ionisation and X-rays (Oskinova et al. 2007).

Sobolev with Exact Integration (SEI) resonance line profile modelling, which has been used extensively in the work behind this thesis assumes a smooth, homogenous wind, and takes no account of clumping – whereas it has been shown that clumping, and by extension porosity, must be taken into account in order to be able to accurately model line profiles in the wind (e.g. Bouret et al. 2005; Kudritzki et al. 2006; Oskinova et al. 2007).

To this end the Si IV $\lambda\lambda$ 1393.76, 1402.77 doublet, taken from UV data of B supergiants, has been analysed in terms of the ratios between the two components (Prinja & Massa 2010). A better understanding of the relationship between the doublet components is key to understanding the nature of the density of the stellar wind: for a smooth, homogeneous wind, the ratio of the optical depths as modelled from the absorption troughs of the doublet components should be equal to the ratio between their respective oscillator strengths. If, however, the star was partially obscured by optically thick clumps, then the ratio between the components would be ~ 1, as the radial optical depth would only depend upon the covering factor of the clumps, which would therefore reduce the doublet ratio by a factor of between 1 and 2.

A key criterion in seeking suitable data, as well as possessing well-developed but unsaturated absorption troughs, is the velocity separation of the two components of the Si IV doublet, namely whether they possess (wind) terminal velocities which are less than 0.5 of the velocity separation between the two: if so, then two two components of the doublet can be modelled *separately*, that is, as if they were two singlets, and hence radiatively decoupled.

The absorption profile modelling is undertaken using the SEI method, and as the two components are able to be modelled as singlets, the modelling process provides a set of $\tau_{\rm rad}(w)$ for each component, which can then be combined to produce a this set of $\tau_{\rm rad}^{\rm blue}(w)/\tau_{\rm rad}^{\rm red}(w)$. Only $\tau_{\rm rad}(w)$ values of between 0.3 – 5.0 were considered so as to avoid lines either too weak or saturated. It is reported that in the vast majority of cases

the ratios yield values which are less than 2.01 (which would be that expected from a smooth wind), and the majority range between 1.0 and 1.5, with the average being 1.46, so it would seem that the results indicate that a porous, heavily clumped (optically-thick) wind. It is also noted that the stars are scattered over the temperature ranges from B0 to B5, and the reduced $\tau_{\rm rad}(w)$ ratio is seen across (almost) this range, which would indicate that the reduced ratio phenomena is not dependent upon the temperature of the star.

An alternative method of investigation was employed for those stars whose Si IV doublet separation was in excess of 1000 $\mathrm{km\,s^{-1}}$, that is they two components could not be effectively decoupled, and therefore could not be modelled (via SEI) separately. Instead SEI models were applied for the doublet in the normal manner, but the difference in this method was that the ratio of the doublet oscillator strengths, f, is now treated as a free parameter, and adjusted so as to obtain a best-fit for the doublet. Most of these best-fit f-values are found to be between ~ 1 and 2. For a fixed mass-loss rate, velocity law and ion fraction, the f-value (the ratio of the oscillator strengths) for the is the equivalent of the optical depth ratios for the decoupled doublets. As with the optical depth ratios of the first group of stars, the results from the second sample, the oscillator strength ratios between the blue and red components fall between 1.0 and 2.0, with the majority between 1.0 and 1.5, and are therefore comparable with the results of the former set.

As this approach has proven beneficial to the study of B stars, particularly in its conclusive demonstration of the validity of the concept of the clumped nature of stellar winds – an assumption which should improve accuracy in the calculation of stellar mass-loss rates – it would seem pertinent to extend this doublet-ratio approach to the modelling of P Cygni absorption profiles in the outflows of central stars.

However, in order to be able to carry on this recent development into the nature of the stellar winds of central stars, and indeed all other aspects of the research outlined in this thesis, there has to be an extensive wealth of data available – particularly given the high-quantity exposure-dependence of time-series analysis. Therefore only until the amount of spectroscopic data available of CSPNs matches the extent of the same for OB stars will one be able to pursue stellar wind investigations into the former as they have been for the latter.

.1 Appendix A: SEI Plots of Two DAC Sequences

Presented here are the two sets of eight SEI models corresponding to the two DAC-progression sequences as mentioned in Chapter 3, and for each the central velocity of the blueward-migrating DAC was estimated, and subsequent estimates of DAC acceleration were obtained.

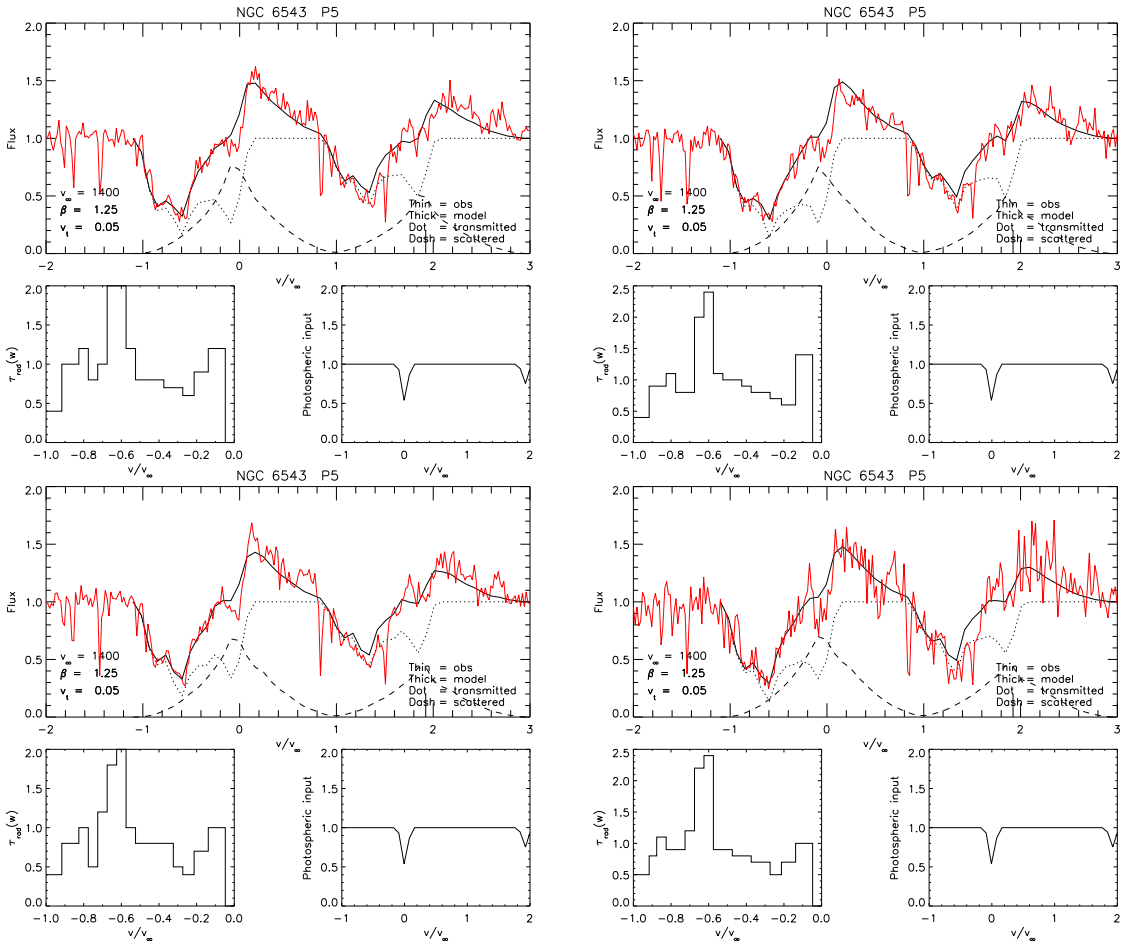

Fig. .1. The first four SEI models of the 1st P V DAC-progressive sequence for Hen 2-138: above No. 1 (l), No. 2 (r); below No. 3 (l), No. 4 (r).

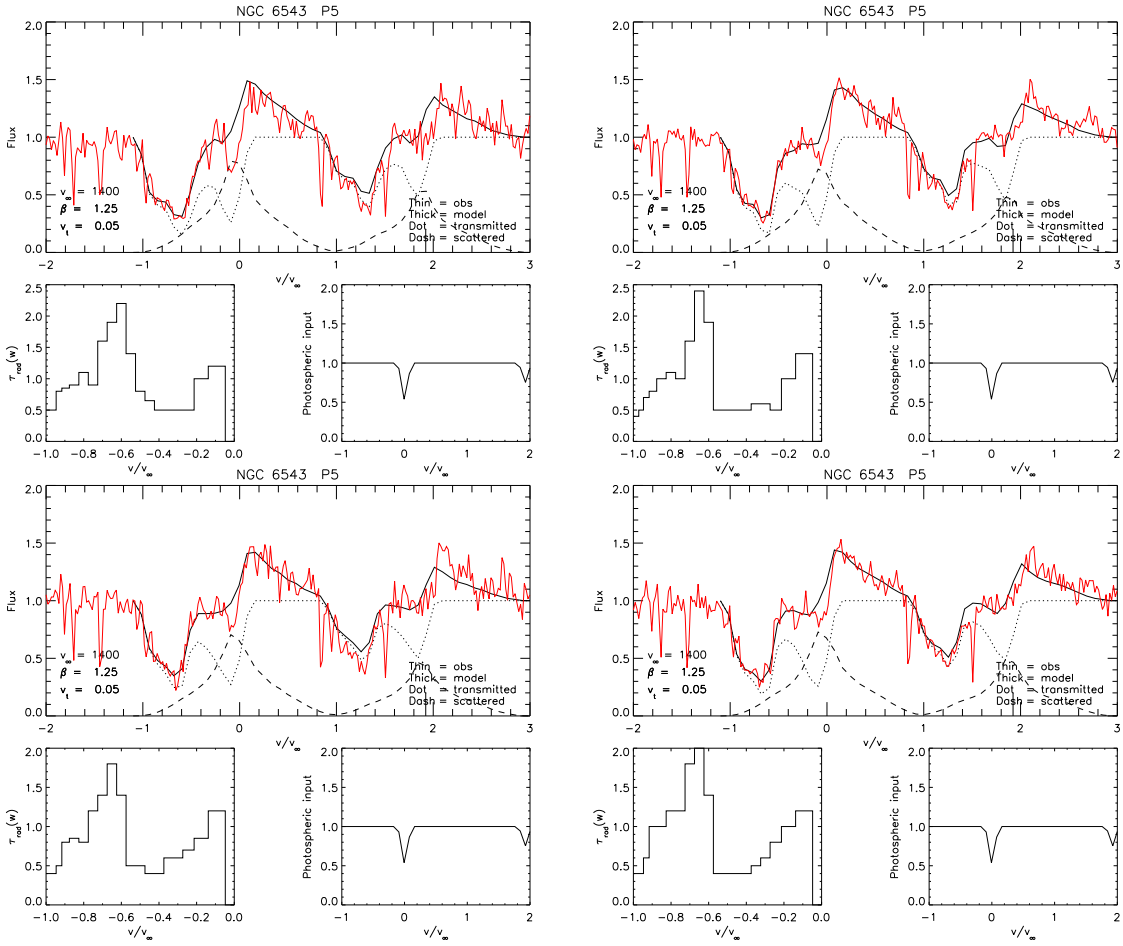

Fig. .2. The second four SEI models of the 1st P v DAC-progressive sequence for Hen 2-138: above No. 5 (l), No. 6 (r); below No. 7 (l), No. 8 (r).

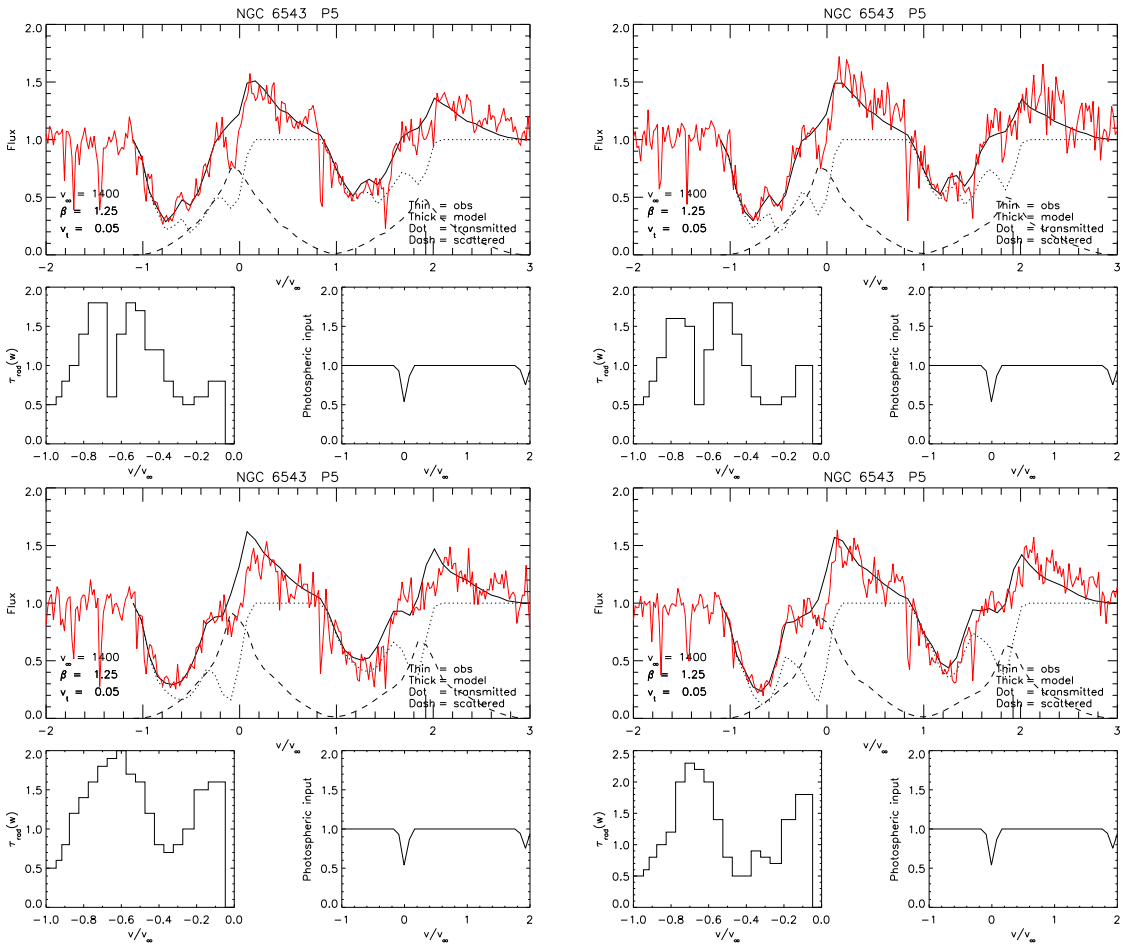

Fig. .3. The first four SEI models of the 2^{nd} P v DAC-progressive sequence for Hen 2-138: above No. 1 (l), No. 2 (r); below No. 3 (l), No. 4 (r).

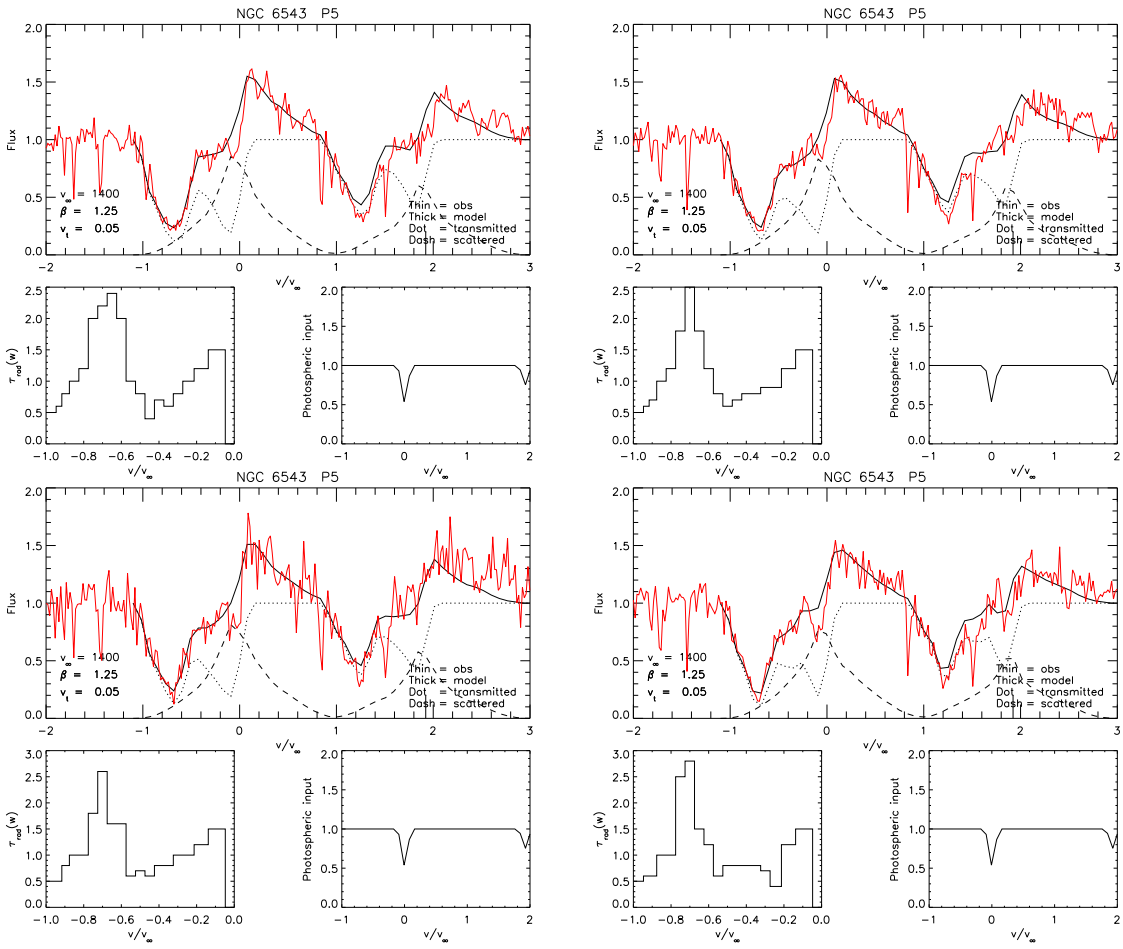

Fig. .4. The second four SEI models of the 2^{nd} P v DAC-progressive sequence for Hen 2-138: above No. 5 (l), No. 6 (r); below No. 7 (l), No. 8 (r).

The last (single) SEI model presented is that of the 'non-DAC case' from which the ratio of τ_{DAC}/τ_{min} for each corresponding central velocity was derived for each individual exposure in these two sequences – also detailed in Chapter 3.

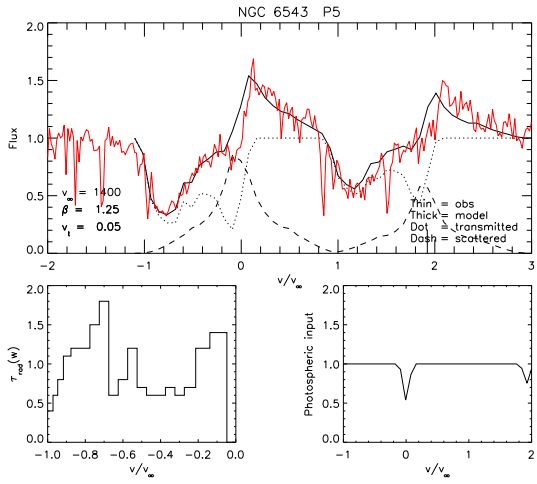

Fig. .5. The SEI model of the 'non-DAC case'.

.2 Appendix B: Full 2-D Fourier Spectra Displays

Presented here are the full two-dimensional Fourier analysis plots for Hen 2-138, Hen 2-131, and NGC 2392 from Chapter 5. Only those lines which produced a substantial response above the 95 % confidence line in the TVS analysis were then subjected to further Fourier analysis; therefore not all lines detailed in the previous appendix, are represented here.

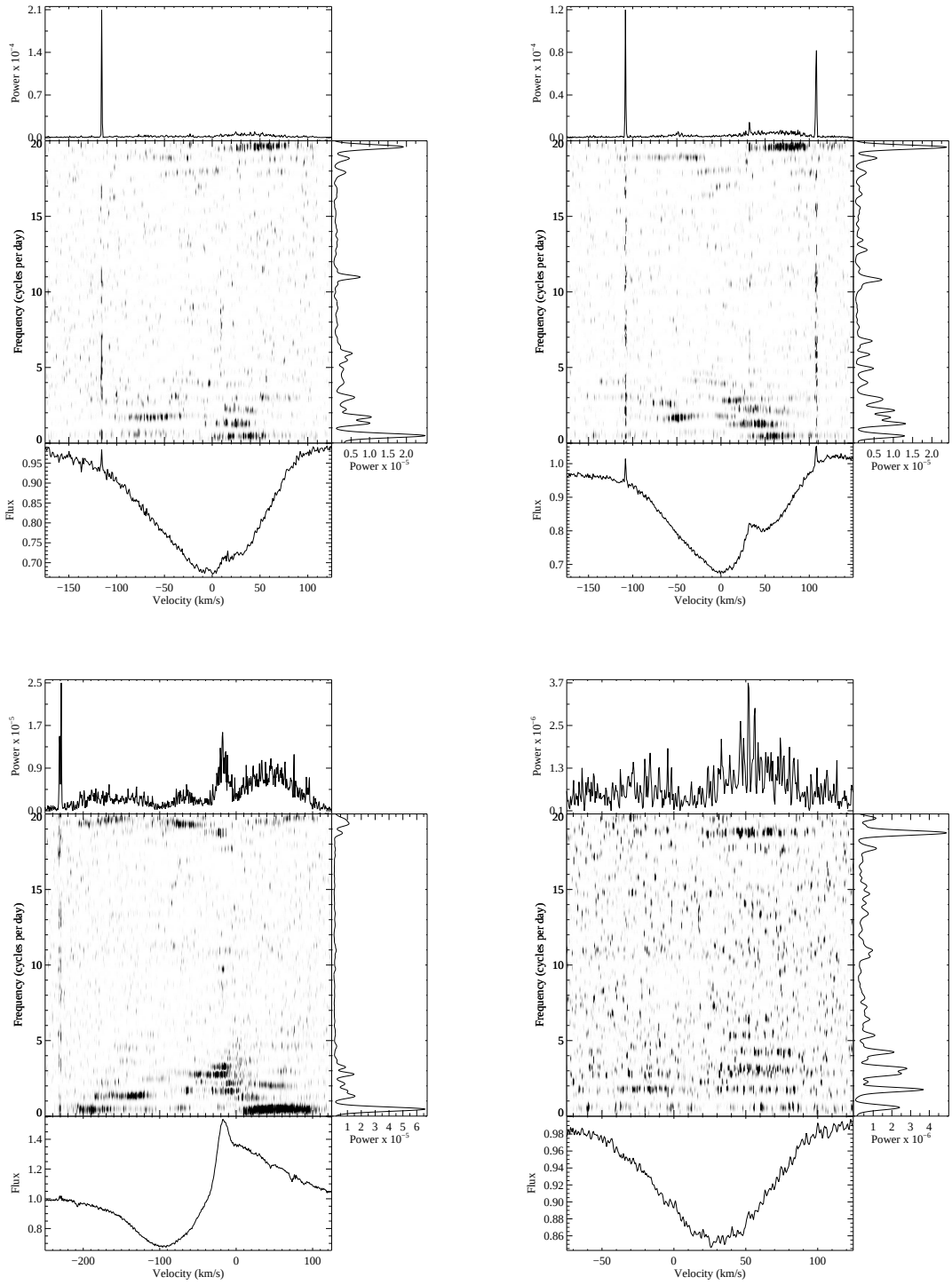

Fig. .6. Full displays of Fourier spectral analysis for Hen 2-138: above He I λ 4026 (l), He I λ 4471 (r); below He I λ 5876 (l), C IV λ 5801 (r).

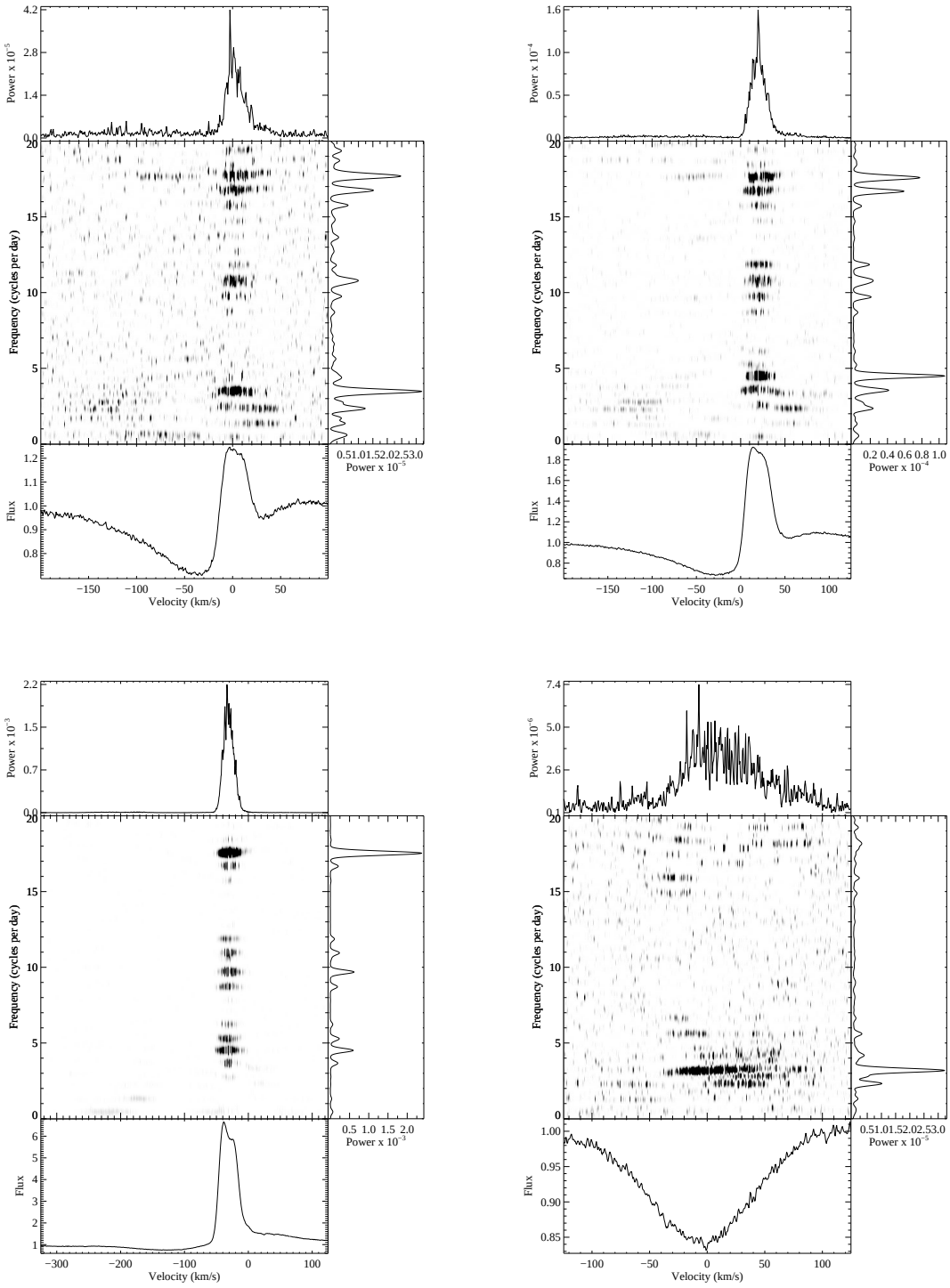

Fig. .7. Full displays of Fourier spectral analysis for Hen 2-131: above He I λ 4026 (l), He I λ 4471 (r); below He I λ 5876 (l), C IV λ 5801 (r).

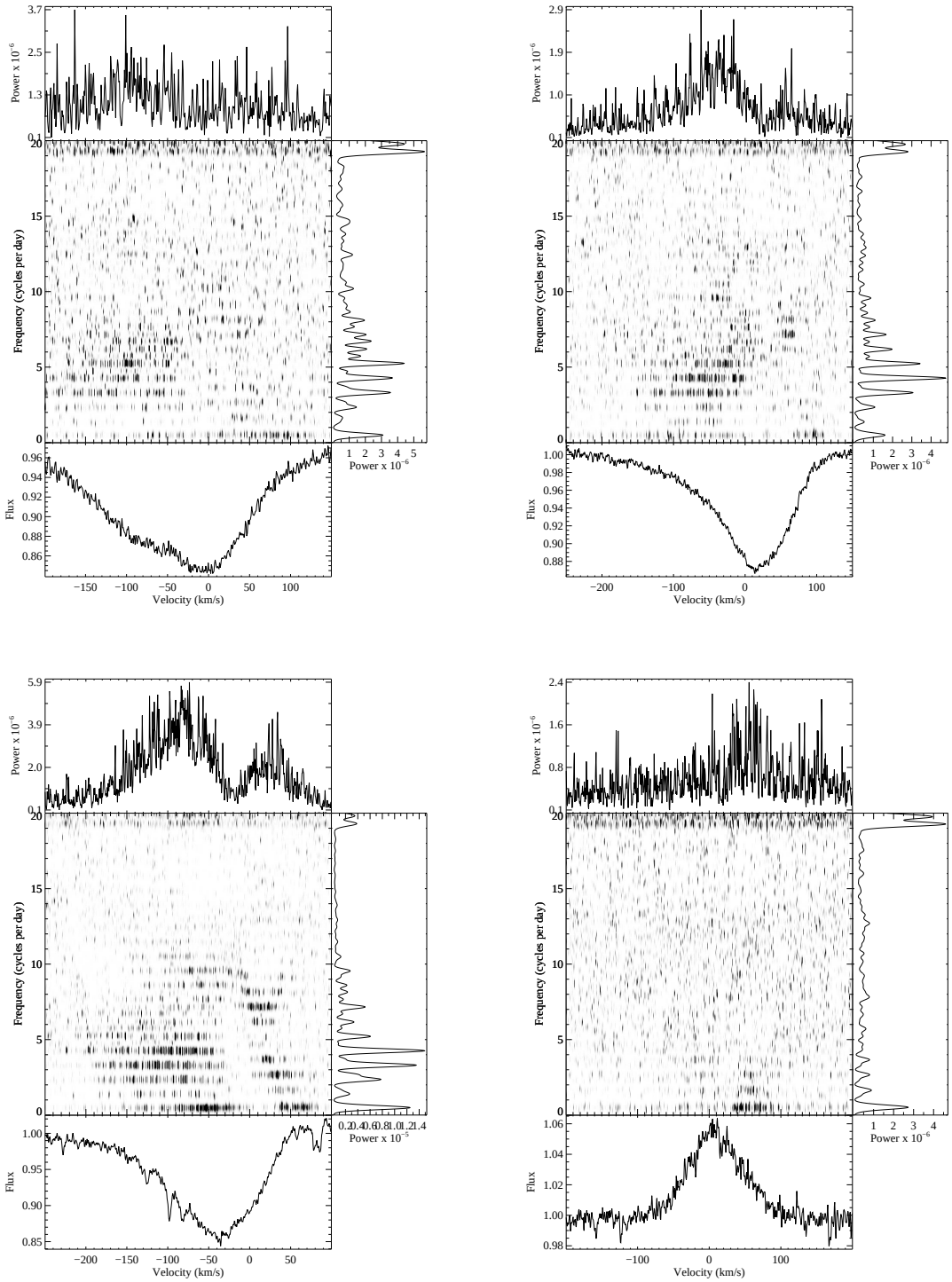

Fig. .8. Full displays of Fourier spectral analysis for NGC 2392: above He I λ 4026 (l), He I λ 4471 (r); below He I λ 5876 (l), C IV λ 5801 (r).

Bibliography

Abbott, D. C., Bieging, J. H. & Churchwell, E., 1981, *ApJ*, **250**, 645

Acker, A., 1976, *Publication de l'Observatoire de Strasbourg*, **4**, 1

Anderson, L. S., 1989, *ApJ*, **339**, 558

Auer, L. H. & Mihalas, D., 1969, *ApJ*, **158**, 641

Balick, B., 2004, *AJ*, **127**, 2262

Bell, S. A., Pollacco, D. L. & Hilditch, R. W., 1994, *MNRAS*, **267**, 1053

Blackman, E. G., Frank, A., Markiel, J. A., Thomas, J. H. & Van Horn, H. M., 2001, *Nature*, **409**, 485

Bond, H. E., 2000, in J. H. Kastner, N. Soker, & S. Rappaport (ed.), *Asymmetrical Planetary Nebulae II: From Origins to Microstructures*, volume 199 of *Astronomical Society of the Pacific Conference Series*, pp. 115–+

Bond, H. E. & Ciardullo, R., 1989, in G. Wegner (ed.), *IAU Colloq. 114: White Dwarfs*, volume 328 of *Lecture Notes in Physics, Berlin Springer Verlag*, pp. 473–+

Bouret, J., Lanz, T. & Hillier, D. J., 2005, *A&A*, **438**, 301

Cassinelli, J. P., Cohen, D. H., Macfarlane, J. J., Sanders, W. T. & Welsh, B. Y., 1994, *ApJ*, **421**, 705

Cassinelli, J. P., Miller, N. A., Waldron, W. L., MacFarlane, J. J. & Cohen, D. H., 2001, *ApJL*, **554**, L55

Castor, J. I., Lutz, J. H. & Seaton, M. J., 1981, *MNRAS*, **194**, 547

Cerruti-Sola, M. & Perinotto, M., 1989, *ApJ*, **345**, 339

Chu, Y., Guerrero, M. A., Gruendl, R. A., Williams, R. M. & Kaler, J. B., 2001, *ApJL*, **553**, L69

Cranmer, S. R. & Owocki, S. P., 1996, *ApJ*, **462**, 469

de Jong, J. A., Henrichs, H. F., Kaper, L., Nichols, J. S., Bjorkman, K., Bohlender, D. A., Cao, H., Gordon, K., Hill, G., Jiang, Y., Kolka, I., Morrison, N., Neff, J., O'Neal, D., Scheers, B. & Telting, J. H., 2001, *A&A*, **368**, 601

de Koter, A., Hubeny, I., Heap, S. R. & Lanz, T., 1996, in C. S. Jeffery & U. Heber (ed.), *Hydrogen Deficient Stars*, volume 96 of *Astronomical Society of the Pacific Conference Series*, pp. 141–+

de Koter, A., Schmutz, W. & Lamers, H. J. G. L. M., 1993, *A&A*, **277**, 561

De Marco, O., Bond, H. E., Harmer, D. & Fleming, A. J., 2004, *ApJL*, **602**, L93

Dreizler, S. & Werner, K., 1993, *A&A*, **278**, 199

Dwarkadas, V. V., 2004, in M. Meixner, J. H. Kastner, B. Balick, & N. Soker (ed.), *Asymmetrical Planetary Nebulae III: Winds, Structure and the Thunderbird*, volume 313 of *Astronomical Society of the Pacific Conference Series*, pp. 430–+

Dwarkadas, V. V. & Owocki, S., 2003, in S. Kwok, M. Dopita, & R. Sutherland (ed.), *Planetary Nebulae: Their Evolution and Role in the Universe*, volume 209 of *IAU Symposium*, pp. 467–+

Eversberg, T., Lepine, S. & Moffat, A. F. J., 1998, *ApJ*, **494**, 799

Fullerton, A. W., Gies, D. R. & Bolton, C. T., 1996, *ApJSS*, **103**, 475

Fullerton, A. W., Massa, D. L. & Prinja, R. K., 2006*a*, *ApJ*, **637**, 1025

Fullerton, A. W., Massa, D. L., Prinja, R. K., Howarth, I. D., Willis, A. J. & Owocki, S. P., 2006*b*, in G. Sonneborn, H. W. Moos, & B.-G. Andersson (ed.), *Astrophysics in the Far Ultraviolet: Five Years of Discovery with FUSE*, volume 348 of *Astronomical Society of the Pacific Conference Series*, pp. 130–+

Fullerton, A. W., Massa, D. L., Prinja, R. K., Owocki, S. P. & Cranmer, S. R., 1997, *A&A*, **327**, 699

Georgiev, L. N., Hillier, D. J., Richer, M. G. & Arrieta, A., 2006, in M. J. Barlow & R. H. Méndez (ed.), *Planetary Nebulae in our Galaxy and Beyond*, volume 234 of *IAU Symposium*, pp. 401–402

Guerrero, M. A., Chu, Y., Gruendl, R. A., Williams, R. M. & Kaler, J. B., 2001, *ApJL*, **553**, L55

Harrington, J. P. & Borkowski, K. J., 1994, in *Bulletin of the American Astronomical Society*, volume 26 of *Bulletin of the American Astronomical Society*, pp. 1469–+

Haser, S. M., Pauldrach, A. W. A., Lennon, D. J., Kudritzki, R.-P., Lennon, M., Puls, J. & Voels, S. A., 1998, *A&A*, **330**, 285

Herald, J. E. & Bianchi, L., 2004, *ApJ*, **609**, 378

Hillier, D. J., 1990, *A&A*, **231**, 116

Hillier, D. J., Kudritzki, R. P., Pauldrach, A. W., Baade, D., Cassinelli, J. P., Puls, J. & Schmitt, J. H. M. M., 1993, *A&A*, **276**, 117

Hillier, D. J., Lanz, T., Heap, S. R., Hubeny, I., Smith, L. J., Evans, C. J., Lennon, D. J. & Bouret, J. C., 2003, *ApJ*, **588**, 1039

Hillier, D. J. & Miller, D. L., 1998, *ApJ*, **496**, 407

Hubeny, I., 1988, *Computer Physics Communications*, **52**, 103

Hubeny, I., 2003, in I. Hubeny, D. Mihalas, & K. Werner (ed.), *Stellar Atmosphere Modeling*, volume 288 of *Astronomical Society of the Pacific Conference Series*, pp. 17–+

Hubeny, I., Hummer, D. G. & Lanz, T., 1994, *A&A*, **282**, 151

Hubeny, I. & Lanz, T., 1995, *ApJ*, **439**, 875

Hummer, D. G., Berrington, K. A., Eissner, W., Pradhan, A. K., Saraph, H. E. & Tully, J. A., 1993, *A&A*, **279**, 298

Hummer, D. G. & Mihalas, D., 1988, *ApJ*, **331**, 794

Hutton, R. G. & Mendez, R. H., 1993, *A&A*, **267**, L8

Iglesias, C. A. & Rogers, F. J., 1991, *ApJ*, **371**, 408

Kaper, L., Henrichs, H. F., Nichols, J. S., Snoek, L. C., Volten, H. & Zwarthoed, G. A. A., 1996, *A&AS*, **116**, 257

Kudritzki, R., Lennon, D. J. & Puls, J., 1995, in J. R. Walsh & I. J. Danziger (ed.), *Science with the VLT*, pp. 246–+

Kudritzki, R. & Puls, J., 2000, *Ann. Rev. Astr. Astrophys.*, **38**, 613

Kudritzki, R. P., Mendez, R. H., Puls, J. & McCarthy, J. K., 1997, in H. J. Habing & H. J. G. L. M. Lamers (ed.), *Planetary Nebulae*, volume 180 of *IAU Symposium*, pp. 64–+

Kudritzki, R. P., Urbaneja, M. A. & Puls, J., 2006, in M. J. Barlow & R. H. Méndez (ed.), *Planetary Nebulae in our Galaxy and Beyond*, volume 234 of *IAU Symposium*, pp. 119–126

Lamers, H. J. G. L. M. & Cassinelli, J. P., 1999, *Introduction to Stellar Winds*

Lamers, H. J. G. L. M., Cerruti-Sola, M. & Perinotto, M., 1987, *ApJ*, **314**, 726

Lanz, T. & Hubeny, I., 2003, *ApJSS*, **146**, 417

Lebouteiller, V., Kuassivi & Ferlet, R., 2005, *A&A*, **443**, 509

Markova, N., Puls, J., Scuderi, S. & Markov, H., 2005, *A&A*, **440**, 1133

Massa, D., Fullerton, A. W., Nichols, J. S., Owocki, S. P., Prinja, R. K., St-Louis, N., Willis, A. J., Altner, B., Bolton, C. T., Cassinelli, J. P., Cohen, D., Cooper, R. G., Feldmeier, A., Gayley, K. G., Harries, T., Heap, S. R., Henriksen, R. N., Howarth, I. D., Hubeny, I., Kambe, E., Kaper, L., Koenigsberger, G., Marchenko, S., McCandliss, S. R., Moffat, A. F. J., Nugis, T., Puls, J., Robert, C., Schulte-Ladbeck, R. E., Smith, L. J., Smith, M. A., Waldron, W. L. & White, R. L., 1995, *ApJL*, **452**, L53+

Massa, D., Fullerton, A. W., Sonneborn, G. & Hutchings, J. B., 2003, *ApJ*, **586**, 996

Méndez, R. H., 1989, in S. Torres-Peimbert (ed.), *Planetary Nebulae*, volume 131 of *IAU Symposium*, pp. 261–272

Méndez, R. H., 1991, in *NATO ASIC Proc. 341: Stellar Atmospheres - Beyond Classical Models*, pp. 331–+

Méndez, R. H., Forte, J. C. & López, R. H., 1986, *Revista Mexicana de Astronomia y Astrofisica*, **13**, 119

Méndez, R. H., Herrero, A. & Manchado, A., 1990, *A&A*, **229**, 152

Méndez, R. H., Kudritzki, R. P. & Herrero, A., 1992, *A&A*, **260**, 329

Méndez, R. H., Kudritzki, R. P., Herrero, A., Husfeld, D. & Groth, H. G., 1988, *A&A*, **190**, 113

Méndez, R. H., Verga, A. D. & Kriner, A., 1983, *Revista Mexicana de Astronomia y Astrofisica*, **8**, 175

Morton, D. C., 2003, *ApJSS*, **149**, 205

Olson, G. L., 1982, *ApJ*, **255**, 267

Oskinova, L. M., Hamann, W. & Feldmeier, A., 2007, *A&A*, **476**, 1331

Owocki, S. P., 1994, *Ap&SS*, **221**, 3

Owocki, S. P., Castor, J. I. & Rybicki, G. B., 1988, *ApJ*, **335**, 914

Owocki, S. P. & Cohen, D. H., 2006, *ApJ*, **648**, 565

Patriarchi, P. & Perinotto, M., 1991, *A&AS*, **91**, 325

Patriarchi, P. & Perinotto, M., 1995, *A&AS*, **110**, 353

Patriarchi, P. & Perinotto, M., 1997, *A&AS*, **126**, 385

Pauldrach, A. W. A., Hoffmann, T. L. & Lennon, M., 2001, *A&A*, **375**, 161

Pauldrach, A. W. A., Hoffmann, T. L. & Méndez, R. H., 2003, in S. Kwok, M. Dopita, & R. Sutherland (ed.), *Planetary Nebulae: Their Evolution and Role in the Universe*, volume 209 of *IAU Symposium*, pp. 177–+

Pauldrach, A. W. A., Hoffmann, T. L. & Méndez, R. H., 2004, *A&A*, **419**, 1111

Pauldrach, A. W. A., Kudritzki, R. P., Puls, J., Butler, K. & Hunsinger, J., 1994, *A&A*, **283**, 525

Perinotto, M., 1989, in S. Torres-Peimbert (ed.), *Planetary Nebulae*, volume 131 of *IAU Symposium*, pp. 293–300

Perinotto, M., 1993, in R. Weinberger & A. Acker (ed.), *Planetary Nebulae*, volume 155 of *IAU Symposium*, pp. 57–+

Perinotto, M., Cerruti-Sola, M. & Benvenuti, P., 1982, *A&A*, **108**, 314

Perinotto, M., Cerruti-Sola, M. & Lamers, H. J. G. L. M., 1989, *ApJ*, **337**, 382

Pringle, J. E., 1981, *Ann. Rev. Astr. Astrophys.*, **19**, 137

Prinja, R. K., 1988, *MNRAS*, **231**, 21P

Prinja, R. K., 1998, in L. Kaper & A. W. Fullerton (ed.), *Cyclical Variability in Stellar Winds*, pp. 92–+

Prinja, R. K., Balona, L. A., Bolton, C. T., Crowe, R. A., Fieldus, M. S., Fullerton, A. W., Gies, D. R., Howarth, I. D., McDavid, D. & Reid, A. H. N., 1992, *ApJ*, **390**, 266

Prinja, R. K., Hodges, S. E., Massa, D. L., Fullerton, A. W. & Burnley, A. W., 2007, *MNRAS*, **382**, 299

Prinja, R. K., Hodges, S. E., Urbaneja, M. A. & Massa, D. L., 2010, *MNRAS*, **402**, 641

Prinja, R. K. & Howarth, I. D., 1986, *ApJSS*, **61**, 357

Prinja, R. K., Massa, D. & Fullerton, A. W., 2002, *A&A*, **388**, 587

Prinja, R. K. & Massa, D. L., 2010, *A&A*, **521**, L55+

Puls, J., Kudritzki, R., Herrero, A., Pauldrach, A. W. A., Haser, S. M., Lennon, D. J., Gabler, R., Voels, S. A., Vilchez, J. M., Wachter, S. & Feldmeier, A., 1996, *A&A*, **305**, 171

Puls, J., Owocki, S. P. & Fullerton, A. W., 1993, *A&A*, **279**, 457

Puls, J., Urbaneja, M. A., Venero, R., Repolust, T., Springmann, U., Jokuthy, A. & Mokiem, M. R., 2005, *A&A*, **435**, 669

Reed, D. S., Balick, B., Hajian, A. R., Klayton, T. L., Giovanardi, S., Casertano, S., Panagia, N. & Terzian, Y., 1999, *AJ*, **118**, 2430

Reid, A. H. N. & Howarth, I. D., 1996, *A&A*, **311**, 616

Roberts, D. H., Lehar, J. & Dreher, J. W., 1987, *AJ*, **93**, 968

Runacres, M. C. & Owocki, S. P., 2002, *A&A*, **381**, 1015

Sahai, R. & Trauger, J. T., 1998, *AJ*, **116**, 1357

Schneider, S. E., Terzian, Y., Purgathofer, A. & Perinotto, M., 1983, *ApJSS*, **52**, 399

Seaton, M. J., 1987, *Journal of Physics B Atomic Molecular Physics*, **20**, 6363

Sorensen, P. M. & Pollacco, D. L., 2003, in R. L. M. Corradi, J. Mikolajewska, & T. J. Mahoney (ed.), *Astronomical Society of the Pacific Conference Series*, volume 303 of *Astronomical Society of the Pacific Conference Series*, pp. 494–+

Wesson, R. & Liu, X., 2004, *MNRAS*, **351**, 1026

Zickgraf, F., Wolf, B., Stahl, O., Leitherer, C. & Klare, G., 1985, *A&A*, **143**, 421